Nuclear Science

OECD
OCDE

Ion and Slow Positron Beam Utilisation

Workshop Proceedings
Costa da Caparica, Portugal
15-17 September 1998

NUCLEAR • ENERGY • AGENCY

OECD PROCEEDINGS

NUCLEAR SCIENCE COMMITTEE

Proceedings of the Workshop on

ION AND SLOW POSITRON BEAM UTILISATION

Costa da Caparica, Portugal
15-17 September 1998

Jointly organised by
OECD/NEA
Centro de Fisica Nuclear da Universidade de Lisboa
Instituto Tecnologico e Nuclear (ITN)

NUCLEAR ENERGY AGENCY
ORGANISATION FOR ECONOMIC CO-OPERATION AND DEVELOPMENT

ORGANISATION FOR ECONOMIC CO-OPERATION AND DEVELOPMENT

Pursuant to Article 1 of the Convention signed in Paris on 14th December 1960, and which came into force on 30th September 1961, the Organisation for Economic Co-operation and Development (OECD) shall promote policies designed:

- to achieve the highest sustainable economic growth and employment and a rising standard of living in Member countries, while maintaining financial stability, and thus to contribute to the development of the world economy;
- to contribute to sound economic expansion in Member as well as non-member countries in the process of economic development; and
- to contribute to the expansion of world trade on a multilateral, non-discriminatory basis in accordance with international obligations.

The original Member countries of the OECD are Austria, Belgium, Canada, Denmark, France, Germany, Greece, Iceland, Ireland, Italy, Luxembourg, the Netherlands, Norway, Portugal, Spain, Sweden, Switzerland, Turkey, the United Kingdom and the United States. The following countries became Members subsequently through accession at the dates indicated hereafter; Japan (28th April 1964), Finland (28th January 1969), Australia (7th June 1971), New Zealand (29th May 1973), Mexico (18th May 1994), the Czech Republic (21st December 1995), Hungary (7th May 1996), Poland (22nd November 1996) and the Republic of Korea (12th December 1996). The Commission of the European Communities takes part in the work of the OECD (Article 13 of the OECD Convention).

NUCLEAR ENERGY AGENCY

The OECD Nuclear Energy Agency (NEA) was established on 1st February 1958 under the name of OEEC European Nuclear Energy Agency. It received its present designation on 20th April 1972, when Japan became its first non-European full Member. NEA membership today consists of all OECD Member countries, except New Zealand and Poland. The Commission of the European Communities takes part in the work of the Agency.

The primary objective of the NEA is to promote co-operation among the governments of its participating countries in furthering the development of nuclear power as a safe, environmentally acceptable and economic energy source.

This is achieved by:

- *encouraging harmonization of national regulatory policies and practices, with particular reference to the safety of nuclear installations, protection of man against ionising radiation and preservation of the environment, radioactive waste management, and nuclear third party liability and insurance;*
- *assessing the contribution of nuclear power to the overall energy supply by keeping under review the technical and economic aspects of nuclear power growth and forecasting demand and supply for the different phases of the nuclear fuel cycle;*
- *developing exchanges of scientific and technical information particularly through participation in common services;*
- *setting up international research and development programmes and joint undertakings.*

In these and related tasks, the NEA works in close collaboration with the International Atomic Energy Agency in Vienna, with which it has concluded a Co-operation Agreement, as well as with other international organisations in the nuclear field.

FOREWORD

Interest in material science and its related issues is increasing in order to improve existing nuclear energy production concepts, as well as to study future or advanced systems such as fusion reactors and accelerator-driven hybrid systems. In this context, the NEA Nuclear Science Committee examined different applications of ion and slow positron beams and noted that:

- The application area of ion beams had expanded in various research fields, for example for the production of new materials by the piling up of atomic layers and by implantation, and for the analysis of the depth profiles of atoms.

- Slow positron beams can form ultra-clean surfaces by identifying very small amounts of impurities at the surface level and annihilating the atoms concerned.

- Materials with precisely designed and controlled structures could be created by utilising a combination of ion and positron beams.

- Positron emission tomography (PET) and radiopharmaceuticals play an essential role in medical diagnosis.

Following this, the Committee decided to organise a workshop on application research using charged particles (ion and positron beams) in Costa da Caparica, Portugal on 15-17 September 1998. The objectives of the workshop were:

- to summarise current research using ion and positron beams, including the combined utilisation of related material diagnostics methods;

- to analyse the future possibilities of charged particle science, with special emphasis on material science applications and on medical applications, typically the ones relevant to PET and to the analysis of impurities in biomaterials;

- to make recommendations to the NEA on future activities suitable for international collaboration.

TABLE OF CONTENTS

EXECUTIVE SUMMARY

In June 1997, the NEA Nuclear Science Committee discussed and approved a proposal by the Japan Atomic Energy Research Institute to organise a workshop on applied research using ion and positron beams. Professor J. Soares (Lisbon University, Portugal) agreed to host the workshop in Portugal in the autumn of 1998.

The workshop was held on 15-17 September 1998 at Costa da Caparica near Lisbon and was attended by 31 scientists from 11 countries.

The scientific programme of the workshop was organised by a committee consisting of Dr. E. Menapace (Ente Nazionale Energie Alternative, Bologna, Italy), Dr. C. Nordborg (OECD/NEA, Paris, France), Dr. S. Okada (JAERI, Takasaki, Japan), Professor S.M. Qaim (Forschungszentrum Jülich, Germany) and Professor J. Soares (Instituto Tecnologico e Nuclear, Lisbon, Portugal).

The programme was divided into individual presentations followed by a free discussion on possible future actions that could be undertaken in the framework of the NEA. The individual presentations covered the following four items: application of positron beams, application of ion beams including radioactive beams, the combined use of ion and positron beams and positron emission tomography (PET).

In the free discussion, it was noted that the ion beam community was well established and that regular conferences were being organised. However, the participants felt that the exchange of information between the ion beam and positron beam communities should be enhanced. It was therefore proposed that the NEA Nuclear Science Committee set up a task force with the initial objective to write an overview report describing different nuclear techniques used to explore material properties. The aim of the report would be to inform the different communities of available methods, their advantages and limitations. It was also envisaged to arrange an educational seminar, providing an opportunity for the different groups to meet and discuss the report.

The participants recommended that the NEA Data Bank put more emphasis on the compilation of charged particle induced activation data, which would be useful not only for material science and PET applications, but also for areas such as transmutation and fusion. The compilation should be co-ordinated through the existing data centres network. In addition, the Data Bank was encouraged to make an inventory of computer programs used in the material science area, keeping in mind that codes based on “first principle” calculations were being covered by a separate community (COSIRIS).

ORGANISATION FOR ECONOMIC CO-OPERATION AND DEVELOPMENT

Pursuant to Article 1 of the Convention signed in Paris on 14th December 1960, and which came into force on 30th September 1961, the Organisation for Economic Co-operation and Development (OECD) shall promote policies designed:

- to achieve the highest sustainable economic growth and employment and a rising standard of living in Member countries, while maintaining financial stability, and thus to contribute to the development of the world economy;
- to contribute to sound economic expansion in Member as well as non-member countries in the process of economic development; and
- to contribute to the expansion of world trade on a multilateral, non-discriminatory basis in accordance with international obligations.

The original Member countries of the OECD are Austria, Belgium, Canada, Denmark, France, Germany, Greece, Iceland, Ireland, Italy, Luxembourg, the Netherlands, Norway, Portugal, Spain, Sweden, Switzerland, Turkey, the United Kingdom and the United States. The following countries became Members subsequently through accession at the dates indicated hereafter: Japan (28th April 1964), Finland (28th January 1969), Australia (7th June 1971), New Zealand (29th May 1973), Mexico (18th May 1994), the Czech Republic (21st December 1995), Hungary (7th May 1996), Poland (22nd November 1996) and Korea (12th December 1996). The Commission of the European Communities takes part in the work of the OECD (Article 13 of the OECD Convention).

NUCLEAR ENERGY AGENCY

The OECD Nuclear Energy Agency (NEA) was established on 1st February 1958 under the name of the OEEC European Nuclear Energy Agency. It received its present designation on 20th April 1972, when Japan became its first non-European full Member. NEA membership today consists of all OECD Member countries, except New Zealand and Poland. The Commission of the European Communities takes part in the work of the Agency.

The primary objective of the NEA is to promote co-operation among the governments of its participating countries in furthering the development of nuclear power as a safe, environmentally acceptable and economic energy source.

This is achieved by:

- *encouraging harmonization of national regulatory policies and practices, with particular reference to the safety of nuclear installations, protection of man against ionising radiation and preservation of the environment, radioactive waste management, and nuclear third party liability and insurance;*
- *assessing the contribution of nuclear power to the overall energy supply by keeping under review the technical and economic aspects of nuclear power growth and forecasting demand and supply for the different phases of the nuclear fuel cycle;*
- *developing exchanges of scientific and technical information particularly through participation in common services;*
- *setting up international research and development programmes and joint undertakings.*

In these and related tasks, the NEA works in close collaboration with the International Atomic Energy Agency in Vienna, with which it has concluded a Co-operation Agreement, as well as with other international organisations in the nuclear field.

SESSION I

Opening

Chairman: S. Okada

Chairman's summary

In his opening remarks, Dr. Nordborg (OECD/NEA) declared a stand-point of the workshop after he explained that the role of the NEA within the OECD is the direction of technically oriented works in developed countries comparable to that of the IAEA in the United Nations. He emphasised the importance of activities not directly related to reactors, e.g. accelerator related researches in the NEA/NSC category, in addition to the evolution of reactors.

In the keynote lecture, Professor Soares (Nuclear Physics Research Centre, Lisbon University and Nuclear Technology Institute, ITN, Portugal) discussed the activities of ion beam related works in various European countries. This will be a core of summary of the relevant research activities in the world.

OPENING REMARKS

Claes Nordborg
OECD Nuclear Energy Agency
Le Seine St. Germain
12, Boulevard des Iles
92130 Issy-les-Moulineaux, France

Abstract

A general introduction to the international organisation OECD (Organisation for Economic Co-operation & Development) and specifically the Nuclear Energy Agency (NEA), one of 15 bodies within the OECD, is given. The NEA contributes to the development of nuclear energy as a "safe, environmentally-acceptable and economical energy source" through co-operation among its Member countries. The NEA committees address scientific, technical, legal and economic issues of nuclear energy development, including safety and regulatory requirements, radiation protection and the disposal of nuclear waste. Information is also given regarding the discussions and decisions within the NEA Nuclear Science Committee that led to the organisation of the present workshop.

PRESENT STATUS OF ION BEAM APPLICATION RESEARCH IN EUROPE

J.C. Soares
Centro de Fisica Nuclear da Universidade de Lisboa,
and Instituto Tecnologico e Nuclear, Estrada Nacional 10, Portugal

Abstract

It is the aim of this keynote lecture to introduce the main and most recent developments in the field of ion beam application research in Europe. Starting from the Ion Beam Analysis Conference held in Lisbon in 1997 and the Conference on Ion Beam Modification of Materials in Amsterdam in 1998, the workshop participants will have the opportunity to discuss what the futures issues of ion beam research will be, taking into account new infrastructures, new challenges, new needs for ion beam research and the latest developments in the field of education and training of young scientists which have to turn towards an interdisciplinary and more application-oriented research.

SESSION II

Application of Positron Beams

Chairman: A. van Veen

Chairman's summary

Positron beam analysis (in the common energy range 0-30 keV) is a technique in its development phase; ion beam analysis is an established technique. Both techniques have nearly the same depth range (1-2 micrometer, dependent on the material) and can in nearly all cases be applied to the same systems. More effort should be given to apply both techniques to the analysis of exactly the same samples. Then it can be better established what the sensitivities are of the techniques for detecting a variety of defects, ranging from low atomic density defects like vacancies and vacancy clusters to high density defects like interstitial loops. Also it will be of interest to determine how both techniques detect the presence of gas atoms (noble gas or hydrogen) at the defects, in particular in nano-cavities.

Positron beam analysis is improving in two directions:

1. Better defect spectroscopy through the use of a second shape parameter W in S-W maps, high resolution measurement of the electron-positron momentum distribution for low momenta (2D-ACAR), for the high momenta background free measurement through two

detector-in coincidence measurements. This development enables to test results of ab-initio calculations of these momenta distributions for different defect complexes. Introduction of pulsed positron beams for life-time analysis.

2. Increasing lateral resolution to about 100 nm which seems feasible for keV positron beams in materials with moderate diffusion length. There are at least four programmes on the development of positron microbeam analysis either based on lifetime or Doppler broadening measurements. In one of the programmes a low intensity source is used to avoid complication with radiation safety in a laboratory environment. The others will be based on 1 000 or 10 000 times stronger sources (positron factory Japan 10^{10} e^+/s, Livermore linac 10^9/s and Delft 2×10^8/s, and later Munich) and therefore use is restricted to certain positron centres (in fact like what has happened to the ion beam analysis centres). The micro-analysis has much in common with ion beam micro-analysis. Positron micro-analysis would profit greatly if positron moderation could be made a factor 100 more efficient (development of field assisted moderation should be promoted).

Other developments are aiming at having positron beam analysis with DC or pulsed MeV energy positron beams, and the use of spin polarised slow positrons. In the latter case annihilation rates are influenced by the character of the electron spin systems in the surface layers of a material. Techniques are improved to build polarimeters and to build positron transport systems which do not deteriorate the longitudinal polarisation of the beam. The coming years will tell whether the technique proves to be useful. Two programmes are underway in Japan.

Surface physics

There are only few groups working on surface physics. Usually it is not easy to combine the regular positron defect-profiling with surface physics. Other additional techniques and better vacuum are required. Therefore specialisation is needed. A good example of surface physics with positrons was given at the workshop: RHEPD, Reflection High-Energy Positron Diffraction. The fact that the work function of positrons is negative or slightly positive compared to electron work functions enable to probe better the outermost layers of the solid material. In particular, this is useful for the study of epitaxial growth.

Materials

In principle ion beam analysis and positron beam analysis give access to the study of all materials. New materials that gain interest are ceramics (e.g. oxides) and polymers. Less efforts are spent in metals (e.g. fusion reactor materials). Research in polymers can profit very much from extended methods to detect positronium in the cavities of the polymer (free volume effects). From the annihilation measured by lifetime or 2D-ACAR information about size and concentration and even the shape of the cavities (ellipsoids measurable with 2D-ACAR) is obtained. In semiconductors positrons are very sensitive for negatively charges and, to a lesser extent, neutral vacancies. This is very important for the device industry.

INDUSTRIAL USE OF POSITRON ANNIHILATION TECHNIQUE CARRIED OUT AT THE UNIVERSITY OF TSUKUBA

Shoichiro Tanigawa
Institute of Materials Science, University of Tsukuba
Tsukuba, Ibaraki 305-0004, Japan

Abstract

The positron annihilation technique has been successfully applied to a variety of practical problems in industrial materials at the University of Tsukuba. Although this technique still challenges to a new field of fundamental physics, at the same time, it is expanding a variety of its new application fields especially on crystalline defects in semiconductors, on free volumes in various types of polymers and so on. Through this kind of application of the positron technique, it is now well recognised as a very unique and powerful tool for nanoscopic diagnosis of industrial materials. In the present contribution, many examples of the successful use of positrons in industrial materials will be shown.

THE POSITRON MICROPROBE – AN INSTRUMENT FOR NON-DESTRUCTIVE MATERIAL TESTING

K. Maier
Institut für Strahlen- und Kernphysik, Nußallee 14-16, D-53115 Bonn

Abstract

Positron annihilation is a well established technique to study defects materials. Positrons are very sensitive probes for vacancies, dislocations and small clusters. Usually, positron lifetime and Doppler broadening are measured with two identical samples and the positron source mounted in between (sandwich geometry); the "information volume" is determined by the source diameter and the positron range in the sample (typical value diameter 1, thickness 0.1 mm). In contrast, a standard energy moderated positron beam provides a sensitive probe for surfaces and thin films with spatial resolution in the mm range. For many technical applications, however, a simple mobile apparatus or a beam with micrometer resolution is necessary. In this work a positron microprobe integrated into a scanning electron microscope will be presented.

This new instrument is the result of a joint three-year development of the Institut für Strahlen- und Kernphysik of the University of Bonn and the commercial electron microscope manufacturer Zeiss/Leo Elektronenmikroskopie Oberkochen. Studies of material fatigue in commercial steels, radiation damage in the transmission electromicroscope and electromigration in electronic devices are presented and discussed.

Introduction

For the application of the sensitive method of positron annihilation in non-destructive material testing special instruments are required. Small portable positron annihilation devices optimised for short data acquisition times and different specimen geometries are the solution for testing areas larger than 1 mm^2 [1,2]. For many applications in the fast growing field of microstructure technology, e.g. in electronics, sensors, and micromechanics a spatial resolution in the micrometer range is necessary. Micrometer resolution is also required in the development of new materials. Defects in different grains, defects in fibres or the surrounding material are difficult to detect with the standard testing techniques. The new scanning tunnelling (STM) and scanning force (AFM) microscopes are only sensitive to the surface and do not deliver any insight into the bulk. Transmission electron microscopy (TEM) and high resolution electron microscopy (HTEM) require delicate sample preparation. For optimised resolution and contrast a sample thickness below 10 nm is necessary. In addition, frenkel defects in the sample are produced with the intense electron beam during microscope operation.

Positron microbeams

The interaction of positrons with defects is well understood. Trapping in vacancies and small defect clusters occurs at concentrations above 10^{-6}, and trapping in dislocations and grain boundaries can also be observed. However, details of the trapping in these one- and two-dimensional defects are still open. Using a positron microbeam as a sensitive probe is an old idea. At present some complicated instruments are under development. Many of them are based on a large intense positron sources, e.g. nuclear reactors or electron linear accelerators. It is planned to reduce the beam diameter in several moderation stages to micrometer dimensions. Resolutions far below a micrometer are not possible with positrons. The diffusion length of about 0.5 μm in the thermalised positron state is the natural limit.

The Bonn positron microprobe

In co-operation with the commercial electron microscope manufacturers Zeiss and LEO Elektronenmikroskopie GmbH Oberkochen a positron microprobe was developed within only three years [3]. The apparatus (Figure 1) is a small laboratory instrument, comparable to a scanning electron microscope (SEM). It can be installed in any laboratory without expensive radiation safety installations. The beam is realised by a very small source of 500 μCi ^{22}Na in combination with a tungsten moderator having an efficiency better than 10^{-4} and several condenser and deflection systems. One of the deflectors is an electromagnetic prism which focuses the positron beam onto the optical axis of a SEM column where the final focusing is done by the objective lens. Due to the magnetic prism's capability to act as an energy filter unmoderated positrons are not deflected into the SEM column which results in a signal-to-background-ratio of 200:1 in the photopeak of the Ge detector. The set-up can also be used as a conventional SEM, reaching a spatial resolution better than 10 nm (energy range 0.5...30 keV). The centre of the positron beam corresponds to the centre of the SEM picture. The Doppler signal is measured by a Ge-detector (energy resolution: 1.26 keV at 478 keV) mounted as close as possible below the sample.

At present the e^+ beam can be tuned between 7 and 30 keV with an intensity of 130 γ counts/s in the photopeak of the Ge-detector (background 0.7 γ/s). Operation is possible with beam diameters between 7 and 200 μm FWHM and no magnetic field at the sample position. A beam diameter

of 1 micron will be attained with a strongly focusing magnetic lens at the sample position. The disadvantage of this geometry is the very limited free space for the sample. Standard operation of the instrument is not difficult. Focusing and selection of the examination areas is performed with the SEM part. The co-ordinates are stored in the controlling computer and the positron measurement process can be run automatically and even unattended at night or on weekends.

An X-ray detector for material analysis and a more intense positron source providing a final counting rate above 600 γ counts/s in the photopeak will be installed at the end of this year.

Experimental results

Welding

Welding in a simple ferritic construction steel (PIN 17100) was examined with lifetime and Doppler-broadening measurements. An instrument based on a ^{22}Na positron source with a position resolution of 0.7 mm was used [4,5]. Small iron carbide clusters are the dominant trapping centres.

In situ positron lifetime measurements in tensile tests and fatigue

Positron lifetime was measured in deformed copper single crystals with a β^+-γ spectrometer optimised for high counting rates. Tensile hardening and cyclic hardening is strong by correlated to positron lifetime (Figures 3 and 4). In fatigue a threshold and saturation for positron trapping is observed (Figure 4).

Plastic zone in front of a cracktip

In a AISI 321 plate of 23×18×18.8 mm^3, which was mechanically and electrochemically polished and annealed at 1000°C in high vacuum, a fatigue crack was produced under strain control in a cyclic deformation device with a maximum amplitude of 75 μm over 4000 cycles (Figure 5). The fatigue damage profile of the plastic zone in front of the cracktip was examined by positron annihilation with a resolution of 20 μm (Figure 6). At present positron annihilation is the most sensitive method to observe plastic deformation in stainless steel at room temperature.

Radiation effects in the TEM

In copper and molybdenum samples radiation defects are observed with the positron microprobe (Figures 7, 8, 9). The investigation of point defects produced in TEM operation is an important preparatory work for a programme of positron dislocation interaction. It is planned to study positron trapping in well characterised dislocation clusters and single dislocations with the improved version of the positron microprobe in 1999.

Acknowledgements

The presented instruments and results are the work of the following PhD and Diploma students during the last four years: K. Bennewitz, H. Greif, M. Haaks, S. Hansen, H. Heußer, Ch. Hugenschmidt, M. Tongbhoyai, T. Wider, Ch. Zamponi. The author is indebted to H. Bihr, B. Huber, J. Lugtenburg, A. Rilk, P. Schlichtmeier, P. Ditzinger and J. Frey of the Zeiss and LEO Elektronenmikroskopie team for their important contributions and the support given in building up the positron microprobe. The funding of the project by the Bundesministerium für Bildung, Wissenschaft, Forschung und Technologie under Contract No. F.u.E.-KZO3N8001 and the fruitful supervision by Dr. Ehrlich are gratefully acknowledged. I want to thank the mechanical and electronic workshop of the Institute and last, but not least, my colleagues P. Herzog and J. Schüth for many discussions, and Mrs. E. Schoppmann for all the paper work.

REFERENCES

[1] S. Hansen, U. Holzwarth, M. Tongbhoyai, T. Wider and K. Maier, *App. Phys*. A 65, 47 (1997).

[2] C. Hugenschmidt, Diplomarbeit, Universität Bonn (1995).

[3] C. Hugenschmidt; U. Holzwarth, M. Jansen, S. Kohn and K. Maier, *J. Radioan. Nucl. Chem*., Vol. 210, No. 2 (1996) 583-589.

[4] C. Hugenschmidt, U. Holzwarth, M. Jansen, S. Kohn and K. Maier, *J. Non-Cryst. Sol*., Vol. 217 (1997) 72-78.

[5] H. Greif, M. Haaks, U. Holzwarth, U. Männig, M. Tongbhoyai, T. Wider, K. Maier, J. Huber, *Appl. Phys. Lett*. 71, 15 (1997).

[6] M. Haaks, Diplomarbeit, Universität Bonn (1997).

[7] T. Wider, S. Hansen, U. Holzwarth and K. Maier, *Phys. Review* B 57, 5126.

[8] M. Haaks, K. Bennewitz, H. Bihr, U. Männig, C. Zamponi and K. Maier, Proc. Slowpos 8 Cape Town (1998).

[9] U. Männig, K. Bennewitz, H. Bihr, M. Haaks, W. Sigle, C. Zamponi and K. Maier, Proc. Slowpos 8 Cape Town (1998).

Figure 1. The realisation of the Bonn Positron Microprobe

The positron microbeam is formed by a point-like ^{22}Na source (1) on a holder, a tungsten moderator (2), an extraction (3), and an acceleration electrode (4). (8) stands for a conventional electron gun. The condenser lenses (5) and (7) form crossovers of the e^+ and the e^- beam on the entry planes of the magnetic prism (6). The condenser zoom (9) and the objective lens (10) are parts of a commercial SEM column. The positioning system (12) is used to centre the selected area of the specimen (11) in the optical axis for positron annihilation measurement. The accuracy to hit the same spot with electrons and positrons is better than the half spot size of the positron beam. The Doppler broadening of the annihilation radiation is measured with a Ge detector (13).

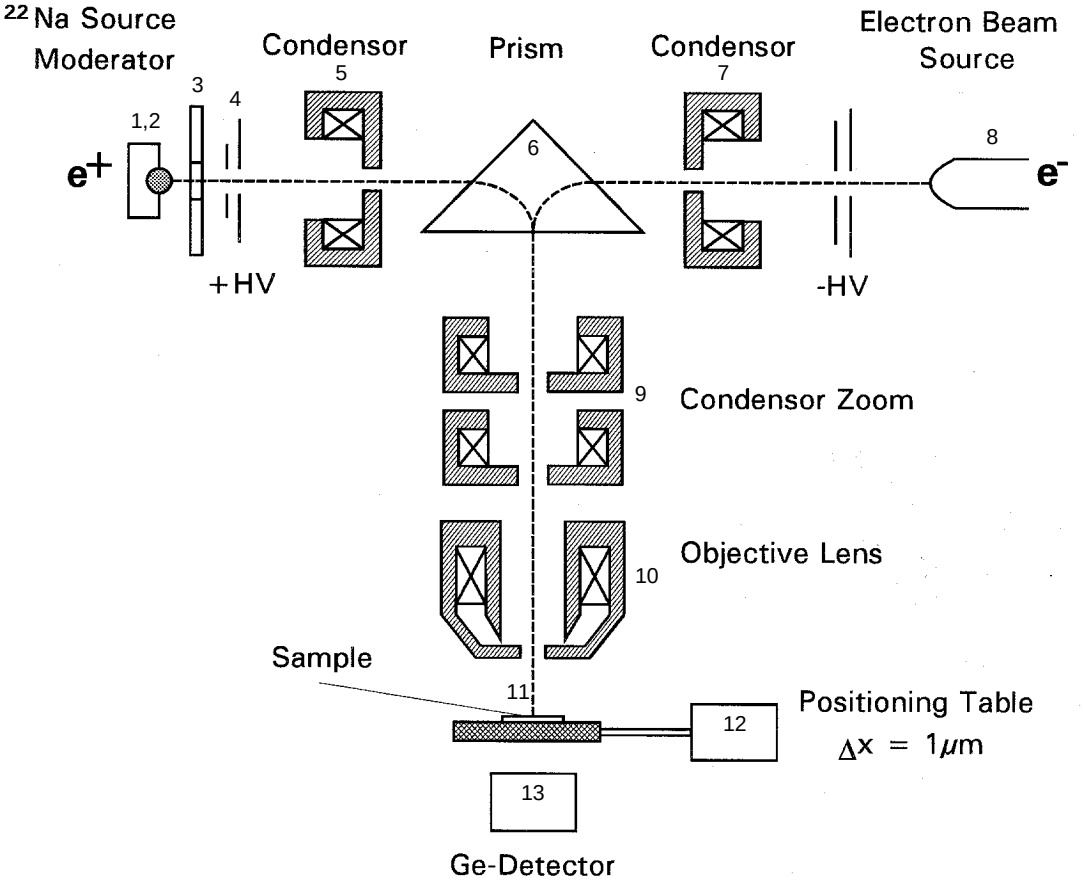

Figure 2. S-Parameter A and mean lifetime measured perpendicular to the plasma welding. NZ = neutral zone, TEZ = hot zone during welding, SWN = liquid during welding. Annealing above ferrite-austenite transition (E) leads to a uniform distribution of carbon.

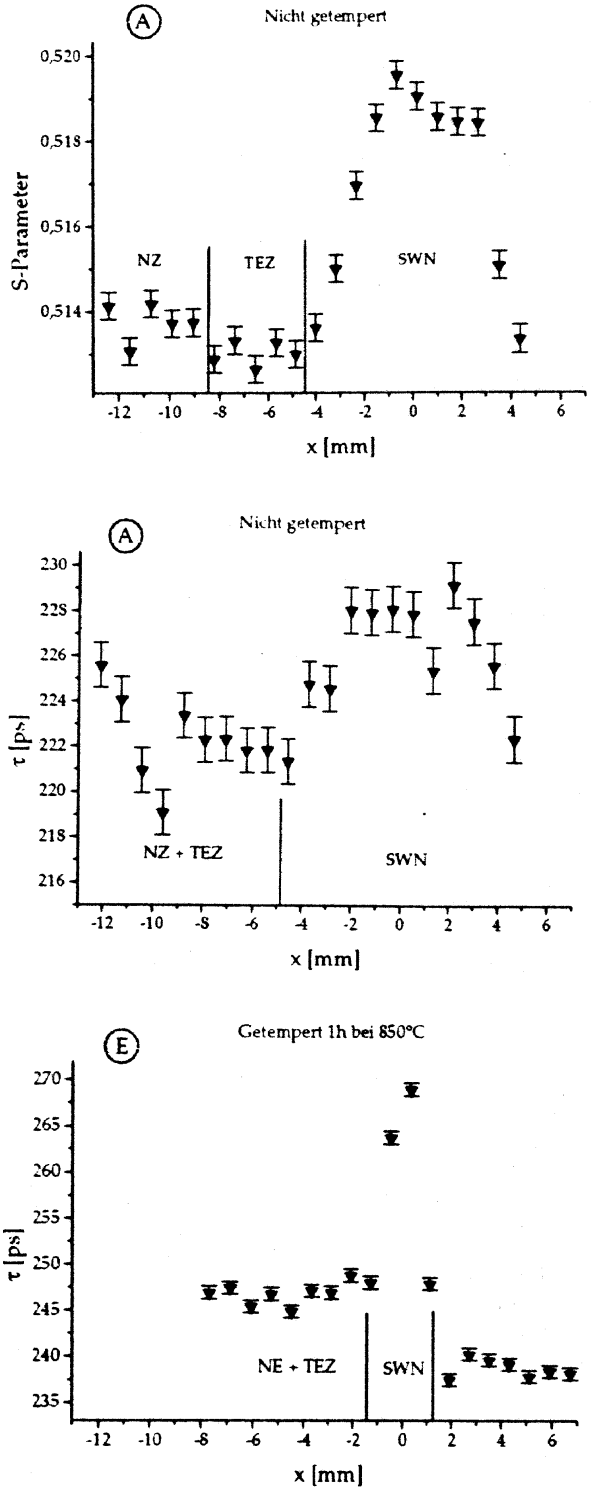

Figure 3. Tensile hardening curves (line), and the development of the mean positron lifetime $1/\lambda$ (❑) during tensile test as a function of the logarithm of the total resolved shear strain γ. The mean positron lifetime $1/\lambda$ remains constant up to strains of 3% and resolved shear stresses of 10 Mpa.

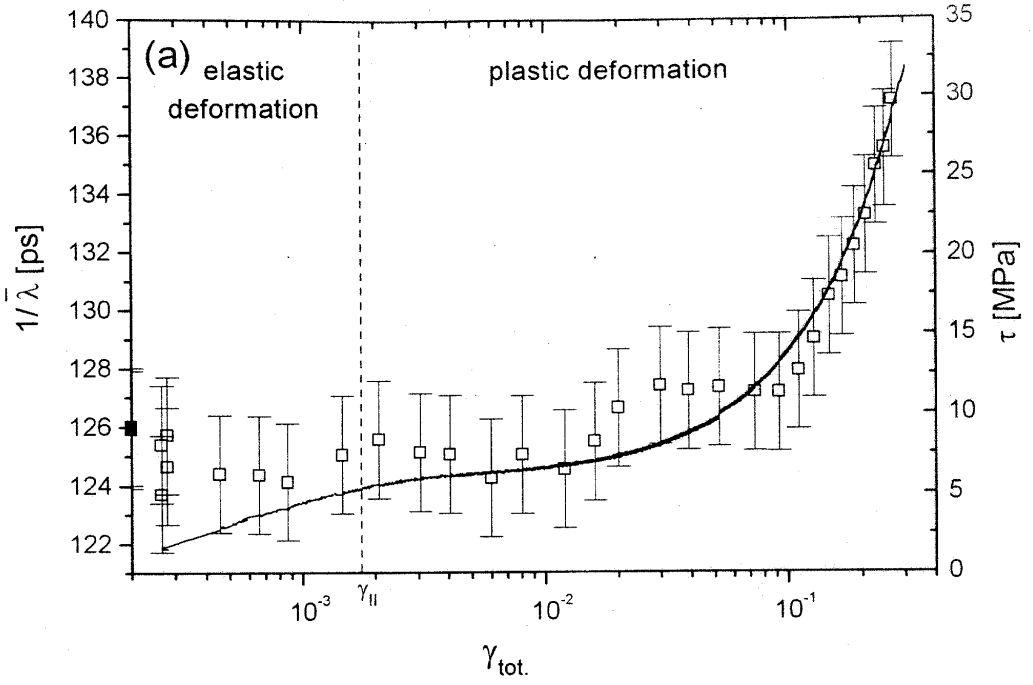

Figure 4. Typical cyclic hardening curve, shear stress amplitude τ (•) in MPa versus cumulative plastic strain γ_{cum} and the related mean positron lifetime $1/\lambda$ (O) in ps. $1/\lambda$ increases from about 130 ps to a saturation value of about 170 to 175 ps. $1/\lambda$ saturates at around 30 Mpa.

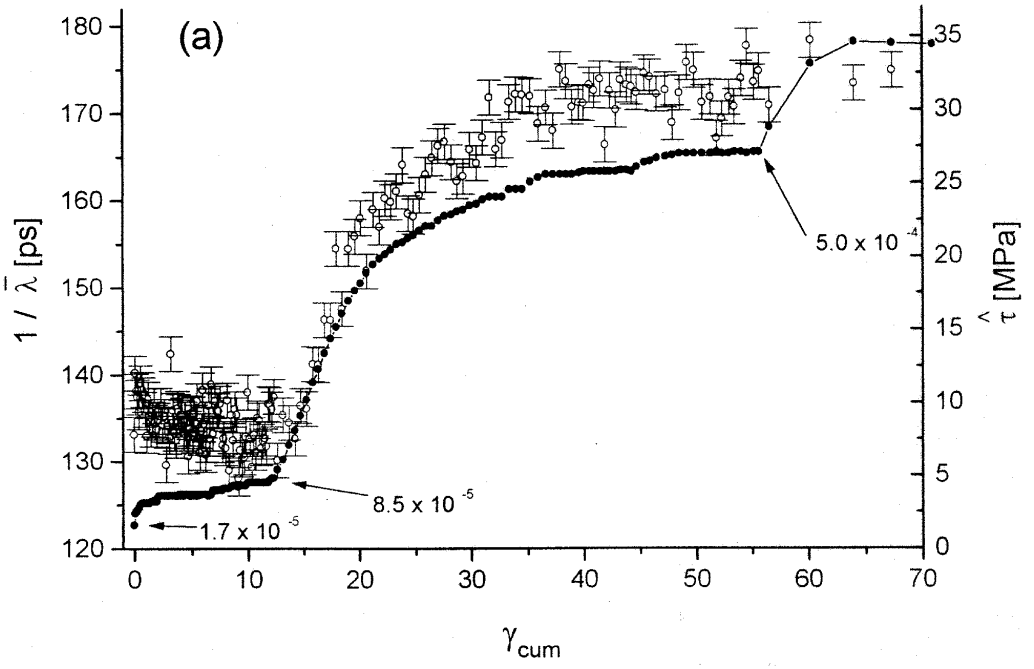

Figure 5. Top: SEM Image of a crack tip in stainless steel AISI 321. Near the cracktip slip lines are clearly visible. Bottom: The surface of the same sample 1 mm far away from the cracktip. In the SEM Image no effects of plastic deformation to the surface are recognisable.

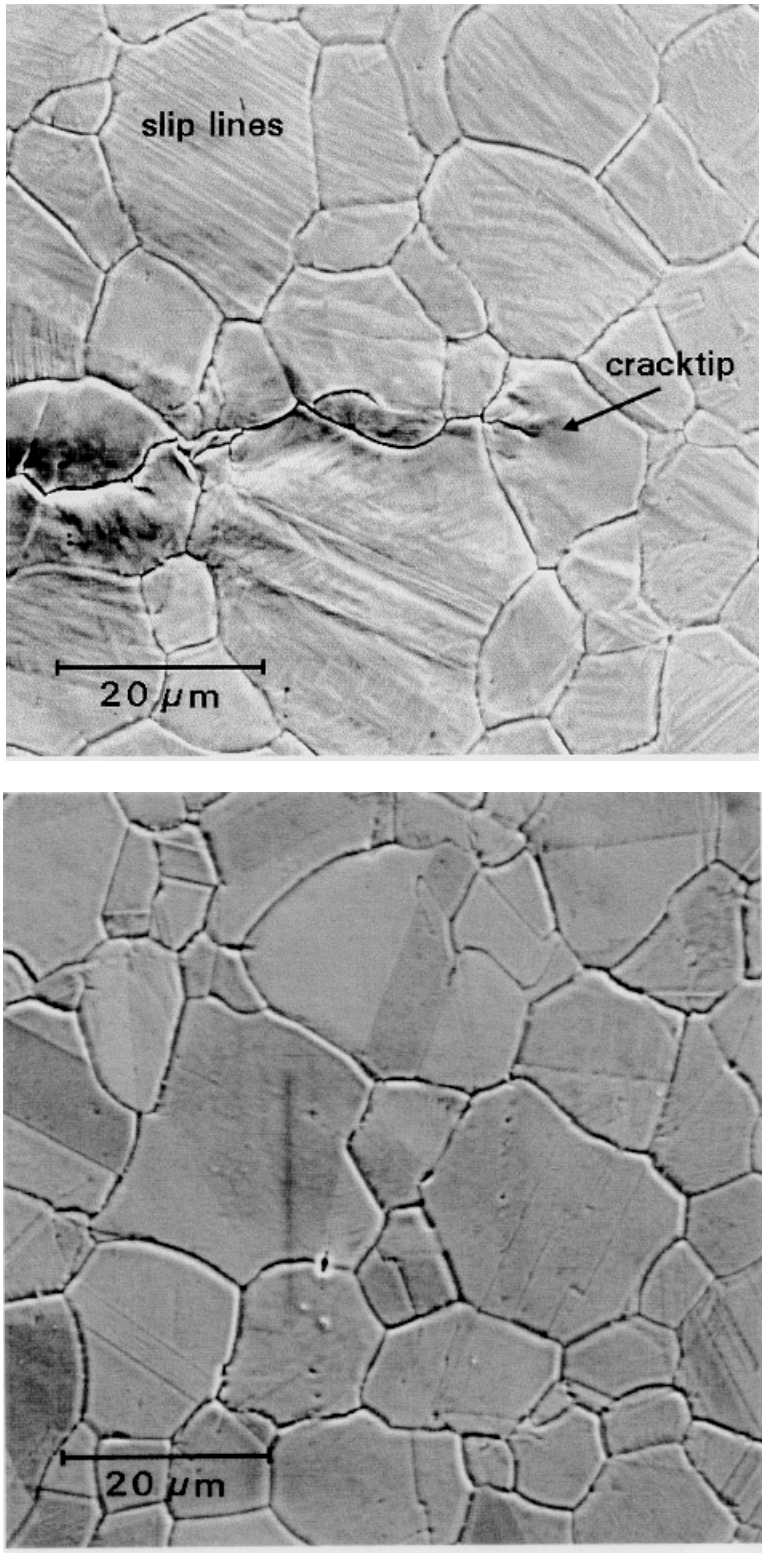

Figure 6. Top: S-Parameter scan 50 μm in front of a cracktip in AISI 321 crosswise to the cracktip. A massive effect of about 10% appears due to the fatigue deformation. Bottom: S-Parameter map of the plastic zone around the cracktip. The size of the grid is 150 μm×150 μm. Resolution of the Ge-Detector: 1,24 keV at 478 keV.

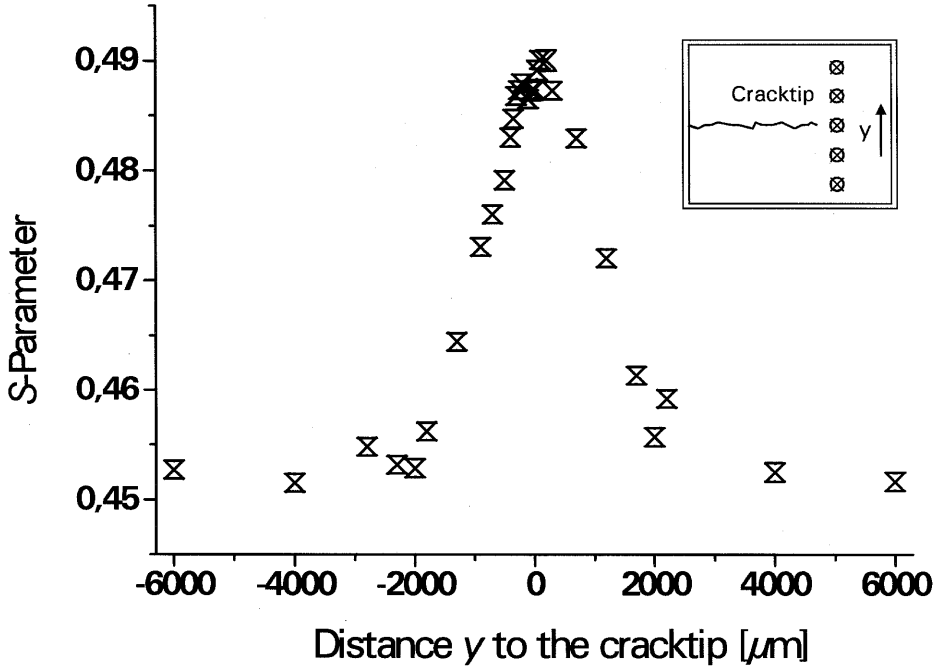

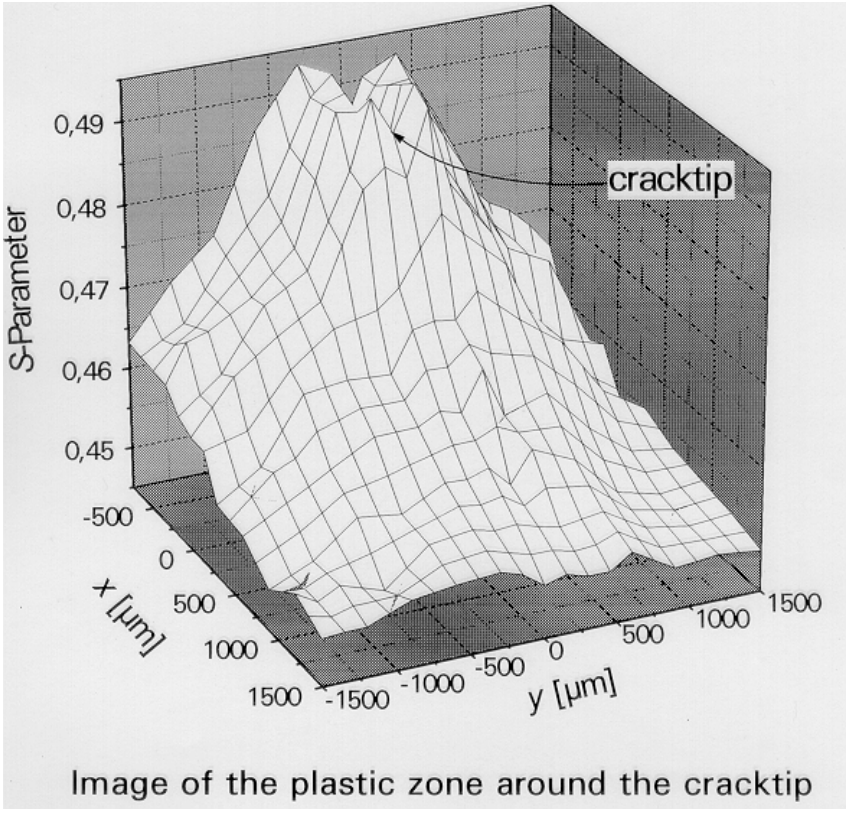

Image of the plastic zone around the cracktip

Figure 7. SEM picture of the irradiated Mo sample mounted on a copper grid

No difference between radiated area and surrounding material can be seen. The irradiated region is at the edge of the foil. To reduce background arising from annihilation in the bottom of the sample chamber an annealed Mo foil is fixed with epoxy below the copper grid after irradiation. The points of positron investigations are indicated.

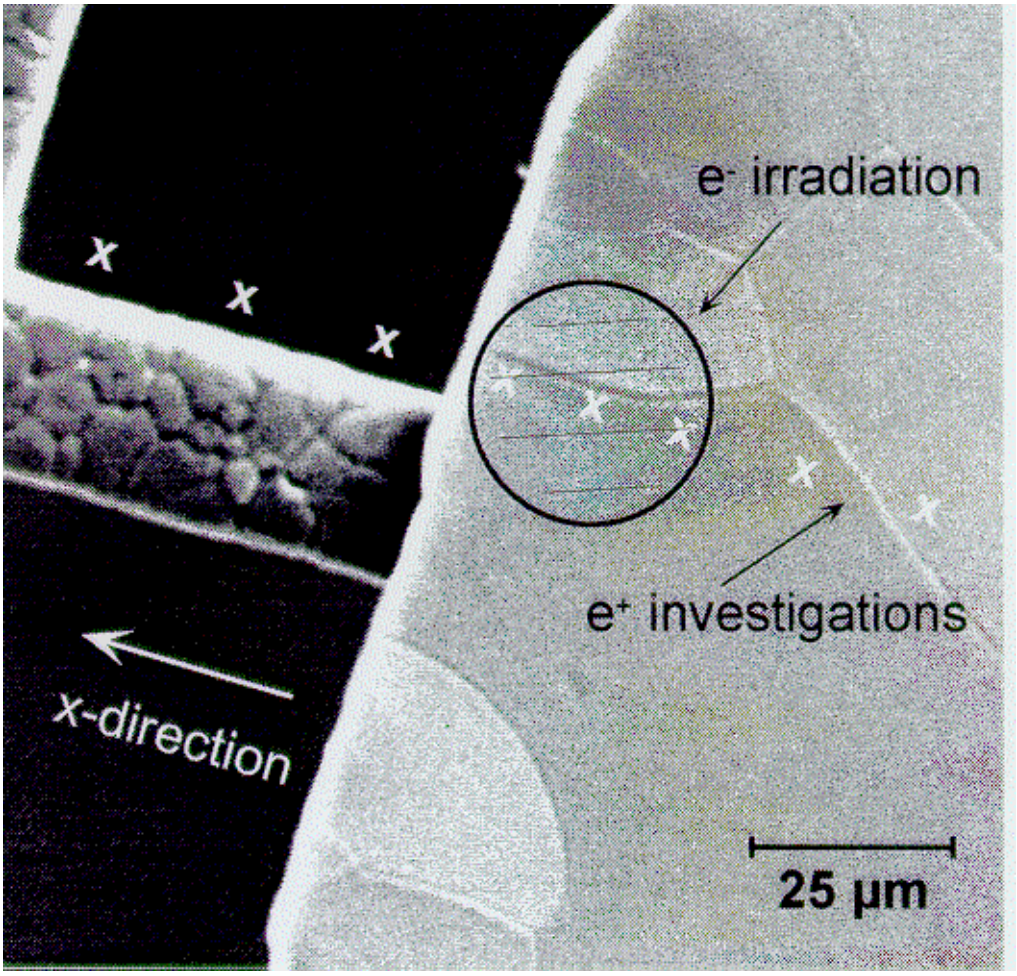

Figure 8. S-parameter measured in the scans over irradiated areas of different defect concentrations D_v caused by different radiation times. The maximum value at x=-10 μm coincides with the centre of the electron beam during irradiation.

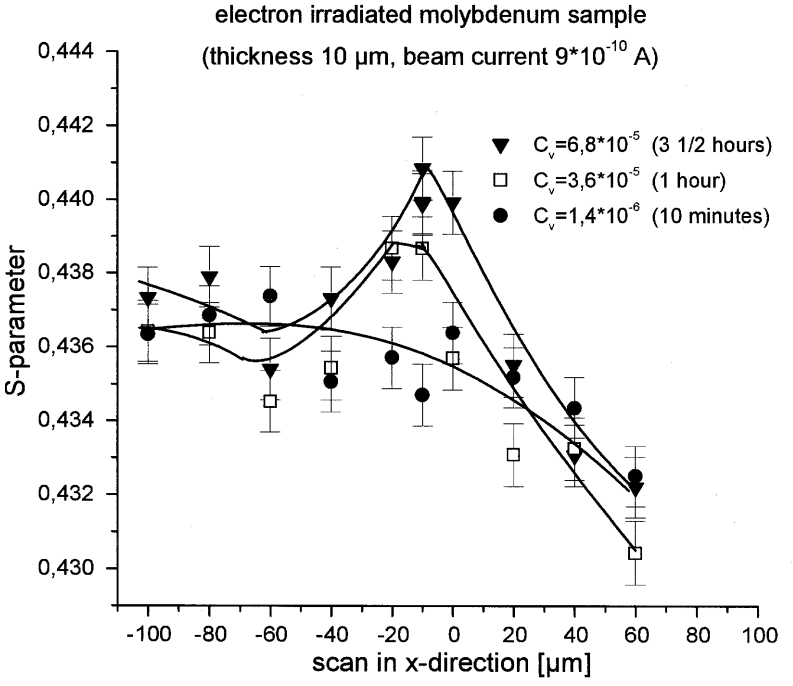

Figure 9. Electron irradiated copper sample. The S-parameter for different irradiation times is shown. Saturation trapping occurs upwards 1000 seconds. This corresponds to a vacancy concentration of about 10^{-5}.

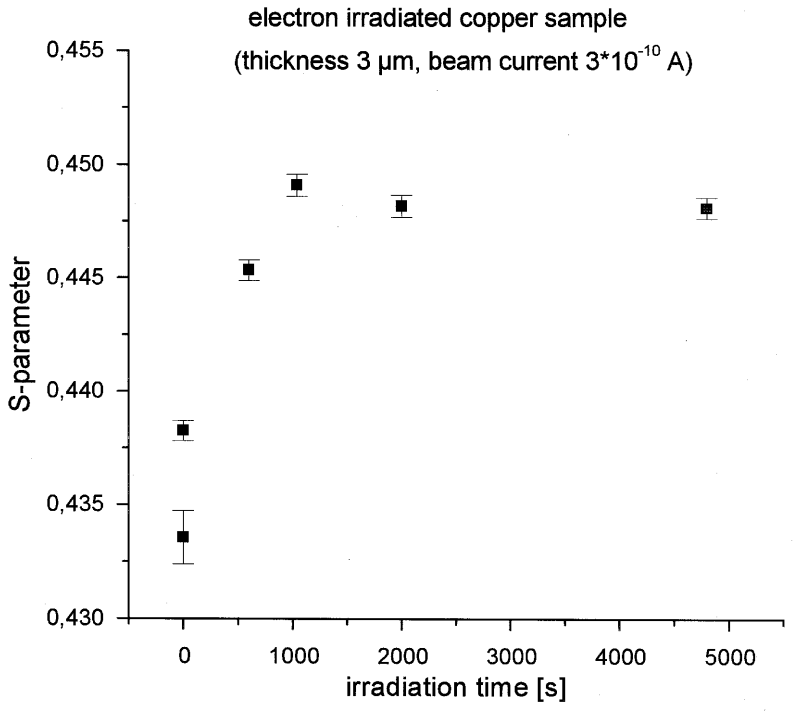

DESIGN STUDY FOR THE POSITRON FACTORY IN JAPAN

Sohei Okada, Hiromi Sunaga, Hirohisa Kaneko,
Haruki Takizawa, Atsuo Kawasuso and Keiichi Yotsumoto
Takasaki Establishment, Japan Atomic Energy Research Institute
1233 Watanuki, Takasaki, Gunma 370-1292, Japan

Abstract

The Positron Factory has been planned by the Japan Atomic Energy Research Institute (JAERI). The factory is expected to produce linac-based monoenergetic positron beams having the world's highest intensities of more than 10^{10} e^{+}/sec, which will be applied for R&D of materials science, biotechnology and basic physics and chemistry. In this article, results of the design studies are demonstrated for the following essential components of the facilities:

1) conceptual design of a high-power electron linac with 100 MeV in beam energy and 100 kW in averaged beam power;

2) performance tests of the RF window in the high-power klystron and of the electron beam window;

3) development of a self-driven rotating electron-to-positron converter and the performance tests;

4) proposal of multi-channel beam generation system for monoenergetic positrons, with a series of moderator assemblies based on a newly developed Monte Carlo simulation and the demonstrative experiment;

5) proposal of highly efficient moderator structures;

6) conceptual design of a local shield to suppress the surrounding radiation and activation levels.

Introduction

New beam technologies with accelerators have been emphasised recently. At the Takasaki Establishment, Japan Atomic Energy Research Institute (JAERI), research on materials science and biotechnology is in progress using a variety of ion beams from an AVF cyclotron, a 3 MV tandem accelerator, a 3 MV single-ended accelerator, a 400 kV ion implantor in TIARA (Takasaki Ion Accelerators for Advanced Radiation Application) facilities. The research fields have stepped into a novel stage of "quality control on matter itself" at the atomic level, which means both observation and manipulation of the microscopic structures. Positron beam, which is generated as "slow" (i.e. monoenergetic) positron beam and sometimes accelerated, is a powerful tool for this purpose as well as ion beam. Unlike neutrons and photons, positrons are charged, and therefore the implantation depth in matters can be controlled by varying the injection energy of the beam. Namely positron and ion beams can probe the same positions such as surfaces and interfaces of materials and devices. On the other hand, microscopic features observed and manipulated are different between positron and ion beams, and consequently the perfection could be pursued with the combined use of the two means. An implanted and thermalised positron annihilates with an electron, which is dominantly followed by emission of two photons that maintain the energy and the momentum of the initial state due to the conservation rule. The positron is attracted to atomic vacancies, voids and free volumes, where the nuclear charge densities are lower, due to its positive charge. This results in the prolonged lifetime, which can be measured also by detecting the annihilation radiations. Thus positron can see the electronic structure and the absence of atoms, whereas ion probes the existence of atoms, that is, the atomic structure. Electrons are also charged. When an electron is accelerated into matter, however, it loses its identity quickly through thermalisation, and thereafter it becomes useless as a spectroscopic particle. Unlike electrons, slow positrons are repulsed by surfaces of solids due to their positive charge. This endows the positron with a high advantage as a topmost surface probe to observe atomic structures by the diffraction [1] and to detect impurity atoms by PAES (Positron Annihilation-Induced Auger Electron Spectroscopy) [2].

By the combined use of ion beams and positron spectroscopy, we found a unique state of vacancy-hydrogen interaction in silicon. Here proton-implanted silicon was studied by positron lifetime in comparison with He ion-implanted and electron-irradiated silicons [3]. We succeeded in the first observation of RHEPD (Reflection High Energy Positron Diffraction) from a silicon surface by the use of an isotope-based electrostatic slow positron beam, and demonstrated usefulness of positron as a topmost surface sensitive probe [4]. Such an isotope-based slow positron beam, however, cannot be applied for advanced analyses like time-dependent observation of transient phenomena and fine structure investigation of sub-micron size local region of materials, because of the insufficient intensity.

We have been promoting design studies for the "Positron Factory" [5], in which linac-based intense monoenergetic positron beams are planned to be applied for materials science, biotechnology and new fields of basic research. A tentative goal of the slow positron beam intensity is 10^{10}/sec, which is larger by two orders of magnitude than those of existing strongest beams in the world. In this paper, some results of the design studies on a dedicated high-power electron linac and the target system to generate the intense slow positron beam are described.

Planned facility

An overview of the planned facility is shown in Figure 1. We have done the conceptual design of the facility, which includes a high-power electron linac, electron beam lines, a target system, slow positron beam lines and building. The results of the design studies, which are indicated by @ in Figure 1, are described in the following sections.

Figure 1. An overview of the planned facility and the design study items

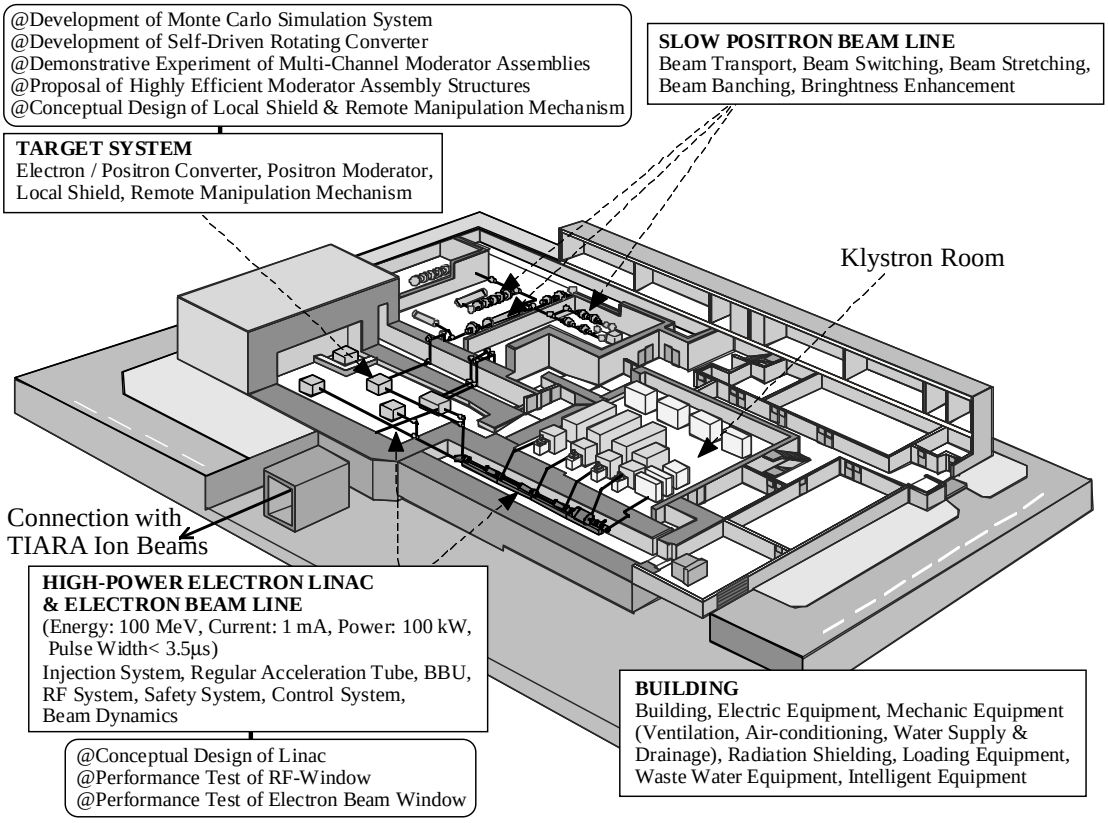

Positron behaviour simulation system

We developed a Monte Carlo simulation system named EGS4-SPG [6] for the design studies. In the process to generate a slow positron beam using an electron linac, as shown in Figure 2, energetic electron beam bombardment from a linac on an electron-positron converter (e.g. tantalum; Ta) causes a cascade shower of Bremsstrahlung and pair production reactions, which results in energetic positron emission. A moderator (e.g. tungsten; W) combined with the converter produces a slow positron beam through a unique emission process due to the negative surface work function for positron.

The EGS4 [7] is a very powerful tool to simulate three-dimensional movements of electrons, positrons and photons in high energy processes like Bremsstrahlung and pair-production. However there is a lower limit of the particle's kinetic energy under which the EGS4 calculations are less reliable. The limit is called cut-off energy, which is usually around 10 keV. In EGS4, when a particle

slows down under the cut-off, the calculation terminates after recording of the three-dimensional co-ordinate and momentum of the particle and goes to the next incident particle.

In our new simulation system EGS4-SPG, the tracking of positrons does not terminate even under the cut-off. When the kinetic energy of a positron becomes less than the cut-off, the calculation is automatically switched from EGS4 to SPG [5] which we had previously developed. The positron is transported from the recorded position in the direction of the recorded momentum by a certain distance z_t, i.e. thermalisation length. To determine the value of z_t, the Makhov expression [8] for the probability density function of the thermalisation length is used:

$$p(z') = -(d/dz') \exp\left[-(z'/z_0)^m\right] \tag{1}$$

Here m and z_0 are constants depending on the particle energy and the material. The co-ordinate z' is along the direction of the positron momentum at the final stage in the EGS4 calculation. This expression is widely used as a stopping profile of positrons having kinetic energies ranging from ~keV to several tens of keV, and the constants can be experimentally determined. Since this formula has a derivative form, it is very suitable for Monte Carlo treatment. The probability distribution function:

$$p(z') = 1 - \exp\left[-(z'/z_0)^m\right] \tag{2}$$

can be easily deduced from Eq. (1). The thermalisation length z_t, corresponding to a uniform random number R, is obtained from Eq. (2) as follows:

$$z_t = z_0(-\ln R)^{1/m} \tag{3}$$

After the above transportation, the positron starts to diffuse, and finally is either annihilated or ejected from the surface of the material, according to the probabilities determined empirically. This part in SPG simulates important processes to produce slow positrons. The treatment of particles in SPG is not physically strict. But it is suitable to practical use in design studies of complicated devices using parameters obtained from experiments of simple materials.

Thus EGS4-SPG can trace the three-dimensional positron behaviour through from the birth by pair-production in a converter and a moderator to the rebirth by slow positron emission from a moderator. A concept of this simulation system is shown in Figure 2.

High-power electron linac

We performed a design study on a high-power electron linac to generate an intense slow positron beam. An optimum electron beam energy for slow positron generation was estimated to be around 100 MeV by using EGS4-SPG. It was calculated that a tentative goal of the slow positron beam intensity (10^{10}/sec) could be attained with a linac of 100 kW class with the above energy range. A technical survey study confirmed the feasibility of manufacturing such a state-of-the-art linac. Further detailed analyses were carried out concerning thermal deformation of the accelerator structures, beam instability, reliability of the components, down-sizing of the machine and a computer-aided control system. A concept of the linac and the expected specification are shown in Figure 3 and Table 1, respectively.

Figure 2. Process to generate slow positrons and a concept of EGS4-SPG

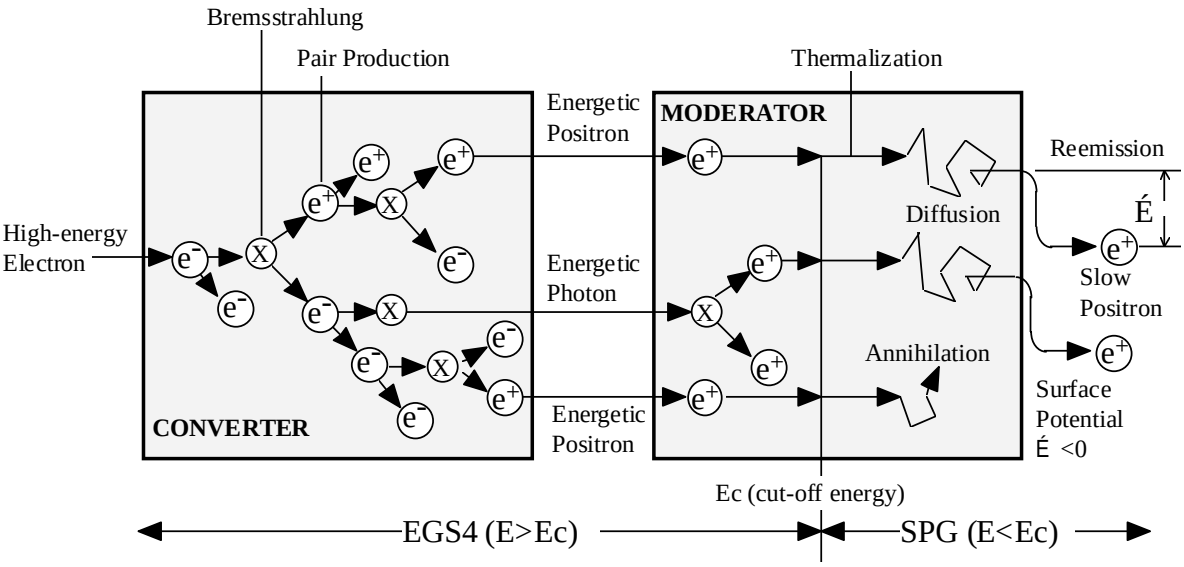

Figure 3. A concept of the high-power electron linac for the Positron Factory

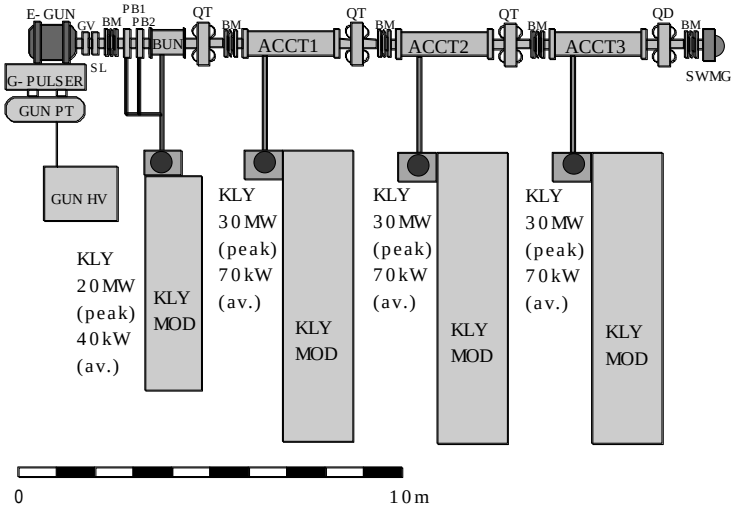

Table 1. Specification of the linac

Beam energy	100 MeV
Beam current	1 mA (average)
Beam power	100 kW (average)
Pulse repetition	600 pps
Pulse width	~3.5 μs

In addition to the linac itself, the durability of the electron beam window and the RF window of the wave guide circuit from the klystron should be investigated.

The electron beam window will be irradiated by an electron beam of 100 MeV and 1 mA. When the beam size is 10 mm in diameter, the energy fluence rates are estimated to be 100 and 300 W/cm^2 for a titanium and a tantalum window, respectively. Here the thickness of the window is assumed to be 0.1 mm. One side of the window will be in vacuum and the other side will be cooled by water (see the following section).

We assembled a beam window test stand as shown in Figure 4, and carried out the irradiation test of a titanium and a tantalum window whose thickness' were both 0.1 mm. The electron beam energy, the beam diameter and the flow rate of the cooling water are 10 keV, 10 mm and 5.2 lit./min, respectively. The beam currents and the energy fluence rates were 11 mA (103 W/cm^2) for the titanium window and 7.5 mA (78 W/cm^2), respectively. These conditions were more severe for the surface parts of the windows in the vacuum sides than an electron beam irradiation of 100 MeV and 1 mA. No significant damages were observed in the irradiation test. Thus the feasibility of the windows was confirmed.

Figure 4. Schematic of the electron beam window test stand

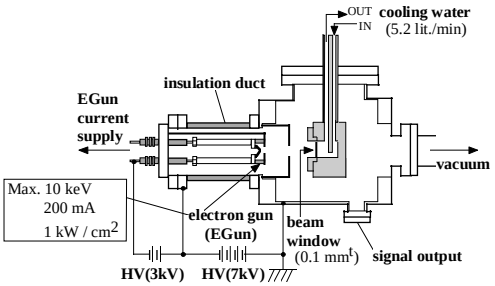

We also made a trial product of the RF window and performed an over-load operation test as shown in Figure 5. In the wave guide circuit for the linac of the Positron Factory, we plan to divide the RF power into two windows, as shown in the left hand of Table 2. Although such powerful klystrons as in Figure 3 do not exist in the world, we only need to consider the reliability of the window for half of the power. We used a modified model of Toshiba E3730A klystron, whose specification is shown in the right hand of Table 2. The RF power is sufficient for the test. We carried out a long term operation (continuous 4 hours, total 60 hours) of the RF window. No damages in the window were observed after the stable operation. The temperature rise of the cooling water of the dummy loads was only 0.5°C. Thus the feasibility of the RF window was confirmed.

Electron-to-positron converter

If an electron beam of 100 MeV and 100 kW is injected onto a tantalum converter with an optimum thickness of 8.2 mm, a power of 38 kW is deposited. To avoid a meltdown, it is necessary to divide the converter into several pieces and rotate in a coolant. However a motor and a penetration may not be available due to radiation degradation of insulating and sealing materials. Consequently we have proposed a "self-driven rotating converter" [9] as shown in Figure 6 which has pivot-type axles and bearings and rotates by a driving force of the coolant itself. The coolant (water) works as a lubricating material as well.

Figure 5. Schematic of the performance test of the RF window

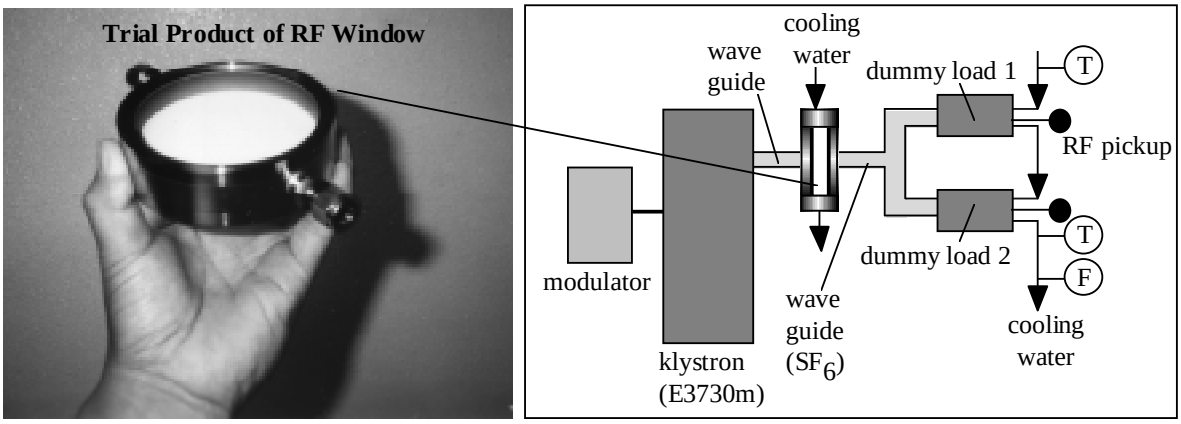

Table 2. Expected and tested conditions of the RF window

	Expected	Tested
Frequency	2856 Mhz	2856 MHz
Peak power	32 MW/2 windows = 16 MW	36.6 MW
Average power	72 kW /2 windows = 36 kW	40.1 kW
Pulse repetition	600 pps	200 pps
Pulse width	3.5 μs	5.3 μs

Figure 6. A concept of the self-driven rotating converter

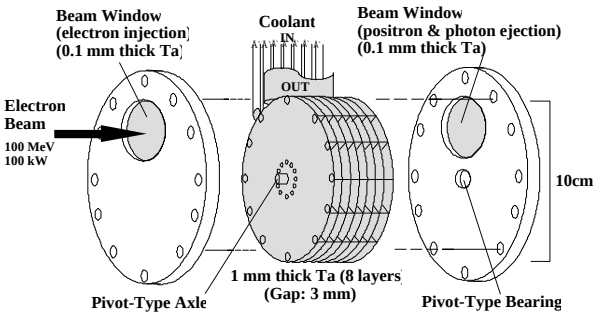

We fabricated a pilot model and confirmed the feasibility by an electron beam irradiation test, three months' performance test and a finite element calculation. According to the calculation, the maximum temperature even at the hottest point of the tantalum disks was about 720°C, which was far lower than the melting point, where the cooling water velocity and the revolution rate of the disk were 470 cm/sec and 300 rpm, respectively.

Multi-channel moderator assemblies

Usually only one slow positron beam is delivered in an operation of one linac. We have proposed "multi-channel moderator assemblies" [9] to supply multiple slow positron beams simultaneously.

To demonstrate the feasibility of the simultaneous extraction of multi-channel slow positron beams, we fabricated a set of two channel tungsten moderator assemblies as shown in Figure 7. The set was composed of 19 tungsten foil layers of 25 μm in thickness. The last layer, which was most distant from the converter, was attached to 1 mm-thick tungsten plates. Slow positrons from the first nine layers (1st channel) and the second ten layers (2nd channel) were separately extracted by two tungsten mesh grids. Each moderator layer was divided into three parts, electrically separated and biased to drift emitted slow positrons by sloping the electric field toward the extraction grids. We observed the slow positron beam profile from the assemblies with a MCP (micro channel plate), using a 100 MeV electron beam from a S-band electron linac at Osaka University.

Figure 7. Experimental set-up of two-channel moderator assemblies for the demonstrative experiment of the simultaneous extraction of multi-channel monoenergetic positron beams

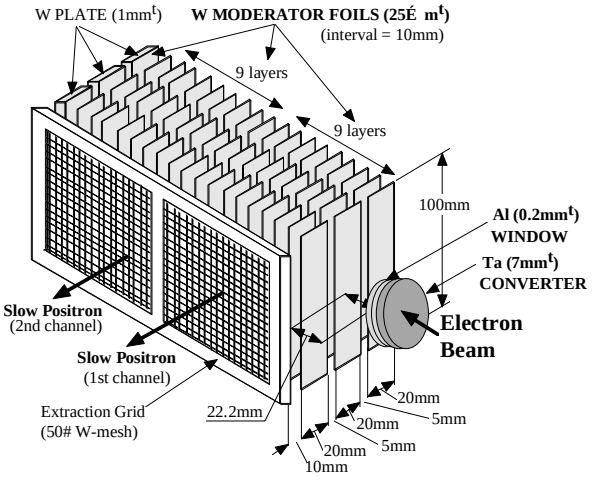

We also calculated slow positron yields, that is a ratio of the number of slow positrons emitted from each layer of tungsten foils to that of incident electrons onto the tantalum converter, for the same structure as used in the experiment, using EGS4-SPG. The result is shown in Figure 8.

Figure 8. Calculated slow positron yields from tungsten foil layers of the two-channel moderator assemblies used in the demonstrative experiment as indicated in Figure 7

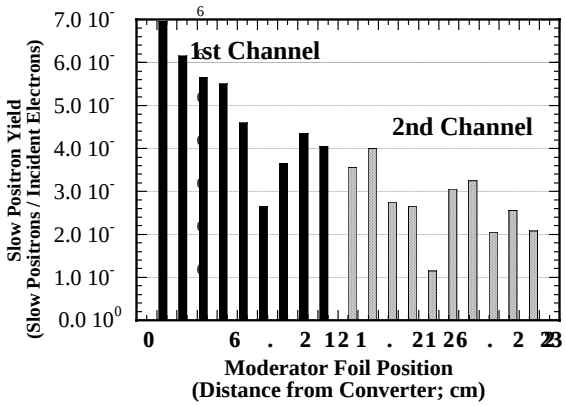

The experimental result is shown in Figure 9. Three peaks were observed in the slow positron beam intensity profile. The largest one was attributed to slow positrons from the first channel which was nearer to the tantalum converter. The second and the third peaks were both attributed to slow positrons from the second channel. It is assumed that backscattered positrons and pair production reactions by photons give rise to the third peak, because thick tungsten plates were placed at the end of the second moderator assembly. This means that positrons and photons passing through the first and second assemblies still have a potential to generate slow positrons, and also that it will be efficient to place a heavy metal at the end in fabrication of moderator assemblies. The result agrees well with the calculated result. This confirms the feasibility of the proposal and also the validity of the simulation system.

Figure 9. The intensity of extracted slow positrons observed with a MCP in the demonstrative experiment of the simultaneous extraction of multi-channel monoenergetic positron beams

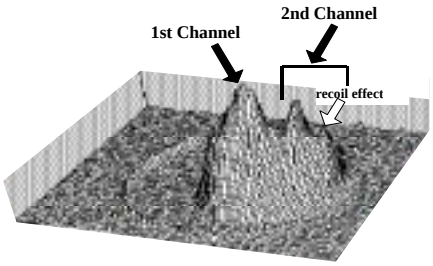

The intensity of slow positrons from the second channel was smaller only by an order of magnitude than that from the first channel. It was concluded that such an extra positron beam will be useful for preliminary or potential researches which are promoted simultaneously with main experiments using the strongest beam.

Efficient moderator structure

The demonstrative experiment result suggests usefulness of a heavy metal plate for a reflector and importance of the assembly structure. To evaluate the structure effect, we calculated slow positron yields for various moderator assembly structures as indicated in the upper side of Figure 10, using EGS4-SPG. The distance between the converter (8.2 mm-thick Ta) and the moderator was assumed to be 1 cm. Tested structures are as follows:

a) a usual one, which consists of ten tungsten foils of 25 μm in thickness vertically placed to the electron beam injection direction (V);

b) a set of these foils whose surrounding planes except for the positron and photon injection side and the slow positron extraction one are enclosed by thick tungsten plates i.e. reflectors (V+R);

c) a honeycomb-like assembly having an additional set of eleven tungsten foils crossing the above vertical foils (C);

d) a honeycomb-like assembly with reflectors.

Figure 10. Moderator structure effect: calculated slow positron yields with EGS4-SPG (bottom) for moderator assemblies having various structures (top)

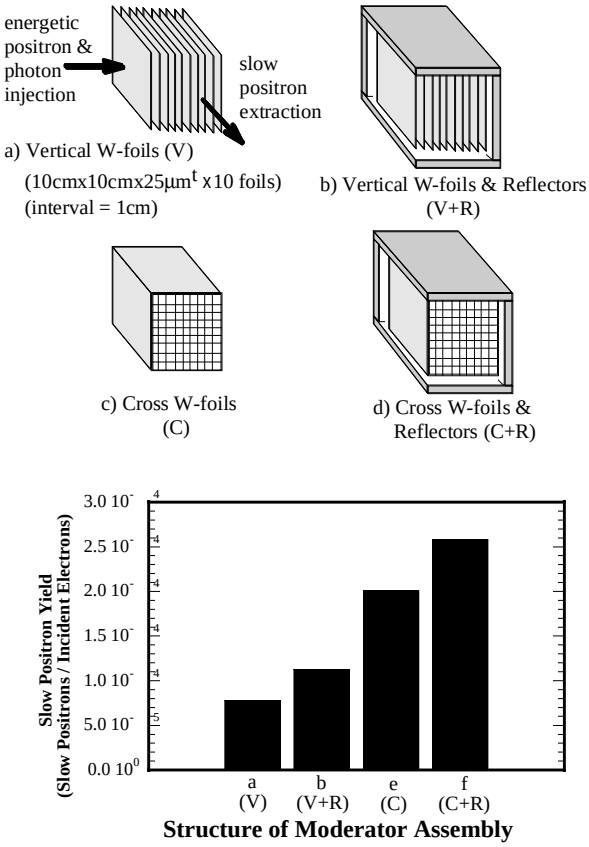

The bottom of Figure 10 shows the calculation result. The reflectors cause several tens per cent increase in the yield. Addition of the cross foils enlarges the yield nearly by three times. It is assumed that reflection of particles in the honeycomb-like structure is effective, because the surface area of the moderator foils for slow positron emission is only doubled by the additional cross foils. The yield in the honeycomb-like assembly with reflectors is more than three times larger than than in the usual one.

It is obvious that the structure effect is remarkable especially in the honeycomb-like assembly with reflectors. In the calculation, if a 100 MeV electron beam of 100 kW is applied to this assembly, a very intense monoenergetic positron beam of 10^{12}/sec in intensity is expected. This structure is practically promising for realising an intense monoenergetic positron beam of more than 10^{10}/sec in intensity, taking empirical efficiencies of beam extraction, transportation and brightness enhancement to reduce the beam size and the energy spread into account.

Local shield and remote manipulation mechanism

To suppress the activation of air surrounding the target system and reduce the thickness of concrete walls of the building, we performed a conceptual design of a local shield as shown in Figure 11, on the basis of the shield calculations. In the design, we intend to reduce the radiation level by two orders with the local shield during the linac operation.

Figure 11. A concept of the local shield of the target system and the remote manipulation mechanism

Top: During the electron bombardment
Bottom: During the manipulation of the converter and the moderator assembly

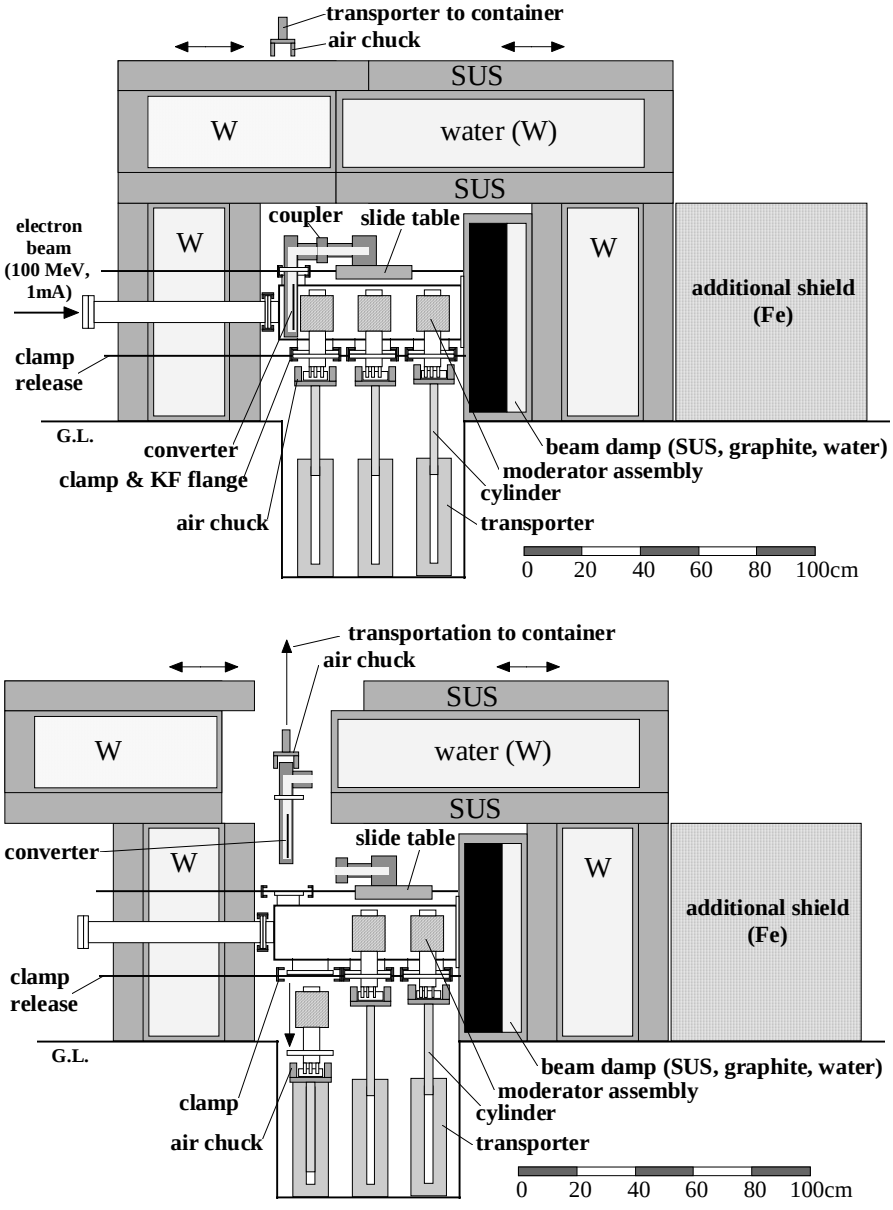

The target system is surrounded by structures consisting of 12 cm-thick steel, 30 cm-thick water and 12 cm-thick steel. The water works as a shield for neutrons and also as a coolant. An additional iron shield of 65 cm in maximum thickness for the forward beam direction will be effective in order to reduce the thickness of the concrete wall. An activated converter and moderator assemblies are manipulated by remote control and transported to containers, using air chucks, a coupler with compressed air, KF-type flanges with clamps and clamp releases with screw drive.

The inside of the local shield is vacuum. Consequently the activation of air in the target room is suppressed to permissible level as shown in Table 3. The calculated result in Table 3 also shows that the saturated activation of the local shield itself is lower than, for example, a typical cyclotron.

Table 3. Calculated activation of air, local shield and target

Activation of air	
^{3}H (12.3y):	5.6×10^{-2} Bq/cm^3
^{7}Be (53.6d):	1.1×10^{-4} Bq/cm^3
^{11}C (20.3 min):	1.1×10^{-3} Bq/cm^3
^{13}N (9.96 min):	5×10^{-2} Bq/cm^3
^{15}O (123 sec):	6×10^{-3} Bq/cm^3
^{16}N (7.14 sec):	2×10^{-7} Bq/cm^3
^{38}C l(37.3 min):	2×10^{-5} Bq/cm^3
^{39}Cl (55.5 min):	1.5×10^{-4} Bq/cm^3
^{41}Ar (1.83h):	1.8×10^{0} Bq/cm^3
Activation of target system (dose rate at 1 m from local shield surface)	
Local shield (Fe):	^{55}Fe (2.6y) 0 Sv/h
	^{59}Fe (45.6d) 15 mSv/h
	^{46}Sc, ^{54}Mn, ^{51}Cr etc. 26 μSv/h
Converter (Ta):	^{180m}Ta (8.1h) 6×10^{-2} mSv/h
	^{180}Ta (115d) 4×10^{-1} mSv/h
Moderator (W):	^{182}Ta (115d) 4×10^{-2} μSv/h
	^{183}Ta (5d) 3×10^{-2} μSv/h
	^{181}W (121.2d) 3 μSv/h
	^{185}W (75.1d) 3 μSv/h
	^{187}W (23.9d) 2×10^{-3} μSv/h
Water:	^{3}H (12.6y) 0 Sv/h
	^{7}Be (53.3y) 1×10^{-2} mSv/h

Conclusion

In the design study for the Positron Factory, we confirmed the feasibility of a dedicated high-power electron linac of 100 kW class with a beam energy of 100 MeV, with investigations including performance tests of the electron beam window and the RF window. We also experimentally demonstrated the availability of the self-driven rotating converter and the simultaneous extraction of multi-channel monoenergetic positron beams, which were proposed based on calculations with a newly developed Monte Carlo simulation system. A more efficient moderator structure, which was suggested by the experimental result, is proposed. The world's highest monoenergetic positron beam of more than 10^{10}/sec in intensity will be realised by the use of the above machines and instruments.

Acknowledgements

The basic idea of the Positron Factory project has been discussed in the Special Committee on Positron Factory Research Plan (Leader: Prof. M. Dohyama). The authors gratefully acknowledge the members for their discussions and encouraging supports. The authors also wish to thank Prof. Hirayama for his advice in using EGS4, and Prof. S. Tagawa, Dr. Y. Honda and their colleagues for their co-operation in the experiment using an electron linac.

REFERENCES

[1] W.E. Frieze, D.W. Gidley and K.G. Lynn, *Phys. Rev*. B31, 5628-5633 (1985).

[2] R. Mayer, A. Schwab and A. Weiss, *Phys. Rev*. B42, 1881-1884 (1990).

[3] A. Kawasuso, H. Arai and S. Okada, *Materials Science Forum* 255-257, 548-550 (1997).

[4] A. Kawasuso and S. Okada, *Phys. Rev. Lett*. 81, 2695-2698 (1998).

[5] S. Okada and H. Sunaga, *Nucl. Instrum. and Meth*. B56/57, 604-609 (1991).

[6] S. Okada and H. Kaneko: *Appl. Surface Science* 85, 149-153 (1995).

[7] W.R. Nelson, H. Hirayama and D.W.O. Rogers, The EGS4 Code System, SLAC Report 265 (1985).

[8] A. Vehanen and J. Makinen, *Appl. Phys*. A36, 97-101 (1985).

[9] S. Okada *et. al*., Proc. 1994 Intl. Linac Conference (Tsukuba, 1994) pp. 570-572.

To demonstrate the feasibility of the simultaneous extraction of multi-channel slow positron beams, we fabricated a set of two channel tungsten moderator assemblies as shown in Figure 7. The set was composed of 19 tungsten foil layers of 25 μm in thickness. The last layer, which was most distant from the converter, was attached to 1 mm-thick tungsten plates. Slow positrons from the first nine layers (1st channel) and the second ten layers (2nd channel) were separately extracted by two tungsten mesh grids. Each moderator layer was divided into three parts, electrically separated and biased to drift emitted slow positrons by sloping the electric field toward the extraction grids. We observed the slow positron beam profile from the assemblies with a MCP (micro channel plate), using a 100 MeV electron beam from a S-band electron linac at Osaka University.

Figure 7. Experimental set-up of two-channel moderator assemblies for the demonstrative experiment of the simultaneous extraction of multi-channel monoenergetic positron beams

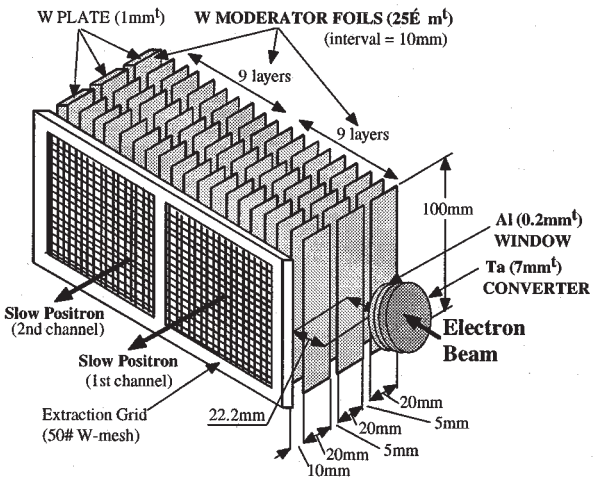

We also calculated slow positron yields, that is a ratio of the number of slow positrons emitted from each layer of tungsten foils to that of incident electrons onto the tantalum converter, for the same structure as used in the experiment, using EGS4-SPG. The result is shown in Figure 8.

Figure 8. Calculated slow positron yields from tungsten foil layers of the two-channel moderator assemblies used in the demonstrative experiment as indicated in Figure 7

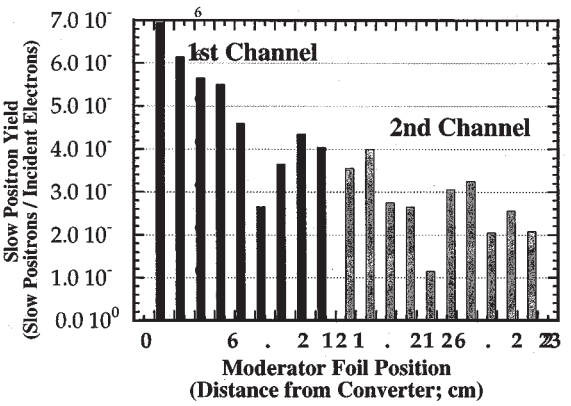

The experimental result is shown in Figure 9. Three peaks were observed in the slow positron beam intensity profile. The largest one was attributed to slow positrons from the first channel which was nearer to the tantalum converter. The second and the third peaks were both attributed to slow positrons from the second channel. It is assumed that backscattered positrons and pair production reactions by photons give rise to the third peak, because thick tungsten plates were placed at the end of the second moderator assembly. This means that positrons and photons passing through the first and second assemblies still have a potential to generate slow positrons, and also that it will be efficient to place a heavy metal at the end in fabrication of moderator assemblies. The result agrees well with the calculated result. This confirms the feasibility of the proposal and also the validity of the simulation system.

Figure 9. The intensity of extracted slow positrons observed with a MCP in the demonstrative experiment of the simultaneous extraction of multi-channel monoenergetic positron beams

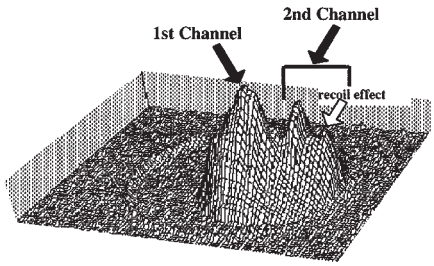

The intensity of slow positrons from the second channel was smaller only by an order of magnitude than that from the first channel. It was concluded that such an extra positron beam will be useful for preliminary or potential researches which are promoted simultaneously with main experiments using the strongest beam.

Efficient moderator structure

The demonstrative experiment result suggests usefulness of a heavy metal plate for a reflector and importance of the assembly structure. To evaluate the structure effect, we calculated slow positron yields for various moderator assembly structures as indicated in the upper side of Figure 10, using EGS4-SPG. The distance between the converter (8.2 mm-thick Ta) and the moderator was assumed to be 1 cm. Tested structures are as follows:

a) a usual one, which consists of ten tungsten foils of 25 μm in thickness vertically placed to the electron beam injection direction (V);

b) a set of these foils whose surrounding planes except for the positron and photon injection side and the slow positron extraction one are enclosed by thick tungsten plates i.e. reflectors (V+R);

c) a honeycomb-like assembly having an additional set of eleven tungsten foils crossing the above vertical foils (C);

d) a honeycomb-like assembly with reflectors.

SESSION III

Combined Use of Ion and Positron Beams

Chairman: S. Tanigawa

Chairman's summary

Prof. van Veen (Delft University of Technology, The Netherlands) elucidated the availability of positron spectroscopy in characterising voids created by ion implantation such as proton and helium ion, using variety of examples of defect analyses for silicon and metal oxides. He also introduced a plan of intense positron beam facilities at Delft with a 2 MW reactor which will produce a slow positron beam having an intensity of 2×10^{8}/s.

Dr. Okada (Japan Atomic Energy Research Institute, JAERI, Japan) reviewed the availability of combined use of ion and positron beams for industry-related matters such as hydrogen behaviour in silicon and ion-beam-induced damage recovery in optoelectronic materials. He also presented the first observation of RHEPD (Reflection High Energy Positron Diffraction), which is a novel tool for topmost surface structure observation.

Dr. Itoh (The Institute of Physical and Chemical Research, RIKEN, Japan) discussed a new technique to produce a polarised positron beam. The method used in this technique is common with PET. She suggested a possibility of collaboration between the two fields.

POSITRON BEAM ANALYSIS OF ION IMPLANTATION DEFECTS IN SILICON AND METAL OXIDES

A. van Veen, H. Schut, P.E. Mijnarends
Interfaculty Reactor Institute, Delft University of Technology
Mekelweg 15, NL2629JB Delft, The Netherlands

Abstract

Positron beam analysis has been applied to ion implanted and subsequently annealed materials to study the nucleation and growth of gas vacancy complexes and the formation of nano-voids. Helium and hydrogen implantation in the tens of keV range in silicon and MgO leads ultimately to voids after annealing to elevated temperatures where the gas is released from gas bubbles. The analysis method with high sensitivity to “open volume” effects is highly complementary to ion beam analysis methods which have their strength in detection of displaced atoms and foreign (implanted) atoms.

Introduction

Ion implantation is an important tool in silicon device technology to create well-defined doping profiles in silicon, create buried oxide layers, and recently to modify optical properties of light conductors and other optical ceramics.

A frequently used method for the study of ion implantation defects is the Rutherford Backscattering (RBS) technique and techniques derived from this technique, i.e. Nuclear Reaction Analysis (NRA), Elastic Recoil Detection (ERD) and Neutron Depth Profiling (NDP) [1]. When the incoming beam is aligned to a channelling direction the presence of atoms is detected that are displaced from their regular position. Thus interstitial atoms or interstitial atom aggregates, e.g. dislocation loops, and incoherent precipitates can be well detected and a depth distribution can be determined. However the method is rather insensitive when the defects have a vacancy type nature, e.g. monovacancies or clusters of monovacancies, or voids. The atoms bordering the cavities are only very little displaced from their lattice position so that no extra backscattering is caused. Positrons used as probe particles to detect defects are much more sensitive to vacancy type defects. When the positrons are implanted with varying energy depth resolved information on the defects becomes available. The method which we call Positron Beam Analysis covers the same depth range as RBS with MeV He when the positron energy can be varied from 0 to 30 keV. The sensitivity is 1 appm defects or better. In this article positron beam analysis results will be shown for ion implantation topics where usually RBS is employed as one of the analysis methods: ion implantation of silicon metaloxides.

In the past, it was shown that microvoids in silicon could be created by helium ion implantation followed by an appropriate thermal annealing scheme. In this article we will discuss the observations that are made by positron beam analysis on ion implanted metals, silicon and metal oxides. We report on the formation of microvoids in tungsten and silicon, and the re-filling of the voids with helium and hydrogen in silicon. Recently we created voids in metal oxides under similar conditions as for silicon. Cleaved MgO(100) single crystals were irradiated with tens of keV ^{3}He and deuterium ions and subsequently thermally annealed from 100°C to 1100°C. Monitoring of the defect depth profile and the retained amount of helium was performed by positron beam analysis and neutron depth profiling, respectively. For all materials implanted with hydrogen or helium a threshold dose of approximately 2×10^{15} cm^{-2} for void formation has been found. Vacancies filled with helium or hydrogen can hardly be distinguished from the bulk material. The voids are recognised by annihilation with little Doppler broadening, indicating the formation of para-positronium in the voids. In this contribution a route to nanovoid formation in oxide materials is discussed based on the property of helium and hydrogen gas that it is bound to the cavities in their early stage of development and thus promote clustering of vacancies, but that once the bubbles are fully grown the helium and hydrogen is released from the bubbles by permeation, exactly as was shown some ten years ago by us for nano-size helium bubbles in silicon [2].

Positron beam analysis

Positron beams

Monoenergetic positron beams with a strength of are generated by moderation of fast positrons from radioactive sources or from pair formation in nuclear reactors and accelerators. The first produce beams produce beams with an intensity of about 10^{5} $e^{+}s^{-1}$. Reactors and accelerators produce beams with an intensity $>10^{8}$ $e^{+}s^{-1}$. The high intensity can be used to convert the beam into a

microbeam for positron micro-analysis [3,4] or for 2D-ACAR measurements in thin layers. In standard positron beams the energy can be varied from 0 to 30 keV corresponding to implantation depths of several μm in most materials.

Observables

By observation of the Doppler-broadened 500 keV positron annihilation peak in the γ-energy spectrum positron fractions annihilating in the bulk, defects in the bulk and at the surface can be distinguished. Positrons have a high affinity to defects with low electron density, e.g. vacancies and micro-cavities or voids and therefore low concentrations (1 appm) of these defects can be detected. Some of the beams have a pulsed time structure (100 ps pulses) so that the lifetime distribution of the positrons can be measured [5,6]. 2D-ACAR measurements which give highly resolved details of the e^+-e^- momentum distribution can only be used in combination with an intense beam.

Reactors and accelerators produce intense beams with an intensity $>10^8$ e^+s^{-1}. In this article we will use mainly the Doppler broadening of the positron annihilation peak to characterise the defects. Before a positron is trapped in a defect it is usually thermalised. When annihilating with an electron the electron will contribute mostly to the momentum of the annihilating positron electron pair. Annihilation with electrons in conduction or valence band will give rise to Doppler shifts, and since the momentum might be in any direction, to Doppler broadening of the order of 1 keV. Annihilation with core electrons will contribute to a broadening of several keV. A practical way of expressing the Doppler broadening is by the *S* (shape) parameter and *W* (wing) parameter as defined in Figure 1. The parameter *S* gives the area under the central part of the profile, divided by the total area under the profile; thus a high value of *S* signals the presence of open-volume defects, whereas a "defect-free" sample will show a low value of the *S*-parameter. The energy windows are set symmetrically around the centre of the peak in such a way as to maximise the sensitivity to vacancies. An *S*-value of ~0.50 for defect free metals is usual. The second parameter, *W*, gives the ration between the area under the wings and the total area and is sensitive to annihilations with core electrons of the atoms in the material. For defect-free MgO in this work $S = 0.48$ and $W = 0.0075$.

Figure 1. A Doppler broadened 500 keV peak measured for perfect silicon. The intervals used for defining the *S*- and *W*-parameters are indicated.

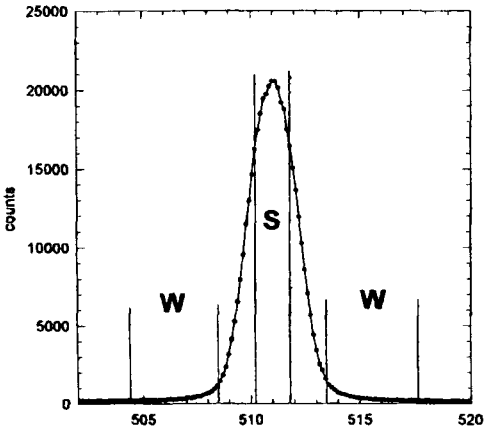

To measure *S* and *W* a single Ge-detector is used to record the energy spectrum of the gammas in the energy region around the 511 keV photo-peak. The background of the photo-peak due to

background gammas or due to compton scattering of high energy gammas can be several orders of magnitude be suppressed and the energy resolution can be improved by a factor 1.4 by employing two gamma-detectors in coincidence [7].

In that case the momentum distribution for core electron annihilations can be measured virtually undisturbed. The shape of the momentum distribution is a fingerprint for the atom composition surrounding the annihilating trapped positrons [8]. The depth distribution of trapping defects and their density is retrieved by fitting the curves of *S* and *W* vs. positron implantation energy to results of model calculations dealing with the transport and trapping of positrons. The program performing the fitting is called VEPFIT [9].

One of the important transport parameters in the program is the positron diffusion length which usually varies from 100 nm for defect-free materials to a few nm for materials with 1000 appm defect concentration.

The size of the vacancy clusters or voids can be derived from the Doppler broadening of the annihilation peak. For monovacancies or divacancies the *S*-parameter increases by about 2% and the *W*-parameter decreases by the same amount because less overlap of positrons takes place with core electrons. This percentage increases when the vacancy clusters grow bigger. When they attain a size of about 0.25 nm the cavity is large enough to accommodate positronium which can be formed by the binding of a conduction electron with the positron. In smaller cavities the energy level of the positronium would be higher than the energy of a dissociated positron electron pair. In a large void positronium will adopt two states, ortho- and para-positronium. Positronium in the first state (triplet state) will live sufficiently long so that annihilation occurs by pick-off occurs with electrons with the surrounding medium. Their momentum distribution is similar to that of defect-free material. But one-fourth of the positronium will be in the latter (para or singlet) state which will decay in a short time 125 ps by annihilation with virtually no momentum. Taking into account the finite resolution of the Ge-detector for para-positronium an *S*-parameter of 0.9 is expected; for the annihilation of positronium in a cavity an *S*-parameter of approximately $S_{cav} = 1/4\ \ 0.9 + 3/4\ \ S_{bulk}$ is expected with $S_{bulk} = 0.58$. For silicon an *S*-value of 0.66 indicates large voids (size > 1 nm). Sometimes $S_{rel} = S/S_{bulk}$ is used; then large voids have $S_{rel} = 1.13$. In semiconductors and in isolating materials positronium is the major state of positrons present in the cavity. In metals positrons can also adopt surface bound.

Implantation defects in materials

Positron beam analysis has been proved to be a very sensitive technique to detect small amounts of defects created by ion implantation in silicon. Nielsen *et al*. [10] were able to detect defects in Si irradiated with MeV Si-ions at dose levels as low as 10^{10} ions cm^{-2}. These defect concentrations are below the appm level. Simpson *et al*. [11] showed by combined use of positron beam analysis, RBS (Rutherford Backscattering Spectroscopy) and infrared absorption that room temperature Si and helium implanted silicon contained divacancies. Some fraction of the defects created by 0.5 to 5 MeV ion implantation at doses varying from 10^{11} cm^{-2} to 10^{16} cm^{-2} annealed at 560 K corresponding to divacancy migration. For the Si implanted crystals recovery took place between 870 and 970 K ascribed to recrystallisation of amorphised silicon. Some of the observations made by the authors on the discrepancy between the calculated and observed defect depth profile in the case of helium could not be explained in the article. Later experiments on hydrogen and helium filling of defects in silicon by Hakvoort *et al*. [12] revealed the reason for this observation. When filling vacancy type defects,

hydrogen and helium do not reduce the positron trapping but lead to an increase of annihilation with the Si matrix atoms. Therefore the highly gas decorated defects are difficult to distinguish from the bulk. Defects not filled with gas which are found in the zone between the surface and the gas implantation profile (which is usually a narrow distribution) will dominate the defect profile measured by positron beam analysis. Proof of the presence of the defects in the gas rich zone is usually found by thermal annealing. At a certain temperature the gas will dissociate and be partly released. Then a strong positron signal indicating vacancy defects is observed. It is not always possible to derive defect densities from the measured positron sink strength because specific trapping rates are not known. However, for monovacancies and divacancies in a number of semiconductors detailed information is available. Hautojärvi *et al*. [13] have shown that the specific trapping rate for point defects (neutral monovacancies) in semiconductors increases in proportion to 1/T, and that negatively charged vacancies trap positrons 100 times faster than neutral vacancies.

Another interesting aspect of implantation depth profiling by positrons is that because of its high sensitivity defects are nearly always observed at depths much larger than the implantation depth of the projectiles [14]. In many implantation experiments defect concentrations at the implantation depth are of the order of 1% so that saturation trapping occurs. Although at larger depths the concentrations decrease rapidly, positrons will still observe defects until defect levels drop 3-4 levels of magnitude. The deep defects might be due to channelling of projectile ions and to migration and clustering of point defects into dislocations. Figure 2 shows the result of a defect tail observed for Rb^+ implantation of tungsten [15]. Tungsten foils were irradiated with 110 keV Rb^+ ions with doses varying from 10^{12} to 10^{16} cm^{-2}. With increasing Rb^+ dose the *S*-parameter developed a maximum at 2 keV positron implantation energy, which corresponds to a mean implantation depth in tungsten of 6 nm. TRIM [16] calculations yield a range of 7 nm. Defects were observed to extend to depths larger than 250 nm (25 keV positron energy). After annealing to 1300 K bubbles developed, mostly at a low depth.

Figure 2. *S* vs. positron energy curves measured for a tungsten foil implanted with 110 keV Rb^+ at the indicated doses

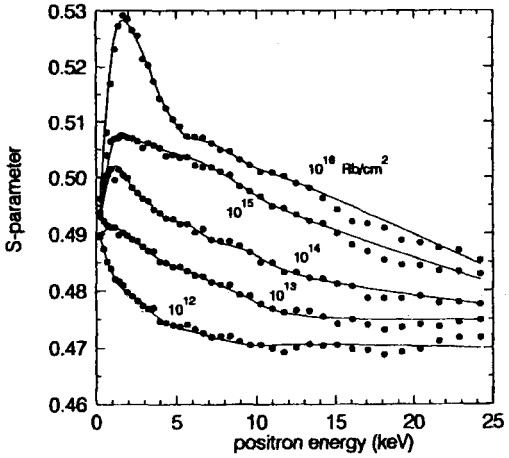

Microcavities in silicon

Light-ion bombardment of silicon with keV ions at doses beyond 10^{16} cm^{-2} and subsequent annealing up to a high temperature (1100 K) have been shown to generate microcavities in the material [2,17]. The point defects cluster together with the hydrogen or helium atoms to form nanometer-sized bubbles. Near the final temperature of 1100 K the gas is dissolved and permeates to

the surface where it is released. Positron beam analysis is very well suited to detect the cavities. The *S*-parameter increases to a value which is 10-12% higher than the value for defect-free silicon. This value can be understood in terms of ps-formation as has been pointed out earlier. Positronium exists only in cavities with a size larger than 0.8 nm. When the cavity becomes decorated with gas a high pressure can be built up which also suppresses the formation of positronium. This has been demonstrated by Hakvoort *et al*. [12] by hydrogen and helium ion implantation and annealing of silicon which contained microcavities. In Figure 3 some of these gas filling results are shown. Results of cavity formation in silicon by 30 keV deuterium implantation (3×10^{16} cm^{-2}) are shown in Figure 4. The *S* and *W* co-ordinates are plotted in *S*-*W* maps. It is observed that by increasing the energy layers are probed with characteristic positron states. Notably, after annealing to 925°C a defect state with high S_{rel} is found, indicating the presence of cavities [18]. Monte Carlo modelling of the gas bubble and void growth in light ion irradiated silicon is described by Fedorov and van Veen [19].

Defects and microcavities in MgO

General

Recently, interest has been growing in the possibilities offered by modification of optical properties of transparent oxide materials by implantation formation of metallic nanoprecipitates [20]. It was shown in MgO that during post-implantation annealing to 1000°C point defects were removed and nanoprecipitates of gold atoms were formed giving rise to a characteristic absorption band at 2 eV photon energy. Apparently the gold atoms are not well soluble in the MgO matrix and therefore precipitates are formed. Similar observations are known for the heavy noble gases implanted into a variety of metal oxides. Gas bubbles of nanosize have been observed in UO_2 [21] and in MgO [22]. It is well known that for a variety of ceramic materials, e.g. Al_2O_3 exposed to neutron irradiation ordered void structures are developed. It is likely that gases are involved who stabilise the growing voids.

Figure 3. The effect of helium filling of nanovoids in silicon

Refilling of the voids by 2.5 keV He to doses of 8×10^{15} cm^{-2} and 1.6×10^{16} cm^{-2} and after annealing at 300 and 800°C, respectively

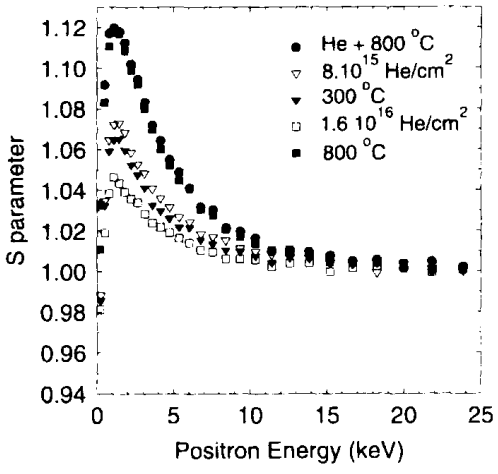

Figure 4. The parameters S_{rel} and W_{rel} for (a) the as-irradiated sample and (b) the annealed sample (925°C)

Measured and fitted values are indicated. Note that besides surface and bulk three more different defect layers are found at RT and only two at 925°C. The energy range of the positrons is indicated.

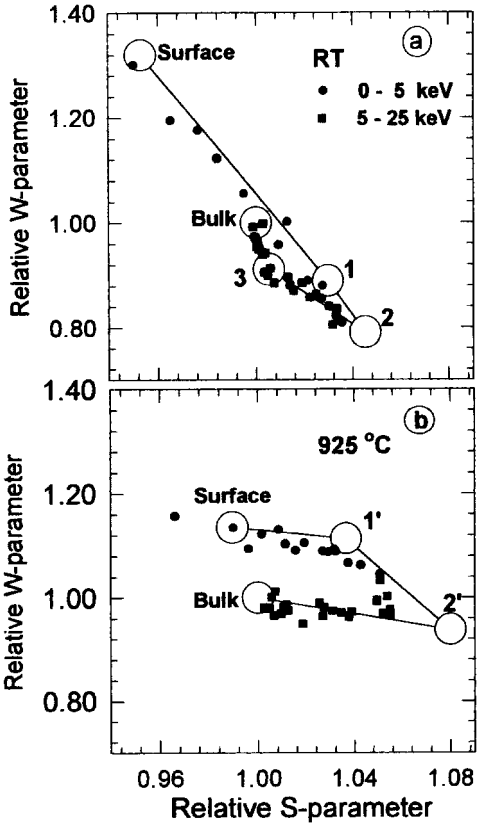

Ion implantation of MgO

Samples 10×10×1 mm were cleaved from the MgO(100) crystals and implanted with 30 keV ^{3}He ions at a current density of about 2 μA/cm^2. The beam was uniformly swept over the implantation area by using deflection plates. Thermal annealing was performed in a tube oven in ambient air for periods of 30 minutes. Samples were checked on the presence of optically active defects by absorption spectroscopy in the visible light.

Positron beam results

In Figure 5 the *S*-parameter is plotted vs. the positron implantation energy for three of the helium implanted samples. For the as-implanted samples little deviation from the *S*-value for the bulk, measured at positron implantation energy >10 keV, is observed. The lowest dose of 10^{15} cm^{-2} shows a decrease at the positron energy (4 keV) corresponding to implantation in the depth zone of maximum displacement damage by the helium. The *S* vs. *E* curves taken after annealing to 1373 K show recovery of the damage for the lowest dose but a considerable increase of *S* in the helium

Figure 5. The *S*-parameter plotted vs. the positron implantation energy for ^{3}He implanted MgO(100)

The curves are shown for the as-implanted case and for the samples annealed at 1373K. The mean positron implantation depth corresponding to the positron energy is indicated at the top scale.

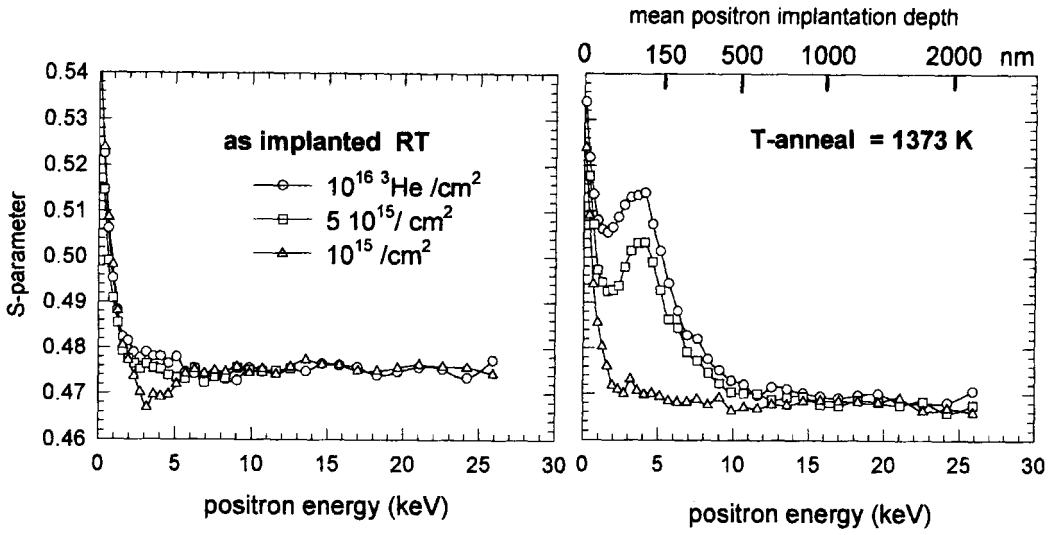

implantation zone for the higher doses. According to the depth scale the cavities that have developed are centred around a depth of 120 nm which is lower than the helium implantation depth according to TRIM calculations. A depth analysis of defects has been performed by employing the positron beam analysis fitting program VEPFIT [9].

A model is used in which we define two layers with defects on top of a substrate. The program will fit the thickness of the layers, the positron diffusion lengths and the *S*-values in the layers and substrate. The following observations are made during thermal annealing in ambient air:

1. From RT to 1000 K defects are observed at a mean depth of about 50 nmin and for T > 1000 K at a depth of 120 nm.

2. Defects at shallow depth show an increased *S*-value for T > 800 K. At the lowest dose there is rapid recovery at higher temperatures, but for the highest dose defects survive to 1375 K.

3. Defects in the main defect layer show a sharp increase of *S* for T > 1000 K. For the highest doses a maximum of *S* is found at about 1400 K. At 1500 K the *S* has recovered to the bulk value.

For the lowest dose first a further reduction of *S* is observed. At 1200 K an increase is observed. Recovery takes place at 1400 K.

In general it is observed that *S* for the defect-free crystal shows low values. This can be understood from the fact that MgO is an ionic crystal and thus charges are transferred from the cation to the anion. Since the positron is a positively charged particle, once thermalised it will dwell most of its time near the anion and therefore annihilate with oxygen electrons which is known to give a low *S*-value. For the helium implanted case it is clear that in the as-irradiated state and also after low temperature annealing irradiation produced point defects, i.e. V_{Mg} and V_O exist in the region from

the surface to the depth zone where the helium is stopped. TRIM results indicate up to a maximum of seven displacements (not included spontaneous and below room temperature recombination) per helium projectile. The displacement energy for both the cation and anion is of the order of 55 eV [23]. In the helium implantation zone helium decorated vacancies will dominate. Furthermore, a large fraction of the Frenkel pairs will recombine so that a large portion of the vacancies will be filled with helium. In the shallow zone vacancies without helium will also be found. It is likely that helium is more strongly bound to the anion vacancy than to the cation vacancy. The radius of the anion (oxygen) in MgO is 0.14 nm and the cation radius is 0.066 nm. Helium under pressures of 1 GPa has an atomic radius of about 0.1 nm [24] and thus will trap only in the anion vacancy or in clusters of vacancies or in agglomerates of Schottky defects. However, trapping in anion vacancies is possible if the cations surrounding the anion vacancies relax outwardly when the helium is trapped. Mg and O interstititials formed in nearly stoichiometric proportions will either recombine with the vacancies or plate out as dislocation structures. During annealing first the non-decorated vacancies will start to move because atom lattice jumps are not hindered by the helium. In literature migration energies for both the anion and cation vacancy are reported with a value of 2.2 and 2.4 eV, respectively. On the time scale of our annealing scheme it can be calculated that the vacancies will have moved to 800 K. At this temperature some reduction of *S* is observed in the first layer, but little is changed in the second layer. Signs of vacancy clustering are observed at T >100 K. We ascribe the delay in vacancy mobility to the stabilising effect of the helium. At 1000 K helium is released and vacancy clusters are created filled with helium. Since the helium/vacancy ratio has dropped a small increase of the *S*-parameter is observed.

We propose that Ostwald ripening occurs, a process in which small clusters dissociate and larger ones grow by collecting the dissociating vacancies and gas atoms. The process will continue until nm size bubbles are produced. Because of the presence of the high pressure gas the *S*-parameter will not increase to high values [12]. It is only until 1200 K that a very drastic increase of *S* occurs. Apparently, at that temperature helium is released from the bubbles, as evidenced by the results of helium depth profiling by the NDP method [25].

The threshold dose needed to accomplish the Ostwald ripening process can be explained as follows. After the first annealing step at 1000 K the density of small helium vacancy clusters should be large enough so that the diffusion length of the dissociating vacancies and helium is smaller than the distance to the sample surface. If larger, the defects will disappear without contributing to the build-up of larger clusters. From our measurements we conclude that the threshold dose is at about $2\ 10^{15}$ ^{3}He cm^{-2}. The depth where the cavity zone develops at about 120 nm is the zone where the vacancy concentration is high but with a relatively low helium concentration. There the probability of clustering is highest. A similar cavity growth process in helium implanted silicon has been successfully simulated by a Monte Carlo program MODEX [19].

Experimental results for 15 keV deuterium implanted MgO are shown in Figures 6 and 7. They also indicate cavity formation for deuterium beyond above dose [18]. However, cavities develop earlier during the annealing. Already at 950 K the *S*-value increases to its maximum value.

Discussion

The above examples have shown that positron beam analysis is a sensitive technique to provide information on open volumes and is therefore highly complementary to the ion beam techniques used for structure and composition analysis. Among them are the earlier mentioned Rutherford Backscattering (RBS), Nuclear Reaction Analysis (NRA), Elastic Recoil Detection (ERD) and

Figure 6. The *S*-parameter plotted vs. positron implantation energy for a high dose deuterium implanted Mg(100) crystal, in the irradiated state and after annealing to 550, 750 and 950 K respectively [18]

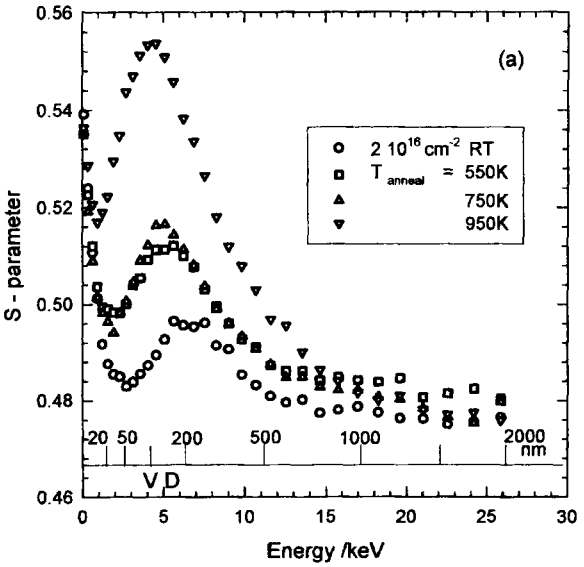

Figure 7. *S*-*W* map for the 950 K annealing measurement in Figure 6

The arrows indicate the increase of energy (implantation depth) from surface via top layer, cavity layer and defect tail region to bulk

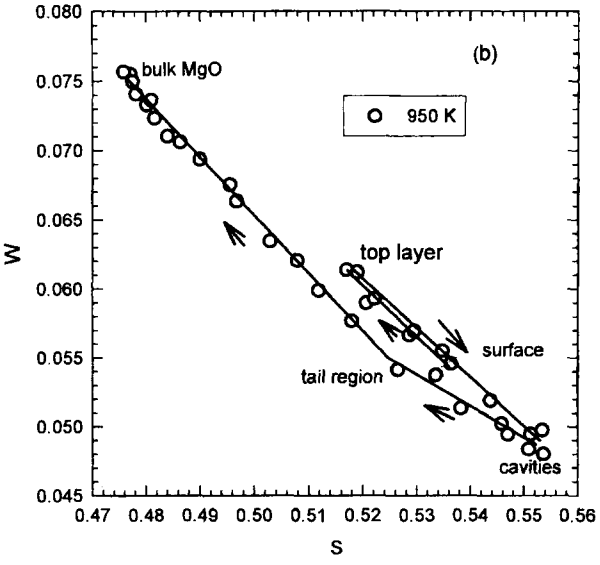

Secondary Ion Mass Spectrometry [3]. These techniques, however, are not sensitive to the presence of open-volume defects. Positron beam analysis has a sensitivity of about 1 appm for non-charged vacancies. RBS and NRA have sensitivities of about 10^{13} cm^{-2} displaced or interstitial atoms which corresponds to damage levels of about 20 appm displaced atoms when the defects are assumed to have been spread over a depth of 100 nm below the surface.

Conclusion

Positron beam analysis is very well suited to observe open-volume defects in materials ranging in size from a vacancy to nano-voids or micro-cavities. Positrons are sensitive to the presence of gases in these defects and can be used to monitor the arrival or gas release at the cavities. In combination with one of the ion beam based depth-profiling techniques, RBS, NRA, NDP and NRA positron beam analysis forms a powerful analysis package to study defects composed of foreign atoms and vacancies. Positron beam analysis is able to detect the very early stages of vacancy cluster nucleation and void growth. In particular ion beam produced defects are in the right observation range of positron beams. Therefore installation of an auxiliary positron beam for analysis in ion beam implantation and analysis chambers would add greatly to the analysis power of such equipment. Suitable designs are available, based on electrostatic guidance of the positron beam [4], to meet the physical requirements for a combination with ion implantation equipment.

REFERENCES

[1] L.C. Feldman and J.W. Mayer, *Fundamentals of Surface and Thin Film Analysis* (Amsterdam, Elsevier, 1986).

[2] G.C. Griffioen, J.H. Evans, P.C. de Jong and A. van Veen, *Nucl. Instrum. Meth*. B27 (1987), 417.

[3] A. van Veen, F. Labohm, H. Schut, J. de Roode, T. Heijenga, P.E. Mijnarends, *Applied Surface Science* 116 (1997), 39-44.

[4] L.V. Jørgensen, A. van Veen, H. Schut, accepted for publication in NIM-A (1998).

[5] R. Suzuki, T. Mikado, H. Ohgaki, M. Chiwaki, T. Yamazaki and Y. Kobayashi, in *Slow Positron Beam Techniques for Solids and Surfaces*, eds., E. Ottewitte and A.H. Weiss, AIP Conf. Proc. 303 (1994), 526-534.

[6] P. Willutzki, J. Störmer, G. Kögel, P. Sperr, D.T. Britton, R. Steindl and W. Triftshäuser, *Mat. Sci. Forum* 175-178 (1995), 237-240.

[7] K.G. Lynn, J.R. MacDonald, R.A. Boie, L.C. Feldman, J.D. Gabbe, M.F. Robbins, E. Bonderup and J. Golovchenko, *Phys. Rev. Lett.* 38 (1977), 241.

[8] P. Asoka-Kumar, M. Alatalo, V.J. Ghosh, A.C. Kruseman, B. Nielsen and K.G. Lynn, *Phys. Rev. Lett.* 77 (1996) 2097-2100.

[9] A. van Veen, H. Schut, J. de Vries, R.A. Hakvoort and M.R. Ijpma, AIP Conf. Proc. 218 (New York, AIP, 1990), 171-196.

[10] B. Nielsen, O.W. Holland, T.C. Leung and K.G. Lynn, *J. Appl. Phys.* 74 (1993), 1636.

[11] P.J. Simpson, M. Vos, I.V. Mitchell, C. Wu and P.J. Schultz, *Phys. Rev.* B44 (1991), 12180-12188.

[12] R.A. Hakvoort, A. van Veen, P.E. Mijnarends and H. Schut, *Appl. Surf. Sci.* 85 (1995), 271-275.

[13] P. Hautojärvi, *J. de Physique IV*, Coloque C1, Suppl. JPIII, 5 (1995), 1-14.

[14] R.A. Hakvoort, A. van Veen, J. Noordhuis and J.Th.M. de Hosson, *Surface and Coating Technology* 66 (1994), 393-397.

[15] H. Schut and A. van Veen, *Appl. Surf. Sci.* 85 (1995) 225-228.

[16] J.F. Ziegler, J.P. Biersack and U. Litmark, *TRIM-87, the Transport of Ions in Matter* (New York, Pergamon Press, 1985).

[17] S.M. Meyers, D.M. Follstaedt and D.M. Bishop, *Material Science Forum* 143-147 (1994), 1635-1640.

[18] A. van Veen, H. Schut, A.V. Fedorov, E.A.C. Neeft, R.J.M. Konings, J.Th.M. de Hosson and B.J. Kooi, accepted for publication in NIM-B (1998).

[19] A.V. Fedorov, A. van Veen, *Computational Materials Science* 9 (1998), 309-324.

[20] A. Yueda, R. Mu, Y.S. Tung, D.O. Henderson, C.W. White, R.A. Zuhr, J.G. Zhu and P.W. Wang, *Materials Science Forum* 239-241 (1997) 675-678.

[21] J.H. Evans, A. van Veen, K.T. Westerduin, *Journal of Nuclear Materials* 195 (1992), 250-259.

[22] M. Grant Norton, E.I. Fleischer, W. Hertl, C.B. Carter, J.W. Mayer, E. Johnson, *Phys. Rev.* B43 (1991) 9291.

[23] F.W. Clinard and L.W. Hobbs, in *Physics of Radiation Effects in Crystals*, eds., R.A. Johnson and A.N. Orlov (North-Holland, Amsterdam, 1986).

[24] R.L. Mills, D.H. Liebenberg and J.C. Bronson, *Phys. Rev.* B21 (1980) 5137.

[25] H. Schut, A. van Veen, F. Labohm, A.V. Fedorov, E.A.C. Neeft and R.J.M. Konings, accepted for publication in NIM-B (1998).

SOME RESULTS IN COMBINED USE OF ION AND POSITRON BEAMS AT JAERI

Sohei Okada, Atsuo Kawasuso, Hideyuki Arai,
Masaki Maekawa and Masakazu Kondo
Takasaki Establishment, Japan Atomic Energy Research Institute
1233 Watanuki, Takasaki, Gunma 370-1292, Japan

Abstract

Some results in combined use of ion beams and positron spectroscopy techniques partly using a slow positron beam at JAERI-Takasaki are reviewed. These include possibilities of future applications of the combined use.

Introduction

At the Takasaki Establishment, Japan Atomic Energy Research Institute (JAERI-Takasaki), researches on materials science and biotechnology are in progress using a variety of ion beams from an AVF cyclotron, a 3 MV tandem accelerator, a 3 MV single-ended accelerator, a 400 kV ion implanter, a LEIBS (Low Energy Ion Beam Deposition System) and an ISOL (Isotope Separator On-Line). We have been using the ion beams combined with conventional positron annihilation spectroscopies and advanced techniques with positron beams in order to characterise materials at the atomic level. In this article, some results related to the combined use are reviewed.

Thermal defect study with an internal positron source produced by a cyclotron

We produced a positron emitter ^{22}Na inside a FZ-silicon specimen by a nuclear reaction ^{28}Si(p,^{7}Be)^{22}Na with a proton bombardment from the JAERI AVF cyclotron. This internal positron source enables thermal defect studies by using positron spectroscopy at high temperature where usual positron sources would be melt down. It is an urgent issue in semiconductor industries whether the thermal defects are formed or not.

The radiation-induced defects were eliminated by annealing up to 900°C. After the annealing the Doppler broadened annihilation radiation energy spectra were measured with elevated temperatures. The S-parameter drastically increases around 1100°C, which suggests formation of thermal defects. The formation energy was evaluated to be about 4.7 eV from the result.

The experiment suffered from squeezing-out of active sodium atoms from the specimen, which might cause uncertainty in the result. Farther detailed investigations will be necessary to get a clear answer. The detail of this research is described in Ref. [1].

Construction of a pulsed MeV positron beam

The above internal positron source technique has advantages in good S/N ratio and availability in extreme conditions such as high temperature. But there is a limitation of materials to produce the internal source by ion beam irradiation.

Positron lifetime measurements with a pulsed positron beam have the same advantages and no such limitations. Pulsed positron beams having energies up to several tens keV for surface study exist in the world [2], whereas higher energy pulsed beams for bulk analysis do not.

We have been constructing a pulsed MeV positron beam line (PUMPS: PUlsed MeV Positron Source) with a pulse width of 100 ps. A schematic view of the beam line is shown in Figure 1. Slow positron generation and transportation with good performance in the part from the source to the chopper tube were confirmed in the beam experiments using a 3.7 MBq ^{22}Na positron source and an electron gun.

The chopper performance was tested with a low emittance electron beam which emulates a slow positron beam emitted from the moderator surface by the negative surface work function. The transmitted current of the accelerated beam was zero when the chopper potential was higher than

Figure 1. Schematic of PUMPS

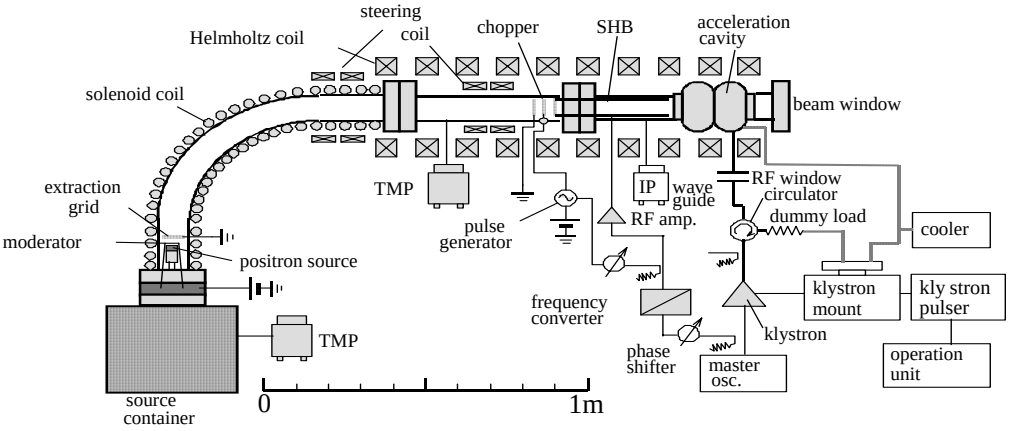

the acceleration voltage, and sharply increased with lowering the chopper potential. The chopping efficiency for a 500 eV beam was estimated to be 75%. Here the pulse level was assumed to be 5 V, which is a maximum of our available pulse generator (HP8131A; rising time <200 ps). A well coincident chopped beam with the pulse level change in a time range of 2 ns was also observed.

The subharmonic buncher (SHB; 178.5 MHz) and the acceleration cavity (2856 MHz) were installed. In the operation test of the klystron (2856 MHz), the performance with 8 μs pulse width and 100 pps repetition was obtained, which is better than its specification (>300 kW, >4 μs, >50 pps). The acceleration efficiency of an injected 500 eV beam with a pulse width of 2 ns from the chopper into the SHB was estimated to be 70% from the acceleration phase width calculated by a simulation.

The waveguide circuit was then installed, and the acceleration up to 1 MeV was confirmed by using an electron beam. The electron gun will be replaced by a 3.7 GBq ^{22}Na positron source by March 1999. The detail of this work is described in Ref. [1].

The pulsed MeV positron beam will enable positron lifetime measurements in combined environments during another beam bombardment as well as in such extreme ambients as at high temperatures and under dynamic stresses.

Vacancy-hydrogen interaction in proton-implanted silicon

Hydrogen behaviour in semiconductors has recently been attracting attention both in industry and in basic material science fields. We studied the vacancy-hydrogen interaction in 6 MeV proton-implanted silicon with positron lifetime measurements in comparison with 6 MeV He-ion-implanted and 3 MeV electron-irradiated silicons.

The lifetimes of positrons trapped at vacancy-type defects in the He-implanted and the electron-irradiated silicons increased monotonically with annealing temperatures up to around 600°C, which shows the evolution of vacancy clusters. On the contrary, the lifetime in the proton-implanted silicon decreased down to 245 ps at 450-500°C and increased again at 600°C. This result suggests the formation of vacancy-hydrogen complexes such as divacancy and multi-hydrogen complexes, which was supported by the fact that the annealing behaviour of some infrared absorption lines associated with local vibration of hydrogen atoms was correlated with that of the positron lifetime and the trapping rates. The detail of this study is described in Ref. [3].

Correlation between optical properties and damages in rare-earth-implanted silicon-based materials

Rare-earth-implanted silicon-based materials were investigated by Cathodoluminescence (CL) measurements and Doppler-broadened line-shape technique with an energy-tuneable positron beam. An erbium (Er) implanted SiO_2/Si (SiO_2 film grown on Si substrate) showed a large luminescence peak around a wavelength of 1.54 μm after annealing up to 900°C. This wavelength corresponds to the minimum loss of silica-based optical fibres. Consequently this result suggests a possibility to develop new optoelectronic devices. It was presumed from the positron spectroscopy results that the annealing is effective on the recovery of the point defects induced by the ion implantation. The detail of this work is described in Ref. [4].

The first observation of RHEPD

We have developed an isotope-based and electrostatically guided slow positron beam as shown in Figure 2. The overall efficiency of slow positron generation and transportation to the specimen was measured to be 2.6×10^{-5} to 5.5×10^{-5} depending on the acceleration energy up to 30 keV. These are fairly good for an electrostatic slow positron beam line.

Figure 2. Schematic of the electrostatic slow positron beam line

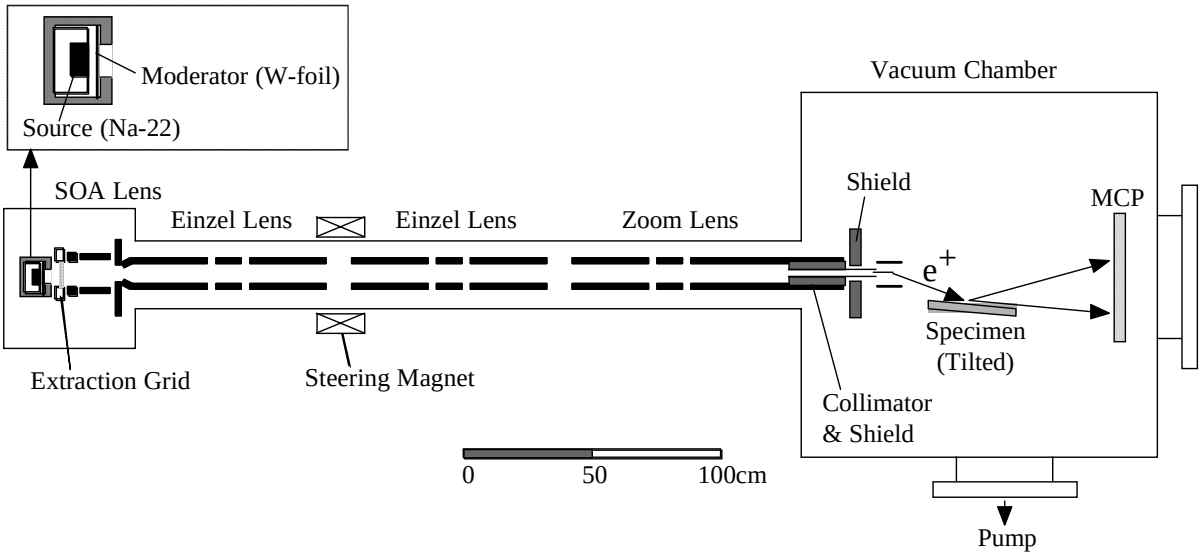

By the use of the electrostatic positron beam, we succeeded in the first observation of RHEPD (Reflection High Energy Positron Diffraction). The 20 keV positron beam was irradiated onto a hydrogen-terminated Si(111) surface. The zero-th Laue zone consisting of a specular and diffraction spots with a shadow edge was clearly observed using a microchannel plate. The rocking curve of the specular spot showed the primary Bragg peak and the total reflection of positrons, which proved the predicted superiority of positron as a topmost surface sensitive probe to others like electron.

The detail of this study is described in Ref. [5] This technique will be applied for the observation of diamond surfaces produced by the LEIBS.

Acknowledgements

The authors wish to thank Dr. Y. Kobayashi, Dr. K. Hirata and Dr. T. Sekiguchi for their co-operation and encouraging discussions in the experiments using a magnetically guided slow positron beam line and a cathodoluminescence measurement system.

REFERENCES

[1] S. Okada *et. al*., Proc. 11th Symposium Accelerator Science and Technology (Harima Science Garden City, 1997) pp. 107-109.

[2] R. Suzuki *et. al*., *Jpn. J. Appl. Phys*. 30 (1991) L532-L534.

[3] A. Kawasuso, H. Arai and S. Okada, Materials Science Forum 255-257 (1997) 548-550.

[4] H. Arai *et. al*., TIARA Annual Report 1997 (JAERI Review 98-016) (1998) 156-157.

[5] A. Kawasuso and S. Okada, *Phys. Rev. Lett*. 81 (1998) 2695-2698.

PREPARATION OF AN INTENSE POSITRON SOURCE BY ELECTRO-DEPOSITION OF ^{18}F ON A CARBON ELECTRODE

Yoshiko Itoh, Tadashi Nozaki, Akira Goto
Cyclotron Laboratory, The Institute of Physical and Chemical Research
Hirosawa 2-1, Wako-shi, Saitama 351-0198 Japan

Ichiro Fujiwara
Department of Economics, Otemon-gakuin University
Nishiai-2-1-15, Ibaraki-shi, Osaka, 567-8502 Japan

Ren Iwata
Cyclotron Radioisotope Centre, Tohoku University
Aramaki, Aoba-ku, Sendai-shi 980-0845 Japan

Abstract

The electro-deposition of ^{18}F-fluoride on a small sized graphite electrode was examined for the preparation of an intense positron source for spin-polarised beam. A small copper hemisphere of 1 ml volume gilded with rhodium was used as both cathode and vessel for water, and a graphite cylinder of 3 mm or 5 mm diameter was used as an anode and a collector of ^{18}F-fluoride. The voltage and period for the most efficient electro-deposition were 90 V and 20 min., respectively, and the recovery of ^{18}F was 70%.

Introduction

Polarised positrons are useful for probing the spin density of electrons in solids [1] and for studying positronium and its chemistry [2]. To produce intense spin-polarised positron beams, various solid targets [3-5] and gas and liquid targets [6,7] were tested by using a compact cyclotron. We selected ^{18}F, β^+ emitter, with a half-life of 110 min. for this purpose. The radioactive ^{18}F (ca. 30 GBq produced in a 1 ml ^{18}O-water target via the $^{18}O(p,n)^{18}F$ reaction with a 14 MeV proton beam at a current of 20 μA in the AVF cyclotron vault in RIKEN (Institute of Physical and Chemical Research). An apparatus for ^{18}O-water irradiation was constructed and connected with the beam line of AVF cyclotron. The product is transferred to an experimental vault (E7) downstairs which is shielded against the radiation of the cyclotron. An automatic apparatus is used for collection of ^{18}F on a small spot. The collected ^{18}F are transferred close to the moderator foil as shown in Figure 1.

Figure 1. Automated apparatus for preparing the ^{18}F positron source

[A]: Adsorption method, [B]: Evaporation method

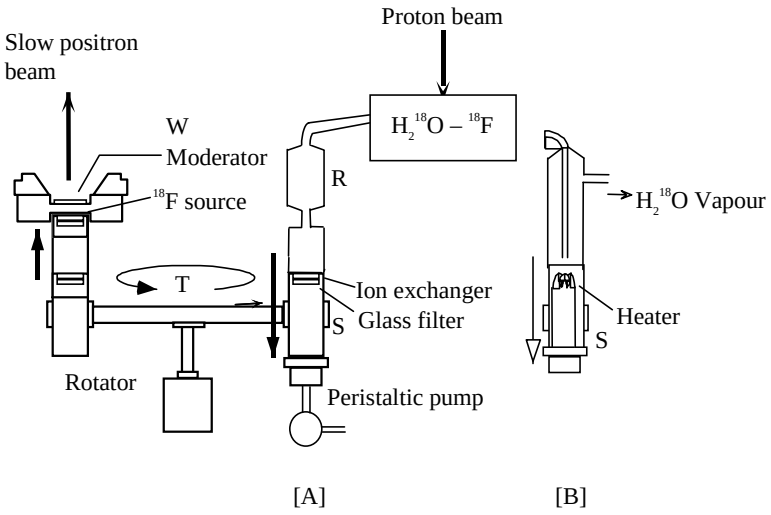

The slow positrons are transferred to the Polarimeter guided with the magnetic field of solenoid coils (SI-4) and Helmholt coils (HI-7) as shown in Figure 2. Polarisation of the slow positron beams is measured by means of magnetic quenching of positronium (Ps) due to the Zeeman effect. High-intensity polarised slow positron beams will provide us with a sensitive probe into the new materials in which they annihilate.

At first anion exchange resin or evaporation was used for the recovery of ^{18}F from the ^{18}O-water [6,7]. The recovery efficiency was as high as 90%, but the spot size of the positron source was not small enough and the emission of positron from the source was not high enough for the purpose above mentioned.

The recovery of ^{18}F-fluoride on graphite from the ^{18}O-water using electric field was investigated by D. Alexoff *et al*. [8]. The purpose of this paper is to examine the parameters which control the efficient recovery of ^{18}F on a very small sized carbon electrode to prepare an intense positron source of ^{18}F.

Figure 2. The slow positron beam line and Polarimeter

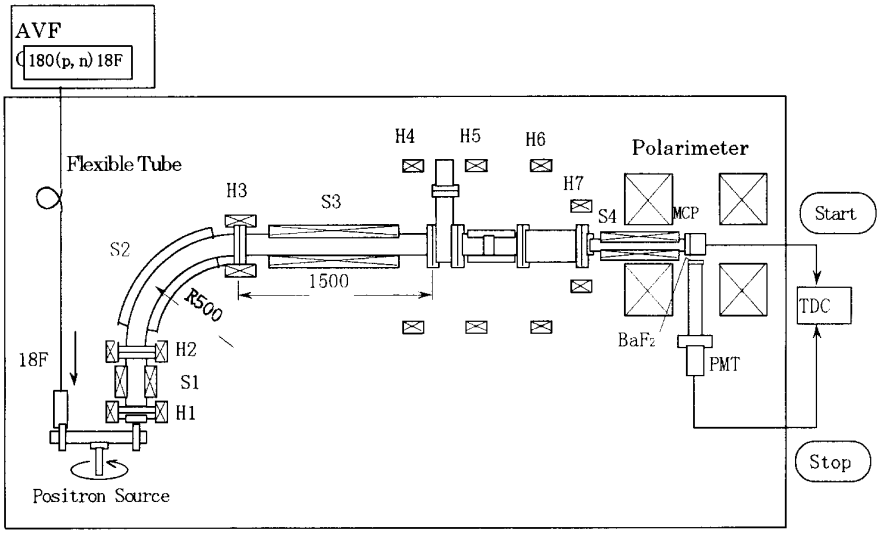

Experimental apparatus

The central body of the cell was made of copper cylindrical block on which a hemispherical hole was drilled and the inside of the hole was gilded with rhodium. The cell acted as both cathode and vessel for the ^{18}F-water. The cylinders of diameter 3 mm and 5 mm were made of high pure graphite for emission chemical analysis and used for an anode. Their sidewalls were covered with a thin polyethylene film to avoid electro-deposition of ^{18}F on them. The cylinder of 3 cm length was held in a Lucite holder to contact the surface of ^{18}O-water in the centre of the cell. The layout of the electro-deposition is shown in Figure 3.

Figure 3. A schematic diagram of an electric cell for deposition of ^{18}F on a graphite electrode from ^{18}O-water irradiated by a cyclotron

(A) Graphite cylinder for ^{18}F deposition. (B) Plastic holder for graphite electrode. (C) Copper vessel for water and as anode, inside is hemispherical of 1.6 cm in diameter (1 cc volume) and gilded with rhodium.

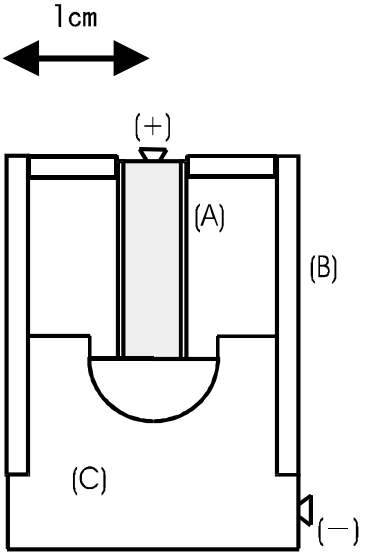

The ^{18}F was produced by $^{18}O(p,n)^{18}F$ reaction using AVF Cyclotron in Radioisotope Centre of Tohoku University Japan. An aliquot of 0.1 ml from the irradiated ^{18}O water was diluted to 10 ml with natural water containing 2 ppm F carrier in the chemical form of NaF, and a 1 ml standard solution was introduced into the cathode cell. The voltages 70-110 volt are applied between the cathode and anode from a constant voltage electric power-supply (0-250 volt). The power supply was switched on for a certain period of time (5 min, 10 min, 20 min) and then turned off. The graphite electrode was removed from the apparatus and 0.511 MeV γ-rays from ^{18}F electro-deposited on the graphite electrode were counted with a pure-Ge detector in a constant distance. The efficiencies of electro-deposition were obtained by comparing the counts with the standard sample prepared from drying the 1 ml standard solution on aluminium foil.

Result

The efficiencies of the electro-deposition obtained in this experiment are shown in Figure 4.

Figure 4. Deposition of ^{18}F on a graphite electrode

○ *5 mm ϕ, 5 min.,* □ *5 mm ϕ, 10 min.,* Δ *5 mm ϕ, 20 min,* ● *3 mm ϕ, 10 min.*

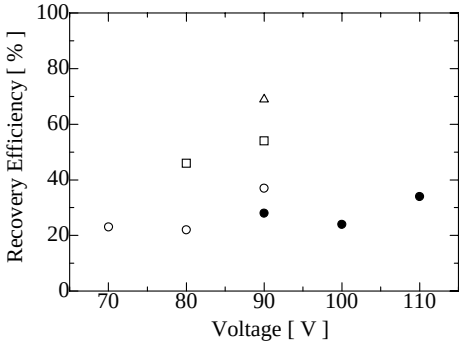

The best result for 5 mm cylinder is 69% in the case of 90 volt and 20 min., and the best result for 3 mm cylinder is 35% in the case of 110 volt and 10 min. The time dependency of efficiency of electro-deposition in the case of 5 mm in diameter is shown in Figure 5. The efficiency of electro-deposition increases and saturates with time. The optimal value of voltage between the both electrodes increases with decreasing the diameter of graphite cylinder (anode).

Figure 5. Time dependence of electro-deposition

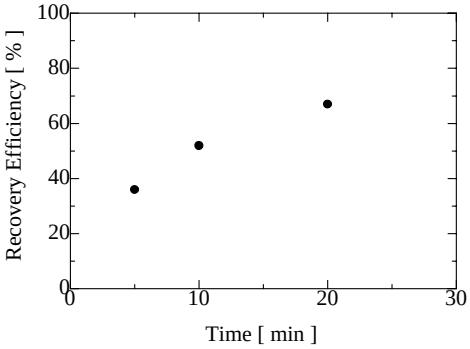

Discussion

Certainly the high intensity spin polarised positron beam will become a sensitive probe to research new materials. Therefore a slow positron beam line, Polarimeter, was constructed in RIKEN. The AVF cyclotron connected with the irradiation and transfer system of ^{18}O-water can produce activity of ^{18}F up to 37 GBq. The only problem remaining was the preparation of an intense positron source for polarised positron beam, ^{18}F was previously recovered with ion exchange resin or evaporation [6,7]. Their recovery was high enough in 90%, but the emission of positron from the source was poor due to absorption and scattering by supporting media, and the size of the source was not so small for this purpose. Alexoff *et al*. recovered ^{18}F from ^{18}O-water by electro-deposition of ^{18}F-fluoride on vitreous carbon electrode. They examined the parameters for the recovery [8]. We have examined the parameters for the intense positron source preparation for polarised positron beam using the electro-deposition method of ^{18}F-fluoride on the carbon electrode from ^{18}O-water irradiated by protons. A hemispherical copper gilded with rhodium was used as both cathode and vessel for water. Since a lower cross section of a graphite cylinder of 3 mm or 5 mm diameter was placed at the centre of hemisphere and contacted with surface of the water, the applied electric field was almost homogeneous resulting in profitable condition for collection of ^{18}F-fluoride. The best condition of voltage between the cathode and the anode is much higher than that obtained by Alexoff *et al*. The electric current between the both electrodes remained in the range from 1 to 6 mA. The best recovery of 69% is available for preparation of an intense slow positron source for polarised beam, and the period of electro-deposition is also reasonable in comparison with the half-life of ^{18}F. Since ^{18}F was deposited on the surface of graphite electrode with only 2 ppm carrier, the self-absorption must be negligible, therefore, the emission efficiency can be expected to be improved. An experimental preparation of a practical intense positron source for the Polarimeter is in progress in RIKEN.

Conclusions

We conclude, that the electro-deposition of ^{18}F-fluoride on a graphite electrode from ^{18}O-water bombarded by proton beam from cyclotron is useful method for preparation of an intense positron source for the spin-polarised slow positron beam.

REFERENCES

[1] S. Berko, in “Positron Solid State Physics”, eds., W. Brandt and A. Dupasquier (North-Holland, 1983) pp. 64-145. See also pp. 125-126.

[2] See “Positron and Positronium Chemistry”, ed., Y.C. Jean (World Scientific, 1990),“Fourth International Workshop on Positron and Positronium Chemistry”, ed., I. Billard, Journal de Physique IV, Volume 3, Colloque C4 (1993) [Supplement au Journal de Physique II, No. 9].

[3] Y. Itoh *et al*., *Appl. Sur. Sci*. 85, 165 (1995) (SLOPOS-6).

[4] Y. Itoh *et al*., *Appl. Sur. Sci*. 116, 68 (1997) (SLOPOS-7).

[5] Y. Itoh *et al*., Proc. Riken Symposium “Basics and Application of Spin Polarized Positron Beam” p. 1(1995).

[6] Y. Itoh *et al*., *RIKEN Accel. Prog. Rep*. 31, pp. 143 (1998).

[7] T. Nozaki *et al*., *Materials Sci. Forum*, 255-257, pp. 545-547 (1997).

[8] D. Alexoff *et al*., *Appl. Radiat. Isot*. 40, 1 pp. 1-6 (1989).

SESSION IV

Material Science Studies Using Positron, Stable and Radioactive Ion Beams

Chairman: M.F. da Silva

COMBINED ION BEAN AND HYPERFINE INTERACTION STUDIES OF $LiNbO_3$ SINGLE CRYSTALS

J.G. Marques [1,2], A. Kling [1], L. Rebouta [3], M.F. da Silva [2], J.C. Soares [1]

[1] Centro de Física Nuclear, Universidade de Lisboa, Av. Prof. Gama Pinto 2, P-1699 Lisboa, Portugal

[2] Instituto Tecnológico e Nuclear, Estrada Nacional 10, P-2685 Sacavém, Portugal

[3] Departamento de Física, Universidade do Minho, Largo do Paço, P-4710 Braga, Portugal

Abstract

A review of recent studies of $LiNbO_3$ crystals doped with Hf and Mg,Hf combining high precision RBS/channelling, PIXE/channelling and hyperfine interaction techniques is presented. The lattice location of Hf was found to depend strongly on the dopant concentration, crystal stoichiometry and Mg co-doping level. At low concentrations Hf occupies Li sites in congruent crystals, while it occupies both Li and Nb sites for higher doping levels or in near-stoichiometric crystals. Co-doping with Mg also forces a split location of Hf in Li and Nb sites and when the MgO amount exceeds 4.5 mol% Hf occupies only Nb sites. Neutron irradiation of these crystals displaces Hf from its initial lattice site and leads to a strong decrease of the Nb site fraction. The results are discussed in the framework of the Li and Nb vacancy models currently proposed in the literature for the defect structure of $LiNbO_3$.

Introduction

Lithium niobate ($LiNbO_3$) is an important material for applications in bulk optoelectronics and integrated optics devices [1]. Doping with suitable ions leads to optical gain and laser emission [2], photo-refractive activity [3], and wave-guiding behaviour [4]. Thus the knowledge of the lattice site location of dopants is essential to understand their role in its non-linear optical properties.

The basic structure of $LiNbO_3$ was established long ago [5]. The room temperature ferro-electric structure is trigonal (space group R3c), point group C_{3v}. The oxygen atoms form distorted octahedra with shared faces and exhibit a quasi-hexagonal arrangement when seen perpendicularly to the c-axis. The Li and Nb cations occupy each one-third of the oxygen octahedra, while the remaining third is vacant. Both the Li and Nb atoms are displaced from the centres of their respective octahedra along the c-axis. The stacking sequence, shown in Figure 1, is Li, Nb, V, Li, Nb, ..., where V is an intrinsic vacant site.

An important feature of $LiNbO_3$ is a significant departure from nominal stoichiometry. $LiNbO_3$ is normally grown with the congruent composition, i.e. with a Li_2O concentration [Li_2O]=48.38 mol% [6], which assures homogeneous crystals with good quality. However, the Li deficiency has to be compensated by a deviation from the ideal structure, in order to maintain overall charge neutrality. Two models have been proposed, involving a certain amount of Nb atoms at Li sites and either Li or Nb vacancies [7]. Thus the lattice location of an impurity is, *a priori*, determined by the interplay of several factors: dopant valence and amount, stoichiometry of the crystal, and eventual co-dopants. In this work we review the influence of these factors taking Hf as dopant and combining ion beam and hyperfine interaction methods. The combination of these techniques in single crystals allows not only the lattice site assignment but also the study of the near surroundings of the probes at an atomic scale [8].

Figure 1. Basic structure of $LiNbO_3$ showing the cation stacking sequence along the polar c-axis and the oxygen octahedra

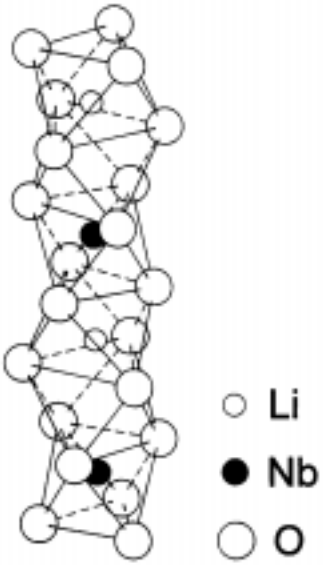

Experimental details

The Perturbed Angular Correlation (PAC) technique is well described in the literature [9] and only a brief introduction will be given here. In a non-magnetic material such as $LiNbO_3$, the PAC technique measures the electric field gradient (EFG) tensor at the lattice site of a radioactive probe ion that has been introduced in the crystal. Specifically, PAC measures the interaction between the nuclear quadrupole moment of an excited level of a suitable nucleus and the EFG produced by the surrounding electric charges, i.e. all the electrons and nuclei that surround the probe nucleus in the crystal lattice. Thus, the PAC technique is an ideal tool for the study of the microscopic lattice surrounding of impurities, providing information about the presence and position of defects in the vicinity of the probes and/or small displacements of the probe atoms from the ideal lattice position. The PAC probe has to be an unstable nucleus, decaying via a γ-γ cascade. Due to the conservation of angular momentum the emission directions of the γ-rays populating and depopulating the intermediate nuclear state are correlated. This correlation is changed by the interaction between the quadrupole moment of the nucleus in the intermediate state and an EFG. The interaction leads to a modulation of the angular correlation pattern depending on the time spent in the intermediate state. In the present work the 133-482 keV cascade from the β^- decay of ^{181}Hf, with anisotropy A_{22}=-0.307 was used. The 482 keV intermediate state has spin I=5/2, half-life of $T_{1/2}$=10.8 ns, and quadrupole moment |Q|=2.36(5) b [10]. The ^{181}Hf parent activity was produced by neutron irradiation in the Portuguese Research Reactor, via the reaction ^{180}Hf(n,γ)^{181}Hf. Natural Hf, in the form of HfO_2, was introduced during growth of all crystals in the Universidad Autónoma of Madrid. For a crystal doped with 1 mol% HfO_2 an irradiation of three hours at a thermal neutron flux of 2×10^{13} n/cm^2/s produces about 15 μCi of ^{181}Hf. The damage introduced by the irradiation was removed annealing the crystals in air at 973 K for 30 minutes.

The PAC experiments were performed at room temperature using a standard four-detector set-up equipped with BaF_2 detectors. The time resolution of this set-up is 0.6 ns (FWHM) for the ^{181}Hf cascade. From the twelve simultaneously recorded coincidence spectra N(θ,t), where θ is the angle between detectors and t is the time delay between events, the time differential anisotropy:

$$R(t) = 2\frac{N(180°,t) - N(90°,t)}{N(180°,t) + 2.N(90°,t)} \sim A_{22}G_{22}(t) \quad (1)$$

was calculated. $G_{22}(t)$ is the perturbation function which describes the modulation of the angular correlation. For a cascade with I=5/2 three frequencies, $\omega_n = C_n(\eta)\nu_Q$, are observed, giving

$$G_{22}(t) = S_{20} + \sum_{n=1}^{3} S_{2n}\cos(\omega_n t)\cdot\exp(-\delta\omega_n t) \quad (2)$$

The quadrupole coupling constant $\nu_Q = eQV_{ZZ}/h$ and the asymmetry parameter $\eta = (V_{XX}-V_{YY})/V_{ZZ}$, which are obtained from the frequency factors $C_n(\eta)$, contain information about the magnitude of the principal component V_{ZZ} and the asymmetry of the EFG. The exponential factor allows for a Lorentzian distribution of EFGs around a mean value. Such a distribution can be caused, e.g. by different lattice defects in the vicinity of the probe atoms. The S_{2n} coefficients, which give the amplitudes for each frequency, can be calculated for polycrystalline as well as for single crystalline samples. The experiments were performed in two complementary geometries, with the c-axis of the single crystal perpendicular to the detector's plane (I) and with the c-axis in the detector's plane,

at 45° with two detectors (II). For V_{zz} parallel to the c-axis, in geometry (I) S_{21} is the dominant coefficient, with small S_{22} and S_{23}, whereas in geometry (II) S_{21} and S_{22} are of the same order, still with a small S_{33}.

Ion beam experiments were done in un-irradiated plates of the same crystals, using the 3.1 MV Van de Graaff accelerator of ITN, Sacavém. The orientation of the virgin crystals was checked using a 1.6 MeV He^+ beam. The channelling investigations of the Nb- and Hf-RBS were performed using a 1.6 MeV H^+ beam. In all cases each measurement was performed on a virgin spot of the sample, to minimise the influence of de-channelling due to radiation damage induced by the analysing beam. The charged particles were detected at an angle near 180° using an annular silicon surface barrier detector with a resolution of 18 keV. PIXE/channelling data were recorded for Mg at the 4 MV Dynamitron accelerator at Stuttgart using a 3.1 MeV He^+ beam. The X-rays were detected by a Si(Li) detector with a 7.5 μm thick Be window and a resolution of 180 eV, located at 135° with regard to the incident beam.

Results and discussion

Figure 2 shows backscattering spectra at 180° for random and aligned incidence of a 1.6 MeV He^+ on a congruent crystal doped with 1 mol% HfO_2. The backscattering due to O, Nb and Hf can be well separated in the depth window of 1000 Å used in this study. The actual amount of Hf found in the crystal is 1.6%, corresponding to a distribution coefficient of 1.6 for Hf. Angular scans performed for the ⟨0001⟩ and ⟨$0\bar{4}41$⟩ axes and the (0001) plane are shown in Figure 3 [11,12]. The perfect overlap of the scans along the ⟨0001⟩ direction show that Hf is aligned with the mixed Li-Nb strings parallel to the c-axis of the crystal, but no definite assignment to either of the cation sites can be made. The reduced half-width of the Hf scan observed for the ⟨$0\bar{4}41$⟩ axis compared with the Nb scan rules out that Hf occupies Nb sites. For the (0001) plane the Hf scan shows a pronounced peak, in contrast to the Nb dip, which indicates that Hf is in a position in the centre of the planar channel, which is the Li site. This was a surprising result, since it was expected that a valence +4 impurity such as Hf would go to Nb sites where the charge compensation would be easier [13].

Figure 2. Backscattering spectra at 180° for random and aligned incidence of a 1.6 MeV He^+ on a congruent $LiNbO_3$ single crystal doped with 1 mol% HfO_2

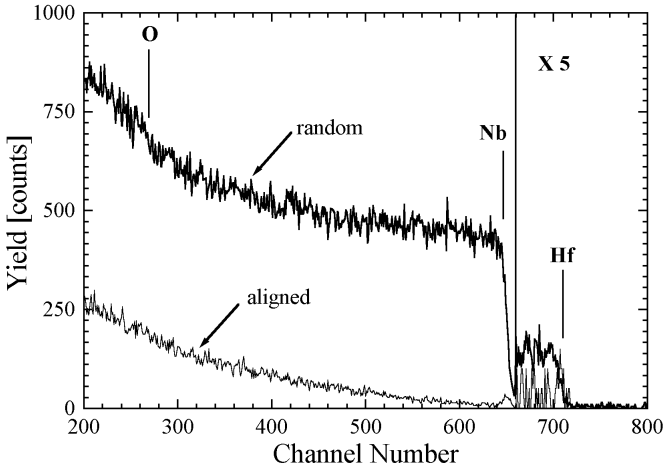

Figure 3. Angular scans performed along the ⟨0001⟩, ⟨ $0\bar{4}41$ ⟩ axes and the (0001) plane in a congruent $LiNbO_3$ single crystal doped with 1 mol% HfO_2; Hf fully replaces Li

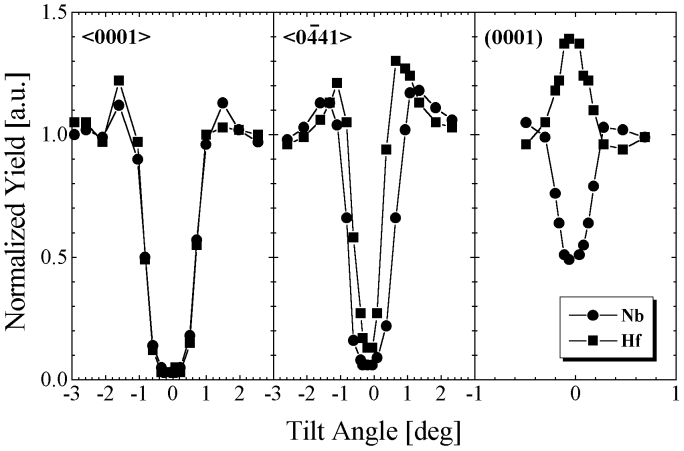

Since the lattice site of Ti, which is isovalent of Hf, was found to depend on its concentration [14] the concentration dependence of the lattice site of Hf was also studied using a crystal doped with 6 mol% HfO_2 in melt. The Hf concentration in the crystal itself was determined to vary between 3.5 and 5.1 mol%. Since the crystal also shows a partly damaged surface layer a depth interval from 1500 to 3000 Å was used for these investigations. Figure 4 shows the angular scans for Hf- and Nb-RBS for the $\langle 11\bar{2}0\rangle$, $\langle 01\bar{1}0\rangle$ and $\langle 02\bar{2}1\rangle$ axes [15]. For all investigated directions the Hf-RBS minimum yield is significantly higher than the one for Nb-RBS, which excludes an exclusive occupation of Nb sites by Hf.

Simulations with the CASSIS code [16] yield a good fit to the experimental data taken in this crystal assuming that 55% of the Hf atoms are located on regular Li sites, 35% on regular Nb sites and 30% on sites displaced 0.1 Å from the Nb site towards the centre of the Nb octahedron.

Another parameter that is expected to affect the lattice site of Hf in $LiNbO_3$ is the stoichiometry of the crystal. In this case a crystal with near-stoichiometric composition ([Li]/[Nb]=0.979) doped with 1 mol% HfO_2 was studied. Figure 5 shows the angular scans obtained for Hf- and Nb-RBS for the $\langle 11\bar{2}0\rangle$, $\langle 01\bar{1}0\rangle$ and $\langle 02\bar{2}1\rangle$ axes [17]. The Hf-RBS scans exhibit symmetric kinks, which are typical for the occupation of both Li and Nb sites. Monte Carlo simulations with a modified version of the FLUX code [12] show that 66% of the Hf occupy Nb positions and 34% Li positions.

To study the effect of Mg co-doping on the lattice site of Hf, crystals with 1 mol% HfO_2 and MgO concentrations of 2.0, 2.5, 3.5, 4.0 and 6.0 mol% (in the melt) were investigated [18,19]. Figure 6 shows the angular scans of Hf- and Nb-RBS yields obtained for the $\langle 02\bar{2}1\rangle$ direction and illustrates the dependence of the Hf dip shape on the Mg concentration. In the case of 2.5% Mg co-doping the Hf dip is narrower than that of Nb indicating that Hf is still mainly occupying Li sites. For higher Mg contents the Hf dips broaden and exhibit symmetric kinks, that shift to lower values of the normalised yield with increasing Mg concentration. This behaviour is consistent with an increasing fraction of Hf located on Nb sites. For the highest investigated Mg co-doping level of 6.0%, the Hf- and Nb-RBS angular yield distributions coincide, which evidences that now Hf exclusively occupies Nb sites. These results, confirmed by the measurements for additional axes, proof that the lattice site of Hf undergoes a change from the Li to the Nb position driven by the Mg co-dopant.

Figure 4. Angular scans performed along the $\langle 11\bar{2}0 \rangle$, $\langle 01\bar{1}0 \rangle$ and $\langle 02\bar{2}1 \rangle$, axes in a congruent $LiNbO_3$ single crystal doped with 6 mol% HfO_2; Hf replaces both Li and Nb

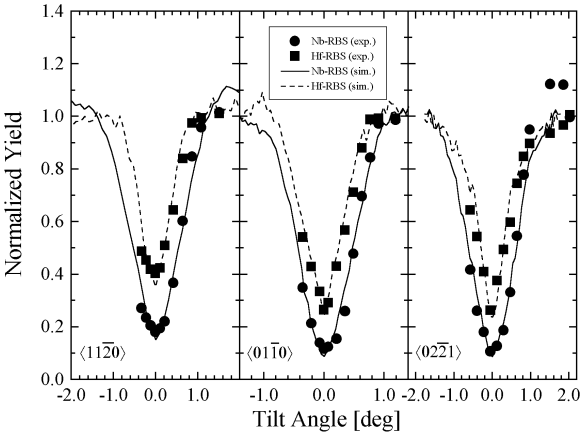

Figure 5. Angular scans performed along the $\langle 11\bar{2}0 \rangle$, $\langle 01\bar{1}0 \rangle$ and $\langle 02\bar{2}1 \rangle$ axes in a near-stoichiometric $LiNbO_3$ single crystal doped with 1 mol% HfO_2; in this crystal Hf also replaces both Li and Nb

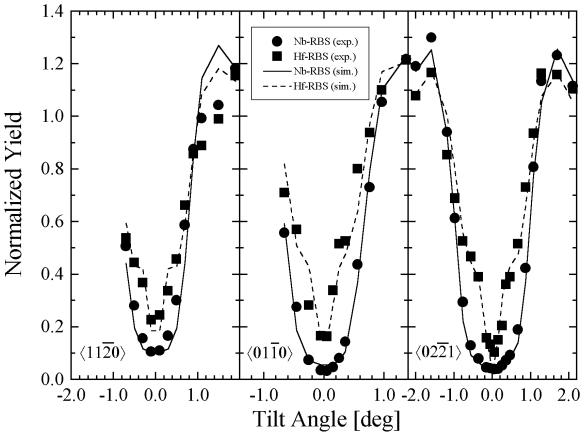

Figure 6. Angular scans for Hf and Nb along the $\langle 02\bar{2}1 \rangle$ axis for different Mg co-doping concentrations in the 2-6% range; a gradual transfer of Hf from Li to Nb sites is observed

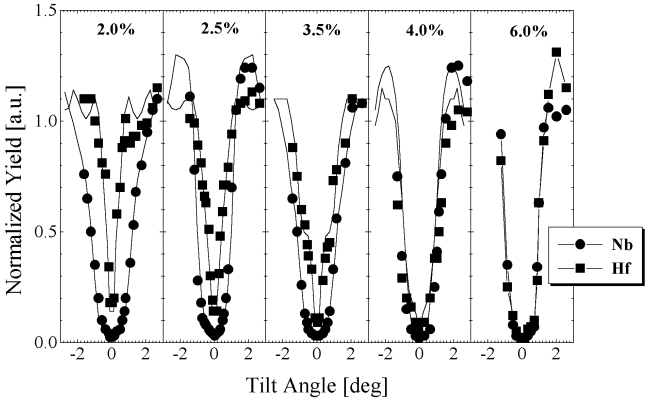

Figure 7 depicts the experimental angular scans of Mg-K PIXE of singly Mg doped (6 mol% in melt) and Hf-Mg co-doped (1 mol% HfO_2, 6 mol% MgO) for the $\langle 11\bar{2}0 \rangle$-direction [20] and the corresponding fits obtained with the simulation program CASSIS. The dip for the singly Mg-doped sample was fitted assuming 2/3 of the Mg occupying the Li site and 1/3 the Nb site [21] while for the co-doped sample Mg was found only in Li sites. Obviously the interaction of Hf and Mg shifts Hf fully to Nb sites and Mg to Li sites.

Figure 7. Mg-PIXE angular scans obtained for 3.1 MeV He^+ incident along the $\langle 11\bar{2}0 \rangle$-axis of $LiNbO_3$ a) doped with 6 mol% Mg and b) co-doped with 1 mol% Hf and 6 mol% Mg together with the respective computer simulations

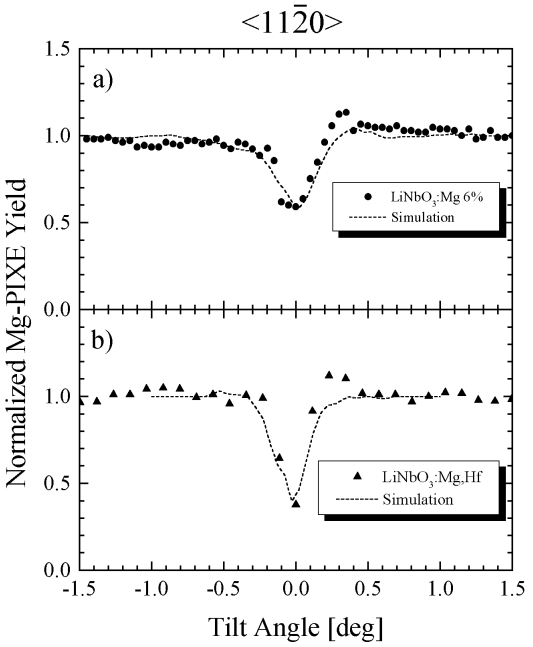

Figure 8 shows the PAC spectra and respective Fourier analyses obtained for the same Mg co-doped samples [22]. The c-axis of the single crystals was oriented perpendicularly to the detectors' plane. While for the crystal doped only with Hf the Fourier analysis shows a single peak at ~1200 Mrad/s, with the increase in the amount of Mg another peak at ~350 Mrad/s becomes dominant. By comparison with the channelling results above described, the peak at ~1200 Mrad/s can be assigned to Hf probes occupying Li sites and the peak at ~350 Mrad/s to probes occupying Nb sites. A detailed analysis of the data with the NNFIT code [23] shows that each of these peaks corresponds to the convolution of two nearby quadrupole interaction frequencies. For Hf in Li sites these frequencies are $\nu_Q(Li^I)$=1154(11) MHz and $\nu_Q(Li^{II})$=1213(11) MHz, with non-zero asymmetry parameters, as shown in Table 1.

The non-zero asymmetry parameter values found are surprising, since the lattice symmetry of $LiNbO_3$ would lead to η=0. Similar results were obtained with the ^{111}Cd probe in congruent $LiNbO_3$, where two frequencies were observed, $\nu_Q(Li^I)$=192(2) MHz and $\nu_Q(Li^{II})$=205(2) MHz, also with non-zero asymmetry parameters [24]. In contrast, in near-stoichiometric crystals only $\nu_Q(Li^I)$=192 MHz with $\eta(Li^I)$=0 is observed [25]. Therefore $\nu_Q(Li^{II})$ is related with the defect structure of congruent $LiNbO_3$ and $\nu_Q(Li^I)$ corresponds to undisturbed Li sites in the crystal. In a similar way, the

Figure 8. PAC spectra and respective Fourier analyses obtained in a) the congruent crystal doped with 1 mol% HfO_2, and b)-d) crystals doped with 1 mol% HfO_2 and different amounts of Mg.

The c-axis of the single crystals was oriented perpendicularly to the detectors' plane. The two peaks visible in the Fourier analysis correspond to the frequencies for Hf in Nb (~350 Mrad/s) and Li sites (~1200 Mrad/s).

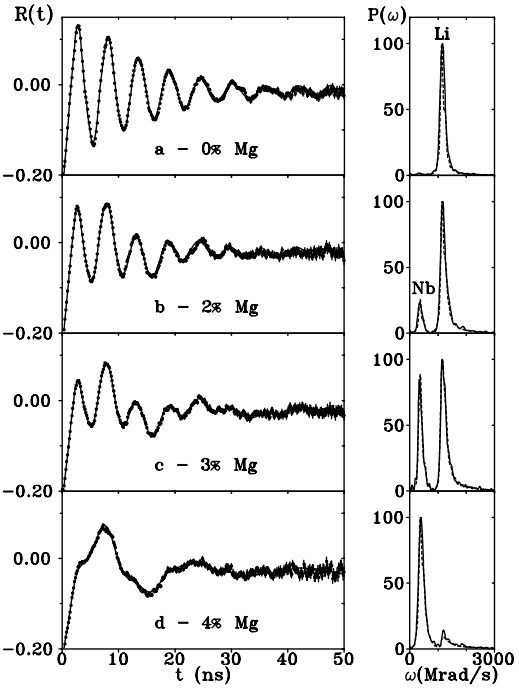

Table 1. Values of the quadrupole interaction of ^{181}Ta in congruent $LiNbO_3$ crystals doped with 1 mol% HfO_2 and 1 mol% HfO_2 plus 6 mol% MgO

Sample	Site	ν_Q (MHz)	η	δ	Fraction
Hf (1%)	Li site I	1154(11)	0.21(1)	0.035(5)	0.68(5)
	Li site II	1213(11)	0.28(1)	0.028(5)	0.32(5)
Hf (1%) + Mg (6%)	Nb site I	327(10)	0.42(2)	0.13(1)	0.51(5)
	Nb site II	398(10)	0.48(2)	0.13(1)	0.49(5)

spectra for 6% Mg co-doping, for which channelling shows Hf to replace Nb, could not be fitted assuming only one quadrupole frequency. Two frequencies were considered, $\nu_Q(Nb^I)$=327(10) MHz and $\nu_Q(Nb^{II})$=398(10) MHz, with non-zero asymmetry parameters, as shown in Table 1. The fits for the other crystals doped with 2-4% MgO were done considering these four sets of parameters. The distribution width δ associated with the Nb^I and Nb^{II} sites increases significantly with the increase of MgO concentration.

Figure 9 shows the total fractions of ^{181}Hf probes at the Li and Nb sites, as function of MgO co-doping. A gradual transfer from Li to Nb positions is seen as a result of the gradual incorporation of Mg. Two slopes are evident, with a transition at about 3.2 mol%, where an equilibrium between the fraction of ^{181}Hf probes in the Li and Nb sites is reached. The transfer of Hf to Nb sites is expected to be complete at about 4.5 mol% MgO concentration.

Figure 9. Transfer of Hf from Li to Nb sites as derived from the PAC experiments; the transfer is complete close to 4.5 mol% MgO co-doping

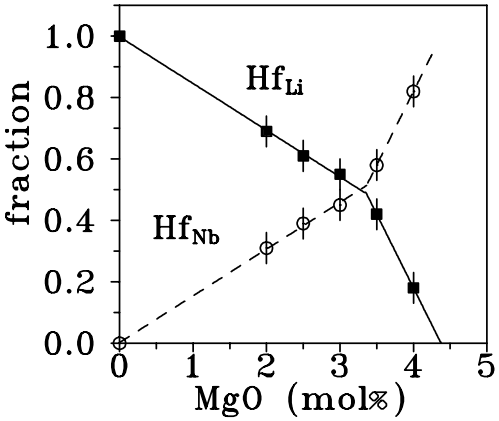

The Mg co-doping amount at which the transfer of Hf from Li to Nb sites is complete coincides with the reported threshold for reduction of the photo-refractive effect [26]. It is not yet known if Mg has the same effect on Fe. Doping $LiNbO_3$ with small amounts of Fe (~ppm) increases the photo-refractive effect [3] and thus this effect has been assigned to Fe impurities in the crystals. However the location of Fe has only been studied in singly doped crystals [27] where it was shown that it occupies Li sites.

Since the ^{181}Hf parent activity for the PAC experiments was obtained via neutron irradiation of the $LiNbO_3$ crystals, it is interesting to compare the PAC spectra obtained after irradiation and after annealing. Figure 10 shows the PAC spectra obtained after irradiation and after annealing at 970 K of the crystal doped with 1 mol% HfO_2 [28]. The c-axis of the single crystal was oriented in the detectors' plane at 45° with two detectors. For this geometry two peaks are visible in the Fourier analysis, corresponding to the frequency for Hf in Li sites (~1200 Mrad/s) and its first harmonic. The only difference between the two spectra is a higher attenuation in the spectrum obtained after irradiation, due to the presence of defects in the neighbourhood of the probes.

Figure 10. PAC spectra and respective Fourier analyses obtained in a congruent crystal doped with 1 mol% HfO_2 after irradiation and after annealing at 973 K

The c-axis of the single crystal was oriented in the detectors' plane at 45° with two detectors. The two peaks visible in the Fourier analysis correspond to the frequency for Hf in Li sites (~1200 Mrad/s) and its first harmonic.

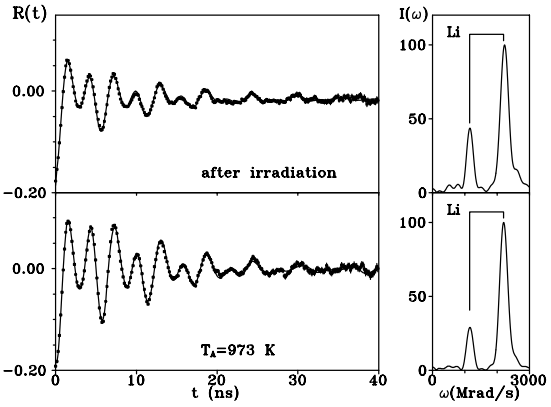

In contrast, the corresponding spectra obtained for the crystal co-doped with 3 mol% MgO, depicted in Figure 11, show significant differences. The Fourier analyses show already that the fraction of probes in Nb sites was strongly reduced after irradiation. A detailed analysis of the data shows that the fractions of probes in Nb sites after irradiation is 18(5)% and after annealing is 47(5)%.

Figure 11. PAC spectra and respective Fourier analyses obtained in a crystal doped with 1 mol% HfO_2 and 3 mol% MgO after irradiation and after annealing at 973 K

The c-axis of the single crystal was oriented in the detectors' plane at 45° with two detectors. The four peaks visible in the Fourier analysis correspond to the frequencies for Hf in Nb and in Li sites and respective first harmonics.

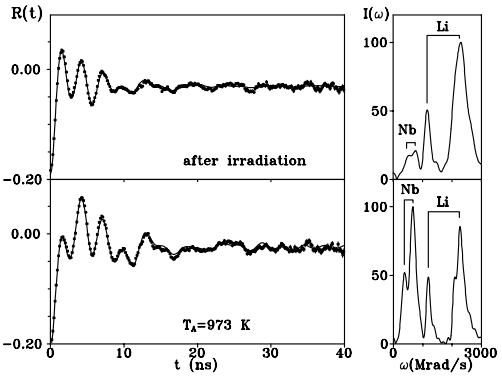

However, a channelling analysis of the crystal after irradiation [29] shows 45(5)% of the Hf ions in Li sites and the remaining 55(5)% in Nb sites, in excellent agreement with the results obtained in a non-irradiated crystal [18]. These two sets of data are compatible only if the change of lattice location after irradiation, as seen by PAC, affects only the radioactive ^{181}Hf atoms, i.e. the ones produced via the (n,γ) reaction. Since these are much less than 1 ppm of the total amount of Hf in the crystal, no effect can be seen with RBS. Thus it seems reasonable to assume that the displacement is due to the recoil induced by the (n,γ) reaction. The maximum recoil that can be induced in a ^{181}Hf probe is 96 eV, corresponding to the emission of a prompt gamma with 5.6 MeV energy [30]. The displacement energy for oxygen in $LiNbO_3$ is known to be 53 eV [31]; if the displacement energy for Hf is of the same order, then only one displacement per recoil can be expected.

The transfer of Hf from Nb to Li sites upon irradiation has some consequences regarding the defect structure of $LiNbO_3$. The deviation from stoichiometry can be compensated by the creation of either Li or Nb vacancies [7]. If there were Nb vacancies in the crystal, then a Hf atom displaced from a Nb site would find easily a vacant Nb site, since there are over 1 million vacancies for every displaced Hf, and no change in the fraction in Nb sites would be seen. Our data is compatible only with the existence of Li vacancies, which theoretical calculations show to be energetically favoured [7]. In this case, the fraction in Nb sites decreases and the one in Li sites increases in a crystal where Hf occupies both Li and Nb sites, while no change is expected in a crystal where Hf occupies only Li sites.

Assuming that the ^{181}Hf probes in both Li and Nb sites are displaced, then it is required that ~60% of all probes are recoiled in the Mg co-doped crystal. From the known energies and intensities of the prompt gamma radiation [30], the minimum gamma quantum which would contribute to the recoil is ~2.9 MeV, corresponding to a displacement energy of E_d=25(1) eV. The E_d value for Hf in derived in this way compares well with the recommended values for Al and O in α-Al_2O_3: E_d(Al)=20 eV and E_d(O)=50 eV [32].

Using the Li vacancy model, we have recently proposed a two-step mechanism for the incorporation of Hf^{4+} in singly doped $LiNbO_3$ [15]:

$$4 \cdot Nb_{Li} + 5 \cdot HfO_2 + V_{Li} \rightarrow 5 \cdot Hf_{Li} + 2 \cdot Nb_2O_5 \quad (3)$$

$$Li_{Li} + 3 \cdot Nb_{Nb} + 4 \cdot HfO_2 \rightarrow Hf_{Li} + 3 \cdot Hf_{Nb} + LiNbO_3 + Nb_2O_5 \quad (4)$$

In a first step, given by Eq. (3), the Nb antisites are dissolved and Hf is incorporated into Li sites. This step proceeds until all antisites are exhausted. For this purpose 1.5% Hf and 1.2% Li vacancies are consumed. The remaining Hf^{4+} is then split between Li^{+} and Nb^{5+} sites, in a ratio of 1:3 to maintain charge balance, according to Eq. (4). Thus, in a crystal doped with up to 1.5% Hf, all Hf should occupy Li sites. In the 3.5-5.1% Hf concentration range, the expected fraction on Nb sites is already in the 43-53% range, in good agreement with the present data. For low concentrations the only available data is for 1.6% Hf (1.0 mol% HfO_2 in melt), from Ref. [11], and shows all Hf in Li sites. However, for this concentration Eq. (4) yields a fraction in Nb sites of only 4%, which is too low to produce significant effects.

In an ideal stoichiometric crystal no Li vacancies and antisites are present. Then the only constraint when incorporating a foreign ion is to maintain charge balance. Therefore, a small amount of Hf would be split between Li and Nb sites in a ratio of 1:3. The deviation observed in the near-stoichiometric crystal can be attributed to the fact that the crystal is still Li deficient, and therefore the fraction in Li sites increases. For the [Li]/[Nb] ratio estimated for this crystal, the expected amount of antisites is about 0.4%, which would lead to a decrease of the fraction in Nb sites from the ideal 75% down to 53%, in good agreement with the observed 60(7)% fraction taken from the PAC data.

It is worth mentioning that so far no universal model exists regarding the incorporation of dopants in $LiNbO_3$. The situation of +3 valence impurities is not clear, since these in principle can replace either Li or Nb sites [33]. Valence +5 impurities, such as Ta, replace only Nb [33] since $LiTaO_3$ is isomorphous. Also W^{6+} was found in Nb sites [34], since this avoids the creation of Nb vacancies.

Conclusions

A combination of ion beam methods with hyperfine interaction techniques is a powerful tool to study complex systems such as lithium niobate. The lattice location of Hf was determined with RBS/channelling, while the location of the lighter Mg dopant was studied with PIXE/channelling. The lattice location of Hf was found to depend strongly on the dopant concentration, crystal stoichiometry and Mg co-doping level. At low concentrations Hf occupies Li sites in congruent crystals, while it occupies both Li and Nb sites for higher doping levels or in near-stoichiometric crystals. Co-doping with Mg also forces a split location of Hf in Li and Nb sites and when the MgO amount exceeds 4.5 mol% Hf occupies only Nb sites.

Neutron irradiation of these crystals displaces Hf from its initial lattice site and leads to a strong decrease of the Nb site fraction. This behaviour is compatible only with the existence of Li vacancies in congruent $LiNbO_3$. Based on the Li vacancy model it was possible to understand the lattice location of Hf in singly doped crystals, as function of the amount of dopant and the stoichiometry of the crystal. First the Nb antisites are dissolved and Hf is incorporated into Li sites. The remaining Hf is then incorporated in both Li and Nb sites, in a ratio of 1:3 to maintain charge balance. The competition between Hf and Mg is more complex and a satisfactory model has not been obtained so far.

Acknowledgements

The authors are grateful to Prof. E. Diéguez and his group at the Universidad Autonoma of Madrid for providing the $LiNbO_3$ single crystals, and to Prof. F. Agulló-López for many discussions. This work was partially supported by Fundação para a Ciência e a Tecnologia, Portugal, via two post-doc grants (J.G.M. and A.K.).

REFERENCES

[1] *Properties of $LiNbO_3$*, EMIS Data Reviews Series No. 5 (INSPEC, London, 1989).

[2] P. Becker, R. Brinkmann, M. Dinand, W. Sohler and H. Suche, *Appl. Phys. Lett.* 61, 1257 (1992).

[3] L. Arizmendi and F. Agulló-López, MRS Bull. XIX, 32 (1994).

[4] L. Thylen, *J. Lightwave Technol*. 6, 847 (1988).

[5] S.C. Abrahams, J.M. Ready and J.L. Bernstein, *J. Phys. Chem. Sol*. 27, 997 (1968).

[6] P.F. Bordui, R.G. Norwood, C.D. Bird and G.D. Calvert, *J. Cryst. Growth* 113, 61 (1991).

[7] H. Donnerberg, S.M. Tomlinson, C.R.A. Catlow and O.F. Schirmer, *Phys. Rev.* B 40, 11909 (1989).

[8] J.C. Soares, *Nucl. Instrum. Methods* B 64, 215 (1992).

[9] G. Schatz and A. Weidinger, *Nuclear Condensed Matter Physics* (Wiley, Chichester, 1996) p. 63.

[10] T. Butz and A. Lerf, *Phys. Lett*. 97A, 217 (1983).

[11] L. Rebouta, J.C. Soares, M.F. da Silva, J.A. Sanz-García, E. Diéguez and F. Agulló-López, *Nucl. Instrum. Methods* B 45, 495 (1990).

[12] L. Rebouta, P.J.M. Smulders, D.O. Boerma, F. Agulló-López, M.F. da Silva and J.C. Soares, *Phys. Rev*. B 48, 3600 (1993).

[13] A. Räuber, in *Current Topics in Materials Science*, Vol. 1, edited by E. Kaldis, North Holland Publishing Company (Amsterdam, 1978) p. 481.

[14] D. Kollewe, A. Kling, B.C. Grabmaier, T. Bremer, W. Heiland and W. Zimmermann, *Phys. Lett*. A169, 177 (1992).

[15] J.G. Marques, A. Kling, J.C. Soares, L. Rebouta, M.F. da Silva, E. Diéguez and F. Agulló-López, *Nucl. Instrum. Methods* B 136-138, 431 (1998).

[16] A. Kling, *Nucl. Instrum. Methods* B 102, 141 (1995).

[17] J.G. Marques, A. Kling, L. Rebouta, M.F. da Silva, A.A. Melo, J.C. Soares, M.D. Serrano, E. Diéguez and F. Agulló-López, *Mat. Sci. Forum* 248-249, 395 (1997).

[18] L. Rebouta, M.F. da Silva, J.C. Soares, M.T. Santos, E. Diéguez and F. Agulló-López, *Opt. Mat*. 4, 174 (1995).

[19] L. Rebouta, M.F. da Silva, J.C. Soares, M.T. Santos, E. Diéguez and F. Agulló-López, *Rad. Eff. Def. Solids* 136, 137 (1995).

[20] A. Kling, J.C. Soares, M.F. da Silva, L. Rebouta, D. Kollewe, H. Krause, R.-H. Flagmeyer and J. Vogt, *X-Ray Spectrometry* (in press)

[21] A. Kling, D. Kollewe and B.C. Grabmaier, *Nucl. Instrum. Methods* B 64, 232 (1992).

[22] J.G. Marques, C.M. Jesus, A.A. Melo, J.C. Soares, E. Diéguez and F. Agulló-López, Proc. 10th Int. Conf. on Hyperfine Interactions, Leuven, 1995, edited by M. Rots, A. Vantomme, J. Dekoster, R. Coussement and G. Langouche, Hyperfine Interact. (C) 1, 348 (1996).

[23] N.P. Barradas, M. Rots, A.A. Melo and J.C. Soares, *Phys. Rev*. B 47, 8763 (1993).

[24] B. Hauer, R. Vianden, J.G. Marques, N.P. Barradas, J.G. Correia, A.A. Melo, J.C. Soares, E. Diéguez, and F. Agulló-López, *Phys. Rev*. B 51, 6208 (1995).

[25] A. Kling, L. Rebouta, J.G. Marques, J.G. Correia, M.F. da Silva, E. Diéguez, F. Agulló-López, J.C. Soares and ISOLDE Collaboration, *Nucl. Instrum. Methods* B 118, 622 (1996).

[26] D.A. Bryan, R. Gerson and H.E. Tomaschke, *Appl. Phys. Lett*. 44, 847 (1984).

[27] L. Rebouta, M.F. da Silva, J.C. Soares, M. Hage-Ali, J.P. Stoquert, P. Siffert, J.A. Sanz-García, E. Diéguez, and F. Agulló-López, *Europhys. Lett*. 14, 557 (1991).

[28] J.G. Marques, A. Kling, J.C. Soares, M.F. da Silva, E. Diéguez and F. Agulló-López, *Mat. Res. Symp. Proc*. 141, 645 (1997).

[29] J.G. Marques, A. Kling, C.M. de Jesus, J.C. Soares, M.F. da Silva, E. Diéguez and F. Agulló-López, *Nucl. Instrum. Methods* B 141, 326 (1998).

[30] G. Alenius, S.E. Arnell, C. Schale and E. Wallander, *Phys. Scr*. 3, 105 (1971).

[31] E.R. Hogdson and F. Agulló-López, *Nucl. Instrum. Methods* B 32, 42 (1988).

[32] R.E. Williford, R. Devanathan, W.J. Weber, *Nucl. Instrum. Methods* B 141, 94 (1998).

[33] L. Rebouta, J.C. Soares, M.F. da Silva, J.A. Sanz-García, E. Diéguez and F. Agulló-López, *J. Mat. Research* 7, 130 (1992).

[34] A. Kling, J.G. Marques, J.C. Soares, M.F. da Silva, E. Diéguez and F. Agulló-López, *Nucl. Instrum. Methods* B 127/128, 520 (1997).

HIGH-T_C SUPERCONDUCTORS STUDIES WITH RADIOACTIVE ION BEAMS AT ISOLDE

J.G. Correia[1,2], and the IS360 Collaboration [1]: E. Alves[3], V.S. Amaral[4], J.P. Araújo[4], P. Bordet[5], T. Butz[6], J.J. Capponi[5], B. Ctortecka[6], S. Le Floch[5], V. Galindo[7], R. Gatt[8], G. Langouche[9], S.M. Loureiro[5], A.A. Lourenço[10], J.G. Marques[3], A.A. Melo[1], T. von Papen[7], A.R. Ramos[1], J.P. Senateur[7], M.F. da Silva[3], J.C. Soares[1], J.B. Sousa[4], P. Toulemonde[5], W. Tröger[6], A. Vantomme[9], U. Wahl[9], F. Weiss[7], and the ISOLDE Collaboration[2]

[1] CFNUL, Av. Prof. Gama Pinto 2, 1699 Lisboa Codex, Portugal

[2] EP/SC Division, CERN, CH-1211 Geneva, Switzerland

[3] ITN, Estrada Nacional 10, P-2685 Sacavém, Portugal

[4] IFIMUP, Dep. Física, FCP, Rua do Campo Alegre 687, P-4150 Porto, Portugal

[5] Lab. de Cristallographie, CNRS, Av. des Martyrs 25, F-38042 Grenoble Cedex 9, France

[6] FPG, Univ. Leipzig, Linnéstraβe 5, D-04103 Leipzig, Germany

[7] UMR CNRS 5628, INPG-ENSPG, BP 46-38402 St. Martin D'Hères Cedex, France

[8] Phys. Dept., Chalmers University of Technology, S-41296 Göteborg, Sweden

[9] IKS, Celestijnenlaan 200 D, B-3001 Leuven, Belgium

[10] Phys. Dept., Univ. Aveiro, P-3800 Aveiro, Portugal.

Abstract

New applications of radio isotopes for research in solid state physics are steadily growing due to the large variety of intense radioactive ion beams which are provided by the on-line coupling of high resolution isotope separators to particle accelerators, such as the ISOLDE facility at CERN. There, new experiments are performed by an increasing number of solid state researchers which combine nuclear spectroscopic techniques such as Mössbauer, Perturbed Angular Correlations and Emission Channelling with the traditional non-radioactive techniques such as Deep Level Transient Spectroscopy and Hall Effect measurements. Recently isotopes of elements not available before were successfully used in new PAC experiments, and the first Photoluminescence (PL) measurements, where the element transmutation plays the essential role on the PL peak identification, have been performed.

In this paper we shortly review the ISOLDE facility, and present a new approach to investigate the oxygen doping and structural point defects in High T_C Superconductor materials (HT_CS). For this purpose radioactive ion beams are used to dope HT_CS thin films and pellets, which are then studied by combining complementary techniques such as Perturbed Angular Correlation, Emission Channelling and Electrical/Magnetic Measurements. As examples we will discuss the most recent studies of Hg doping high quality $YBa_2Cu_3O_{6+x}$ thin films, and the first results obtained in the characterisation of the order/disorder of Hg in the Hg-planes of the HT_CS family $Hg_1Ba_2R_{(n-1)}Cu_nO_{(2n+2+\delta)}$ (Tc>130 K).

Introduction

New applications of radio isotopes for research in solid state physics are steadily growing due to the large variety of intense radioactive ion beams, which are provided by the on-line coupling of high resolution isotope separators to particle accelerators, such as the ISOLDE (Isotope Separator On-Line) facility at CERN [2]. There, new experiments are performed by an increasing number of solid state researchers, which combine well-established nuclear techniques with new "tracer" techniques. Such "tracer" techniques rely on standard electrical and optical measurements performed as a function of time during the decay of the implanted radioactive elements. They provide signal-to-element identification, and have a great potential for widespread applications [3]. The more sophisticated nuclear techniques, in particularly the so-called "hyperfine interaction" techniques that have been developed to investigate the nuclear structure phenomena, are used today to probe the local fields into the materials via its interactions with the nuclear moments. Mössbauer Effect (ME) [4], Perturbed Angular Correlations (PAC) [5], Nuclear Orientation (NO) [6] and the β-Nuclear Magnetic Resonance (β-NMR) [7] are examples of such.

Nowadays, the usefulness of applying *less-common* nuclear techniques to new fields in solid state research depends essentially on three factors, e.g. the availability of a broad range of appropriate radioactive isotopes, an adequate sample preparation, and a good interaction between the solid state community and the physicists which have the nuclear techniques know-how.

ISOLDE is the first example of such radioactive ion beam facilities where the structural and electronic environment of impurity dopants implanted in bulk, surfaces, and interfaces of metals and semiconductors, are currently studied. Finally, such an atmosphere is particularly good to run and develop new applied nuclear techniques, by an increasing number of interdisciplinary collaborations that submit research proposals in new fields of materials science [1,3].

In this paper the ISOLDE facility is shortly reviewed and new approaches to investigate the oxygen doping and structural point defects in High T_C Superconductors (HTS) are presented. As examples are shown first results obtained in the characterisation of the oxygen doping of the Hg planes of the $Hg_1Ba_2R_{(n-1)}Cu_nO_{(2n+2+\delta)}$ HTS family, and recent studies of Hg doping $YBa_2Cu_3O_{6+x}$ thin films.

The ISOLDE facility at CERN

At ISOLDE radioactive nuclei are produced through spallation, fission or fragmentation reactions in thick targets by the 1 GeV proton beam from the CERN's PS-Booster [2]. The target products are vaporised and extracted through a transfer line into a selective ion source. The extracted ions are then accelerated to 60 keV and mass (M) separated by analysing magnets. Two different mass separators are available. The first one, the General Purpose Separator (GPS), provides mass separation with a resolving power $M/\Delta M = 2400$. It is designed to provide up to three simultaneous beams, within a mass range of ±15%, delivered to the beam lines in the experimental hall. The second mass separator, the High Resolution Separator (HRS), is equipped with two bending magnets achieving routinely $M/\Delta M = 10{,}000$. The ISOLDE group develops different types of element-specific target-ion-source combinations that today allow the use of more than 600 radioactive isotopes of about 70 elements [8]. Recently the implementation of chemically selective laser-ion-sources provided new and clean Ag, Ni, and Mn radioactive ion beams [9] and clean beams of Be, Cu, Zn and Cd have also been attained [10].

A post-accelerator for radioactive ion beams is being installed and optimised to nuclear physics purposes that will provide energies ranging from 1 MeV/A up to 2.2 MeV/u [11]. For energies below 1 MeV/A, a low charged radioactive ion beam (4+) will be injected through an electrostatic high voltage 0-260 kV acceleration lens.

High T_C superconductors – Overview

An intense experimental and theoretical research program in high T_C superconductivity has been underway around the world, since the discovery of this effect twelve years ago [12,13]. As a result of this program, hundreds of new materials structurally related to HTS were synthesised and new families of superconductors with increasing critical temperature (T_C) up to 135 K (at 1 atm.) [14] were produced. However, many problems in this field still remain unclear.

One essential step to model the fundamental electron pairing mechanisms and to reliably control the production and application of HTS materials, is to understand the cuprates structural properties. The cuprates are ceramic materials with rather complex crystal structures, although they can be described by the inter-growth, along the crystallographic c-axis, of two different types of block layers [15]. The first type of block layers presents an oxygen deficient perovskite-like structure in which n CuO_2 layers alternate with cation layers (M). These are the superconducting (Sc) block layers and it is well established that the valence electrons or holes involved in the n or p-type superconductivity, respectively, are located in the CuO_2 planes. The second type of block layers present generally a rock salt-like structure containing two different cations A and B. The cations are arranged in two B-O outer planes which are directly bound to the Sc block layers, while m planes of the composition A-O are located in between the B-O planes (Figure 1). These layers are defined as the charge reservoirs (CR) which have, in contrast to the Sc blocks, several chemical configurations and behave as insulators or metals, depending on the presence of chemical or structural defects. Changes of the oxygen concentration in these blocks can originate metal to insulator transitions and structural changes, and will induce an injection of charge carriers in the superconducting blocks.

Figure 1. Schematic representation of the HTS [15]

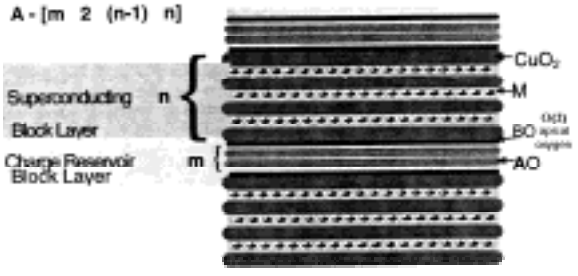

Nowadays the understanding of the structural mechanisms that regulate the transfer of the charge carriers between the CR and the Sc blocks represents a major point of the experimental research [16]. In particular, the replacement of elements in the CR block layer by elements or chemical groups with different oxidation states is being intensively studied, since it is expected that such “doping” induces distinct changes of the HTS properties [17]. However, these studies are limited by a relatively small number of interesting impurities that can be introduced during growth. Furthermore, the traditional techniques [18] which are used to characterise the new CR structures are often not able to distinctly characterise the order/disorder and the interaction with point defects of both the lattice constituent and the dopant elements, at an atomic scale.

Up to now, the specific advantages of nuclear spectroscopic techniques to study HTS are still far from being exploited. Early studies using ME [19], PAC [20], and Emission Channelling (EC) [21] were limited by the small number of adequate probe elements and by the doubtful quality of the available materials.

^{199}Hg PAC studies in Hg-1201

A new family of HTS that can achieve at ambient pressure the highest critical temperature up to 135 K, crystallise in a tetragonal lattice and is represented by the general formula $Hg_1Ba_2R_{(n-1)}Cu_nO_{(2n+2+\delta)}$. R represents an alkaline-earth element (Ca,Sr,...), and $0 < \delta < 0.5$ is the content of the extra oxygen (O_δ) that is located within the Hg planes. O_δ is considered to be the dopant whose amount regulates the superconducting charge carriers, enhancing or inhibiting T_C. While the bond-length between Hg and the apical oxygen (O(2) in the insert of Figure 2) seems to be quite incompressible the Cu-O(2) bond length is pressure dependent, and at 30 Gpa T_C as high as 164 K can be achieved in the Hg1223 (n = 2) compound. These facts created the expectation that precise measurements of the structural properties would allow a better understanding of the charge transfer mechanisms that generate carriers in the superconducting CuO_2 planes. However, it was soon discovered that the Hg planes are particularly disordered. In spite of the big effort put into several studies [22] it was not possible to understand clearly how Hg interacts with Cu, Au defects and with impurities like CO_3^{2-}, partially replacing Hg atoms in the Hg planes. Furthermore, the activation energy for the mobility and stability of the extra oxygen O_δ, which is weakly bound to Hg, is not known.

To study at an atomic scale the order/disorder of Hg in $HgBa_2CuO_{4+\delta}$ (Hg1201, n = 1) and the weak interaction of Hg with O_δ, the PAC technique is being used, which is particularly sensitive to the atomic vicinity of the probe's nuclei. Its sensitivity is given by the electric field gradient (EFG) that is caused by the deviation from cubic symmetry of the charge distribution around the probes. This results in a modulation of the PAC spectrum, R(t) [5].

First experiments have been done during 1997 that have successfully shown the feasibility of the proposed studies [23,24]. First, Hg1201 pellet samples were implanted with very low doses ($<5.10^{-11}$at.cm^{-2}) of ^{199m}Hg ($T_{1/2}$ = 42m). Then, in order to reproduce the treatments usually performed to change the O_δ concentration, the PAC measurements were done during annealing at 216°C under Ar or O_2 flow. Figure 2 shows the experimental PAC data functions, R(t), (left) and the corresponding Fourier transforms (FFT) (right). In order to enhance the excellent agreement of the fits with the data (continuous lines at the R(t) spectra) the corresponding Fourier transforms of the fit functions (thicker line on the FFT plots) are included. When annealing under Ar flow, the PAC/FFT spectra (top figures) show a frequency triplet that characterises a highly symmetric EFG_1, corresponding to ^{199}Hg nuclei placed on perfect sites with the tetragonal symmetry of the Hg1201 lattice. When annealing under O_2 flow, the PAC/FFT spectra (bottom figures) show two frequency triplets that correspond to two slightly different EFGs. One is still the same highly symmetric EFG_1, being the second one a non axially symmetric EFG_2, reflecting the ^{199}Hg nuclei which are placed on lattice sites with less than tetragonal symmetry.

X-ray refined measurements were further performed on the same samples where the PAC experiments occurred, showing that the lattice parameters have changed when annealing under O_2 flow, as expected, due to the O_δ doping of the Hg1201 lattice.

Figure 2. PAC experiments with ^{199m}Hg implanted Hg1201, detailed in text

The figure shows the R(t) functions (left) and corresponding Fourier transforms (right), measured under annealing in Ar flow (top) and O2 flow (bottom) [23].

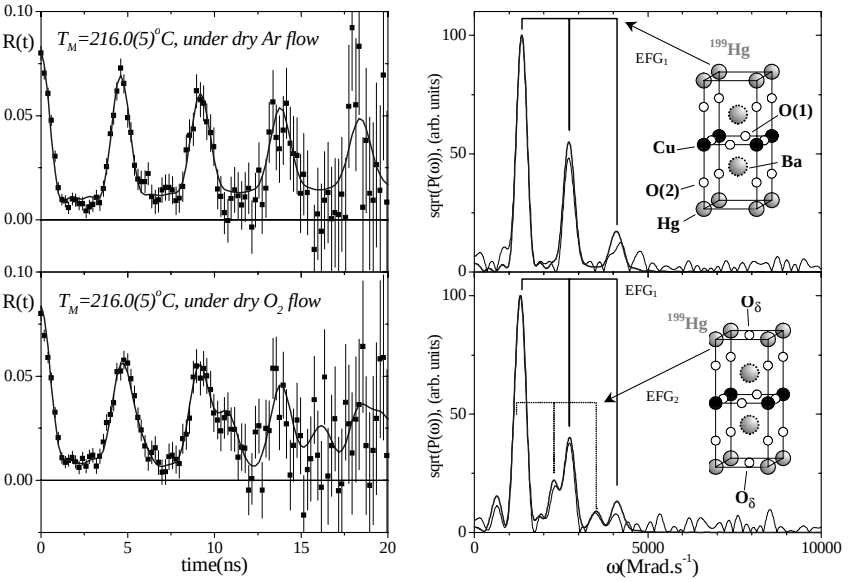

First principle calculations of the EFG (at the Hg site) were performed for both the undoped and O_δ doped cases, which have reproduced the strength and symmetry of EFG_1 and EFG_2, respectively [24].

The agreement between experiments, consistency of the theoretical simulations, and the fact that these results are reproducible, show that we are on the right road to locally study the O_δ doping of the Hg1201 compound.

New experiments are now being analysed where the concentration, diffusion, and the O_δ position have been studied as a function of annealing and measurement temperature. The extension of such experiments to the other members of the HTS Hg-compounds family is being further prepared.

^{197m}Hg studies in YBCO

The $YBa_2Cu_3O_{6+x}$ (YBCO) compound is one of the most studied and interesting HTS materials for applications. Doping studies have shown that the superconducting properties of YBCO are always degraded, except when doping with Au or Hg that increase T_C by 2 K [25] and 10 K [26], respectively. In these studies Hg was introduced to several per cent during sintering by changing the composition of the reactants. Therefore the Hg site was not known, and the presence of different crystalline phases cannot be excluded.

Recently, radioactive ^{197m}Hg ($T_{1/2}$ = 24h) was introduced into YBCO thin films by ion implantation to low dose of 1×10^{13}at.cm^{-2}, at ISOLDE [27,28,29]. The atomic environment of Hg and its lattice site position were studied with the e^--γ PAC [30], and the EC [31], nuclear techniques. For control T_C was measured with the Alternate Susceptibility (χ_{ac}) technique in the as-grown state and after the implantation and annealing treatments.

Figure 3 shows R(t) spectra measured at several temperature steps up to 757 K. All spectra were fitted assuming one frequency triplet that, below 587 K, characterises a slightly unsymmetrical but unique EFG_1. The strong attenuation of the as-implanted spectrum, which disappears at 511 K, is due to Hg nuclei that interact with randomly distributed defects. Within the PAC range of sensitivity, a few nanometers around the Hg probe nuclei, one annealing step is identified at 511 K where the lattice recovers and no point defects remain in the Hg neighbourhood. For annealing temperatures above 511 K EFG_1 becomes axially symmetric, thus revealing that the orthorhombic-to-tetragonal structural transition occurred in our thin films between 511 K and 587 K. In agreement, the χ_{ac} measurements have shown that, due to the vacuum annealing, the superconductor compound was transformed into an anti-ferromagnetic insulator. Superconductivity was then re-established, and T_C recovered to the as-grown value, after 6 h annealing at 723 K under O_2 flow.

Figure 3. PAC spectra measured after implantation and during annealing in vacuum up to 757 K [28]

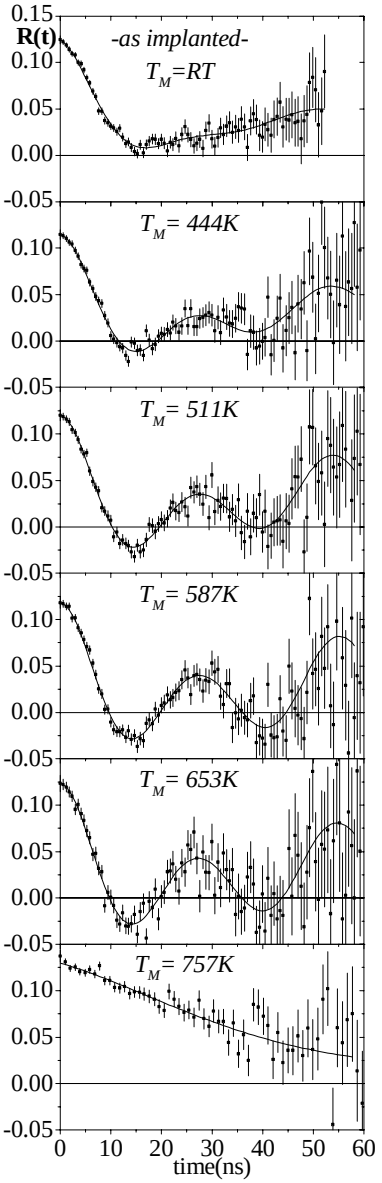

Single crystalline-like films have been used to measure the orientation of the EFG_1 principal system of axis. It was found that V_{zz} (the principal component of EFG_1) is aligned along the YBCO c-axis. By further analysing the strength, symmetry and orientation of EFG_1 it was suggested that Hg occupies the Cu(1) site, bonded to two linearly co-ordinated (apical) oxygens [28].

When annealing in vacuum above 653 K Hg starts to diffuse out and the R(t) spectra change irreversibly. The Hg diffusion mechanism is not known, however, the lower strength of EFG_2 (lower frequency in Figure 3, bottom), suggests that Hg is no more bound to oxygen and occupies higher symmetry lattice sites.

Figure 4 shows the ^{197m}Hg normalised conversion electron yield measured after implantation, as a function of the angle off the [001] axis. For this purpose are used 30×30 mm^2 position sensitive detectors developed at CERN for high-energy physics experiments, and recently adapted for EC experiments [32]. The preliminary analysis revealed that the increase of the electron yield along the [001] axis is explained by a majority of Hg ions that lie along the c-axis. Hg should be either on the Y/Ba or the Cu rows, since EC effects along pure O rows are expected to be much less pronounced. This fact agrees with the high symmetry of EFG_1, whose principal component (V_{zz}) was found to be aligned with the [001] axis. Refined fitting analysis and new EC experiments investigating different crystalline axes are in progress.

Figure 4. Normalised conversion electron intensities measured off the [001] direction, after implantation [28]

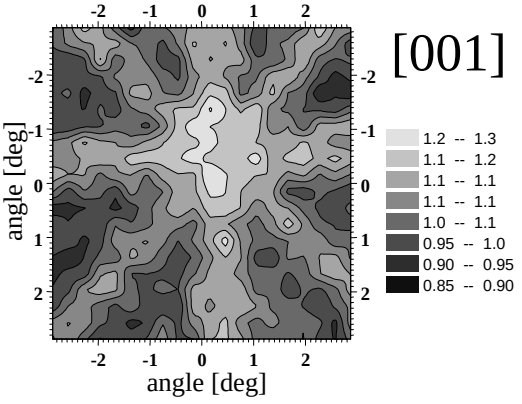

The Hg stability was studied by measuring the γ and the PAC coincidence rates during annealing in vacuum. It has been observed that Hg starts to out-diffuse above 653 K. With a simple model that neglects surface trapping and surface reflection, the Hg *apparent* diffusion coefficients at different temperatures, and the migration energy, E_M, for Hg in an oxygen deficient YBCO lattice have been estimated.

Finally, the abundance of oxygen seems to delay diffusion since that after annealing at 723 K under O_2 flow only small amount of Hg was lost and the EFG_1 did not change.

In conclusion, in this work the PAC and EC nuclear techniques have been applied to study the stability and lattice site of implanted Hg into YBCO thin films. We found that Hg occupies one unique lattice site, already after implantation that is stable up to 653 K. Both the EC and the PAC results suggest that Hg occupies a highly symmetric lattice site, most likely the Cu(1) site, bonded to

two apical oxygen atoms. A first annealing step of the implantation defects was found at 511 K, and the orthorhombic-to-tetragonal phase transition occurred between 511 K and 587 K, under vacuum annealing. Hg diffusion starts only above 653 K. The PAC results at 757 K show that Hg is no more bound to oxygen and is now occupying higher symmetry sites in the YBCO lattice.

Figure 5. Arrhenius plot of the apparent Hg diffusion coefficients [29]

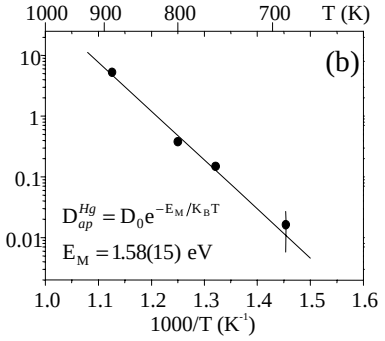

Conclusions

The interface between nuclear and solid state physics has always been a fertile ground for discovering new phenomena and attractive applications. Nowadays the solid state community can profit from a large set of new and powerful nuclear characterisation techniques, provided that the correct dialogue is established with the laboratories that have the nuclear techniques know-how.

At ISOLDE, combined nuclear and non-nuclear standard experiments are applied in particularly, to research in the field of High T_C superconductors. New results of undergoing experiments have been shown, which were motivated by the interest in correlating macroscopic properties with microscopic structural phenomena in the HTS materials.

Acknowledgements

This work has been supported by a post-doctoral grant from JNICT, Portugal under contract PRAXIS XXI/BPD/4180/94 and CERN project S/FIS/2041/96.

REFERENCES

[1] J.G. Correia *et al.*, Studies of High T_C Superconductors Doped with Radioactive Isotopes, CERN/ISC 96-30, ISC/P86, IS360 (1996).

[2] E. Kugler, D. Fiander, B. Jonson, H. Haas, A. Przewloka, H.L. Ravn, D.J. Simon, K. Zimmer and the SOLDE Collaboration, *Nucl. Instr. and Meth.* B70 (1992) 41; B. Jonson, H.L. Ravn and G. Walter, *Nucl. Phys. News* 3, 2 (1993) 5.

[3] J.G. Correia, *Nucl. Instr. and Meth*. B136-138 (1998) 736.

[4] D.L. Williamson, L. Niesen, G. Weyer, R. Sieleman and G. Langouche, in Hyperfine Interactions of Defects in Semiconductors, ed. G. Langouche (Elsevier, Amsterdam, 1992) p. 1.

[5] Th. Wichert, N. Achziger, H. Metzner, and R. Sielemann, *Perturbed Angular Correlation*, in Hyperfine Interactions of Defects in Semiconductors, ed. G. Langouche, (Elsevier, Amsterdam 1992) p. 1.

[6] N.J. Stone, in Low-temperature Nuclear Orientation, eds. N.J. Stone and H. Postma (North-Holland, Amsterdam, 1986) p. 641.

[7] J. Christiansen, ed., Hyperfine Interactions of Radioactive Nuclei (Springer, Berlin 1983) p. 1.

[8] H.L. Ravn, *Nucl. Instr. and Meth*. B70 (1992) 107; E. Hagebø, P. Hoff, O.C. Jonsson, E. Kugler, J.P. Omtvedt, H.L. Ravn and K. Steffensen, *Nucl. Instr. and Meth*. B70 (1992) 165.

[9] Y.Jading *et al*., *Nucl. Instr. and Meth.* B126 (1997) 76; A. Jokinen *et al*., *Nucl. Instr. and Meth.* B126 (1997) 95; V.N. Fedoseyev *et al*., *Nucl. Instr. and Meth*. B126 (1997) 88.

[10] J. Lettry *et al*., in Proc. 7th Int. Conf. on Ion Sources, (Taormina, Sep. 1997) to be published.

[11] D. Habs *et al*., *Nucl. Instr. and Meth*. B126 (1997) 218.

[12] J.G. Bednorz and K.A. Müller, *Z. Phys*. B64 (1986) 189.

[13] *Vide references in [1].*

[14] S.N. Putilin, E.V. Antipov, O. Chmaissem, and M. Marezio, *Nature* 362 (1993) 226; A. Schilling, M. Cantoni, J.D. Guo and H.R. Ott, *Nature* 363 (1993) 56.

[15] M. Lagues *et al*., in Coherence in High Temperature Superconductors, eds. Guy Deutscher and Alex Revcolevschi (World Scientific, Singapore, 1996), p. 70-98.

[16] J.T. Market, Y. Dalichaouch and M.B. Maple, in Physical Properties of High Temperature Superconductors I, ed. by D.M. Ginsberg (World Scientific, Singapore, 1989) p. 265; C.L. Chien, G. Xiao, M.Z. Cieplak, D. Musser, J.J. Rhyne and J.A. Gotaas, in Superconductivity and Its Applications, ed. H.S. Kwok and D.T. Shaw (Elsevier, New York, 1988) p. 110.

[17] S.M. Loureiro, E.V. Antipov, E.T. Alexandre, P.G. Radaelli, J.L. Tholence, J.J. Capponi and M. Marezio, to be published.

[18] e.g. electron microscopy, raman and infra-red spectroscopy, synchrotron radiation and x-ray analysis, neutron diffraction and iodometry (for determination of oxygen content).

[19] L. Bottyán, B. Molnár, D.L. Nagy, I.S. Szücs, J. Tóth, J. Dengler, G. Ritter, and J. Schober, *Phys. Rev*. B38 (1988) 11373; I.S. Lyubutin, V.G. Terziev and A.Ya. Shapiro, *Hyp. Int*. 61 (1990) 1105.

[20] P. Singh, M.N. Nyayate, S.H. Devare and H.G. Devare, *Phys. Rev*. B39 (1989) 2308; M.Uhrmacher, and A. Bartos, *Hyp. Int*. 61 (1990) 1073; W.Tröger and T. Butz, Z. Naturforsch. 47a, (1992) 12.

[21] A. Bartos, H. Plank, D. Forkel, S.Jahn, J.Markel, R. Polewka, M. Uhrmacher, S. Winter, W. Witthuhn, and the ISOLDE Collaboration, *J. Less-Comm. Metals*, 164 & 165 (1990) 1121.

[22] M.H. Julien, P. Carretta, M. Horvatic, C. Berthier, Y. Berthier, P. Ségransan, A. Carrington, and D. Colson, *Phys. Rev. Lett*. 76 (1996) 4238; M.H. Julien, M Horvatic, P. Carretta, C. Berthier, Y. Berthier, P. Ségransan, S.M. Loureiro, and J.J. Capponi, *Physica* C 268 (1996) 197; C.H. Booth, F. Bridges, E.D. Bauer, G.G. Li, J.B. Boyce, T. Claeson, C.W. Chu and Q. Xiong, *Phys. Rev*. B 52 (1995) R15745.

[23] J.G. Correia and the IS360 collaboration, CERN Ann. Rep. Vol. II (1997), p. 101.

[24] J.G. Correia and the IS360 collaboration, to be published.

[25] G. Ganakas, M. J. Morgan, G. Jakovidis, *J. Mater. Sci.: Mater. Electr*. 6 (1995) 244.

[26] A.K. Chakraborty, K. Bose, G. Som, B.K. Chaudhuri, *J. Mater. Sci.: Mater. Electr*. 5 (1994) 22.

[27] V.S.Amaral *et al*., *J. Magn. Mag. Mater*. 177-181 (1998) 511.

[28] J.P.Araujo *et al*., in proc. of E-MRS 98, *Nuclear Instruments and Methods* B, (1998), in press.

[29] J.P.Araujo *et al*., in proc. of IBMM 98, *Nuclear Instruments and Methods* B, (1998), in press.

[30] J.G. Marques, J.G. Correia, A.A. Melo, M.F. da Silva, J.C. Soares and ISOLDE Collaboration, *Nucl. Instr. and Meth*. B99 (1995) 645.

[31] H. Hofsass and G. Lindner, *Phys. Rep*. 201 (1991) 121.

[32] U. Wahl, J.G. Correia, S. Cardoso, J.G. Marques, A. Vantomme, G. Langouche, and the ISOLDE Collaboration, in Proc. 13th Int. Conf. on Ion Beam Analysis, *Nucl. Instr. and Meth.* B136-138 (1998) 744.

SAPPHIRE (α-AL_2O_3) BEHAVIOUR UNDER HEAVY ION IMPLANTATION

E. Alves* , M.F. da Silva, J.C. Soares
Dep. Física-ITN, E.N. 10, 2685 Sacavém, Portugal

Abstract

The surface region of sapphire was modified by the implantation of heavy ions. Single crystalline α-Al_2O_3 samples were implanted at room and liquid nitrogen temperatures with energies in the range of 100 keV to 200 keV. Several fluences have been implanted in order to study the evolution of the implantation damage and the formation of new microstructures. The amorphisation and the damage recovery was observed to be strongly dependent on the chemical nature of the implanted ions. For example, while fluences of 1×10^{15} Hg^+/cm^2 were enough to amorphise the implanted region we need to implant a fluence one order of magnitude higher of Pt to obtain the same result. The implanted metallic ions occupy mainly substitutional Al sites in the sapphire corundum structure, while the rare earth ions go to the free octahedral site along the c-axis. Post-implantation annealing at high temperature allows the complete re-crystallisation of the amorphous region and induces the redistribution of the implanted ions, decreasing the maximum peak concentration. During this process the formation of metallic precipitates epitaxially aligned with the c-axis of the α-Al_2O_3 structure are observed.

* E. Alves: Tel. +351.1.9550021 (ext.1124); Fax.+315.1.9941525; e-mail:ealves@itn1.itn.pt.

Introduction

Irradiation effects in sapphire have been widely investigated for several implanted species leading to a global understanding of the amorphisation and defect recovery processes [1]. In order to amorphise α-Al_2O_3 at room temperature it is necessary to implant high fluences ($\geq 1\times10^{16}$ at/cm^2) of heavy ions, while at liquid nitrogen temperature a fluence of 10^{14} at/cm^2 is sufficient [1,2]. Although the nature of the implanted species influences the damage production, the interplay between ballistic and chemical effects is still an open question [3,4]. Also, the crystal orientation with respect to the implantation direction can influence the damage production [5]. These aspects together with the possible influence of the implanted ions on the re-growth process, which was never reported, need to be understood.

In this work we show that by the implantation at room temperature of a moderate dose of Hg in α-Al_2O_3 we are able to create an amorphous layer while we need an order of magnitude more Pt, W, Hf or Er to reach the same state, despite the fact that these elements have similar masses. We observe a fast re-crystallisation of the amorphous phase into the α-Al_2O_3 phase at a temperature as low as 800°C in the samples implanted with Hg. On the other hand the re-growth of the amorphous layer was not complete, even at temperatures of 1400 °C, in samples implanted with Pt ions.

Experimental details

High purity α-Al_2O_3 single crystals with optically polished surfaces with $<01\bar{1}0>$ (m-samples) and <0001> (c-samples) orientations were implanted with Hg^+, Pt^+, E^{r+}, Hf^+ and W^+ ions to fluences in the range of 1×10^{14} to 1×10^{16} at/cm^2 and energies of 100 keV or 200 keV. The implantation conditions were the same for all the species implanted at room temperature (RT). The current density was kept at 0.5 μA/cm^2 to avoid heating the samples. Some samples were implanted at liquid nitrogen temperature (LN) in order to study the influence of the implantation temperature on the damage production. Thermal annealings were carried out in the temperature range of 800-1400°C under a pressure less than 10^{-6} mbar and ambient atmosphere.

After implantation and after each annealing stage, RBS/channelling studies were performed with a 1.6 MeV He^+ beam to characterise the structural changes. The backscattered particles were detected at 140° and 180° using silicon surface barrier detectors located in the standard IBM geometry, with resolutions of 13 and 16 keV, respectively. A Ni mask with a 4 mm hole was used in front of the sample in order to minimise the effect of charge accumulation on the Al_2O_3 surface during the analysis. Computer simulations of the angular scans were performed using a modified version of a Monte Carlo code previously described [6].

Results and discussion

Orientation and temperature effects

Figure 1 shows the random and aligned RBS spectra obtained for a sample with a <0001> orientation implanted with Er before and after annealing.

Figure 1. RBS spectra of the sample implanted with 4×10^{15} Er^{+}/cm^{2} with 200 keV at RT, as implanted and after the annealings indicated in the figure

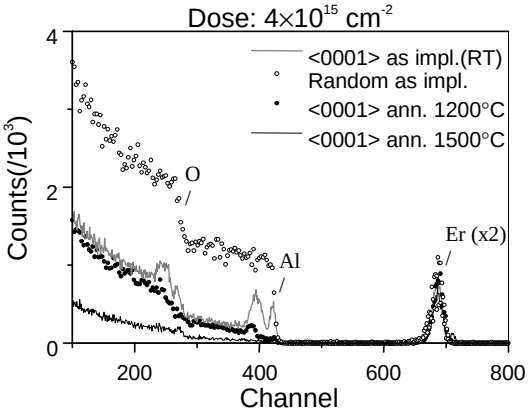

As we can see the defects produced in the Al and O sub-lattices are different. The degree of disorder for several fluences, indicated by the value of the minimum yield, χ_{min} (χ_{min} is the ratio between the random and aligned spectra in the damaged region), is plotted in Figure 2 for <0001> and <01$\bar{1}$0> samples . In the <0001> samples the damage in the anion sub-lattice (oxygen) is much higher compared to the cation (aluminium) reaching almost the full disorder ($\chi_{min} = 1$) for the highest fluence. These results indicate a non stoichiometric damage production. For the <01$\bar{1}$0> samples the disorder is the same in both sub-lattices and identical to the damage produced in the cation sub-lattice of the <0001> samples. The differences in the damage production must be related with the different displacement energies of the O and Al along the two directions [7]. The recovery of the implantation damage is complete at 1500°C without any noticeable change in the Er profile. The same result was observed for the <01$\bar{1}$0> samples. The anisotropy observed in the damage level on the anion sub-lattice correlates well with the intensity of the photoluminescence (PL) emission of Er at 1.54 μm [8]. The PL intensity as a function of the fluence is plotted in Figure 3 for the c- and m-samples. Since the optical activity of erbium is related with the existence of the Er^{3+} state, which depends on the amount of oxygen available, it is natural that the intensity is higher in the c-samples where there are more free oxygen in agreement with the experimental results.

Figure 2. Minimum yield as a function of the Er fluence for the O and Al sub-lattices in the m and c-samples

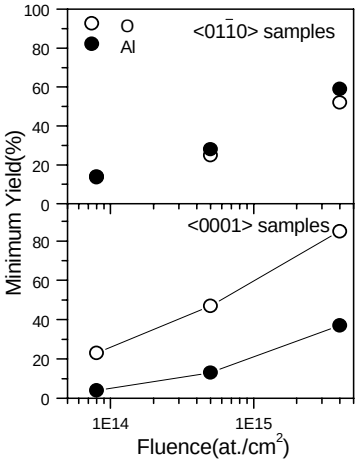

Figure 3. Photoluminescence intensity as a function of the Er fluence for the m and c-samples

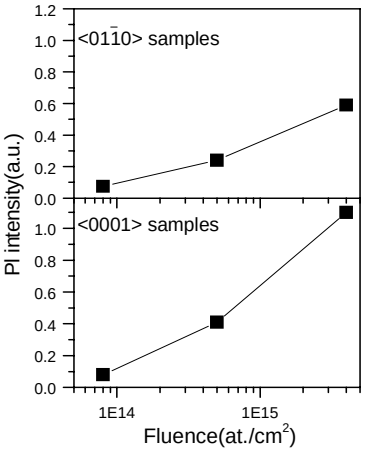

The temperature of implantation plays also an important role on the damage production. At LN temperature in the case of Er a dose of 5×10^{14} Er^{+}/cm^{2} is enough to produce a continuous amorphous layer over all the implanted region, Figure 4. At these temperature the dynamic recovery processes are attenuated and the amorphisation is reached at much lower fluences. In these case the re-growth process induces the segregation of Er to the surface.

Figure 4. RBS spectra of the sample implanted with 6×10^{14} Er^{+}/cm^{2} with 200 keV at LN as implanted and after the annealings indicated in the figure

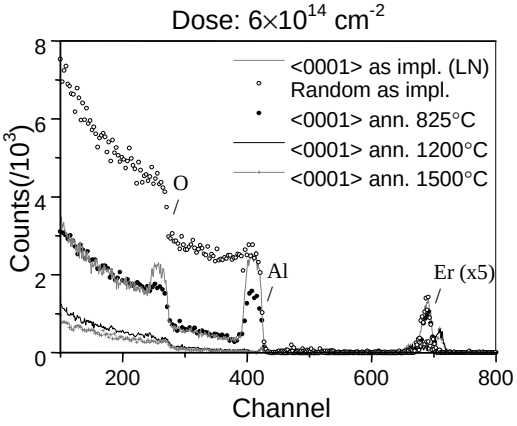

Chemical effects

Figure 5 compares the random and aligned RBS spectra obtained for the samples implanted with different doses of Pt (Figure 5a) and Hg (Figure 5b) ions. The amorphisation of the implanted layer (350 Å), indicated by the overlap of the random and the aligned spectra, is reached after the implantation of 1×10^{15} at/cm^{2} for Hg and 1×10^{16} at/cm^{2} for Pt. Since Pt and Hg have nearly the same mass we can exclude ballistic effects as being responsible for the observed difference in the defect production rate.

Figure 5a. RBS spectra showing the damage accumulation as a function of the Pt fluence for <0001> samples

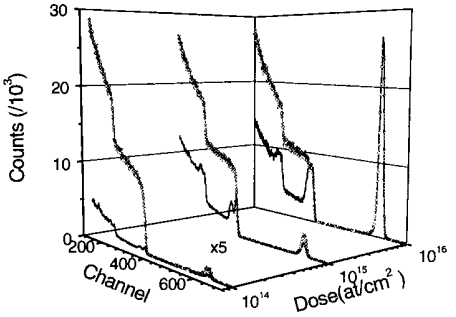

Figure 5b. RBS spectra showing the damage produced in <0001> samples as a function of the Hg fluence

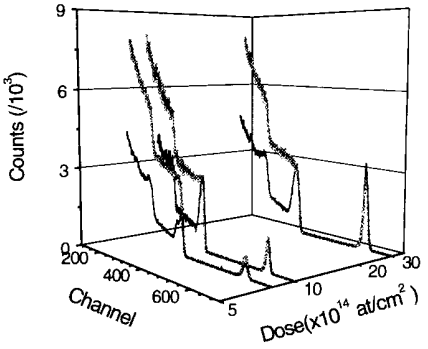

The damage annealing is also strongly influenced by the implanted species. No change on the amorphous layer was seen in the sample implanted with Pt which had the surface fully amorphised (Figure 6a) up to a temperature of 900°C. Increasing the temperature to 1100°C the amorphous layer starts to re-grow epitaxially. The thickness of the layer reduces from 560 Å to 380 Å, giving a re-grow velocity of 3 Å/min. An additional annealing at 1400°C for 1 h did not produce any changes. For all the implanted doses the Pt profile remain undisturbed during the annealing treatments in vacuum.

A totally different behaviour was observed for the samples implanted with Hg. The annealing at 800°C not only removes the surface damage observed in the sample implanted with the lowest dose but also induces the complete re-crystallisation of the amorphous layer (Figure 6b).

Figure 6a. RBS spectra showing the annealing behaviour of the <0001> samples implanted with 1×10^{16} Pt^{+}/cm^{2}

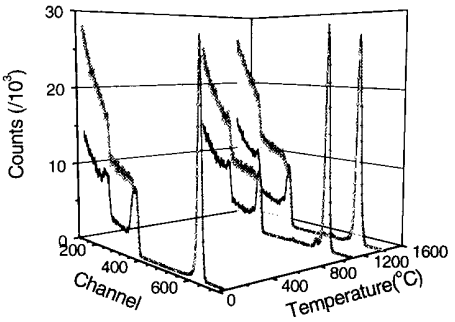

Figure 6b. RBS spectra showing the annealing behaviour of the <0001> samples implanted with 1×10^{15} Hg^{+}/cm^{2}

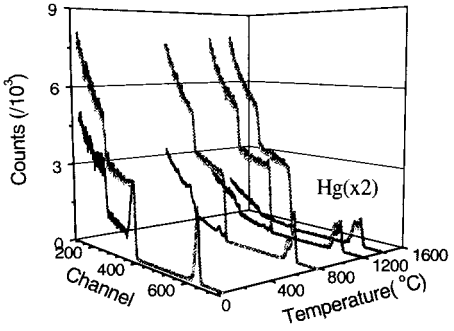

As the sample implanted with 3×10^{15} Hg^{+}/cm^{2} also shows a complete re-crystallisation after a 10 min anneal at 800°C, we can estimate for the epitaxial re-grow velocity a lower limit of 52 Å/min, nearly three orders of magnitude higher then the value reported before [9]. Considering the re-crystallisation a short range diffusion process, we can interpret this fast re-growth in the following way: Hg diffuses fast through the amorphous layer forming Hg rich precipitates; these precipitates then allow the dissolution of the Al and O from the amorphous phase and enhance its transport to the crystalline/amorphous interface where they can find empty sites to bind to the crystalline side. Such a melt-mediated process was used before to explain the explosive re-crystallisation of amorphous silicon implanted with In [10]. Additional studies should be performed in order to get a clear picture of this process.

During the epitaxial re-growth of the amorphous layer some of the Hg segregates towards the surface in the sample implanted with 1×10^{15} at/cm^{2}, Figure 6b. The flat region of the Hg profile after the annealing at 800°C corresponds to atoms trapped in the re-crystallised layer (1.7×10^{20} at/cm^{3}). The difference observed between the random and aligned profiles also shows that a fraction of the trapped Hg is in regular lattice sites. The Hg at the surface starts to diffuse towards the bulk when the annealing temperature is increased forming a flat profile with a concentration of 2.3×10^{20} at/cm^{3} after annealing at 1400°C. The complete overlap of Hg profile in the random and aligned directions indicates that now all the ions are located in random positions. The amount of Hg in the sample remained constant during all the changes observed as consequence of the thermal treatments. For the sample implanted with the highest dose, Hg reached a flat profile with the same concentration of 2.3×10^{20} at/cm^{3} immediately after annealing at 800°C with the excess of Hg being lost through the surface. For the sample implanted with the lowest dose (8×10^{14} at/cm^{2}) we observe a slight outdiffusion of Hg only after the annealing at 1100°C, which did not increase after an additional annealing at 1400°C for 1 h.

Lattice location

Figure 7a shows the complete angular scans through the <0001> and <01$\bar{1}$0> axes after the implantation of Hg. The most significant feature of these scans is the narrow dip of Hg in the <01$\bar{1}$0> axis, which excludes the presence of Hg in substitutional sites. Monte Carlo simulations of the results show that 30% of the Hg atoms are located in a displaced octahedral site (0.7 Å along the c-axis) and the rest are randomly distributed. The Hg ions in regular sites remain stable up to annealing temperatures of 1200°C. For low doses a fraction of 90% of the Er ions also occupy the same

displaced position in the lattice. For Pt the results are displayed in Figure 7b. In this case the simulations show that 70% of ions are occupying Al substitutional lattice sites. The fraction of Pt ions in substitutional sites decreases to 50% after the annealing at 1400 °C.

Figure 7a. Angular scans for the <0001> sample implanted with 5×10^{14} Hg^{+}/cm^{2}. The lines are the result of the simulations.

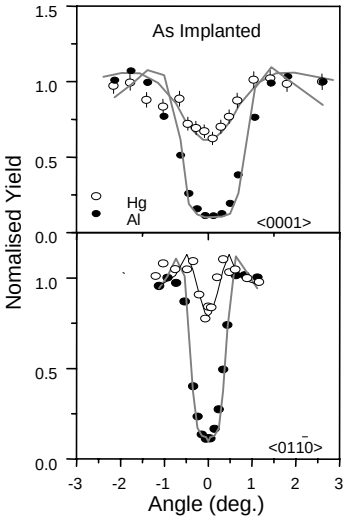

Figure 7b. Angular scans for the <0001> sample implanted with 1×10^{14} Pt^{+}/cm^{2}. The lines are the result of the simulations.

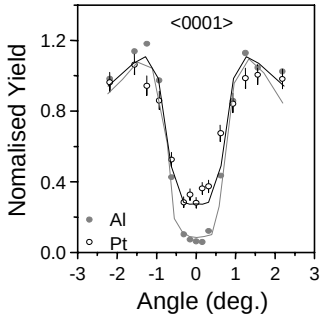

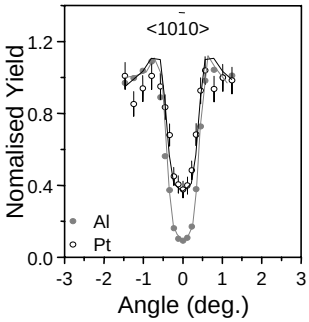

A similar behaviour was observed for Hf and W with substitutional fractions of 92% and 80% respectively, after the implantation [11,12].

When the implanted doses are above 10^{16} at/cm^2 the implanted ions form nanoprecipitates. This behaviour was observed for Pt and Er and is related with the low solubility of these elements in sapphire [13,14]. We observe the growth of Pt precipitates with the <111> axis aligned with the <0001> axis of the α-Al_2O_3 structure.

Conclusions

Several ions were implanted into sapphire, at room and liquid nitrogen temperature, with identical implantation parameters. We observe that a fluence of 1×10^{15} Hg^{+}/cm^{2} creates a continuous amorphous layer through the implanted region and the epitaxial re-growth of this layer was observed

directly after annealing at 800°C with a velocity of 52 Å/cm^2. A significant fraction of the Hg ions are incorporated into displaced free octahedral sites along the c-axis. The RBS/channelling measurements also show that the Hg redistributes in the implanted region forming a flat profile with a maximum concentration of 2.3×10^{20} at/cm^3. In contrast, for the case of Er, Pt, Hf or W, the production of an amorphous layer requires doses of the order of 1×10^{16} at/cm^2, and the re-growth process is very slow. When the implanted doses are below the amorphisation threshold Pt, Hf and W are mainly incorporated into Al substitutional sites of the α-Al_2O_3 lattice while Hg and Er occupy the empty octahedral site. These results prove that both the amorphisation and re-crystallisation processes in sapphire are influenced by the nature of the implanted species and crystal orientation.

REFERENCES

[1] C.W. White, C.J. McHargue, P.S. Sklad, L.A. Boatner and G.C. Farlow, *Mat. Sci. Rep*. 4 (1989) 41.

[2] E. Alves, M.F. da Silva, G.N. van den Hoven, A. Polman, A.A. Melo and J.C. Soares, *Nucl. Instr. Meth*. B106 (1995) 429.

[3] C.J. McHargue, G.C. Farlow, C.W. White, J.M. Williams, B.R. Appleton and H. Naramoto, *Mater. Sci. Eng*. 69 (1985) 123.

[4] E. Alves, J.G. Marques, M. F. da Silva, J. C. Soares and K. Freitag, *Nucl. Instr. Meth.* B141 (1998) 353.

[5] M.E. O'Hern, L.J. Romana, C.J. McHargue, J.C. McCallum and C.W. White, 15th International Symposium, ASTMSTP 1125, R.E. Stoller, A.S. Kumar and D.S. Gelles, eds., American Society for Testing and Materials, Philadelphia, 1992, pp. 740-748.

[6] P.J.M. Smulders and D.O. Boerma, *Nucl. Instr. Meth*. B29 (1987) 471.

[7] R.E. Williford, R. Devanathan and W.J. Weber, *Nucl. Instr. Meth*. B141 (1998) 904.

[8] G.N. van den Hoven, A. Polman, E. Alves, M.F. da Silva, A.A. Melo and J.C. Soares, *J. Mater. Res*. 12 (1997) 1401.

[9] C.W. White, L.A. Boatner, P.S. Sklad, C.J. McHargue, J. Rankin, G.C. Farlow and M.Z. Aziz, *Nucl. Instr. Meth*. B32 (1988) 11.

[10] J. Narayan, O.W. Holland and B.R. Appleton, *J. Vacuum Sci. Tech*. B1 (1993) 871.

[11] J.G. Marques, A.A. Melo, J.C. Soares, E. Alves, M.F. da Silva and K. Freitag, *Nucl. Instr. Meth*. B106 (1995) 602

[12] E. Alves, R.C. da Silva, M.F. da Silva and J.C. Soares, to be published *Nucl. Instr. Meth*. B.

[13] E. Alves, R.C. da Silva, M.F. da Silva, and J.C. Soares, *Nucl. Instr. Meth*. B139 (1998) 313.

[14] E. Alves, R.C. da Silva, M.F. da Silva and J.C. Soares, to be published *Nucl. Instr. Meth*. B.

MODIFICATION AND CHARACTERISATION OF AL SURFACES IMPLANTED WITH CR IONS

R.C. da Silva*, L.M. Prudêncio, M.F. da Silva, J.C. Soares
Dep. Física, ITN – E.N. 10, 2685 Sacavém, Portugal

O. Conde
Dep. Física, FCUL – Ed. C1, Campo Grande, 1700 Lisboa, Portugal

R. Vilar
Dep. Eng. Mat., IST – Av. Rovisco Pais, 1000 Lisboa, Portugal

Abstract

In this work metastable Al-Cr surface alloys were produced by high fluence Cr implantations into polycrystalline aluminium, under different conditions of temperature and fluence.

Clear evidence for the direct formation of $Al_{86}Cr_{14}$ and $Al_{13}Cr_2$ intermetallic phases by ion implantation is reported, as well as investigations on the influence of implantation temperature, fluence and annealing treatments on the formation and evolution of Al-Cr intermetallic compounds. It was also found that the $Al_{86}Cr_{14}$ phase forms first and is transformed into $Al_{13}Cr_2$ by a proper thermal annealing.

* R.C. da Silva: Tel: +351-1-9550021 (ext. 1121), Fax: +351-1-9941525, E-mail: rmcs@itn1.itn.pt

Introduction

Aluminium based surface alloys attract much interest due to their technological importance. In particular, Al-Cr alloys are well known as having improved corrosion and wear resistance, without loss of the high elastic limit-to-density ratio, allowing to devise the preparation of valuable stainless aluminium [1-3].

Although different techniques of preparation exist [4], ion implantation is specially well suited, due to the precision and degree of control it provides over concentration depth distributions. In general the preparation and study of the behaviour of this type of surface alloys requires the combination of ion implantation with thermal treatments, usually furnace annealing [5,6]. In previous work the possibility of obtaining and controlling very intense Cr^+ beams for the preparation of Al-Cr buried intermetallic phases, *in situ* during the implantation, has been demonstrated [7]. In this work we follow the application of these concepts: Al-Cr alloys were produced by implantation of 140 keV Cr^+ ions into Al, with fluences of 1, 2 and $5\times10^{17}/cm^2$, at different target temperatures. The formation of the Al-Cr intermetallic phases was investigated by means of Rutherford Backscattering Spectrometry (RBS), in combination with X-ray diffraction at grazing incidence (GIXRD).

The results showed that, depending on the fluence, $Al_{86}Cr_{14}$ and $Al_{13}Cr_2$ intermetallic phases immediately form upon implantation. Also, depending on the temperature of the aluminium surface during the implantation process, the same intermetallic phases will form under similar fluences. It was also found that $Al_{86}Cr_{14}$ phase forms first and is transformed into $Al_{13}Cr_2$ if proper thermal annealings are performed. Both the $Al_{86}Cr_{14}$ and $Al_{13}Cr_2$ phases form as embedded crystalline precipitates which grow and transform by annealing.

Experimental details

High purity (99.999%, Goodfellow) polycrystalline aluminium samples were implanted with 1, 2 and 5×10^{17} /cm^2 Cr^+ ions of 140 keV energy, without target heating. Other samples were implanted with 2×10^{17} /cm^2 Cr^+ ions of the same energy, but at temperatures of 250, 400 and 510ºC. Target temperatures were measured by a chromel-alumel thermocouples, placed into a hole carved 1 mm below the sample surface.

Some of the implanted samples were submitted to a sequence of one hour furnace annealings, under a pressure of 10^{-6} mbar, at temperatures of 300, 400 and 500ºC.

The Cr profiles were measured by RBS spectrometry, in the as-implanted state and after each step of annealing. Beams of 1.6 MeV He^+ were used to perform these analyses. The backscattered He^+ ions were detected by means of two silicon surface barrier detectors, placed at angles of 140º and 180º to the beam direction, with energy resolutions of 13 and 16 keV respectively.

The GIXRD technique was used to investigate the formation and evolution of intermetallic phases. The analyses were carried out in the as-implanted state and after those annealing stages for which changes in the depth profiles were detected with the RBS technique. A Siemens D-5000 spectrometer, allowing for conventional (Bragg-Brentano) and grazing incidence geometries, was used to perform the X-ray diffraction studies. The diffraction patterns were recorded using Cu K_α radiation at an incidence of 1º angle to the specimen surface. The identification of crystalline phases was done by using the JCPDS database cards [8].

Results and discussion

As-implanted state – Influence of implantation temperature and fluence

Figure 1 displays the RBS spectra obtained from the as-implanted state of the samples implanted with 1, 2 and 5×10^{17} Cr^{+}/cm^{2} without target heating, while in Figure 2 the corresponding GIXRD spectra are shown.

Figure 1. RBS spectra of Al as-implanted with 1, 2 and 5×10^{17} Cr^{+}/cm^{2}, without target heating

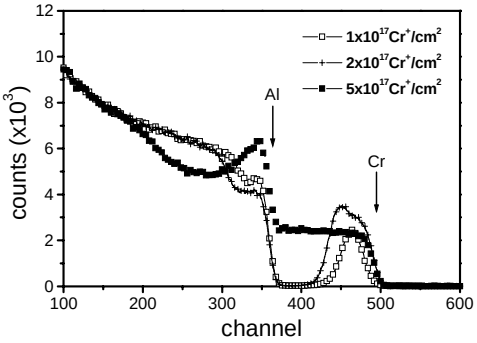

Figure 2. GIXRD spectra of the samples referred to in Figure 1. Notice the diffraction peaks characteristic of $Al_{86}Cr_{14}$ and $Al_{13}Cr_{2}$ intermetallic compounds.

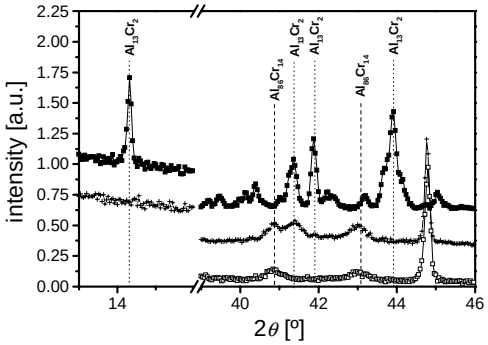

From the RBS spectra in Figure 1 it is clear that only the implantation with 5×10^{17} Cr^{+}/cm^{2} leads to a flat Cr profile, with a constant atomic concentration ratio [Al]:[Cr] of 13:2, which extends over a wide depth region (from the surface to 0.5 μm, assuming for the implanted region the same density as of aluminium). In previous work we have shown that the existence of such a plateau, with constant [Al]:[Cr] concentration ratio, is usually associated with the formation of an extended layer of intermetallic compounds [7]. On the contrary, the Cr profiles of the samples implanted with lower fluences, 1 and $2\times10^{17}/cm^{2}$, do not show any such plateau.

From the GIXRD spectra in Figure 2 it can be seen that there are no precipitates of metallic Cr, in either samples. The implanted Cr is either in solid solution or may have formed intermetallic compounds. For the sample implanted with $5\times10^{17}/cm^{2}$ there are diffraction peaks in the 2θ regions of 40-45º and near 14.7º. This last one is a (−111) reflexion of the $Al_{13}Cr_{2}$ intermetallic and is a clear cut fingerprint of this compound. For the two other fluences the presence of a Cr-richer intermetallic, $Al_{86}Cr_{14}$, is detected instead. It is to be noticed that, to our knowledge, the formation of these $Al_{86}Cr_{14}$ precipitates on a solid solution of Al:Cr, has never been reported.

In order to establish the role of the implantation temperature in the formation of different intermetallic compounds, the samples implanted with $2\times10^{17}/cm^2$ at different temperatures were analysed by RBS and GIXRD as shown in Figures 3 and 4.

Figure 3. RBS spectra of the samples implanted with 2×10^{17} Cr^+/cm^2 at different temperatures

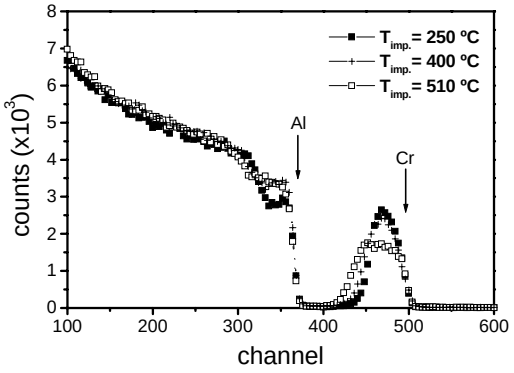

Figure 4. GIXRD spectra of the samples implanted with 2×10^{17} Cr^+/cm^2 at different temperatures

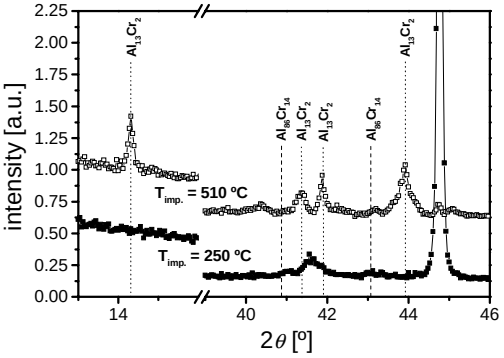

The RBS spectra (in Figure 3) show that the implantation at 510ºC yields a constant Cr distribution, with an atomic concentration ratio [Al]:[Cr] of 13:2, over a depth of 0.2 μm from the surface (using the density of aluminium). For the samples implanted at 400 and 250ºC Gaussian like Cr profiles develop instead, with maximum Cr concentrations around 20 at.%.

The GIXRD spectra depicted in Figure 4 show the presence of $Al_{13}Cr_2$ after implantation at 510ºC, while after the implantation at 250ºC it was not possible to identify any of the known Al-Cr intermetallic compounds (whether $Al_{13}Cr_2$, $Al_{86}Cr_{14}$ or the intermediate compositions, e.g. the $Al_{11}Cr_2$). For the implantation at 400ºC a mixture of both intermetallics, $Al_{13}Cr_2$ and $Al_{86}Cr_{14}$, was found by GIXRD (not shown).

These results clearly show the importance of the implantation temperature in what concerns the formation of Al:Cr intermetallic compounds. It can be stated that $Al_{86}Cr_{14}$ precipitates begin to form at a temperature between 250 and 400ºC, while $Al_{13}Cr_2$ precipitates form at higher temperatures. The results also indicate that the Cr-richer $Al_{86}Cr_{14}$ transforms into $Al_{13}Cr_2$ at temperatures in the vicinity of 400ºC, since the two compounds coexist at 400ºC.

The influence of annealing

In order to study the stability of $Al_{86}Cr_{14}$ precipitates, the sample implanted with 2×10^{17} Cr^{+}/cm^{2} in which it was reported the presence of $Al_{86}Cr_{14}$, was annealed at 300, 400 and 500ºC.

The corresponding RBS and GIXRD spectra are displayed in Figures 5 and 6 respectively, and show the evolution of the Cr concentration profiles as well as of the type of intermetallic compounds present.

Figure 5. RBS spectra of one 2×10^{17} Cr^{+}/cm^{2} implanted Al, after 1 hour annealings at the indicated temperatures

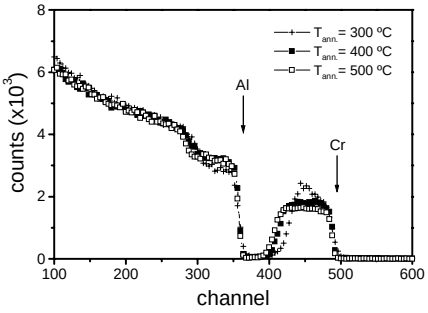

Figure 6. GIXRD spectra of the sample referred to in Figure 5

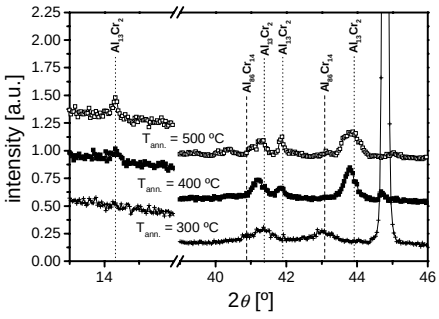

The annealing at 300ºC did not have any noticeable consequences; the Cr RBS profile and GIXRD spectra did not change, indicating roughly the same $Al_{86}Cr_{14}$ content as before annealing. On the contrary, the annealings at 400 and 500ºC caused a redistribution of Cr. At 400ºC, the Cr profile becomes flat, with an almost constant concentration around 15 at.%, in a 0.23 μm deep layer, while the $Al_{86}Cr_{14}$ precipitates disappear and are being replaced by $Al_{13}Cr_{2}$ (in the GIXRD spectrum). After the 500ºC annealing the Cr profile shows a constant concentration of 13.5 at.%, over a region of 0.28 μm.

Analyses of the GIXRD line widths corresponding to the samples where $Al_{86}Cr_{14}$ and $Al_{13}Cr_{2}$ precipitates arise, give an indication of the average dimension of these precipitates. Using the Scherrer formula [9], and assuming that no other effects cause the line broadening, we estimate that the $Al_{86}Cr_{14}$ precipitates have an average dimension of 20 nm, while the $Al_{13}Cr_{2}$ precipitates grow to a size larger than 100 nm.

Recently performed TEM analyses allowed to confirm the 20 nm estimate, and to derive a value of 200 nm for the average size of the $Al_{13}Cr_{2}$ precipitates.

Summary and conclusions

The results obtained so far show that, depending on the fluence, $Al_{86}Cr_{14}$ and $Al_{13}Cr_2$ intermetallic phases immediately forms upon implantation. Also, depending on the target temperature during the implantation process, these same intermetallic phases will form for similar fluences. It was also found that the $Al_{86}Cr_{14}$ phase forms first and is transformed into $Al_{13}Cr_2$ if proper thermal annealing is performed. Both phases form as embedded crystalline precipitates which grow and transform by annealing. No evidence for the formation of other intermetallics, e.g. $Al_{11}Cr_2$, was found. The formation of $Al_{86}Cr_{14}$ occurs at lower temperatures, probably in the range 250-300ºC, and the temperature of transformation to $Al_{13}Cr_2$ was estimated to lay around 400ºC.

Further work is under way in order to determine more precisely the formation and transformation temperatures of the intermetallic phases, and its relation to the implantation fluences, by following the evolution of the surface temperature, i.e. the temperature in the implantation region, by means of a near-IR optical pyrometer recently available.

REFERENCES

[1] R. Vilar and A. Almeida, *in* Proc. of the LANE'94 Conference on "Laser Assisted Net Shape Engineering", Vol. 1, ed. M. Geiger, F. Vollertsen Meisenbach Bamberg, 1994.

[2] P. Petrov, R. Vilar, and A. Almeida, *in* Proc. of the NATO ASI on "Laser Processing: Surface Treatment and Film Deposition", ed. J. Mazumder, O. Conde, W. Steen and R. Vilar, Kluwer Acad. Press (in press).

[3] J.M. Williams, A. Gonzales, J. Quintana, I.-S. Lee, R.A. Buchanan, F.C. Burns, R.J. Culbertson, M. Levy and J.R. Treglio, *Nucl. Instr. Meth.* B, 59/60 (1991) 845.

[4] S.T. Picraux and D.M. Follstaedt, *in* "Surface Modification and Alloying by Laser, Ion and Electron Beams", ed. J. M. Poate *et al.*, New York, Plenum Press, 1983.

[5] R.B. Benson Jr., S.P. Withrow and S.J. Pennycook, *Mat. Letters*, 6, 4 (1988) 93.

[6] R.C. da Silva, M.F. da Silva, A.A. Melo, J.C. Soares, E. Leitão and M. Barbosa, *Nucl. Instr. Meth.* B, 50 (1990) 423.

[7] R.C. da Silva, R.C. Sousa, O. Conde, M.F. da Silva, J.C. Soares, *Surf. and Coatings Technology*, 83 (1996) 60.

[8] Joint Committee on Powder Diffraction Standards, Powder Diffraction File, ASTM, Philadelphia, PA, 1992.

[9] B.D. Cullity, *in* "Elements of X-Ray Diffraction", 2nd ed., Addison-Wesley, Reading, MA, 1978.

DESIGN AND APPLICATIONS OF MICROPROBES FOR MATERIALS ANALYSIS

M.B.H. Breese
Physics Department, University of Surrey, Guildford, Surrey, GU2 5XH, UK

L.C. Alves, M.R. Silva, M.F. da Silva and J.C. Soares
Instituto Tecnologico e Nuclear, ITN, Estrada Nacional 10, 2685 Sacavém, Portugal

Abstract

The use of a series of quadrupole lenses to focus beams of MeV light ions, such as protons or He, to spot sizes of 1 micron or less is becoming increasingly common in accelerator laboratories. This is because the use of such a microprobe enables the analysis of the elemental, crystallographic and electronic properties of a wide range of materials with high spatial resolution. Here, the basic hardware required for the construction of a high spatial resolution microprobe, such as is presently being built at ITN are described. Applications in the analysis of integrated circuits and dislocation networks are reviewed.

Introduction

A nuclear microprobe focuses a beam of MeV light ions on the surface of a sample. The focused beam is then scanned over the sample region of interest and the relevant analytical signal is fed into the data acquisition computer together with the position co-ordinates from the scan generator. A spatially resolved image of the sample structure is built up in this way, in a manner very similar to a scanning electron microscope. All aspects of nuclear microprobe hardware, optics and its use for materials analysis are covered in Ref. [1].

Since MeV light ions are much heavier and at higher energies than keV electrons, axially symmetric solenoid lenses which are used in a scanning electron microscope cannot be used to focus MeV ions because their magnetic field is too weak. This necessitates the use of a series of 2, 3 or 4 magnetic quadrupole lenses to focus the MeV ions, such as shown in Figure 1. In a quadrupole lens the magnetic flux lines are perpendicular to the beam and so produce a strong deflection, compared with a solenoid lens where the field lines are almost parallel to the beam direction. A series of quadrupole lenses is needed to focus the beam to a point, since a single lens will focus the beam in one plane and defocus it in the orthogonal plane. The merits of the different quadrupole configurations used to focus MeV ions is discussed in [1,2]. Figure 2 shows beam envelopes in the horizontal x-plane (upper) and vertical y-plane (lower) through a triplet a quadruplet lens configuration. The triplet produces a steeply convergent beam, with different demagnifications in the x- and y-direction. In comparison, a quadruplet produces an orthomorphic focus, i.e. equal demagnifications in the x- and y-directions. Although this property makes a quadruplet configuration better for some microprobe applications, it gives a lower demagnification than the triplet, which is consequently very popular despite its highly asymmetric focusing.

The best reported spatial resolution with a nuclear microprobe is ≈100 nm [3], at a very low beam current of ≈1fA (i.e. ≈6,000 ions per second). This is the beam current which is used for many microprobe applications in materials analysis, such as energy loss imaging using scanning transmission ion microscopy (STIM) [1], ion beam induced charge (IBIC) microscopy [4] and transmission channelling analysis [1] (or see Ref. [5] for a good description of conventional modes of ion channelling). When other ion beam techniques are used for elemental analysis or depth profiling using a nuclear microprobe, such as particle induced X-ray emission (PIXE), Rutherford backscattering spectrometry (RBS), or nuclear reaction analyses (NRA), a higher beam current of at least 100 pA is needed for analysis within a reasonable time. At this beam current a spot size of ≈350 nm is attainable [6], but most microprobes routinely use a spot size of 1 micron at this beam current.

Although MeV ions are more difficult to focus than keV electrons, this same property makes the analysis of thick or buried layers with high spatial resolution more attainable with MeV ions. Figure 3 demonstrates this by showing the generation volume of electron-hole charge carriers produced in silicon by (a) 10 keV electrons and (b) 3 MeV protons. These charge carriers are produced by electronic energy loss in the slowing down of the incident charged particles in collisions with the lattice atoms, and gives a measure of the lateral scattering of the different particles as a function of depth. Because electrons are light particles, they are heavily scattered in the first micron of the sample, so the finely focused electron beam mushrooms into a spherical generation volume. Because MeV light ions, such as protons, are much heavier, they suffer much less lateral scattering in passing through tens of microns within the sample, giving a “teardrop” shape for the carrier generation volume, where lateral scattering only causes significant degradation of the focused beam spot towards the end of range.

Figure 4 shows a schematic of a typical microprobe sample chamber, which may contain a variety of different detectors to measure signals from the range of different interaction processes which can occur when the ions move through the sample. Such detectors might include a lithium-drifted SiLi detector to measure X-rays, semiconductor particle detectors for recording backscattered or transmitted incident ions, charged particle reaction products or displaced ions of the sample. A channel electron multiplier (channeltron) or a photomultiplier may be used to detect secondary electrons emitted from the surface, or a photomultiplier may detect ion induced luminescence from the sample. A commonly used microprobe technique for semiconductor analysis is IBIC microscopy, in which the sample itself acts as the detector. This is described in more detail below. The chamber will also contain one or more optical microscopes, which are used both for focusing the beam by observing its fluorescence on a piece of glass, and also for navigating round various sample features of interest.

Applications in materials analysis

Most work using nuclear microprobes has been for detecting and quantifying elemental distributions using PIXE, RBS and NRA. It is beyond the scope of this paper to review these applications, which are covered in [1]. Here, some new applications of a microprobe in materials analysis are described.

Spatially resolved channelling images of defects

In ion channelling a well-focused beam of MeV protons or helium ions with a low divergence angle is aligned with a major crystallographic axis or plane. When this happens the rate of energy loss of the ions and the probability of them interacting with the lattice nuclei and inner electron shells is reduced [5]. This is because the ions are steered by the positive lattice walls into regions of low electron density in between the planes. If a channelled ion encounters some kind of lattice defect such as a stacking fault or a dislocation, there is a high probability that the ion will be de-channelled at the fault plane and continue its trajectory with a higher non-channelled rate of energy loss. If the crystal thickness is less than the ion range (3 MeV protons travel 90 μm in silicon) then by measuring the average energy loss of the channelled beam as a function of position within the scanned area, any defects present are imaged as regions of high energy loss, and the surrounding perfect crystal as areas of low energy loss.

Figure 5(a) shows an example of a transmission channelling image of misfit dislocations in a strain-relaxed silicon-germanium epilayer using this procedure. Figure 5(b) shows a channelling image of oxidation induced stacking faults, where the faults appear as dark regions, representing areas of high transmitted energy loss. Both these images were measured from sample thicknesses of ≈40 μm and data was collected for 15 minutes to produce sufficient statistics. In comparing the capabilities of this dislocation imaging technique with others, it can image defects through 50 μm, over areas of hundreds of microns. This means that it has an analytical volume much better than transmission electron microscopy (TEM), but lower than X-ray diffraction (XRD). Conversely, it has a much poorer spatial resolution of ≈200 nm than TEM which has a resolution of ≈1 Å, but better than XRD which is limited to a few microns.

IBIC microscopy

IBIC has become a widely-used microprobe technique since it was developed five years ago [4]. It is important because it gives a method of analysing integrated circuits through their thick surface layers, without the need to strip off any layers prior to analysis, which is common for electron microscope techniques. This is possible owing to the high MeV proton penetration together with the low lateral scattering, as shown in Figure 3. An advantage over optical microscopy techniques for integrated circuit analysis is that there is no strong absorption in passing through metallic layers.

The sample geometry used for IBIC analysis of integrated circuits and dislocations or grain boundaries in semiconductor wafers is shown in Figure 6. In Figure 6(a), some ion energy is lost in passing through the device surface layers, which can be up to 10 μm thick. Most of the ion energy is lost in the creation of electron-hole carrier pairs in the semiconductor active junctions and in the substrate. For IBIC a charge sensitive preamplifier is connected directly across a collecting junction within the scanned area, and the number of charge carriers created by each individual ion is measured. By displaying this as a function of scan position, an IBIC image is built up which can be interpreted to give information on the device surface layer thickness, the distribution of the underlying *pn* junctions, and to check for any mask misalignment errors which may occur during device fabrication. A typical data collection period for the IBIC images shown below is 5 to 10 minutes.

IBIC microscopy of integrated circuits

Figure 7 shows an example of IBIC images working integrated circuits, from beneath several microns of surface layers. These three IBIC images show the same region of an EPROM memory device, with different biasing connections and voltages for the four field effects transistors present in this area. In these IBIC images, dark regions correspond to areas of large measured charge pulses, so it shows which regions are connected to the measurement electronics. The changing image contrast shows how IBIC is able to detect changes in transistor connections within working devices.

IBIC microscopy of semiconductor wafers

Figure 8 shows two IBIC images of misfit dislocations in a strain-relaxed silicon-germanium epilayer. Here the epilayer was 4 μm thick, and the sample was prepared for IBIC by depositing a Schottky barrier on the wafer surface, which acts as the collecting junction, as shown in Figure 6(b). These two IBIC images show orthogonal bands of bright and dark contrast, due to bands of dislocations running along {011} planes. Dark again corresponds to large measured pulses and light regions to small pulses. The interpretation of the image contrast here is that the light regions correspond to regions of higher dislocation density than the dark regions, since more charge carriers are being trapped and recombine here.

Conclusions

Many new nuclear microprobe facilities are presently under construction, most driven by its ability to provide spatially resolved information from micron-size areas. For materials analysis its importance lies in the ability to provide crystallographic and electronic analysis from samples which are tens of microns in thickness, together with elemental analysis using conventional ion beam analysis techniques.

REFERENCES

[1] M.B.H. Breese, D.N. Jamieson and P.J.C. King, *Materials Analysis Using a Nuclear Microprobe*, Wiley, New York (1996).

[2] G.W. Grime and F. Watt, *Beam Optics of Quadrupole Probe-Forming Systems*, Adam Hilger, Bristol (1984).

[3] F. Watt, T.F. Choo, K.K. Lee, T. Osipowicz, I. Orlic and S.M. Tang, *Nucl. Instrum. Meth.* B104 (1995) 101.

[4] M.B.H. Breese, G.W. Grime and F. Watt, *J. Appl. Phys.* 72(6) (1992) 2097.

[5] L.C. Feldman, J.W. Mayer and S.T. Picraux, *Materials Analysis by Ion Channelling*, Acad. Press (1982).

[6] G.W. Grime and F. Watt, *Nucl. Instrum. Meth*. B75 (1993) 495.

Figure 1. Schematic of a magnetic quadrupole lens

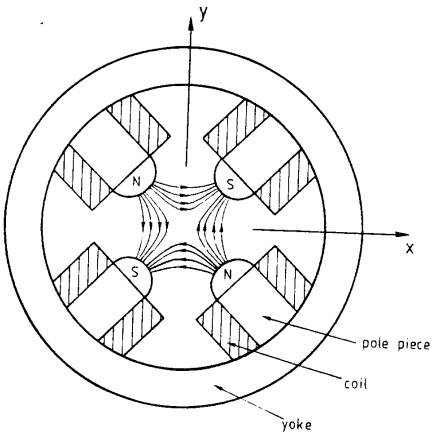

Figure 2. Beam envelope in the horizontal x-plane (upper) and vertical y-plane (lower) through a triplet (left side) a quadruplet (right side) lens configuration

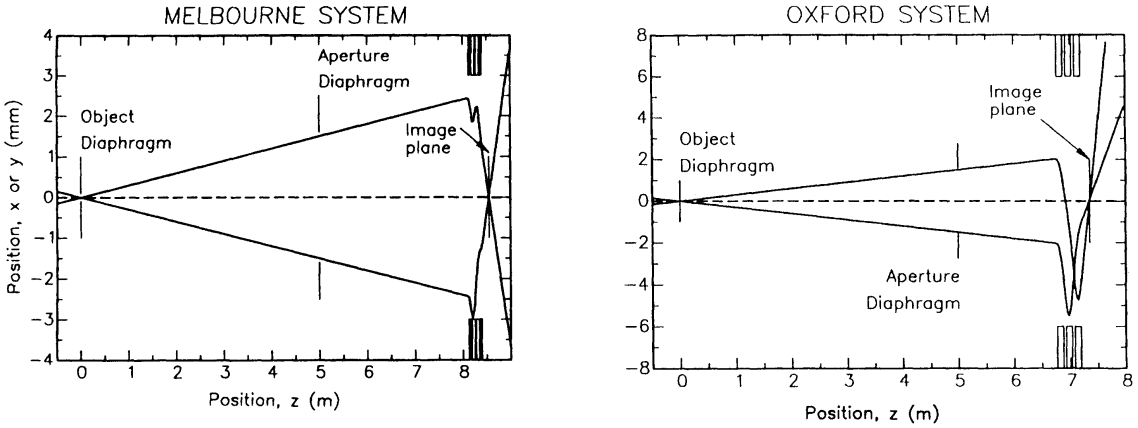

Figure 3. Contours showing the radial charge carrier generation intensity as a function of penetration depth for (a) 10 keV electrons and (b) 3 MeV protons in silicon. The axes are normalised to (a) the electron range Re and (b) the proton range Ri.

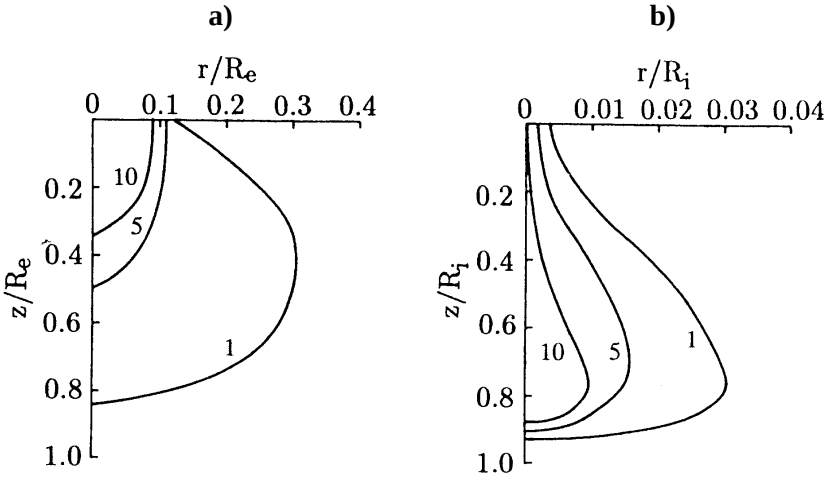

Figure 4. Schematic of the layout in a typical microprobe sample chamber, showing various detectors and optical microscopes

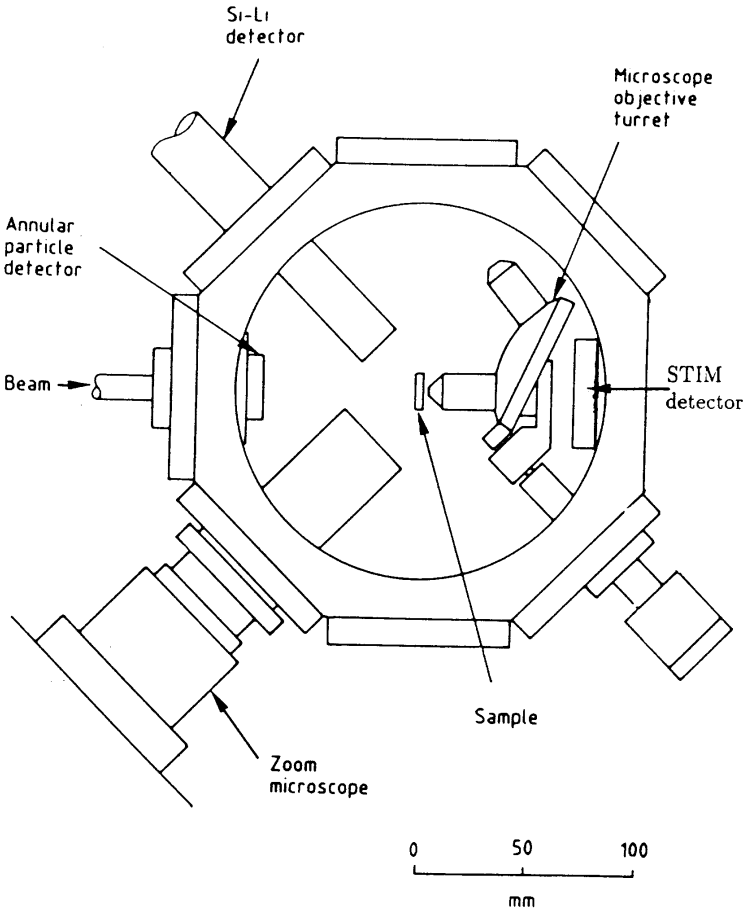

Figure 5. (a) Channelling image of misfit dislocations in a strain-relaxed silicon-germanium epilayer and (b) channelling image of oxidation induced stacking faults. The scan size is 100 μm in both cases.

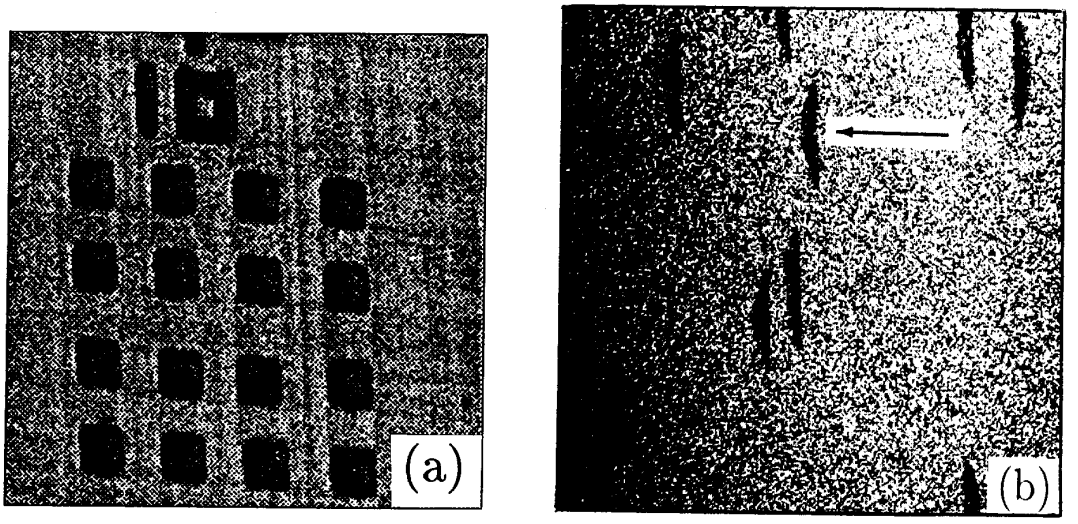

Figure 6. Schematic showing the geometry used for IBIC analysis of (a) integrated circuits and (b) the analysis of dislocations or grain boundaries in semiconductor wafers

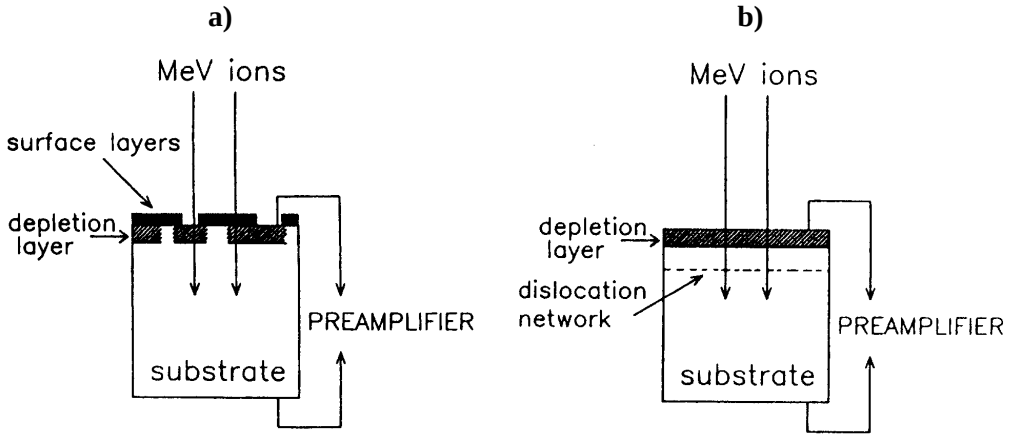

Figure 7. Three IBIC images of an EPROM integrated circuit, recorded from beneath several microns of surface layers using 3 MeV protons. The scan size is 300 μm.

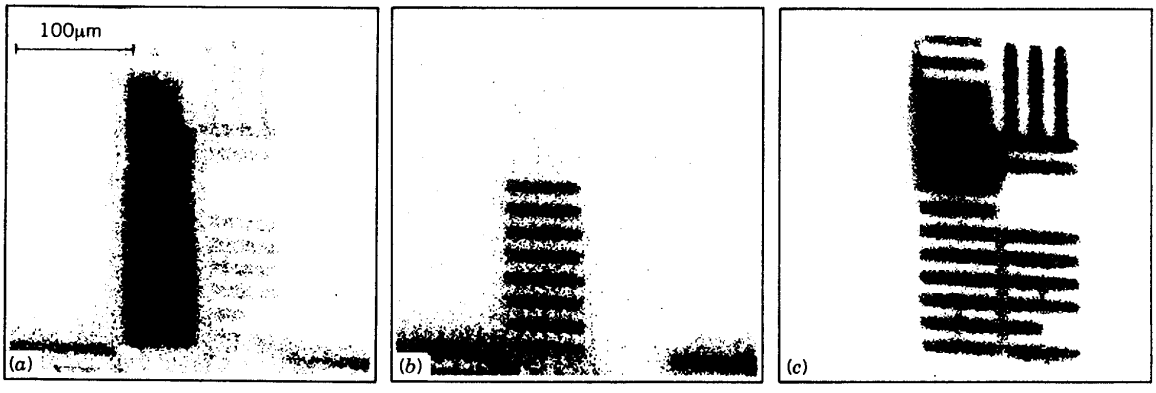

Figure 8. Two IBIC images of misfit dislocations in a strain-relaxed silicon-germanium epilayer, for scan sizes of (a) 250 μm and (b) 100 μm

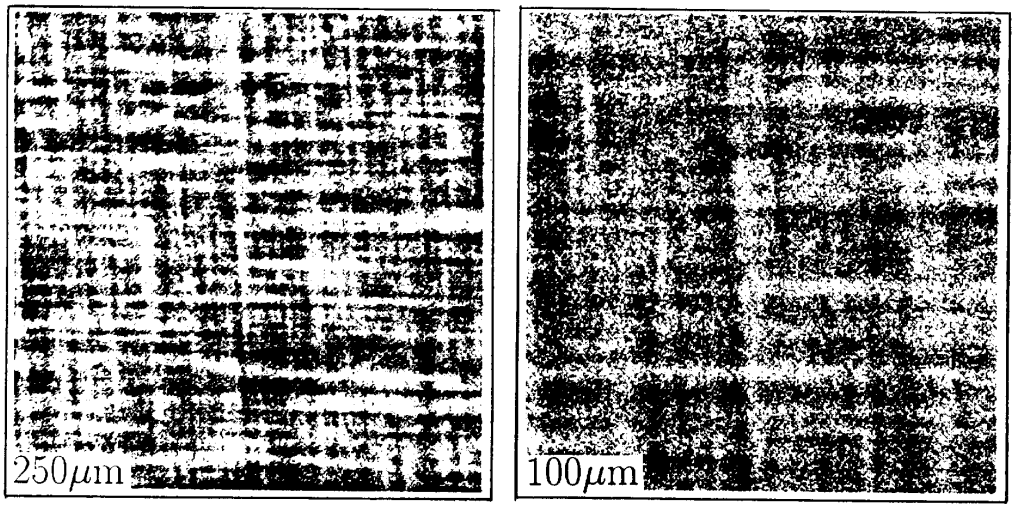

INITIAL RESULTS WITH A VARIABLE ENERGY POSITRON SYSTEM AT COIMBRA

A.P. de Lima, C. Lopes Gil, P.M. Gordo and M. Duarte Naia[1]
Departamento de Física da F.C.T.U.C., P-3000 COIMBRA, Portugal
[1]Secção de Física da U.T.A.D., P-5000 VILA REAL, Portugal

Abstract

The first depth profile studies using the slow positron beam constructed at Coimbra are briefly presented. An electrostatic lens system to be implemented in the magnetically guided beam is also discussed.

Introduction

The positron is a very sensitive probe for non-destructive material studies. When implanted in a material the positron is thermalised within a short time interval (order of the ps). During diffusion it can be trapped in open volume defects, like vacancies, vacancy loops or dislocations. As a consequence of the energy and momentum conservation in the annihilation process, the angular correlation and the energies of the emitted photons carry information on the electron momentum distribution at the annihilation site. Also the electron density at those sites is inversely related to the positron lifetime.

Therefore, defect-related information can be obtained from measurements of the positron lifetime, the angular correlation between the two photons or the Doppler broadening of the annihilation radiation.

In a positron beam system it is possible to implant monoenergetic positrons on the surface of the material. For that, energetic positrons from e.g. a radioactive source are thermalised in a moderator with a negative positron work function. Positrons remitted from the moderator surface, with energies of 2-3 eV and with very low energy spread, are then guided and accelerated to form a well collimated beam on the sample to be studied. The implantation depth may be controlled by varying the beam energy and the depth profile of the defects on the sample can be determined.

In fact positron beams with energies up to 50 keV are now commonly used for the characterisation of defects in sub-superficial zones modified by electron, laser or ion beams, in thin-film coatings, epitaxially grown layers or multilayers and interfaces.

In this work we present recent results obtained in Coimbra with a magnetically guided positron beam (see Figure 1) with energies up to 30 keV. These results show the great possibilities of the technique for depth profile studies. We also present simulation results for the electron optics system to improve the quality of our positron beam.

Figure 1. Schematics of the variable energy positron system of Coimbra

A – Radioactive source
B – Moderator
C – Extraction grid
D – Sample
E – Detector
F – Ion gauge
G – Ultra-high vacuum pump
H – High voltage

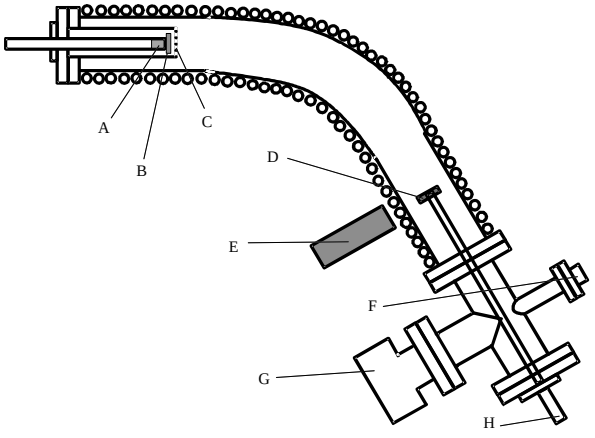

Depth profile studies

In the last fifteen years the use of slow positrons for the characterisation of defect profiles in the near surface region has been used with great success. For detailed revisions see [1,2,3]. Initially the technique was only applied to simple systems where positron attenuation length and diffusion parameters were well known. Nowadays the technique and its analysing tools are also applied to more complex systems like layered structures and semiconductors.

At Coimbra the work started with the study of treated metal surfaces and, having acquired a better knowledge of the slow positron technique, we are now studying amorphous semiconductors. We present here a resume of the results obtained.

Defects in Ni produced by Hf^+ implantation

Polycrystalline Ni samples with 99.995% purity were annealed at 950ºC during one hour before being implanted with 100 keV Hf^+ ions to doses of 10^{16} and 10^{17} ions/cm^2. The implantation profile of Hf was then determined using RBS and estimated by simulation with the program TRIM [4]. As shown in Figure 2 the profile obtained by RBS extends much deeper than predicted by TRIM. Both implantations and the RBS experiments were performed at ITN, Sacavém.

Figure 2. Comparison of the Hf^+ implantation profiles calculated with TRIM and determined by RBS

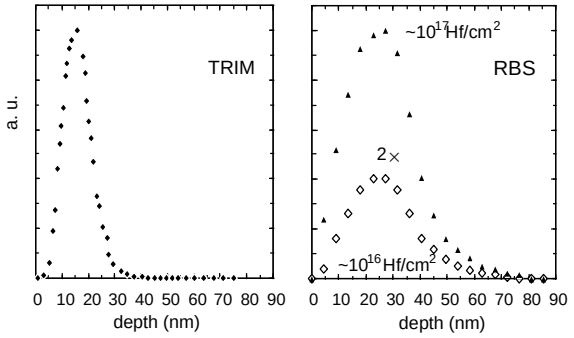

The slow positrons results on as-implanted samples show that the open volume defects are present until a depth of 300 nm, well bellow the Hf^+ implantation depth calculated by the RBS analysis.

Positron studies were then carried out after each isochronal annealing stage of the implanted samples from 100ºC until 700ºC in steps of 50ºC. The evolution of the S(E) curves for different annealing temperatures (Figure 3) clearly shows, besides the relaxation of the defects, the diffusion to the surface of the positron trapping centres. This effect, due to Hf precipitation and segregation towards the surface, was confirmed by RBS studies on the samples after the 700ºC annealing.

Laser treated Ni surfaces

Well annealed Ni, similar to the one used in the previous section, was surface melted with a 10 Hz pulsed KrF laser with 192 mJ per pulse, focused on a spot area of 0.47mm^2 on the surface. The energy density delivered per pulse on the sample was 122 kJm^{-2}. During the irradiation a scanning of the beam was performed in order to obtain a total irradiated area of 1 cm^2.

Figure 3. Evolution with the annealing temperature of the normalised S parameter for the Ni sample implanted with 10^{17} Hf^{+} ions. The data are presented as a function of the positron energy.

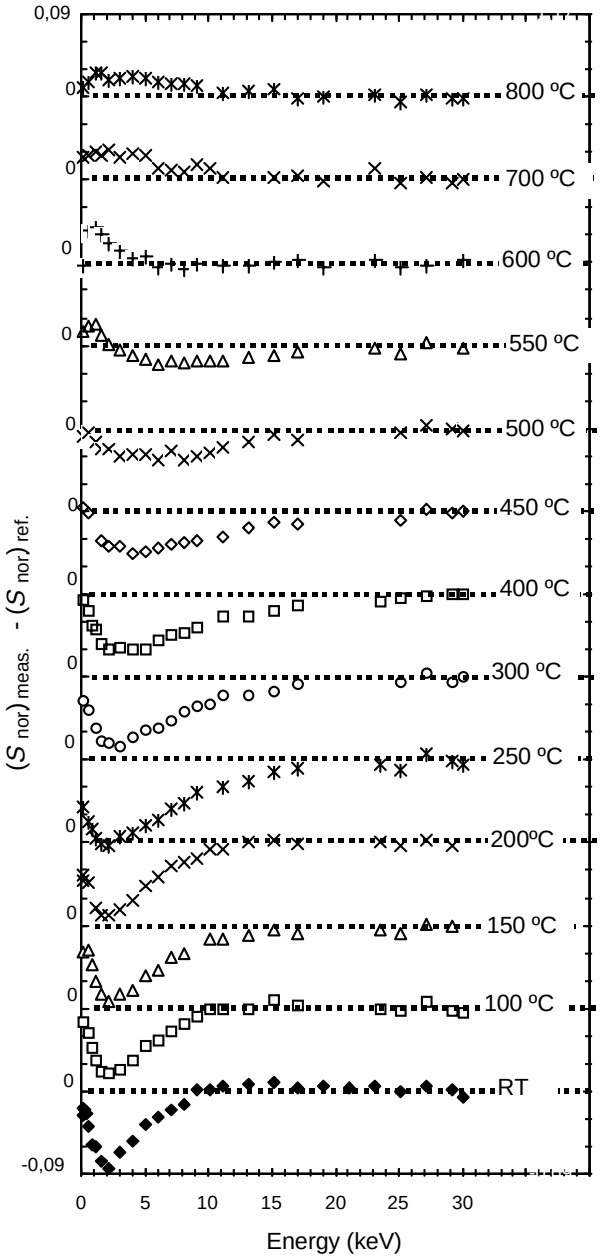

The thickness of the melted region was measured as 2 μm through SEM observations on a 45° cut on one of the samples. Electron microbeam analysis revealed the presence of oxygen in the melted zone in spite of the vacuum on the irradiation chamber.

Slow positron and classical positron measurements were performed during the successive stages of an isochronal annealing procedure of the irradiated samples until 900ºC in steps of 50ºC.

Inside the melted region the slow positron results show a high density of dislocations but no evidence for vacancies could be obtained from the evolution of the S(E) curves.

Lifetime measurements performed with conventional positrons incident on the irradiated and on the non-irradiated sides of the sample show clear evidence of vacancy clustering in the annealing stages between 300ºC and 650ºC. Figure 4 represents, as a function of the annealing temperature, the lifetimes and corresponding intensities for conventional positrons incident on the non-irradiated surface. The lifetime τ_4 = 380 ps, due to the oxide inclusions near the irradiated surface, is obviously not seen here. Through the comparison of the results for both incidences it was possible to estimate that the clustering occurs in a region with a depth of the order of 200 μm which has been heat affected by the laser irradiation.

Figure 4. Lifetime results with conventional positrons incident on the non-treated side of the Ni irradiated sample

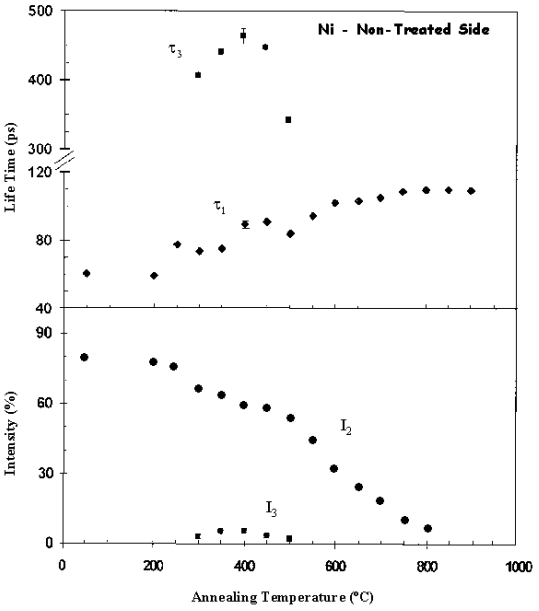

Characterisation of a-Si:H thin-films

Positron annihilation and other techniques are now being used for the structural characterisation of hydrogenated amorphous silicon (a-Si:H) and for the investigation of its correlation with production parameters like SiH_4 pressure, substrate temperature and radio-frequency power. The a-Si:H films were deposited by rf PECVD, at IST, Lisbon, on AF45 type glass and on monocrystalline silicon (c-Si) wafers. The electro-optical characteristics of the a-Si:H were determined using light transmission and electrical conductivity measurements.

Positron results in a-Si:H films of different thickness', ranging from 0.5 to 2.0 μm, deposited on AF45 glass subtract, Figure 5, show the good uniformity of the film for depths higher than tens of namometer and a quite good agreement with the values of the thickness obtained by other techniques. The fittings of the S(E) curves with VEPFIT [5] suggest the presence of internal electric fields in the film/substrate interface. To investigate that behaviour new experiments are being prepared in order to measure the dependence of the positron mobility with the strength of an applied electric fields. Using c-Si substract the correlation between the positron parameters and the electro-optical characteristics of the film for different deposition conditions are also under investigation.

Figure 5. S(E) curves obtained for a-Si:H films with different thickness deposited on AF45 glass

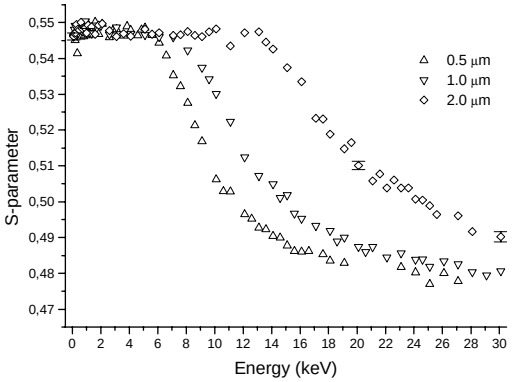

Improvements on the positron beam

The actual beam uses, as positron emitter, a ^{22}Na radioactive source which has a typical beta spectrum with 545 keV end point energy. A 4 μm tungsten foil moderator reemits, with an efficiency of 10^{-4}, the moderated positrons in a direction almost perpendicular to its surface (70% of the positrons are within a cone of 10º and 90% within 20º). The positrons are then softly accelerated by an extraction grid (≈100 V) to form the beam. The positrons are transported at low energy to the measurement zone by an axial magnetic field produced by a bent solenoid. The bend prevents the non-moderated positrons from reaching the sample. The final kinetic energy of the positrons is imposed applying a high voltage to the sample. The focusing of the beam can only be controlled through correction coils placed along the bent solenoid.

The technical simplicity of these magnetically guided systems have the drawback of leading to a large beam spot whose shape and position changes with the beam energy. The actual beam diameter varies between 3-7 mm. In order to overcome this problem we are developing a set of electrostatic lenses to be coupled to the existing magnetic system in order to produce a constant size (≈5 mm diameter) beam spot in a fixed position on the sample for the entire range of positron energies (100 eV to 30 keV) without reduction of beam intensity.

The purely electrostatic extraction and acceleration allow, according to Liouville's theorem [6], very large reductions in beam diameter. In fact the large radial momentum created during the acceleration is accompanied by the focusing of the beam; however, when electrostatic lens are immersed in an axial magnetic field the angular momentum imposed upon the beam particles prevents them from approaching the axis. To combine electrostatic focusing with magnetic transport it is important to keep radial electric fields to a minimum and, where they exist, the axial magnetic field has to be small. With these rules in mind a new focusing system was designed and investigated with the Simion [7] ray tracing program. A sketch of this system is shown on Figure 6 and the voltages and simulation parameters are presented on Table 1.

The basic idea is to extract the beam from the magnetic field with an electrostatic lens placed at the end of the solenoid. The focusing on the sample with the desired energy and fixed position is then obtained with a set of electrostatic zoom lenses in the magnetic free zone. For the acceptable configuration a compromise had to be made in order to find an extraction lens neither too weak to blow the beam nor so strong that would prevent very low energy positron experiments. The proposed configuration also conserves the beam intensity for the desired energy range.

Figure 6. Sketch of the electrostatic focusing lens system; positron trajectories are also presented

A – Extraction electrode *C – Acceleration electrode*
B– Control electrode *D – Sample*

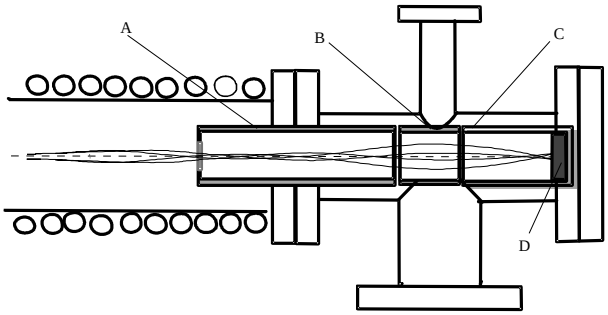

Table 1. Results of a simulation for the lens system as represented in Figure 6

The values used for the constant parameter are:
Axial magnetic field: B = 60 Gauss; Extraction grid voltage: 100 V; Voltage of electrode A: -3000 V

Acceleration potential [-V]	Focusing potential [-V]	Spot diameter [mm]	
		for ±10º emission	for ±90º emission
100	600	4.1	4.1
300	500	4.1	4.4
500	480	4.0	4.2
1000	500	3.6	4.1
3000	750	4.3	4.4
5000	1000	4.1	4.2
10000	1700	3.8	4.2
20000	3500	3.5	4.2
30000	7000	2.6	4.0

Conclusion

Due to the high sensitivity of positrons to open volume defects the variable energy positron beams are a unique technique for depth profiling studies in near surface regions. In this paper the importance of the technique is emphasised through the application to treated metal surfaces and to semiconductor amorphous films. The importance of the results provided by other nuclear techniques such as RBS was also made evident; in particular, complementary information relative to deeper regions inside the sample, obtained with conventional positrons from radioactive sources, was discussed. A modification to be introduced in the system presently used in Coimbra for the purpose of improving the quality of the beam was also presented.

REFERENCES

[1] P.J. Shultz and K.G. Lynn, *Rev. Mod Phys.* 60, 701 (1988).

[2] P. Asoka-Kumar, K.G. Lynn and D.O. Welch, *J. Appl. Phys.* 76, 4935 (1995).

[3] A.P. de Lima, C. Lopes Gil, in "Nuclear Physics of our Times", ed., A.V. Ramayya, World Scientific (1992) 288.

[4] J.F. Ziegler, J.P. Biersach and U. Littmark, *Stopping and Range of Ions in Solids* (*TRIM*), Pergaman, New York (1995).

[5] A. van Veen, H. Shut, J. de Vries, R.A. Hakvoort and M.R. IJpma in *Slow Positron Beams for Solids and Surfaces*, eds., P.J.Shultz, G.R. Massoumi and P.J. Simpson, AIP, New York (1995).

[6] K.F. Canter, in *Positron Spectroscopy of Solids*, eds., A. Dupasquier and A.P Mills, Jr., North-Holland, Amsterdam (1995).

[7] D.A. Dahl and J.E. Delmore, *EGG CS-7233 Rev. 2, Informal Report*. Idaho National Engineering Laboratory (1988).

SESSION V

Application of Ion Beams Including Radioactive Beams, Part I

Chairman: J.C. Soares

THE USE OF ION BEAM ANALYSIS IN THE SYNTHESIS OF MATERIALS: A REVIEW OF THE DETERMINATION OF LIGHT ELEMENTS BY HIGH-ENERGY RESONANT BACKSCATTERING

Michael Nastasi
Materials Science and Technology Division
Los Alamos National Laboratory

Abstract

The following subjects will be discussed:

- ion synthesis of materials and plasma immersion ion processing;
  - plasma immersion ion processing;
- Rutherford Backscatting Spectrometry (RBS);
- High Energy Backscattering Spectrometry (HEBS).

A series of examples will also be provided.

PIIP technology

PIIP is a low-cost, non-line-of-site surface modification process that makes plasma-based deposition practical on a large scale. PIIP technology:

- is partly immersed in a plasma;
- uses organometallic gases ($Ti[N(CH_3)_2]_4$;
- uses ion implantation to:
  - increase coating adhesion;
  - control coating stress;
- produces coatings with:
  - superior adhesion;
  - thickness of tens of μm.

Plasma Immersion Ion Processing (PIIP): The next generation ion beams materials process

What is PIIP?

The Plasma Immersion Ion Processing (PIIP) is:

- a plasma-based synthesis approach;
- uses energetic metallic and metalloid ions;
- combines the benefits of ion implantation and ion beam deposition;
- is not limited by thermodynamics;
- a process by which plasmas are derived from volatile organometallic complexes:
  - $M[N(CH_3)_2]_4$ M = Ti, Zr, Hf, Sn, Si;
  - $M[CH_2C(CH_3)_3]_4$ M = Ti, Zr, Hf, Cr;
  - $B_3N_3H_6$.

PIIP is an evolution of Plasma Source Ion Implantation (PSII). Possible coatings include:

- metal nitrides, carbides, oxides, borides;
- metal carbonitrides, oxynitrides, boronitrides, etc.;
- BN, BC_4 and ternary combinations of B-C-Ti, B-C-N, B-N-Ti, etc.

PIIP structures

PIIP creates a graded interface as well as graded multi-layers.

The PIIP process

The PIIP process can be broken down to the following three steps:

1) **Pre-deposition implantation** – promotes coating adhesion by creating a composition gradient intimately mixed with the original surface.

2) **Deposition** – microstructure and composition are controlled by plasma chemistry, bias, gas mixture and pressure.

3) **Ion irradiation to reduce stress** – as deposition proceeds, stress increases, and periodic ion irradiation processes can reduce stress and increase allowable thickness of an adherent coating.

Industrial pull

PSII/PIIP won a 1997 R&D 100 Award, and PIIP technology has been highlighted in several magazines and news services, such as *Advanced Manufacturing Alert*, *Tech Alerts* (Construction Industry Manufacturer's Association) and the *Design News Technology Bulletin*. A partial list of current and interested customers includes GM, Ford, Fiat, Harley-Davidson, Boeing, Pratt & Whitney, GE, Kennametal, AO Smith and DuPont.

GM Die for PSII treatment in CTX

The GM Die for PSII treatment in CTX can be characterised as follows:

- 2600 lbs.;
- full-scale tool:
  - controlled experiment;
  - 1/2 masked;
- being used in production:
  - long-term test;
- nitrogen implant into Cr plated surface;
- $4\times10^{17}/cm^2$ retained dose.

PSII/PIIP research for industrial applications

The LANL PSII/PIIP facility can be characterised as follows:

- test processing of >1000 piston surrogates;
- very large scale target (>16 m^2);
- complex system involving plasma physics, plasma chemistry and material science.

Ion Beam Materials Laboratory

The Ion Beam Materials Laboratory allows the capability to perform:

- ion beam analysis;
- microprobe
- ion implantation;
- *in situ* ion implantation/analysis;
- T of F.

Figure 1. The Ion Beam Materials Laboratory

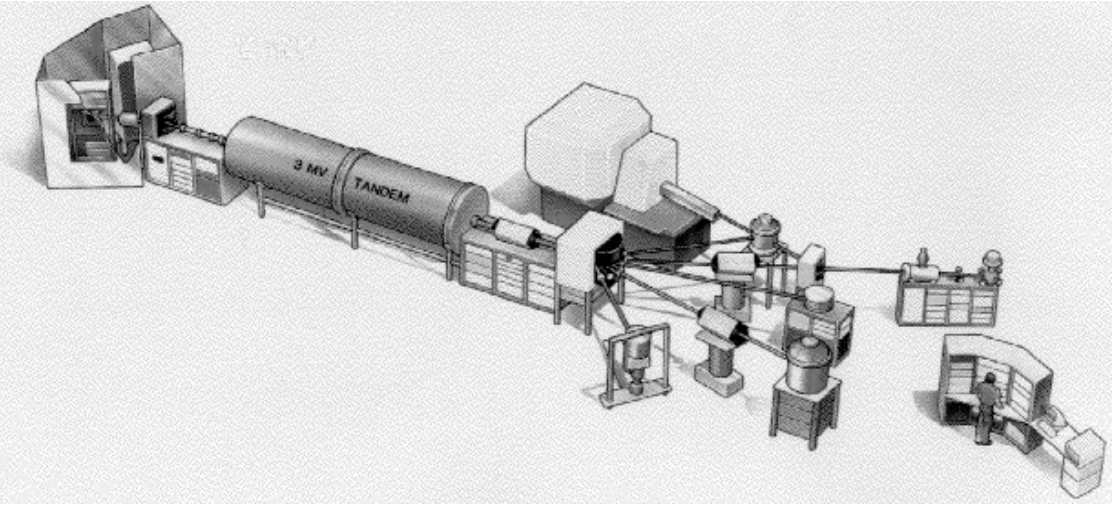

Alpha particle Rutherford Backscattering Spectrometry (RBS)

Characteristics of alpha particle Rutherford Backscattering Spectrometry (RBS) are as follows:

- incident energy below 2.2 MeV;
- particles scattered at angles near 170°;

- cross-sections well-known and can be calculated;
- stopping cross-sections optimised;
- low sensitivity to the light elements.

Figure 2. RBS example

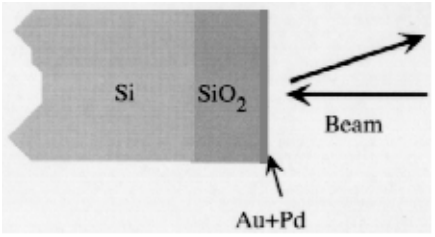

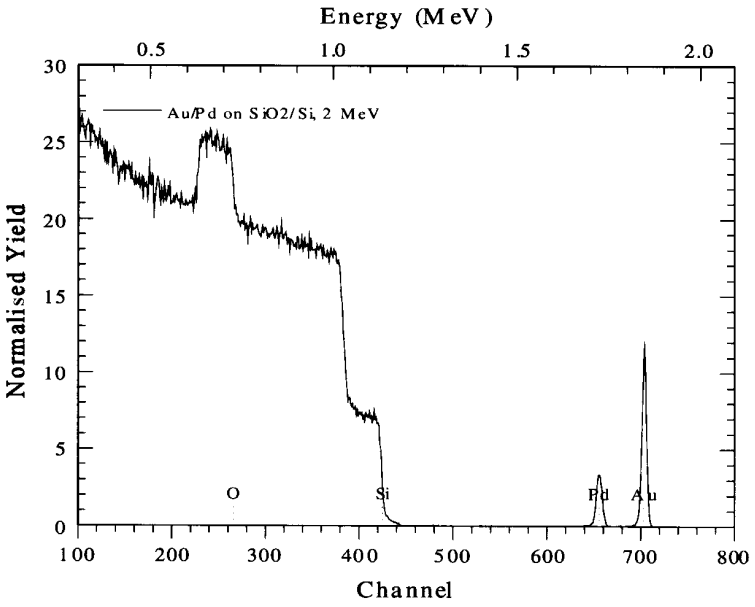

Figure 3. RBS example + fit

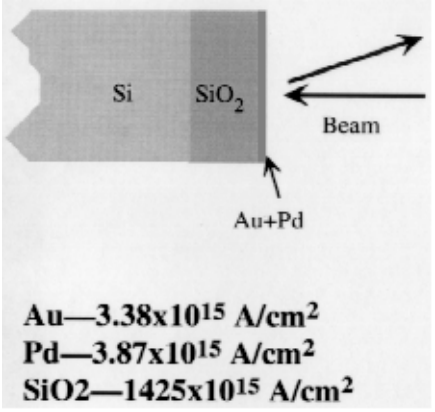

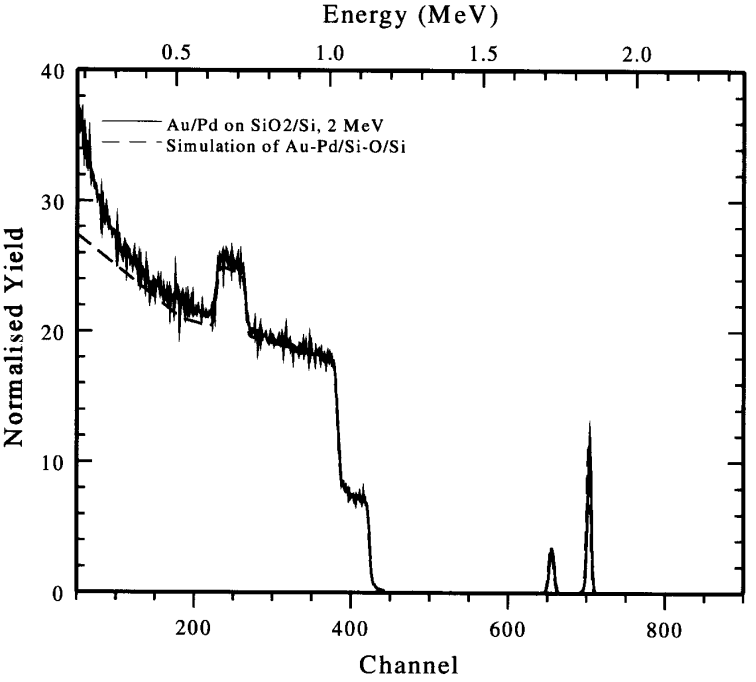

High-Energy Backscattering

Characteristics of High-Energy Backscattering include:

- signal strengths many times larger than RBS;
- detection of light elements in presence of large backgrounds from high-z substrates;
- better mass separation of elements;
- cross-sections must be measured;
- larger accelerator.

High-Energy Backscattering has several disadvantages, such as:

- larger accelerator;
- unwanted nuclear reactions;
- non-uniform background from light elements;
- activate samples;
- prompt radiation (neutrons).

Figure 4. Example of High-Energy Backscattering

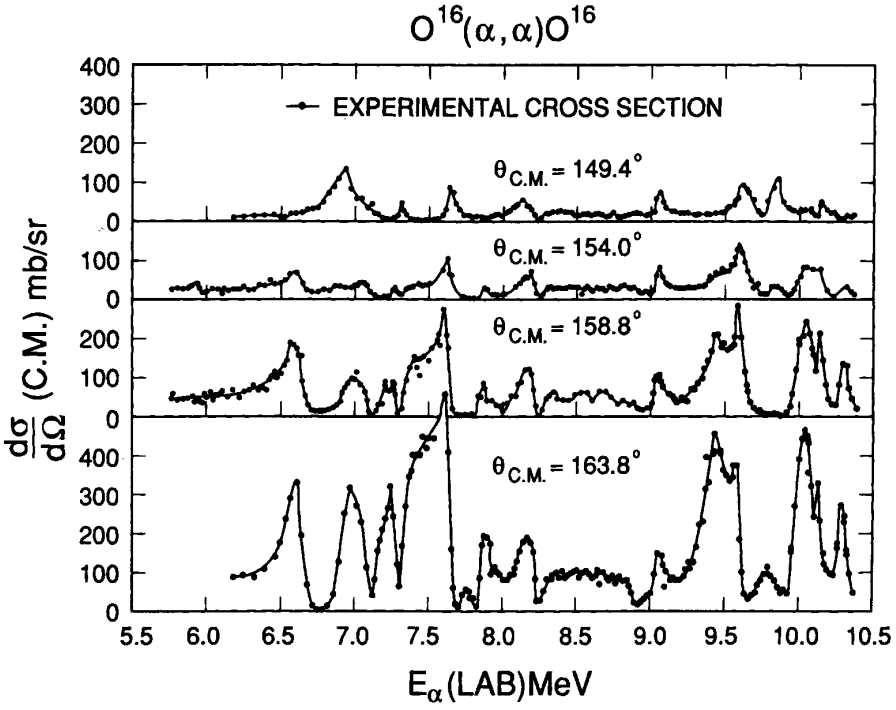

Figure 5. High Tc film – example of oxygen analysis

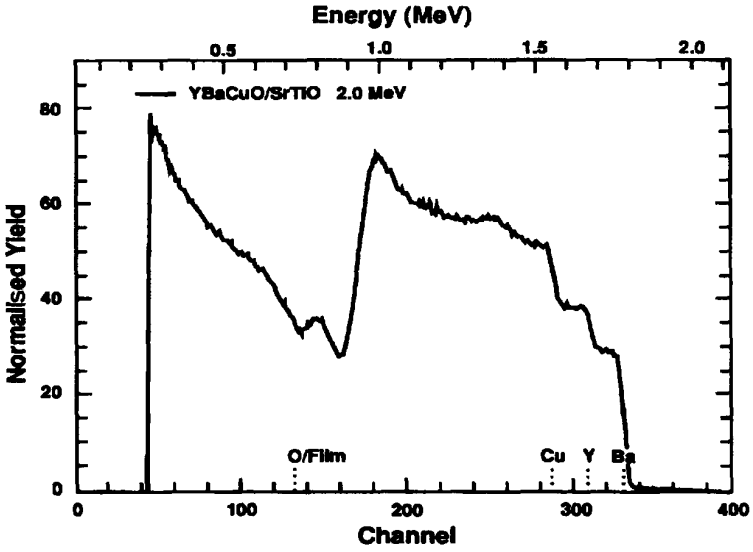

Figure 6. High Tc film – example of oxygen analysis

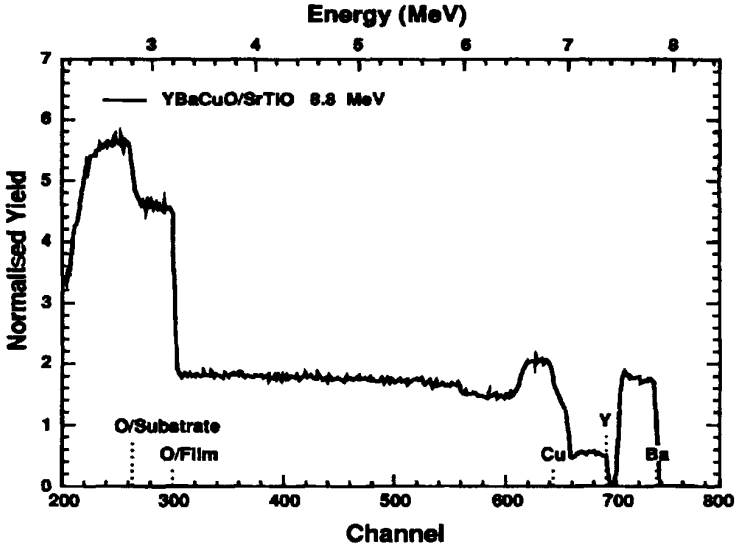

Table 1. Elements easily detected by high-energy alpha resonances *

Element	Energy	Enhancement
Boron-11	6.6 MeV	90x
Carbon	3.5 and 6.6 MeV	6x, 50x
Nitrogen	8.8 MeV	70x
Oxygen	7.6 and 8.8 MeV	175x, 25x

** Many other possibilities exist.*

Figure 7. Sample for ^{11}B cross-section measurement

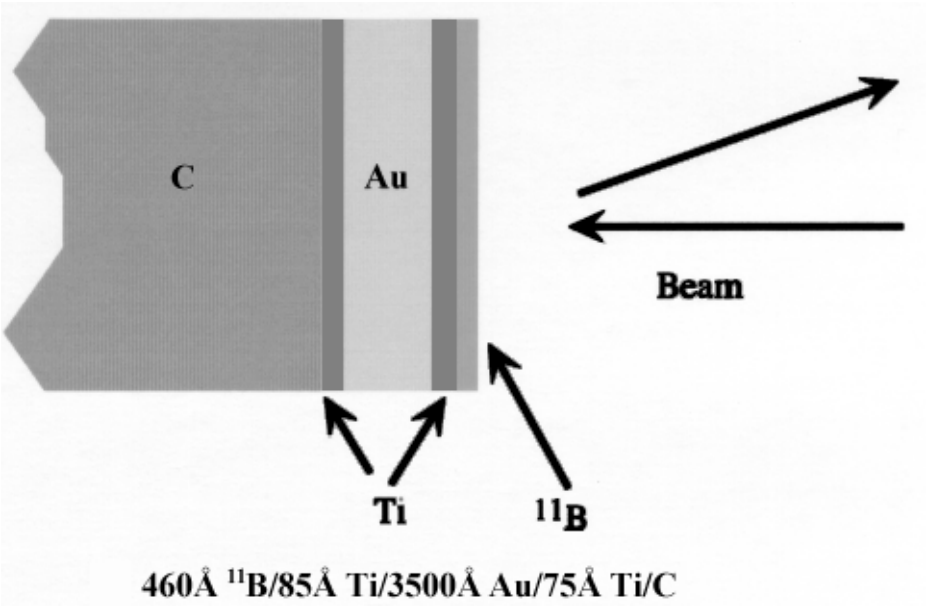

Figure 8. Simulations of ^{11}B/Au/C spectra at 2 and 6.6 MeV

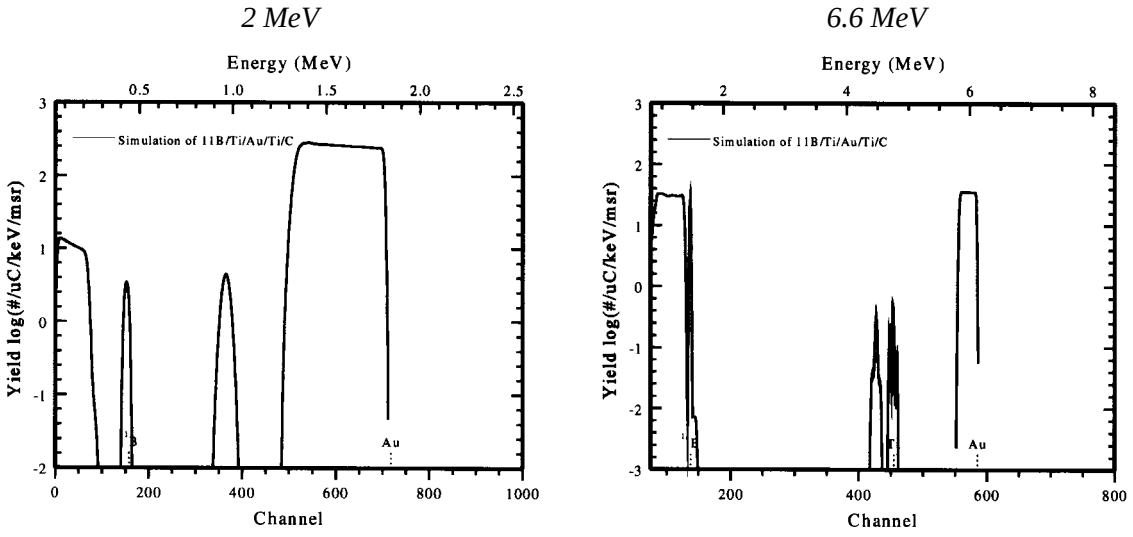

Figure 9. Cross-section ratio

$$\left(\sigma_B(E)/\sigma_R\right) = \frac{\left(A_B/A_{Au}\right)_E}{\left(A_B/A_{Au}\right)_R}$$

Figure 10. C/B on Mo – 2 MeV

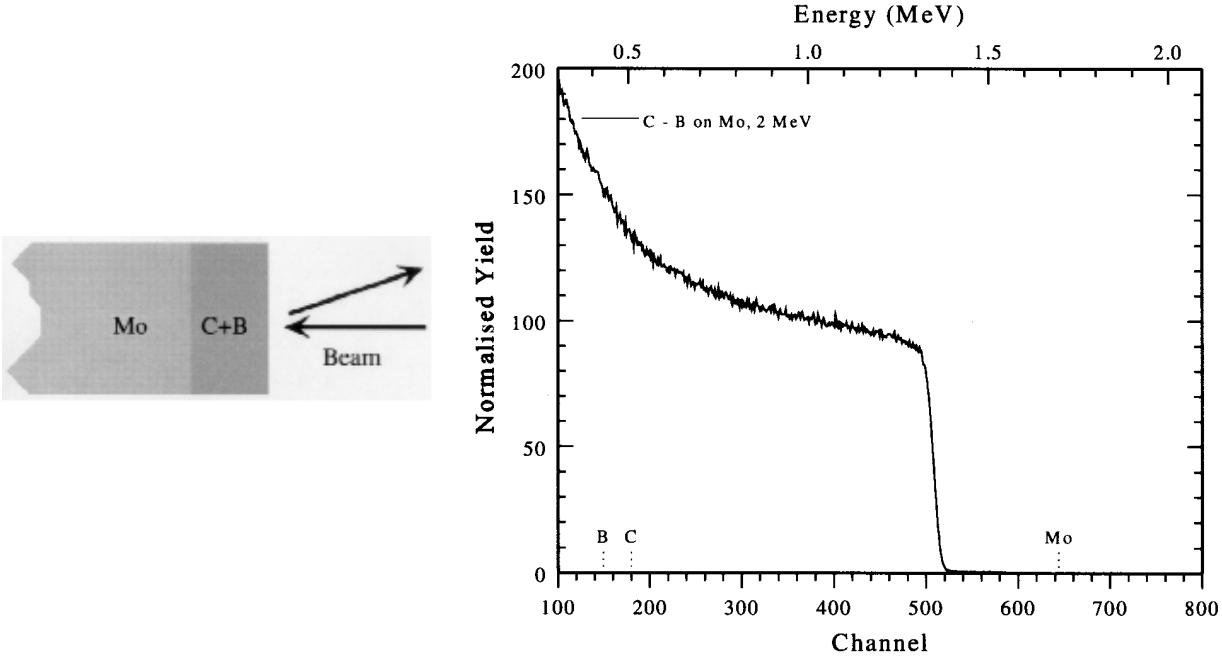

Figure 11. C/B on Mo – 3.5 MeV

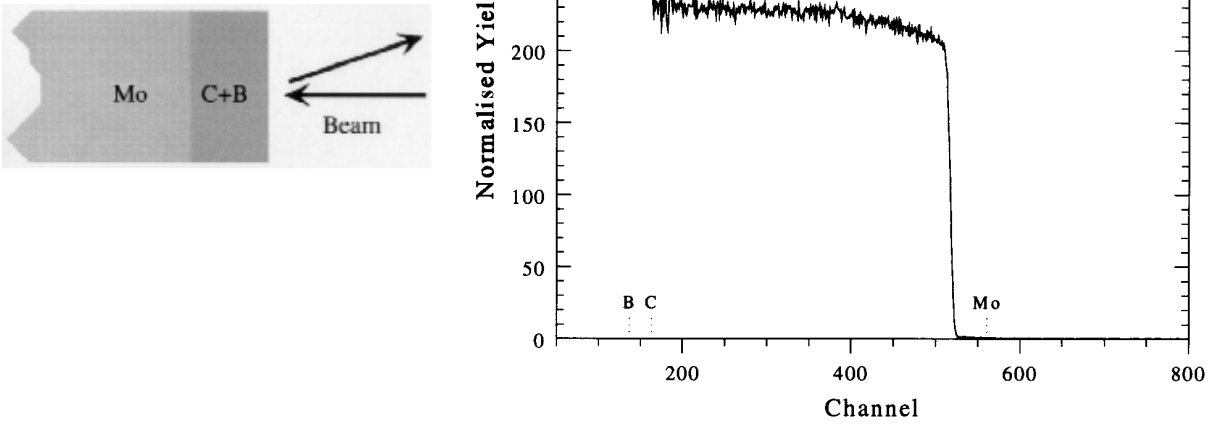

Figure 12. C/B on Mo – 6.6 MeV

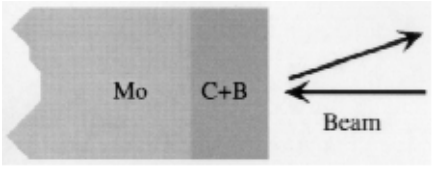

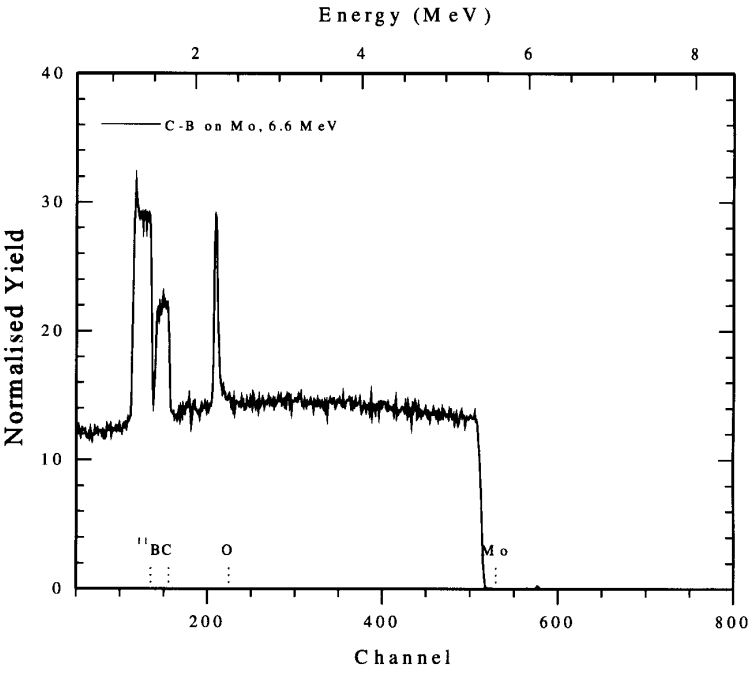

Figure 13. C/B on Mo – 7.6 MeV

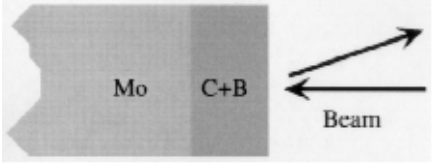

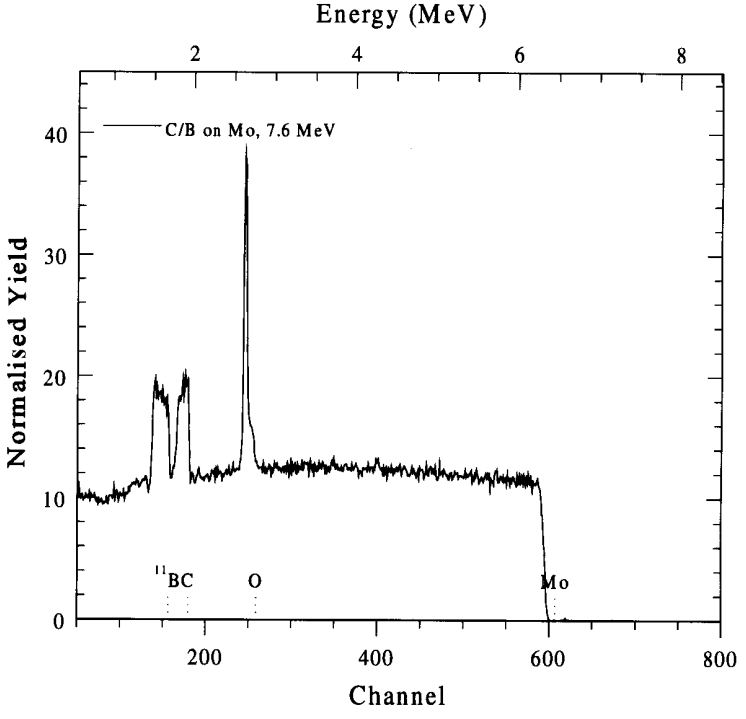

Figure 14. C/B on Mo – 8.8 MeV

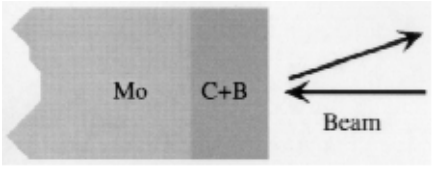

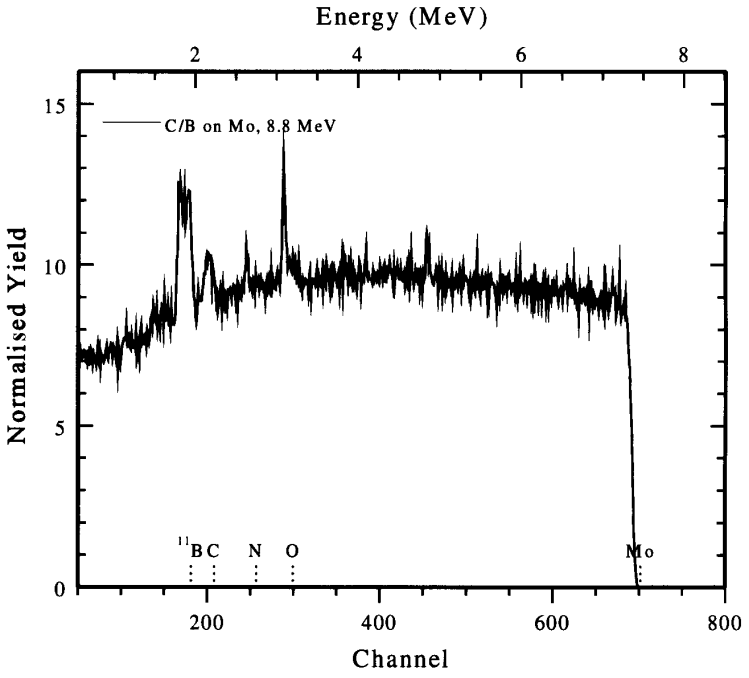

Figure 15

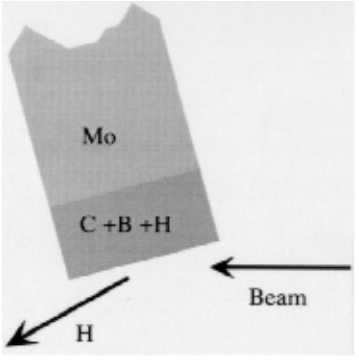

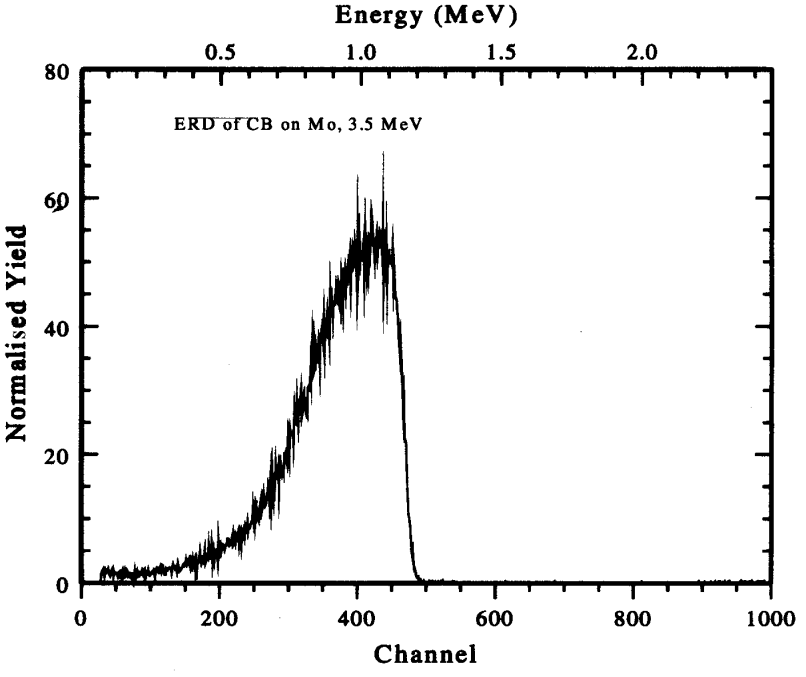

Figure 16. C/B/N on Mo – 6.6 MeV

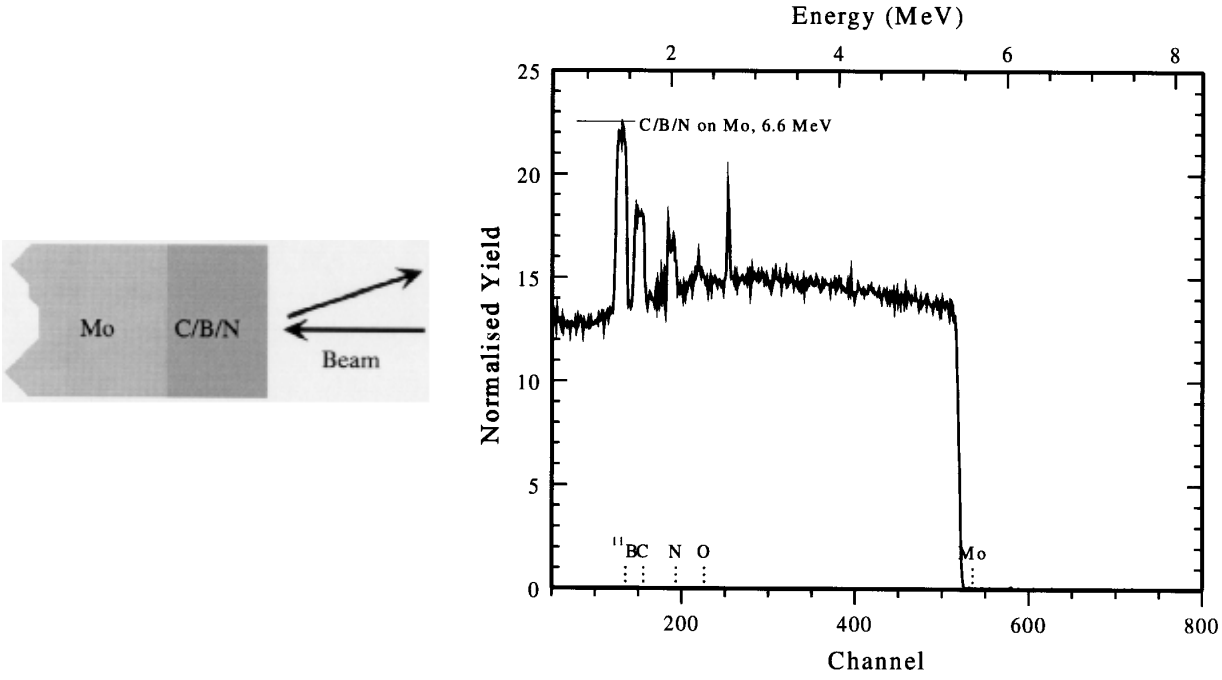

Figure 17. C/B/N on Mo – 8.8 MeV

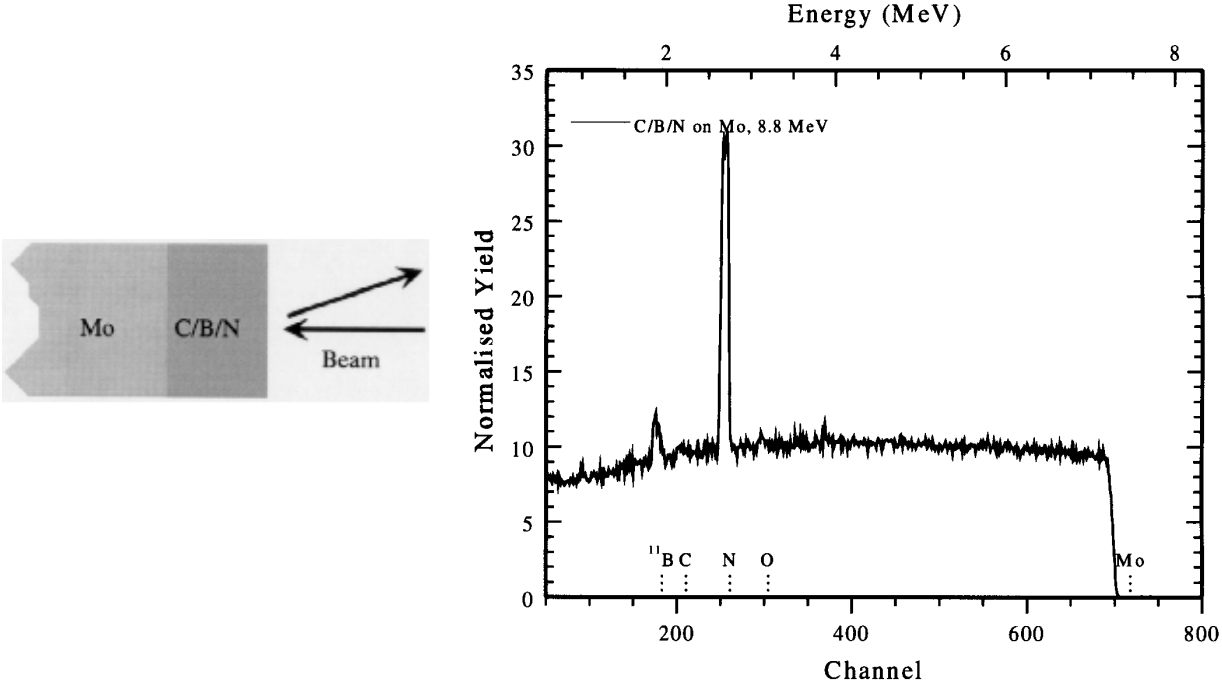

Figure 18. Au/Pd on SiO_2 – 7.6 MeV

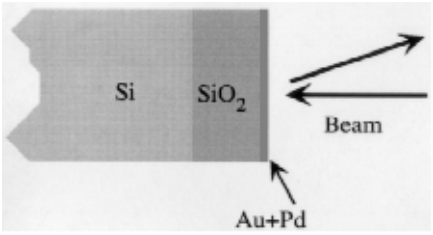

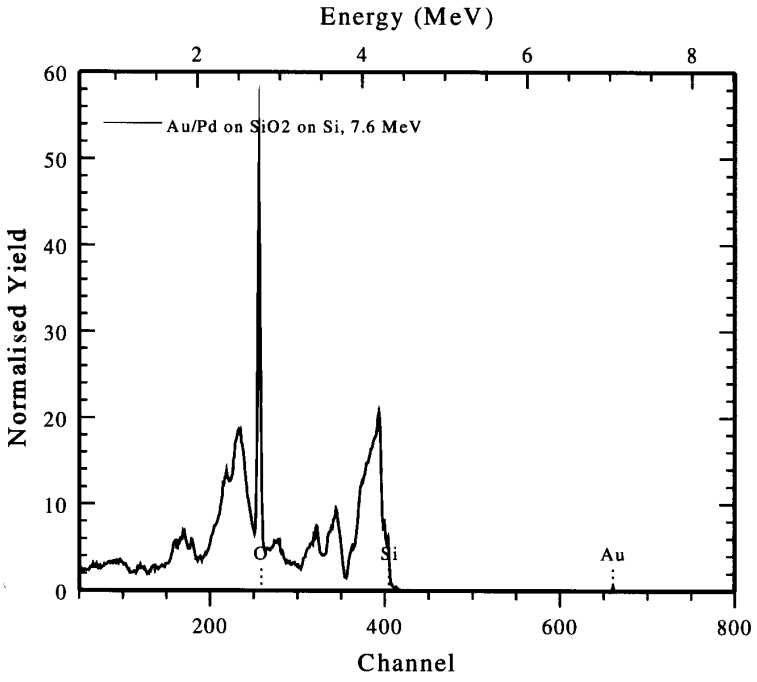

PORE STRUCTURE DETERMINATION IN POROUS SILICON BY RESONANT BACKSCATTERING SPECTROMETRY

Ferenc Pászti, Edit Szilágyi, Asrama Manuaba
KFKI-Research Institute for Particle and Nuclear Physics
P.O.B. 49, H-1525 Budapest, Hungary

Zsolt Endre Horváth, Gábor Battistig, Zoltán Hajnal, Éva Vázsonyi
KFKI-Research Institute for Technical Physics and Materials Science
P.O.B. 49, H-1525 Budapest, Hungary

Abstract

In backscattering spectroscopy measurements at ion energies slightly above the energy where a sharp resonance exists in the elastic scattering cross-section, a characteristic resonance peak appears in the energy spectra of the backscattered particles. Unlike homogeneous samples, where the position and width of this peak are mainly determined by the experimental set-up, for porous materials the peak width depends on the structure of the sample, as well. This effect is caused by fluctuations in the stopping power along the trajectories of individual ions. Using the 3045 keV resonance of the $^{16}O(\alpha,\alpha)^{16}O$ reaction for analysing oxidised porous silicon samples, it was demonstrated both experimentally and theoretically that i) the widening of the resonance peak is easily observable, ii) its variation with the tilt angle is closely related to the morphology of the samples and iii) it can be applied to determine morphological details, as porosity, average pore diameter and anisotropy of the pore directions.

Introduction

Since ions neither loose energy nor suffer large angle scattering in cavities embedded in porous samples, it was generally accepted that backscattering spectrometry (BS) [1] cannot be sensitive to the pore structure of these samples. It was shown recently, however, that because the individual ions on their way in and out penetrate fluctuating amounts of material, an extra, so-called "structure induced energy spread" appears in the energy spectra of the backscattered particles [2,3]. This effect was also demonstrated for resonant nuclear reactions, like $^{15}N(p,\alpha\gamma)^{12}C$ [4]. A short review together with theoretical explanations is given in Ref. [5].

In this article it will be shown how the structure induced energy spread appears in resonant BS measurements of different kinds of partially oxidised porous silicon (PS) samples. Its application to characterise porous structure and the structural changes caused by ion implantation is also presented. The well known resonance of $^{16}O(\alpha,\alpha)^{16}O$ elastic backscattering at 3045 keV incident energy was applied for the measurements. In this case the effect can be observed without special preparations, since the measured signal is not connected to an interface and the internal surface of PS get oxidised even at ambient atmosphere and room temperature.

Experimental

The following kinds of PS samples were prepared by anodic etching of single crystalline silicon wafers in an electrolyte containing HF (50%), ethanol and water [6].

- *Spongy* sample: fine pores of ~3.6 nm average diameter are randomly distributed in the sample.
- *Columnar* sample: straight pores of larger diameter run predominantly parallel to the <100> axis of the sample, hence parallel to each other and perpendicular to the surface in <100> Si substrates (see larger depths in Figure 1).
- *Mixed* type sample: the pores run more or less parallel to each other, but with a large fluctuation in their directions, representing an intermediate structure between the previous two cases.

Conditions of sample preparation, the main characteristics of the samples including porosity, P, (the volume fraction occupied by pores) and the average inter-pore distance, D, are listed in Table 1.

After porous layer formation and rinsing in de-ionised water, the electrolyte was changed to 0.1 Mol KNO_3 and the samples were anodically oxidised at 2 mA/cm^2 current density. The composition of the oxidised samples (given in Table 1) was determined from BS spectra taken at 60° tilt. As it can be seen, while the spongy layer almost completely transformed into SiO_2, the other two samples suffered only partial oxidisation. The morphology of the samples probably remained unchanged during the oxidisation, only their porosity decreased according to the density ratios of Si and SiO_2. The estimated new porosity values are also given in the table.

BS measurements of the above samples were carried out in a two-axis goniometer chamber under high vacuum (~1×10^{-4} Pa) using MeV energy $^4He^+$ ions provided by a 5 MeV Van de Graaff accelerator. The incident ion beam was collimated to a 1×1 mm^2 spot with a divergence of ~0.05°.

Figure 1. Cross-sectional TEM micrograph taken on the N implanted PS sample

From top-right to bottom-left one can clearly see the following features: some residual glue, compact layer at the surface, partially compacted region with curved pore walls and unchanged columnar structure of straight parallel pores.

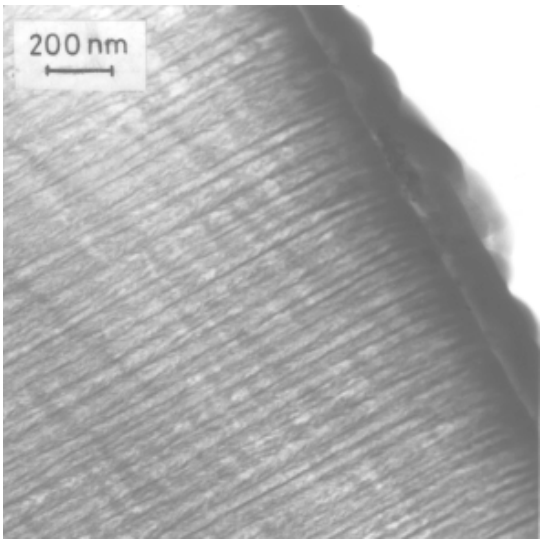

Table 1. Main manufacturing conditions and characteristics of the un-implanted PS samples

Sample	Spongy	Columnar	Mixed
Manufacturing			
Wafer type	6 Ωcm p <100>	0.003 Ωcm p+ <100>	0.01 Ωcm p+ <111>
Electrolyte HF:water:etanol	1:0:0	1:1:2	1:1:2
Current density	10 mA/cm^2	38 mA/cm^2	38 mA/cm^2
Anodisation time	30 min	8 min	8.5 min
Characteristics before oxidation:			
Pore distribution	spongy	columnar	mixed
Porosity (*P*)	63%	66%	76%
Thickness	17 μm	12 μm	9 μm
Average pore distance (*D*)	~4.4 nm	27 nm	18 nm
Characteristics after oxidation:			
Composition	$Si_1O_{1.85}$	$Si_1O_{1.16}$	$Si_1O_{0.80}$
Assumed porosity	21%	42%	66%

The ion energy (3145 keV) was set at 100 keV above the resonance in the $^{16}O(\alpha,\alpha)^{16}O$ elastic scattering. Therefore, ions contributing the resonance peak in the obtained spectra had to loose this ΔE=100 keV excess energy prior to their scattering. This corresponds to 0.521 μm in compact Si and 0.465 μm in compact SiO_2, which is equivalent to 0.6-1.5 μm path length in the investigated PS materials. The energy distribution of backscattered ions was determined by a surface barrier detector of 15 keV energy resolution. The detector was placed at Θ=165° scattering angle in Cornell geometry (in the plane defined by the beam and the tilt axis of the goniometer) and had a solid angle of 2.5 msr. The obtained energy spectra were evaluated by the RBX code [7]. First the samples were oriented taking advantage of their compact regions remaining intact during the PS formation, then measured at various tilt angles along an azimuth direction that included the main crystal axis. A BS measurement was carried out also on a compact SiO_2 sample at 60° tilt.

The collection time for each spectra was ~5 min (10 μC collected dose), so a complete angular scan lasted ~2 hours for each sample.

Prior to BS measurements, an oxidised columnar sample was subjected to *in situ* ion implantation with 0.5 MeV $^{14}N^{+}$ ions at a grazing incidence of 86° with a fluence of 6×10^{15} ions/cm^2. A cross-sectional TEM (transmission electron microscopy) micrograph of the implanted sample is shown in Figure 1. The predicted depth distribution of the induced lattice damage as calculated by TRIM code [8] for compact Si is given in Figure 2. The sample was measured under conditions similar to those previously described, but with three different excess energies of 15, 50 and 100 keV. In the figure the depths where the above excess energies would be lost in compact Si are also indicated.

Figure 2. Calculated depth distribution of lattice damage caused by 500 keV $^{14}N^{+}$ ions bombarding compact Si at a grazing angle of incidence of 86°. Those depths, where $^{4}He^{+}$ ions of the indicated energy slow down to the resonance energy, E_r, are also indicated.

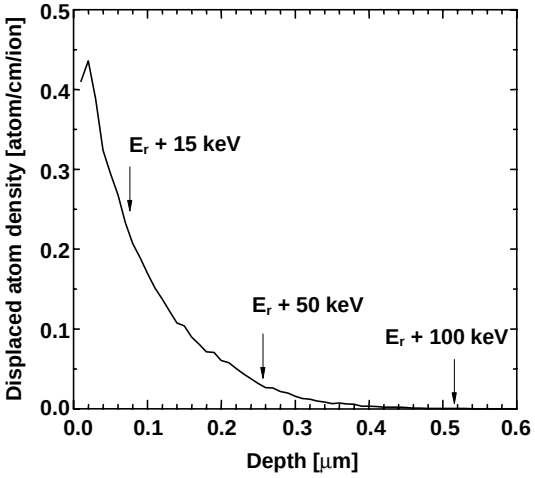

Theoretical considerations

It is difficult to describe analytically the effect of the porous structure on the backscattering spectra, because it depends not only on the porosity and the average interpore distance, but also on the shape or size distribution of the pores. To take into account all these properties, the actual paths of the individual ions have to be followed by Monte Carlo type calculations, for example using the RBSMAST code [2]. The following theoretical treatment will be rather rough, it can just help to understand the experimental results.

Let us discuss first the case of the un-implanted columnar sample. The ions first have to slow down from the incident energy, E_0, to the resonance energy, E_r. This $\Delta E=E_0-E_r$ excess energy will be lost by the individual ions at various depths (see Figure 3). The distribution is characterised by the average depth $\bar{x}$ and the depth spread, Δx.

$$\bar{x} = \frac{\Delta E \cos\alpha}{(1-P)S_{in}} \tag{1}$$

Here, S_{in} is the average stopping power of the incoming ions in the material forming the pore walls and α is the tilt angle of the sample. In most cases, one might assume that α coincides with α', the angle between the direction of the incident ions and the pores.

Figure 3. Schematic drawing of the mechanism responsible for porosity induced effects in a columnar structure

Incident ions of energy E_0 slow down to the resonance energy, E_r, at fluctuating depth, hence after the scattering event they have to travel various path lengths outward, resulting in an energy spread. The fluctuating amount of wall material crossed along the outward path even for ions scattered at the same depth also contributes to the energy spread.

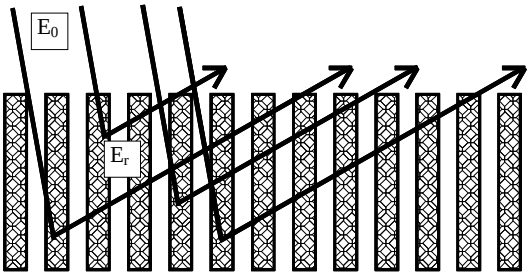

Δx depends mainly on the average number of the pores crossed by the ions, N, and on the average distance that the ions travel in each crossed pore, L_{path}:

$$\Delta x \approx \sqrt{N} L_{path} \cos\alpha \approx \sqrt{N}\sqrt{P} D_{path} \cos\alpha \tag{2}$$

where D_{path} is the average interpore distance along the ion track, which, for columnar samples

$$D_{path} = \frac{D}{\sin\alpha'} \tag{3}$$

where D is the interpore distance. Furthermore:

$$N \approx \frac{\Delta E}{(1-P) S_{in} D_{path}} \tag{4}$$

Along the outward path of scattered ions Δx will transform into an energy spread which is related to the structure induced fluctuations along the inward path:

$$\Delta E_{in} \approx \frac{\Delta x \, S_d (1-P)}{\cos\beta} \tag{5}$$

Here S_d is the stopping power at the detected energy and β is the angle between the surface normal and the direction of the detector. In Cornell geometry $\cos\beta = \cos\alpha \cos(\pi-\Theta)$. Combining Eqs. 2-5 we get:

$$\Delta E_{in} \approx \sqrt{\frac{\Delta E D P (1-P)}{S_{in} \sin\alpha'}} \frac{S_d}{\cos(\pi-\Theta)} \tag{6}$$

Eq. 6 describes how the fluctuations along the inward path contribute to the "width curve" (the width of the resonance peak as a function of tilt angle). This expression has a singularity at $\alpha' = 0°$ and decreases continuously with increasing tilt angles. We will see, that at $\alpha' = 0°$ a special effect appears, resulting in that ΔE_{in} does not increases to infinity, instead, it reaches its maximum around a tilt angle where the average number of the crossed pores is ~1, i.e. where $\sin\alpha'_{max} \approx S_{in}(1\text{-}P)D/\Delta E$. The maximum value at this angle is:

$$\Delta E_{in}^{max} \approx \frac{\sqrt{P}\Delta E S_d}{S_{in} cos(\pi - \Theta)} \tag{7}$$

For the un-implanted columnar sample we get $\Delta E_{in}^{max} \approx 100$ keV at $\alpha'_{max} = 1.6°$, and $\Delta E_{in} \approx 19$ keV at $\alpha' = 60°$. These values are large enough to observe easily.

Similarly, an additional energy spread appears also along the outward path:

$$\Delta E_{out} \approx \sqrt{\frac{\Delta E D P(1-P)}{S_{in}\sqrt{1/cos^2(\pi-\Theta) - cos^2\alpha'}}} \frac{S_d}{cos(\pi-\Theta)} \tag{8}$$

In our case Eq. 8 gives ~34 keV for $\alpha'_{max}=1.6°$ and ~19 keV for $\alpha' = 60°$.

ΔE_{in} and ΔE_{out} are both structure induced energy spread contributions. A conventional energy spread, ΔE_{conv}, due to the finite width of the resonance, the detector energy resolution, energy straggling, etc., will also contribute to the total energy spread. One can calculate ΔE_{conv} using the DEPTH code [9], or obtain it from a measurement performed on a compact sample. In our case, both methods give $\Delta E_{conv} \approx 50$ keV. ΔE_{in}, ΔE_{out} and ΔE_{conv} can be assumed to be independent of each other, but their shapes are not Gaussian. As a rough approximation we will add them linearly:

$$\Delta E_{tot} = \Delta E_{in} + \Delta E_{out} + \Delta E_{conv} \tag{9}$$

There is still one more thing to be discussed. If the columnar sample is of good quality, i.e. the columns are really straight and run parallel to each other, at $\alpha' = 0°$ the following special effect appears. Those ions entering the pores will penetrate very deep without any interaction, hence do not contribute to the resonance peak. On the other hand, ions entering the walls will remain there and slow down to the resonance energy without resulting in structure induced energy fluctuation, i.e. $\Delta E_{in} = 0$. Therefore, in this case, a sharp decrease in the width of the resonance peak can be observed, hence, a sharp valley appear in the width curve. The width of this valley can be approximated as:

$$\Delta\alpha \approx 2Arctg\left(\frac{d}{\Delta E/S_{in}}\right) \tag{10}$$

where $d \approx \left(1-\sqrt{P}\right)D$ is the thickness of the pore walls. For the columnar sample, we obtain $\Delta\alpha \approx 2.2°$. The appearance of the valley will cancel the singularity at 0° tilt and lead to a maximum at α'_{max}. The depth of the valley strongly depends on the regularity of the columnar structure, e.g. in the mixed sample the valley will not appear at all.

To follow the above processes in the un-implanted columnar sample, detailed calculations were performed by RBSMAST. Figure 4 shows the evolution of the resonance peak as a function of tilt angle. Near 0° a sharp peak appears, then, while its amplitude decreases, a second peak forms at a lower energy. This second peak continuously sharpens and, correspondingly, increases in amplitude. At intermediate angles (e.g. 1.2°) the two peaks coexist. Please note that both peaks stand at fixed positions, only their width and amplitude changes. We can explain this phenomenon in the following way. The sharp peak at higher energy is produced by those ions which remain in the walls until they reach E_r at a well determined shallow depth. The other peak is formed by ions crossing numerous pores inward, hence slowing down to E_r deeper, at various depths. The depth transforms into energy loss (see Eq. 5), hence the depth fluctuation causes energy spread.

Figure 4. Oxygen contribution to the spectra, simulated by RBSMAST [2] at various tilt angles

The sample was modelled by a periodic pattern of cylindrical cavities in Si, each cavity surrounded by a SiO_2 sheath. P = 42%, D = 40 nm. Oxygen surface step and selected tilt angles are indicated. Please note the competition of peaks, a sharp one at high energy and a smeared out one at smaller energies.

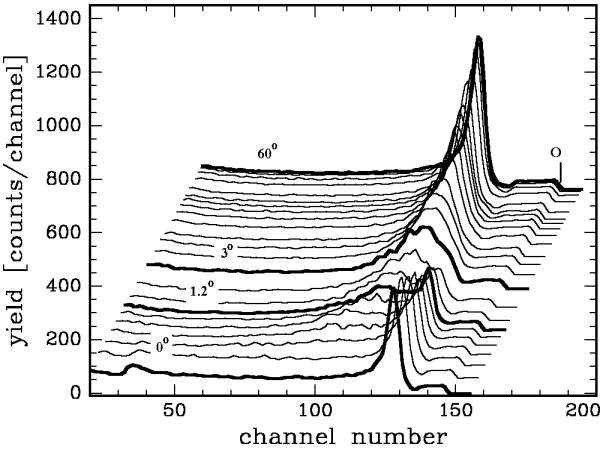

For the isotropic spongy sample D_{path} does not depends on α, hence $\alpha = \pi/2$ has to be substituted into Eqs. 6 and 8, resulting in a constant peak width.

As it is seen in Figure 1, on the implanted sample an approximately 60 nm thick layer became compacted (cf. section entitled *N implanted sample*). Such compact layers of thickness t do not contribute to the structure induced effects, hence we can take them into account simply by decreasing the excess energy:

$$\Delta E' = \Delta E - \frac{t\,S_{in}}{\sin\alpha} \tag{11}$$

Otherwise, all the statements made so far (Eqs. 6-10) remain valid, only one should substitute ΔE with $\Delta E'$.

As one can see in Figure 1, however, the case of the implanted sample is even more difficult. Under the compact layer there is a damaged region, where the porosity is decreased and the walls are bent. These effects might be taken into account by averaging both the porosity and the pore direction over the region extending from the compact layer to the depth where the ions reach the resonance

energy. Then, in Eqs. 6-10 one has to replace P by the averaged porosity and α′ by the angle measured from the averaged pore direction. Therefore, we can anticipate that for the implanted sample the valley becomes wider and shifts according to the new direction of the pore walls.

Let us see, now, how the above predicted effects will appear in the experimental results.

Results and discussions

Un-implanted samples

Two typical experimental spectra are shown in Figure 5. As can be seen, in the columnar sample the shape and the width of the resonance peak really changes in a large extent with the tilt angle.

Figure 5. Experimental spectra taken on the columnar sample at two different tilt angles

Surface steps of O and Si are indicated. The resonance peaks around channel 210 are produced by the $^{16}O(\alpha,\alpha)^{16}O$ resonance at 3045 keV. Please note the extreme wide peak at tilt 0°, where the beam is nearly parallel to the pores. In this case, the maximum of the peak is shifted towards higher energies (cf. Figure 4).

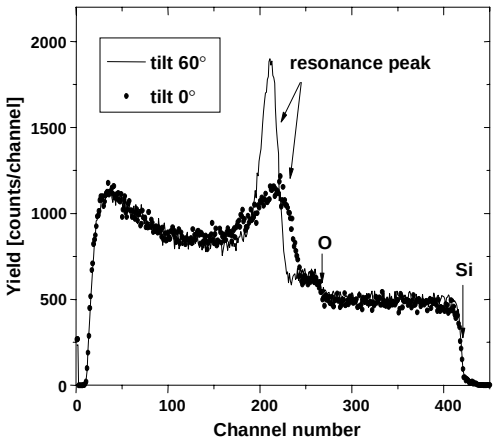

The widths of the resonance peaks were determined by fitting the spectra with the sum of a linear background and an asymmetrical peak (the sum of two Gaussian curves):

$$f(x) = Ae^{-\frac{(x-x_0)^2}{2.773\,W^2}} + Ae^{-\frac{(x-x_0+0.8W)^2}{4\times 2.773\,W^2}} \qquad (12)$$

Here A, W and x_0 are fitting parameters and the half-width of the peak is $1.775\times W$.

The experimental width curves (see Figure 6) show all the properties that were predicted in the section entitled *Theoretical considerations*. For the spongy sample the peak width remains practically constant, while for the columnar one it rises near 0° up to a value of more than twice as high as that at $\alpha = 60°$. The experimental values are close to the predicted ones. For example, the maxima are reached at ±1.0° instead of the calculated ±1.6° and the maximum value is ~210 keV instead of 184 keV, the value obtained from Eqs. 6-9. Similarly, at 60° the experimental width is 75 keV instead of 88 keV. For the mixed sample, in good accordance with the predictions, the width curve lies between the two extreme cases; it has a maximum around 0° but its central valley is missing.

Figure 6. Width curves

Symbols: experimental results, solid line without symbols: simulated curve for the columnar PS sample (RBSMAST)

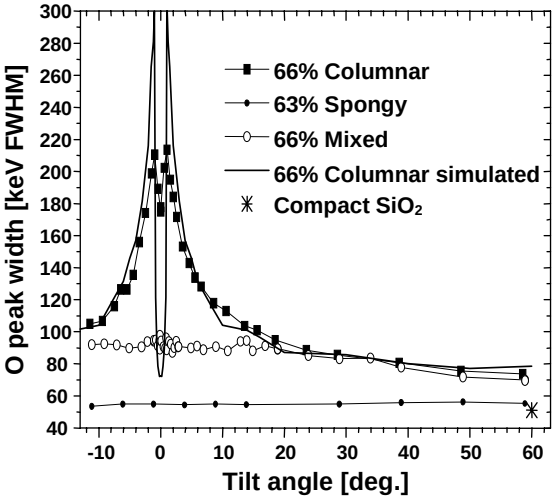

For the columnar sample we determined the width curve also from spectra simulated by RBSMAST. During the simulations, the sample was represented by an infinite lattice of cylindrical cavities, each cavity surrounded by an oxide sheath. The average pore distance, oxygen content and porosity were set according to the values given in Table 1. To avoid the problems connected to the periodic structure, the elementary cell contained four different cylinders and the sample was rotated randomly. Since RBSMAST does not contain the conventional contributions (except the shape of the resonance peak), all the calculated peak widths were increased by 38 keV, a value given by DEPTH code when excluding the 10 keV width of the resonance. As can be seen in Figure 6, the calculated width curve roughly coincides with the experimental one. It has the right shape and width and the quantitative values are close to the measured ones. The most significant difference appears around tilt 0°. The width of both the experimental and theoretical valleys coincides well with the value estimated by Eq. 10 (2.2°), the depth of the experimental valley is too shallow. This is not surprising, since the sample does not have an ideal structure (the pores are not strictly regular). Another mechanism also decreases the deepness of the valley: due to multiple scattering (also not included in RBSMAST), the ions soon or later would escape even from the walls of an ideal sample.

Please note that even at $\alpha = 60°$ the peak width for all the PS samples is significantly higher than that for the compact SiO_2. Here the anisotropy effect caused by the parallel running pores in the columnar sample is almost negligible, (~7% cf. Eq. 6). Furthermore, as it should be according to Eqs. 6 and 8, the difference is roughly proportional to $\sqrt{DP(1-P)}$.

The difference between the compact and the spongy sample might seem to be insignificant in Figure 6. When repeating the measurement several times on the same spot, however, the difference always appeared (see Figure 7), moreover, a strong beam effect could be observed. The width of the resonance peak gradually decreased towards the value of the compact oxide. This effect probably is a consequence of the densification of the porous material under ion implantation [10] and it clearly demonstrates the sensitivity of the method. On the other two un-implanted samples no beam effect was observed.

Figure 7. Peak width vs. cumulated measuring dose in the spongy sample

Solid and dotted lines represent the width for compact SiO_2 and an exponential fit to the experimental points (dots), respectively. Errors can be judged from the scattering of the points. (To avoid beam effect, all the points of the width curve of the spongy PS sample in Figure 6 were measured on fresh spots.)

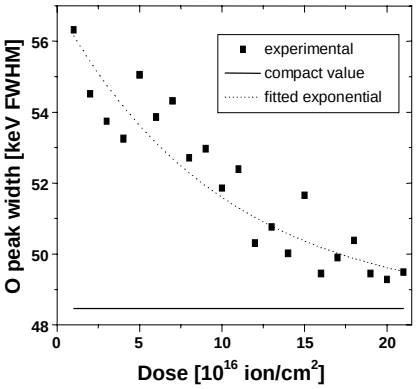

N implanted sample

As is shown in Figure 1, this sample suffered significant changes due to the ion implantation. Its surface region compacted similarly to the case of He implantation in Ref. [10]. Furthermore, the pore walls under the compact layer became thicker due to a decreased porosity and they are inclined as if the incident ions have been dragged them along. The mechanism of compaction and wall bending is not yet identified, it needs further investigations.

Figure 8 shows width curves obtained for the virgin and N implanted samples at ΔE = 15 keV, 50 keV and 100 keV. It is clearly seen that the theoretical predictions of Eqs. 6-11 are fulfilled. The compacted layer and the decreased effective porosity of the implanted sample decreased the width of the resonance peak at almost all tilt angles and significantly widened the width of the central valley. Furthermore, according to the changed average direction of the pore walls, the central valley is distorted and it is shifted by 3° in the case of ΔE = 15 keV.

Figure 8. Width curves obtained for the virgin, V, and, 15N+, implanted samples at various excess energies of ΔE = 15 keV, 50 keV and 100 keV. The vertical line indicates the original position of the valley.

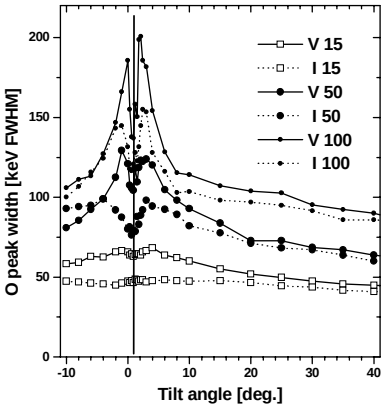

At smaller excess energies the effect of the compact layer is relatively larger and only shallower depth regions contribute to the average porosity and pore direction. As a result, the above mentioned changes appear most obviously in the case of the ΔE = 15 keV measurement.

Summary

It was demonstrated both theoretically and experimentally that in porous samples the resonance peak is smeared out. The angular dependence of the peak width (width curve) bears information on the pore structure and it can be applied to observe the changes caused by different processes, e.g. ion implantation.

Acknowledgements

The work was supported by Hungarian OTKA grants No. T019147, F019165 and F020736. The authors are indebted to the technological laboratory of KFKI-RIMS for sample preparation and to the staff of the Van de Graaff accelerator for their faithful assistance during the measurements.

REFERENCES

[1] J.A. Leavitt, L.C. McIntyre Jr, in Handbook of Modern Ion Beam Materials Analysis, eds. J.R. Tesmer *et al*., (MRS, Pittsburgh, 1995) p. 37.

[2] Z. Hajnal, E. Szilágyi, F. Pászti, G. Battistig, *Nucl. Instr. and Meth*., B118 (1996) 617.

[3] F. Pászti, E. Szilágyi, Z.E. Horváth, A. Manuaba, G. Battistig, Z. Hajnal, É. Vázsonyi, *Nucl. Instr. Meth*. B136-138 (1998) 533.

[4] G. Amsel, E. d'Artemare, G. Battistig, V. Morazzani, C. Ortega, *Nucl. Instr. Meth*. B122 (1997) 99.

[5] F. Pászti, E. Szilágyi, *Vacuum* 50 (1998) 451.

[6] É. Vázsonyi, M. Koós, G. Jalsovszky, I. Pócsik, *J. Luminescence* 57 (1993) 121.

[7] E. Kótai, *Nucl. Instr. Meth*. B85 (1994) 588.

[8] J.P. Biersack and L.G. Haggmark, *Nucl. Instr. Meth*. 174, (1980) 257.

[9] E. Szilágyi, F. Pászti, G. Amsel, *Nucl. Instr. Meth*. B100, (1995) 103.

[10] F. Pászti, A. Manuaba, E. Szilágyi, É. Vázsonyi, Z. Vértesy, *Nucl. Instr. Meth*. B117 (1996) 253.

NARROW NUCLEAR RESONANCES AND THEIR APPLICATION IN ION BEAM ANALYSIS

G. Battistig
MTA – Research Institute for Technical Physics and Materials Science
H-1525 Budapest, P.O. Box 49, Hungary
Tel: (+36-1) 395-9220 • Fax: (+36-1) 395-9284 • E-mail: battisti@mfa.kfki.hu

I.C. Vickridge, G. Amsel
Groupe de Physique des Solides, UMR 7588 du CNRS, Université Paris 6 et 7,
Tour 23, 2, place Jussieu, 75005 Paris, France

Abstract

Narrow resonances in various proton induced nuclear reactions provide a very useful tool to determine not only the concentration but also the depth profile of a given element. This technique, being isotopically sensitive, gives the possibility to perform isotopic tracing experiments, in which the atomic movement of light elements due to various treatments can be followed.

Low energy and narrow resonances have several advantages such as high sensitivity, high near surface depth resolution, good separation from other reactions occurring on different nuclei, and easy derivation of the concentration profile from the recorded excitation curve. The ion accelerator and experimental set-up used for this method are similar to those used in Rutherford backscattering experiments but require lower beam energies, higher ion beam energy stability and probably an automatic energy scanning system to vary the beam energy during the experiment. Depending on the nuclear reaction different types of detector are needed: surface barrier semiconductor detector with or without filtering foil, BGO or NaI(Tl) γ-ray detector, etc.

As illustrations some experimental results will be shown. In these applications the resonance technique provides unique and easy to understand information on the location of the given isotope in the sample.

Introduction

Since the early 60s depth profiling of light elements using nuclear reaction resonances is a widely used ion beam technique [1-6]. Many nuclear reaction cross-sections were measured, some with high precision, and in (p,α), (p,γ) and (p,p′γ) reactions on different light isotopes, narrow resonances often appear, which can be used to study the concentration of the given isotope in the near surface region of the sample. The isotopic sensitivity of the technique opens the possibility of performing isotopic tracing experiments.

Theoretical details

When an energetic proton beam hits a target a nuclear reaction may occur on one of the light nuclei of the target. In the cross-section of the reaction narrow resonances may show up where the cross-section is sharply peaked. A resonance is considered narrow if the full width of half maximum (FWHM) of the resonance, Γ, is less than a few hundred eV. As an illustration, the cross-section of the $^{18}O(p,\alpha)^{15}N$ reaction is shown in Figure 1. Here some narrow resonances can be seen, the two most important resonances in the energy range of 100-1000 keV are the 2.1 keV wide resonance at 629 keV and a very narrow ($\Gamma < \approx 100$ eV) one near 152 keV. Let us note that the cross-section increases by ≈ three orders of magnitude at the 152 keV resonance.

Figure 1. Differential cross-section for the $^{18}O(p,\alpha)^{15}N$ reaction after H. Lorenz-Wirzba *et al*. [7]. Detection angle is 135°. The resonances are marked with their energy.

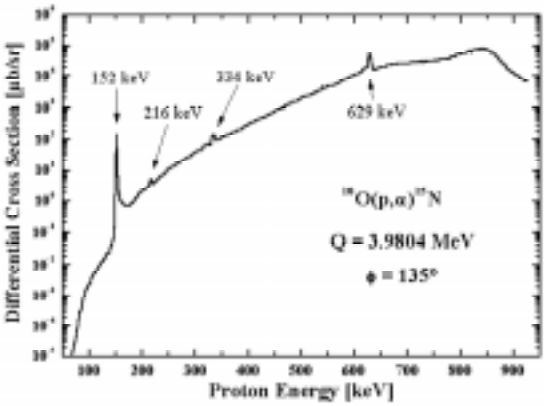

To use this nuclear resonance for probing ^{18}O isotopic concentration profiles a beam of protons bombards the sample and the characteristic α-particles are detected and recorded. With reference to Figure 2, consider protons of energy E incident on the sample surface. The protons lose energy as they penetrate the sample. If E is equal to the resonance energy E_R, then the cross-section is very high in the surface region, but rapidly falls to nearly zero deeper in the sample. The yield of the nuclear reaction is thus proportional to the surface concentration of ^{18}O. If E is greater than E_R by some amount ΔE, then the resonance energy occurs below the surface, at a depth x determined by:

$$x = \frac{\Delta E}{dE/dx}$$

where dE/dx is the stopping power of the sample for the protons. The yield $N(E)$ of the reaction as a function of the bombarding energy is thus an image of the concentration profile of ^{18}O in the sample.

Figure 2. Schematic representation of the nuclear reaction resonance profiling method for uniform concentration profile of finite thickness

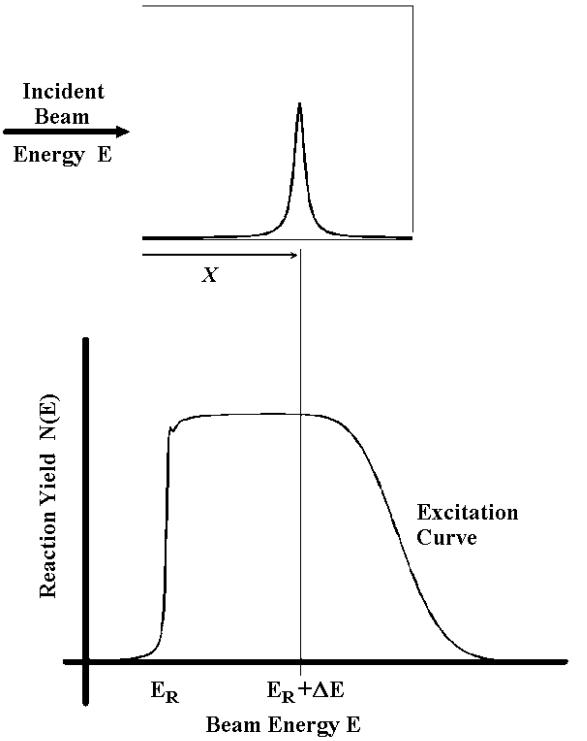

In reality the situation is more complicated than the simplistic description above suggests, since the proton energy loss in the sample is statistical in nature, giving rise to the well-known phenomenon of energy straggling. It may be shown [8,9] that in the vicinity of a narrow resonance and in the small energy loss approximation ($\Delta E << E$) the yield $N(E)$ at the accelerator setting E may be expressed theoretically as:

$$N(E) = n_0 \Omega \zeta \sigma_\Theta(E) * h_B(E) * h_D(E) * \int_0^\infty C(x) g(\Delta E; x) dx$$

where n_0 is the number of bombarding ions, Ω the detection solid angle, ζ is the overall detection efficiency, Θ the angle of detection, $\sigma_\Theta(E)$ the reaction differential cross-section at energy E, $h_B(E)$ is the actual accelerator beam energy spread, $h_D(E)$ is the apparent beam energy spread due to the thermal agitation induced Doppler broadening, and $C(x)$ is the concentration profile of the reacting nuclei, $g(\Delta E;x)$ the probability density for an incoming ion to loose energy ΔE before reacting with a nucleus at the depth x in the target. The line shape of the reaction cross-section, $\sigma_\Theta(E)$, is usually Lorentzian with FWHM of Γ. Both the beam energy spread and Doppler broadening has Gaussian shape.

Overall beam energy spread and resonance shape dominate the form of the leading edge, while energy straggling dominates at the trailing edge of the excitation curve. Simulation and calculation of excitation curves for different concentration distributions can be done using SPACES computer program [10,11], which has recently been further developed. Its up to date version can be obtained from vickridge@gps.jussieu.fr.

There are several contributions to the effective proton energy spread:

Beam energy spread

The energy spread of ion beams delivered by an accelerator is usually Gaussian in shape, with a width that depends on the high voltage stabilising system of the accelerator. For slit feedback stabilised Van de Graaff accelerators this value is typically few hundred eV, but with special care, it can be as low as 80 eV. For very well stabilised cascade type accelerators beam energy spreads of a few eV, largely determined by ion source thermal energy spread, may be obtained under ideal conditions.

Straggling

The energy loss of a projectile in the target is a statistical process, and for an originally monoenergetic beam, the beam energy will spread as the projectiles penetrate the sample. Straggling may be estimated using the Bohr formula:

$$\Delta E_S = 2.355(4\pi e^4 z^2 ZNx)^{1/2}$$

where ΔE_s is the FWHM of the beam energy distribution, e is the electron charge, z and Z are the atomic number of the projectile and the target nucleus, respectively, N is the target atomic density, and x is the depth in the target. For large enough x the straggling may be assumed to be Gaussian, but for very small x, such as when studying very shallow layers, the straggling distribution is very asymmetrical and must be calculated exactly by SPACES.

Doppler effect

Target atoms in a solid vibrate thermally. If we consider the rest frame to be that of the target atom, then the thermal vibrations can easily be seen to correspond to an energy spread in the incoming proton beam. Assuming a simple harmonic oscillator model for the thermal atomic vibrations, the Doppler broadening is Gaussian, with a FWHM given by:

$$\Delta E_D = 2.355\left(\frac{2m}{M} EkT\right)^{1/2}$$

where m and M are the projectile and target nucleus masses respectively, E is the energy of the projectile, k is the Boltzman constant, and T is the target temperature.

All these factors, among others, are taken into account in the DEPTH code, which calculates the depth resolution functions for different ion beam analysis methods and set-ups [12].

Experimental

If narrow resonances are used the FWHM of the energy stability must be smaller than Γ, the resonance width, since poor energy stability will degrade the very good near surface depth resolution achievable with this method. The ideal ion accelerator for performing narrow nuclear resonance

profiling is a high energy stability, high ion current single ended machine with energies of 100-800 keV. The beam energy stability of low energy Van de Graaff accelerators is a crucial question. The high precision computer controlled beam energy scanning system of Paris group for performing nuclear resonance experiments is presented in details in [13].

Often the cross-sections of low energy narrow resonances are small, and so high beam current and/or high detection efficiency are required. Since the quantity of interest is the total intensity of the particular nuclear reaction, detector energy resolution can usually be sacrificed in order to gain high detection efficiencies. For example large volume NaI(Tl) or BGO gamma detectors may be used in place of the higher resolution but lower efficiency HpGe detectors, and particles may be detected with a large solid angle at the expense of large kinematic energy spread of the detected particles. The (p,α) reactions exploited are usually sufficiently exothermic that the energy of the α-particles is much higher than that of the high flux of backscattered protons, which may be kept out of the detector by a foil sufficiently thick to stop them, but thin enough to allow the α-particles into the detector.

Ion bombardment may cause hydrocarbon build-up from the residual vacuum to occur, forming an additional layer on the sample surface. Energy loss of the incoming particles in this layer may also disturb the rising edge of the excitation curve. To avoid or minimise this hydrocarbon layer deposition a very good, clean vacuum is needed. Usually a liquid nitrogen cooled trap is placed near the sample in the vacuum chamber. For delicate samples, the beam impact point may be changed during the measurement if the sample may be assumed to be laterally homogeneous and a large enough surface area is available. This is often the case, for example, when studying thin film behaviour on semiconductor wafers.

Illustration

The most important resonances for material analysis are listed in Table 1. In the literature numerous applications of resonances can be found. Here we present only some simple experiments to illustrate the technique. Also we would like to give some ideas about the scientific areas where resonances can provide useful information and can help solve problems.

Table 1. Characteristics of the most useful proton resonances

Energy [keV]	Nuclear reaction	Width [eV]
152	$^{18}O(p,\alpha)^{15}N$	< 100
413.9	$^{29}Si(p,\gamma)^{30}P$	< 50
419	$^{24}Mg(p,\gamma)^{25}Al$	< 80
429	$^{15}N(p,\alpha\gamma)^{12}C$	120
620	$^{30}Si(p,\alpha)^{31}P$	70
629	$^{18}O(p,\gamma)^{15}N$	2100
987.5	$^{23}Na(p,\gamma)^{24}Na$	30
992	$^{27}Al(p,\gamma)^{28}Si$	70
1005	$^{52}Cr(p,\gamma)^{53}Mn$	50
1417	$^{23}Na(p,\gamma)^{25}Mg$	90
1747	$^{13}C(p,\gamma)^{14}N$	135
2312	$^{27}Al(p,\gamma)^{28}Si$	320

Depth profiling of ^{18}O

The abundance of ^{18}O in naturally occurring oxygen is 0.204%. The use of oxygen highly enriched in ^{18}O (which is chemically identical to ^{16}O), combined with depth profiling via the 152 keV narrow $^{18}O(p,\alpha)^{15}N$ resonance offers a high resolution technique to investigate the movement of oxygen in the near surface region – of interest in microelectronics processing, corrosion research, thin film growth and so on [14,15]. In Figure 3 an example is shown in which the depth profiling capability of this resonance is well expressed.

Figure 3. Excitation curves recorded on anodically oxidised 97% ^{18}O enriched Ta_2O_5 samples. The origin is at the resonance energy, 152 keV. Solid lines represent SPACES simulations. No background is subtracted.

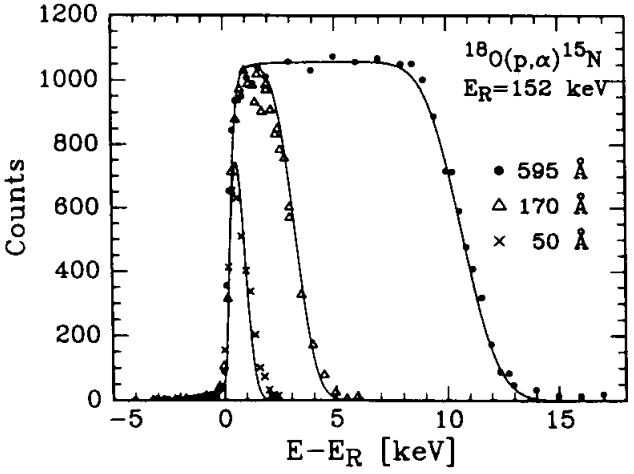

Anodically oxidised thin Ta_2O_5 layers were investigated here [16,17]. The solution in which the anodic oxidation took place was prepared from water in which 97% of the oxygen was ^{18}O. The very thin layer, 50 Å, appears as a peak in the excitation curve. The excitation curve of the 170 Å layer reaches the plateau value, and in the case of the ≈600 Å thick sample the uniform ^{18}O concentration shows up as a broad well-defined plateau.

Note that the excitation curve falls to zero for low and high energies because the cross-section of the reaction in the vicinity of this resonance is negligible. The next resonance is about 60 keV above this resonance allowing Ta_2O_5 oxide layers up to ≈3500 Å to be studied without background counts. A further advantage of the low resonance energy is the high dE/dx in this energy range: the greater dE/dx, the better the depth resolution. The simulations calculated by SPACES agree well with the experimental points.

For comparison experimental curves are presented in Figure 4, now for the 2.1 keV wide 629 keV resonance.

Here the curve recorded on the very thin (50 Å) Ta_2O_5 layer appears as a small peak. Only the layers thicker than ≈550 Å seem to reach a plateau. Comparing with the 152 keV resonance, here the wider resonance clearly degrades the depth resolution. Because of the resonance's higher off-resonance cross-section, all the curves sit on a background, which reduces sensitivity.

Figure 4. As comparison, excitation curves for anodically oxidised $Ta_2{}^{18}O_5$ layers measured by the 2.1 keV wide, 629 keV energy resonance. No background is subtracted.

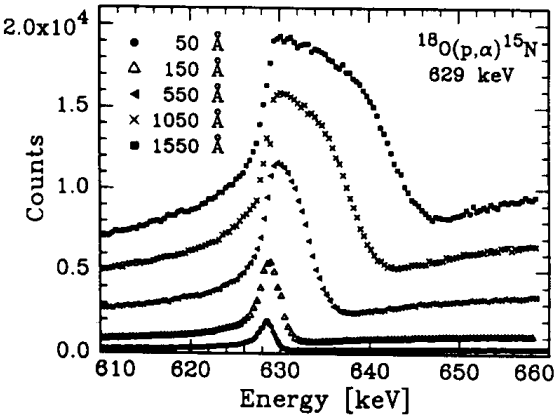

These two examples demonstrate that:

- The smaller the resonance energy the better the sensitivity. When the resonance is first, usually no contribution appears from the deep regions, the excitation curve has no background from the off-resonance cross-section.

- At low energy the stopping power for protons is large (depending on the material, its maximum is in the range of 100 keV), meaning better near surface depth resolution.

We can also note that:

- At low energy less heat is deposited onto the sample during the measurement, so larger ion currents are possible.

- Better depth resolution also means greater sensitivity to surface contamination.

Isotopic tracing with ^{18}O

In microelectronics one of the most important technological steps is the formation of very thin gate oxide layers. Hence there is an essential need for knowledge of the basic mechanism of silicon oxidation.

Figure 5 shows excitation curves for a very thin SiO_2 surface layer formed by thermal oxidation of silicon in low pressure dry oxygen [15,17]. To study the transport mechanism of oxygen or silicon during oxidation the layer was grown first in ^{16}O gas and then in 97% enriched ^{18}O gas. Here we can really follow the movement of oxygen atoms, since the ^{18}O distribution can be measured. Most of the ^{18}O can be seen at the inner interface, with a surface peak also present. Previous NRA work 18] has shown that virtually all oxide growth occurs at the SiO_2/Si interface, and the explanation of such a distribution is that the oxygen atoms travel interstitially from the gas through the already formed SiO_2 layer without any exchange with the existing oxide, rather than via a step-by-step motion with exchange. The surface peak is due to exchange without oxide growth, and is probably related to the presence of surface-specific defects.

Figure 5. Excitation curves for SiO_2 layer formed at first in ^{16}O and after ^{18}O ambient. Thermal oxidation took place at 930°C, 10 mbar dry oxygen gas. The curves were recorded 0° tilt angle (upper part) and 70° tilt angle (lower part).

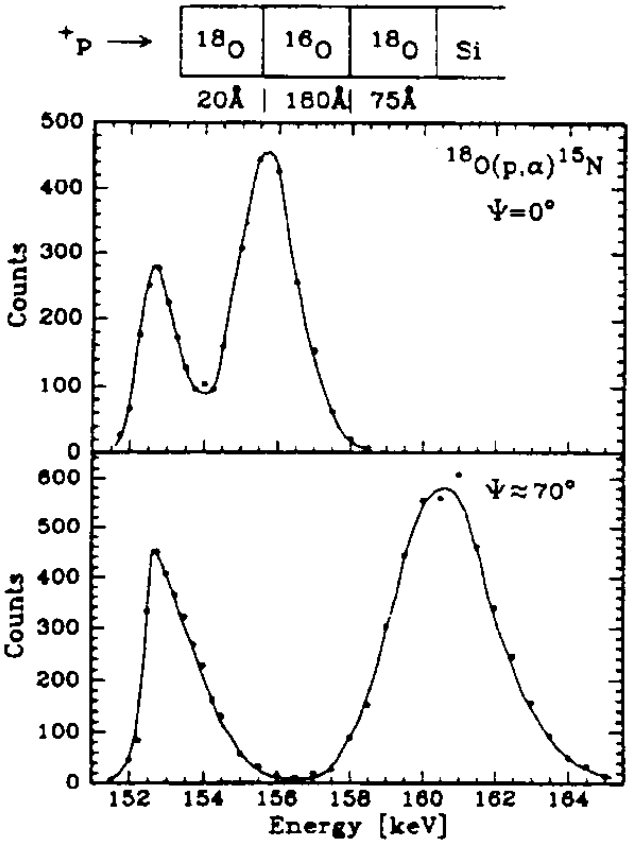

Depth resolution may be improved by tilting the sample with respect to the beam direction. The lower part of Figure 5. was recorded at 70° tilt angle (the angle between beam direction and sample surface normal), increasing the apparent thickness of the layer by a factor of ≈ three. Now the separation of the surface peak and the deeper ^{18}O profile is more expressed, and the assertion that there is no exchange more convincingly supported.

Let us note that for thicker layers and high tilt angles small angle multiple scattering degrades very quickly the depth resolution [19]. When we plan an experiment this phenomenon has to be taken into account.

As mentioned above, due to a physical exchange of O atoms between the gas and the surface of SiO_2 some ^{18}O is located at the surface. The ^{18}O profile which best reproduces the surface region of the excitation curve, after simulation by SPACES (Figure 6), is an error function type profile: neither a constant concentration, nor a linearly decreasing concentration (of same total ^{18}O quantity) fits the experimental points. The erfc profile is consistent with a diffusion process, and allows us to exclude, for example, the hypothesis that Si atoms are transported from the Si substrate and oxidised at the surface (which would lead to a constant surface concentration profile). We emphasise the depth sensitivity achieved here: the concentration profile of oxygen is measurable in the 100 Å thin surface layer.

Figure 6. Similar experiment to Figure 5, here the depth distribution of surface ^{18}O layer is calculated more precisely. The error function type of distribution is shown in the inset. Solid line is SPACES calculation.

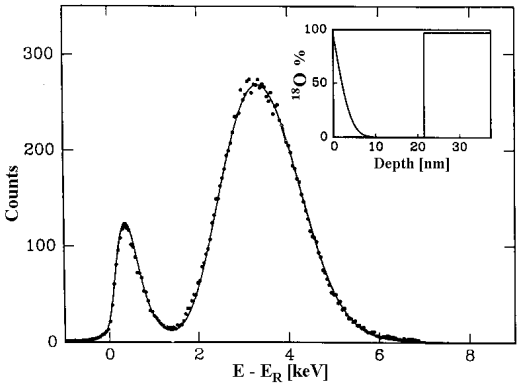

^{15}N decoration and the morphology of porous silicon

As a final example the morphology of highly porous silicon films of the "columnar" type was studied by decoration of the large internal surface of the films with ^{15}N and subsequent measurement of the excitation curves of the 120 eV wide resonance in $^{15}N(p,\alpha\gamma)^{12}C$ reaction at 429 keV for various angles of sample tilt [20]. Columnar type porous silicon consists of long pores perpendicular to the surface. The average pore diameter is around 150 Å, the thickness of the single crystalline walls between the pores is 50-100 Å. The main feature of porous silicon is its very high internal surface area. For a pure 66% porous film the specific internal area is close to 200 m^2/cm^3. A general work on the use of ion beams to characterise porous silicon was presented in [21].

In our studies the porous Si samples were nitrided at high temperature in NH_3 labelled to 97% in ^{15}N. The recorded curves exhibit a flat plateau demonstrating the uniformity of the decoration of internal surface by ^{15}N, and a trailing edge significantly broader than that due to the usual energy straggling processes (Figure 7). The corresponding excess of the energy loss fluctuations at the film-substrate interface is related to the morphology of the porous structure.

Figure 7. A columnar type porous silicon sample was nitrided by ^{15}N and studied by the narrow $^{15}N(p,\alpha\gamma)^{12}C$ resonance at 429 keV with different sample tilt angles. The broadest trailing edge corresponds to 0° tilt angle and the steepest trailing edge to 30° tilt angle.

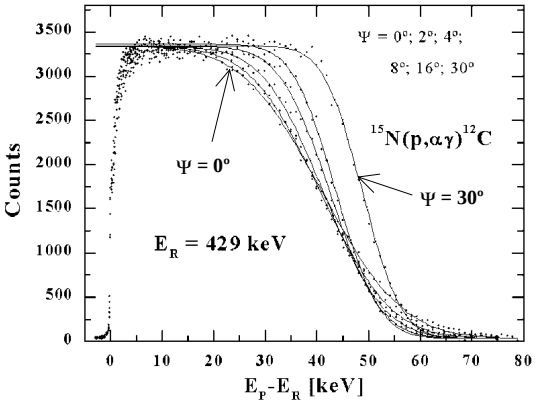

A simple picture of this behaviour is the following: when an energetic proton arrives perpendicular to the surface of the porous layer, it hits either a pore wall or a hole. In a pore wall the proton looses energy as it slows down, while in the hole it can penetrate deeply without any energy loss. Therefore there is great difference in the energy of protons at a given depth or, alternatively, the depth at which all protons have the same energy (resonance energy), scatters very widely.

Using higher tilt angles, all the incoming protons have to travel through both, walls and holes, hence the difference in the history of each proton becomes similar. The different trailing edges corresponding to different tilt angles reflect the path length fluctuations of the protons. Comparing the path length fluctuations corresponding to various hypotheses (e.g. about pore size, wall linearity, etc.) with those determined from the excitation curves provides insight into the microscopic structure of a porous layer.

The interesting fact in this experiment is that we use a large beam of protons with a diameter of ≈1 mm, but each proton senses the material at an atomic scale. In the measurement the information coming from the individual protons is combined statistically but from statistical features of the recorded curve we can learn about microscopic properties of the material.

Concluding remarks

In this short paper, we have chosen to concentrate on two specific examples which illustrate certain features of resonance profiling: isotopic sensitivity; the interest of narrow low energy resonances; the high sensitivity of the excitation curve to the form of surface concentration profiles, and exploitation of the very local nature of the charged-particle energy loss processes involved. But the reader should be aware that all of the resonances cited in Table 1 have been used in materials science, geology, or biology [5,6,22]. It is also worth noting that narrow resonances may be exploited for measuring hydrogen depth profiles by directing a beam of the resonant nucleus onto a target containing hydrogen [W. Lanford, in 5]. In many cases, for example the measurement of sodium depth profiles in rare archaeological artefacts, it is not the isotopic specificity that is of interest (^{23}Na is the only stable isotope of sodium; stable isotopic tracing is impossible), but simply the ability to profile quickly, cheaply (given an installed accelerator), and often without leaving discernible damage on the sample. Unfortunately there is, to our knowledge, no suitable review article to which interested readers may be directed, but it is our hope that the examples presented in this paper will leave the reader with a good appreciation of some of the possibilities for materials analysis and materials science research that are made possible by the application of very narrow nuclear resonance reactions to high resolution concentration depth profiling.

Acknowledgement

We would like to take this opportunity to highlight the crucial early contributions of J.-P. Nadai (now in Montpellier), B. Maurel (now in Toulouse), and D. Samuel (at the Weisman Institute, Israel), which put in place the foundations for depth profiling and isotopic tracing with narrow nuclear resonances.

REFERENCES

[1] G. Amsel and D. Samuel, *J. Phys. Chem. Solides* 23 (1962) 1707.

[2] G. Amsel, J.P. Nadai, E. d'Artemare, D. David, E. Girard and J. Moulin, *Nucl. Instr. and Meth.* 92 (1971) 481.

[3] Ion Beams for Materials Analysis, eds., J.R. Bird and J.S. Williams, Academic Press (1989).

[4] Ion Beam Handbook for Materials Analysis, eds., J.W. Mayer and E. Rimini, Academic Press, New York 1977.

[5] Microanalysis of Light Element (Hydrogen to Neon) Using Charged Particles Accelerator, ed., G. Demortier, *Nucl. Instr. and Meth*. B66 (1992) 1-305.

[6] Handbook of Modern Ion Beam Materials Analysis, eds., J.R. Tesmer and M. Nastasi, Materials Research Society, Pittsburgh (1995).

[7] H. Lorenz-Wirzba, P. Schmalbrock, H.P. Trautvetter, M. Wiescher and C. Rolfs, *Nuclear Physics* A313 (1979) 346.

[8] B. Maurel, G. Amsel and J.P. Nadai, *Nucl. Instr. and Meth*. 197 (1982) 1.

[9] G, Amsel and B, Maurel, *Nucl. Instr. and Meth*. 218 (1983) 183.

[10] I. Vickridge and G. Amsel, *Nucl. Instr. and Meth*. B45 (1990) 6.

[11] I. Vickridge and G. Amsel, *Nucl. Instr. and Meth*. B45 (1990) 12.

[12] E. Szilágyi, F. Pászti and G. Amsel, *Nucl. Instr. and Meth*. B100 (1995) 103.

[13] G. Amsel, E. d'Artemare, G. Battistig, E. Girard, L.G. Gosset and P. Révész, *Nucl. Instr. and Meth*. B136-138 (1998) 545.

[14] J.-J. Ganem, G. Battistig, S. Rigo and I. Trimaille, *Applied Surface Science* 65/66 (1993) 647.

[15] G. Battistig, G. Amsel, I. Trimaille, J.-J. Ganem, S. Rigo, F.C. Stedile, I.J.R. Baumvol, W.H. Schulte and H.W. Becker, *Nucl. Instr. and Meth*. B85 (1994) 326.

[16] G. Battistig, G. Amsel, E. d'Artemare and I. Vickridge, *Nucl. Instr. and Meth*. B61 (1991) 369.

[17] G. Battistig, G. Amsel, E. d'Artemare and I. Vickridge, *Nucl. Instr. and Meth*. B66 (1992) 1.

[18] I. Trimaille and S. Rigo, *Applied Surface Science*, 39 (1989) 65.

[19] G. Battistig, G. Amsel, E. d'Artemare and A. L'Hoir, *Nucl. Instr. and Meth*. B85 (1994) 572.

[20] V. Morazzani, G. Amsel, E. d'Artemare, G. Battistig and C. Ortega, *Nucl. Instr. and Meth.* B122 (1997) 99.

[21] F. Pászti and E. Szilágyi, *Vacuum* 50 (1998) 451.

[22] F. Béjina, O. Jaoul, *Phys. Earth. Planet. Int*. 97 (1996) 145.

ION BEAM IRRADIATION OF POLYMERS

Irene T.S. Garcia
Curso de Pós-Graduação em Ciência dos Materiais, Porto Alegre, Brasil

Fernando C. Zawislak
Instituto de Física – UFRGS, Caixa Postal 15051, 91501-970 Porto Alegre, Brasil

Dimitrios Samios
Instituto de Química, Porto Alegre, Brasil

Eduardo Alves, Maria Fernanda da Silva
Instituto Tecnológico e Nuclear, Sacavém, Portugal

José C. Soares
Centro de Física Nuclear, Universidade de Lisboa, Lisboa, Portugal

Abstract

In this contribution we discuss the use of ion irradiation in the study of the thermal stability of AZ-1350J novolac-diazoquinone photoresist films. The structural and chemical properties of the irradiated and heat treated photoresist films are investigated using the techniques of RBS, ERDA, NRA, FTIR spectroscopy, SEM and GPC. The films have been irradiated by He, N and Ar ions at energies from 380 to 760 keV and fluences from 10^{13} to 10^{16} ions.cm^{-2}. It is shown that an adequate irradiation improves the thermal stability of the photoresist from ≈200°C, when the non-irradiated films start to decompose, to 350°C after irradiation. This effect is due to the cross-linking mechanism induced by the ion irradiation.

Introduction

Irradiation of polymeric chains gives rise to complex modifications of their molecular structure and induces changes in the chemical, optical, electrical, mechanical and thermal properties of the polymer. One of the important effects is the change of solubility due to the irradiation. If the solubility increases in the irradiated area, the photoresist is called positive; if the solubility decreases, it is termed a negative resist. Usually in the first case there is chain scission (breaking of chains) and in the second case, cross-linking between the chains. Polymer resists have been exposed to light, γ-rays, electrons and more recently to ion beams. The use of ion beams is an interesting alternative because much higher energy density transfers are possible. An He ion of 1 MeV may ionise only about 1 in 2500 of the molecules it traverses. The published work also shows that surface-sensitive properties of polymers such as resistance to wear and erosion as well as fatigue and especially hardness, are greatly improved by an adequate exposure to ion irradiation [1-3].

Because of the inherent softness of most of the polymeric materials, the improvement of their mechanical properties, and especially of the thermal stability at higher temperatures, is very important in many technological applications. The present work is mainly focused on the ion irradiation induced effects in the AZ-1350J photoresist and the consequent improvement of thermal stability. The novolak-diazoquinone AZ-1350J photoresist is very important in the semiconductor industry. Because the novolak based photoresists have a relatively low sensitivity to γ-rays and to electrons, the ion irradiation transferring much higher energy density can be more efficient in the cross-linking process. In addition, the correlation between the ion irradiation induced chemical and physical transformation of polymers and the deposited energy and energy density is an area waiting for more detailed investigation.

The thermal stability, the composition and the chemical structural changes of the photoresist irradiated with He, N and Ar ions, transferring different electronic and nuclear energy densities to the films are investigated using ion beam analysis techniques, IR spectroscopy and scanning electron microscopy.

Experimental procedures

The AZ-1350J photoresist is composed of 70% in weight of novolak resin plus 30% of the photoconductive compound diazonaftoquinone. The composition of the photoresist is $C_{6.17}H_6O_1N_{0.14}S_{0.06}$ with a density of 1.3 g.cm^{-3}. Films of ≈1.8 μm were produced by spin coating onto clean silicon wafers. The samples were irradiated with He, N and Ar at energies and fluences shown in Table 1. The film thickness, the projected ranges R_p of the ions and the electronic (S_e) and nuclear (S_n) stopping powers have been calculated via TRIM (1995 version) [4]. Table 1 also shows the averaged total energy density $\overline{\sigma}_t = \phi(S_n + S_e)$ deposited by the ions in the film.

The photoresist films were irradiated at room temperature using the 500 kV ion implantor of the Instituto de Física, Porto Alegre. The beam current densities were lower than 50 nA.cm^{-2}, in order to avoid local beam heating. The pristine and irradiated films have been exposed to heat treatments at various temperatures between 300 and 400°C in a vacuum better than of 10^{-6} Torr.

The Rutherford backscattering (RBS) nuclear reaction analysis (NRA) and elastic recoil detection analysis (ERDA) measurements have been done in the 3 MV HVEE Tandetron of the Instituto de Física, Porto Alegre and in the 3.1 MeV Van de Graaff accelerator in Sacavém (Portugal).

Table 1. Parameters for He, N and Ar irradiation of the 1.8 μm AZ-1350J films

Ion	E (keV)	ϕ (at.cm^{-2})	R_p (μm)	$\bar{\sigma}_t = \phi(S_n + S_e)$ (eV/Å^3)
He	380	10^{13}	2.1	0.02
		10^{14}		0.2
		10^{15}		2
		10^{16}		20
N	760	2×10^{15}	1.5	10
Ar	760	2×10^{15}	0.95	15

The chemical structural changes of some of the irradiated films have been studied via Fourier transform infrared spectroscopy (FTIR) and their surface morphology was characterised by scanning electron microscopy (SEM). The thermally treated films were submitted to extraction with tetrahydrofurane to separate the soluble components and to measure the gel content.

Results

The RBS technique has been used to evaluate the thickness of the photoresist films before and after the irradiation and also after the heat treatments. Figure 1 shows the measured spectra of the pristine AZ-1350J film and after annealings at 350°C. During the first two hours at 350°C the film looses 50% of the material, as is seen through the movement of the Si edge to higher energy. In fact, what probably remains of the photoresist film, after the heat treatment, is only a layer of carbon. The effect of irradiations is seen in Figure 2, showing clearly that only the He irradiation with fluence of 10^{16} cm^{-2} did not affect the RBS spectrum. After N and Ar irradiations the films are thinner and for Ar, the RBS spectrum shows an apparent loss of oxygen. Two hours of heat treatment of the Ar irradiated film resulted in the movement of the Si edge toward the surface, as shown in Figure 3, characterising a completely ruined film as is confirmed by SEM measurements.

Figure 1. RBS spectra of the pristine AZ-1350J film and after annealings

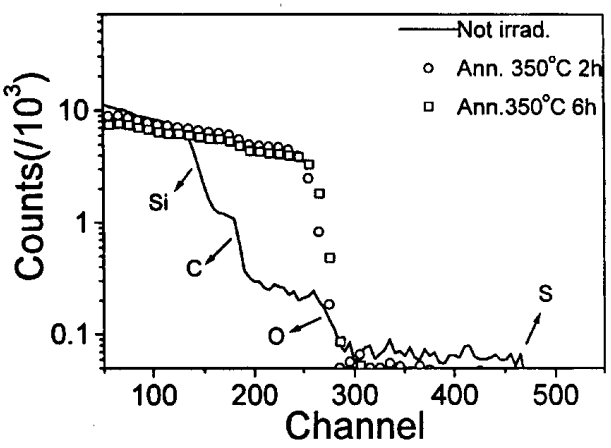

Figure 2. RBS spectra of the pristine AZ-1350J film and of films irradiated with He, N and Ar

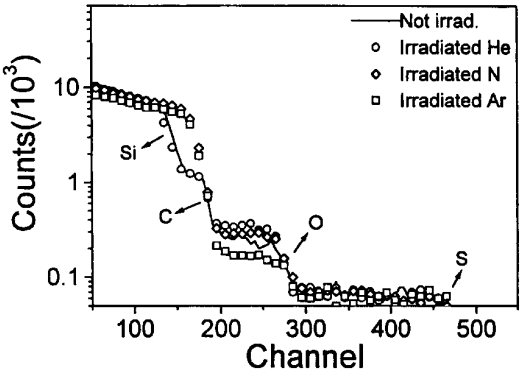

Figure 3. RBS spectra of the pristine and of Ar irradiated and subsequently annealed AZ-1350J films

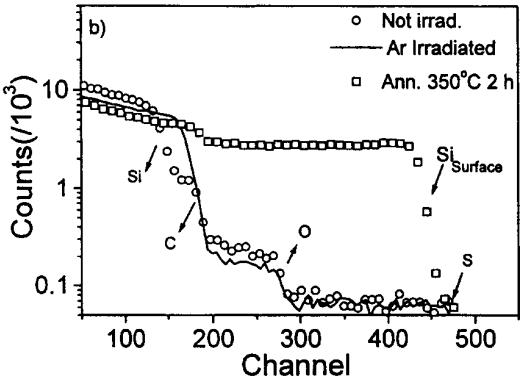

The He irradiated film with a fluence of 10^{16} He.cm^{-2} resulted in the most stable sample of AZ-1350J, under isothermal heat treatment for 6 h at 350°C. However, the ERDA data revealed a relatively large loss of H (≈40%) during the irradiation at this high fluence of He (this is not seen in an RBS spectrum). Such a large loss of H and perhaps of oxygen, can modify the structure of the photoresist. As a result of this fact, the effect of lower He fluences on the thermal stability of the photoresist was investigated. As shown in Figure 4, the Si edge moves toward higher energy for the films irradiated with the lower fluences of 10^{13} and 10^{14} He.cm^{-2} and annealed, showing a loss of 52% of the matter in the case of irradiation with 10^{13} He.cm^{-2}. On the other hand the irradiation with 10^{15} He.cm^{-2} induces, similarly as for 10^{16} He.cm^{-2}, an obvious improvement in the thermal stability, as is shown by the very small shift in the RBS Si edge, what corresponds to an also very small loss of matter due to the heat treatment.

The concentration of H in the pristine, irradiated and heat treated films was measured through the ERDA technique using an incident He^+ beam of 2.15 MeV, with incident and exit angles of 75° with the normal to the sample. The H concentration profiles for the pristine and various irradiated films is shown in Figure 5. The film irradiated with the lowest fluence of 10^{13} He.cm^{-2} loses only ≅2% of H, but under annealing is the least stable (see Figure 4). The irradiation with 10^{15} He.cm^{-2} causes a loss of ≅20% of H, and shows an excellent thermal stability as shown in Figure 4. Irradiations with higher He fluence and with heavier ions results in large loss of H; as shown in Figure 5 the irradiation with Ar ions causes a loss of 70% of the H atoms present in the film.

Figure 4. RBS spectra for three films of AZ-1350J irradiated at different fluences and subsequently heat treated

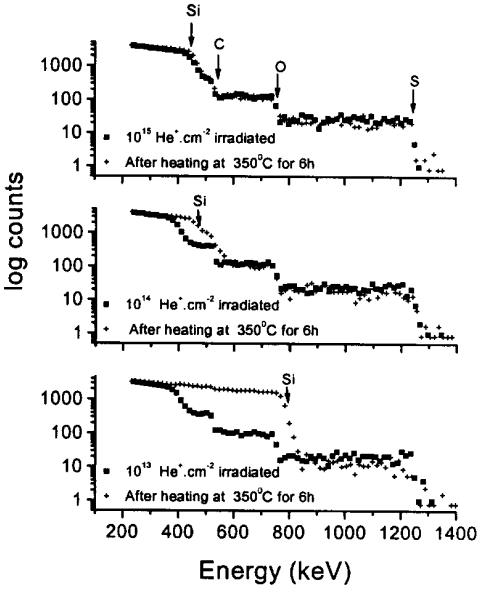

Figure 5. H concentration profiles obtained from ERDA spectra for pristine and various irradiated AZ-1350J films

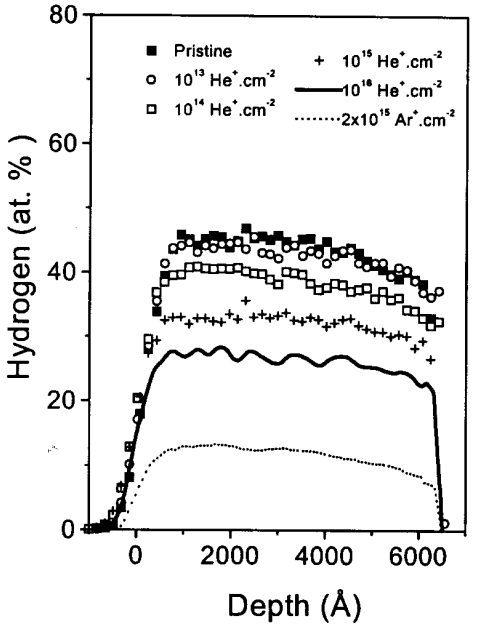

The elastic nuclear scattering resonance reaction $^{16}O(\alpha,\alpha')^{16}O$ at 3.045 MeV was used to profile the oxygen content in some of the films. Figure 6 shows the profiles of oxygen in the pristine film and in the 10^{13} and 10^{15} $He.cm^{-2}$ irradiated and annealed films. The results show that the photoresist film irradiated with 10^{15} $He.cm^{-2}$ and heat treated at 350°C for 6 h did not lose oxygen as compared to the pristine photoresist. On the other hand the film irradiated with 10^{13} $He.cm^{-2}$ shows some loss of oxygen.

Figure 6. O concentration for pristine and irradiated and annealed AZ-1350J film

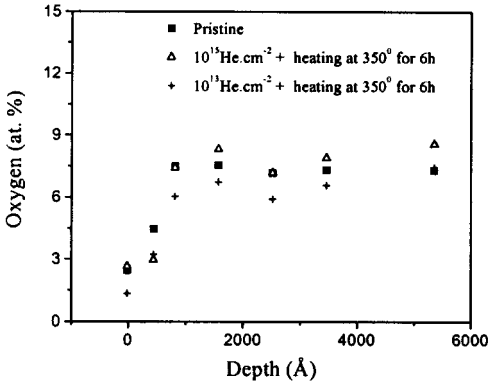

Two films, one irradiated with He at 380 keV, fluence of 10^{16} cm^{-2}, annealed at 350°C for 6 h and another with Ar at 760 keV, fluence of 2×10^{15} cm^{-2} heat treated for 2 h at 300°C have been analysed with scanning electron microscopy. Figure 7 shows micrographs of both films. The He irradiated film has a smooth surface, in contrast to the destroyed Ar irradiated sample showing bubbles and blisters. The RBS spectrum of the Ar irradiated and annealed film is shown in Figure 3.

Figure 7. SEM micrographs of AZ-1350J films irradiated with He (a) and Ar (b) and heat treated

(a) (b)

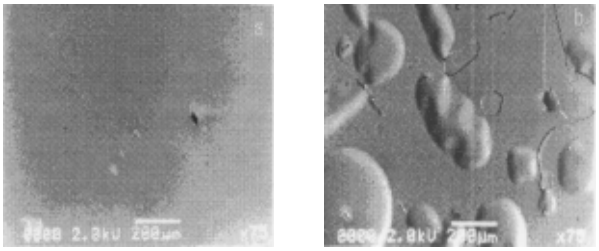

The effects of irradiation and thermal treatment on the chemical structure of the photoresist films were observed via IR measurements. Figure 8 shows:

i) The decrease of the bands at 2860 and 2920 cm^{-1} with the irradiation indicating the cleavage of C-H, with a loss of H in agreement with the ERDA data.

ii) The O-H stretching band at 3380 cm^{-1} shifting to higher values with irradiation and annealing. This is due to spatial blocking of the O-H systems caused by the cross-linking.

iii) The decrease of the C-O absorption bands at 1200 and 1258 cm^{-1} due to the cleavage of C-O in the diazonaftoquinone.

The gel content of the film irradiated with 10^{15} $He.cm^{-2}$ and annealed was determined by submitting the sample to extraction in tetrahydrofurane. The insoluble part was separated, dried and weighted until constant weight. The measured gel content of the film was 88%

Figure 8. FTIR spectra of various AZ-1350J film showing the regimes of O-H, C-H and C-O stretching bands

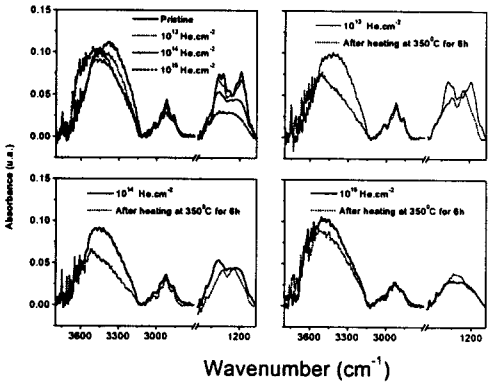

Discussion

Our results show that the pristine film of the AZ-1350J photoresist decomposes and loses part of the material after an annealing of 2 h at 350°C. In fact the pristine film of AZ-1350J starts to decompose at 220°C. The irradiation of the film with 380 keV He ions at fluences $\geq 10^{15}$ He.cm^{-2} improves considerably their thermal stability in isothermal heat treatments at 350°C for six hours. A similar thermal treatment of the photoresist film submitted to shallower implantation of 760 keV Ar ions with a range $R_p = 0.95$ μm, reaching only half of the film thickness, results in the destruction of the photoresist as shown in Figures 3 and 7. The blisters and bubbles seen in the SEM micrograph originate from the gases evolved from the non-irradiated deeper half of the film. On the contrary the range of 380 keV He ions is larger than the 1.8 μm thickness of the film, indicating that similarly as irradiations with γ-rays and electrons, the energy deposition due to the ion has to occur homogeneously over the whole volume of the photoresist in order to induce a beneficial thermal effect. The analysis of the samples irradiated with He ions as a function of the fluence of 10^{15} cm^{-2} is sufficient to induce the thermal stability of the AZ-1350J photoresist for isothermal heating at 350°C during six hours. In addition our RBS and FTIR data show that irradiations with lower fluences of He ions do not improve the thermal stability of the photoresist. It is interesting to analyse these results in terms of the ERDA data. The irradiations induce a loss of H atoms, increasing with the fluence, reaching 40% for 10^{16} He.cm^{-2}. The fact that the films irradiated with lower fluences (see Figure 5) and which have lost less H are not thermally stable means that the adequate level of dehydrogenation of the photoresist chains is a crucial mechanism in the creation process of an interconnected cross-linking network stable at higher temperatures. These results show that there is an adequate transference of energy density to the photoresist in order to simultaneously activate adjacent polymeric chains in order to develop an effective cross-linking process, without the destruction of the photoresist via the irradiation. The SEM, NRA and FTIR results show that the chemical structure of the film irradiated with 10^{15} He.cm^{-2}, transferring an total averaged, mainly electronic, energy density $\overline{\sigma}_t = 2$ eV/Å^3 to the film, was not affected by the irradiation nor by the thermal treatment. Concerning the irradiation with AR ions the contribution of the nuclear stopping cross-section to the total transferred energy (≈20%) probably also affects the structure of the photoresist. Our results do not show any evidence of graphitisation of the layer after the irradiation with He and the heat treatment. Finally, we would like to point out that these results are partially in publication elsewhere [5].

Conclusions

The above results and discussion lead us to the following conclusions:

a) The irradiation of the photoresist film with 380 keV 10^{15} He.cm^{-2} induces a 20% loss of hydrogen and results in a film stable during heat treatment of 6 h at 350°C. This irradiation did not produce graphitisation of the photoresist layer.

b) The irradiation with lower He fluences induces smaller losses of H but the films suffer degradation during the heat treatments.

c) The improvement in the thermal stability of the He irradiated photoresist is due to the cross-linking mechanism produced by the deposited average energy density of 2.0 ev/Å^3, mainly of electronic origin. The measured gel content of 88% confirms the efficiency of the cross-linking process developed by the irradiation.

d) The deposition of energy by the ion has to occur homogeneously over the whole volume of the photoresist in order to produce a beneficial thermal effect.

Acknowledgements

This work was partially supported by the exchange programme CAPES/ICCTI between Brazil and Portugal, and by the Brazilian agencies FIPEN/PRONEX and CNPq.

REFERENCES

[1] T. Venkatesan, L. Calcagno, B.S. Elman and G. Foti, in *Ion Beam Modification of Polymers*, eds., P. Mazzoldi and G.W. Arnold (Elsevier, N.Y. 1987), p. 301.

[2] E.H. Lee, M.B. Lewis, P.J. Blau and L.K. Mansur, *J. Mater. Res.* 6 (1991), 610.

[3] G.R. Rao and E.H. Lee, *J. Mater. Res.* 11 (1996), 2661.

[4] J.P. Biersack and L.G. Haggmark, *Nucl. Instrum. Meth.* 174 (1980), 257.

[5] F.C. Zawislak *et al*., Mat. Res. Soc. Simp. Proc., Vol. 504, 1998, to be published.

Application of Ion Beams Including Radioactive Beams, Part II

Chairman: K. Maier

RADIATION DAMAGE, LATTICE SITE OCCUPATION AND ELECTRICAL CONDUCTIVITY OF ION IMPLANTED RUTILE

O. Meyer, R. Fromknecht
Forschungszentrum Karlsruhe, INFP, POB 3640, D-76021, Karlsruhe, Germany
E-mail: meyer@infp.fzk.de

I. Khubeis
Faculty of Applied Science, Al-Balqa University, Al-Salt, Jordan

Abstract

Ions with different oxidation states were implanted in TiO_2 (rutile). The lattice disorder as well as the lattice site location of the implanted ions were determined using Rutherford Backscattering and Channeling (RBS-C) spectrometry. The production of disorder as a function of dose and temperature, and its recovery was studied in detail. Important results are the observation of dynamic recovery at 293 K and above, and one isothermal at 77 K and two thermal recovery stages between 170 K and 210 K and between 260 and 293 K. The recovery at 77 K is proportional to *ln*t, indicating that the activation energy increases with decreasing disorder density. The results concerning the lattice site location of 14 ion species reveal that 13 ions occupy Ti lattice site. With increasing netcharge, the maximum soluble concentration decreases by the formation of impurity-defect complexes probably enforced by charge compensation. Directed displacements from the substitutional lattice site provide some hints on the structures of these complexes.

The electrical conductivity of the implanted samples increased by about 12 orders of magnitude irrespective of the oxidation state of the implanted species. From the temperature and dose dependence of the electrical conductivity as well as from its similar behaviour for noble-gas ions and other species, it is concluded that the carrier transport occurs by single energy states excitation at low doses and by variable-range hopping between localised states at high doses.

Rutile with a bandgap of 3 eV and a conductivity of $<10^{-13}\Omega^{-1}cm^{-1}$ in the pure state can readily be n-type doped to about $10^{19}/cm^3$ in the melt with many cation impurities including Nb, Ta, W, etc., which are substitutional (on Ti-lattice sites) under oxidation conditions [1,2]. The conductivity can also be changed by orders of magnitude in a reducing atmosphere as well as by ion implantation [3-8]. This study is an attempt to find a guideline to relate the influence of doping and structural changes to the electrical conductivity and to explain the resulting current transport mechanism close to an Anderson transition [9].

Since ion implantation is a non-equilibrium process, metastable near surface alloys can be produced. The implantation process is unavoidably accompanied by damage production, which is a complex field of study in strongly bonded compounds. A review on the damage accumulation during implantation of insulating materials has been presented previously by White *et. al*. [10]. Although in TiO_2 a mixture of ionic and covalent bonding prevails, the Ti and O atoms in different sublattices reveal about the same displacement energies of about 50 eV [11]. Since electrical charge balance in the crystal is required, electronic processes can lead to changes in the charge state of dilute impurities. Charge states may also be compensated by the association of opposite charged point defects by forming neutral impurity-point defect complexes.

In the case of TiO_2 single crystal many studies on the lattice site location and the electrical conductivity have been performed [8,12]. We now have up to 18 elements implanted in order to study a possible effect of the size mismatch energy, electronegativity and charge state on the lattice site occupation. Low ion doses have been used in order to obtain low damage levels and to avoid effects of precipitation and compound formation to a large extent. Damage production and annealing was studied in a temperature region between 6 K and 1400 K [13,14]. Dynamical recombination has been the main argument that the critical energy density for amorphisation is strongly reduced for low temperature irradiation and implantation of many oxides [10]. From our results, we conclude that thermally activated recombination processes may also contribute to this effect. The possible effects of radiation enhanced annealing, especially its influence on lattice site occupation, was studied by ion implantation performed as a function of temperature and the results compared with an isochronal annealing process.

Since the maximum concentration of implanted ions on Ti lattice site may exceed that obtained by conventional doping [1] it is of interest if enhanced electrical doping, with elements which have a higher oxidation state as the host element Ti, may be obtained by ion implantation. Therefore the influence of disorder and possible doping in the electrical conductivity has to be separated. One has to consider the most important question which is the relation between lattice site occupation, oxidation state and electrical conductivity in order to apply a bandgap engineering by the ion implantation technique. In the following we present a short review of our results.

Polished single-crystal TiO_2 (rutile) slices of (001) and (100) orientation as obtained from the manufacturer were used in our experiment. The single crystals were of high crystalline quality with minimum yield values smaller than 3% for the (100) and 2% for the (001) crystalline directions, with a surface disorder of about 2×10^{15} Ti atoms/cm^2 corresponding to less than three Ti monolayers.

A liquid He cooled two-axis goniometer and a three-axis goniometer at RT were used, coupled to a 350 keV Danfysik heavy ion accelerator for ion implantation performed between 6 K and 1100 K. During all *in situ* performed ion implantations the ion beam was tilted 15° off the crystal direction. A 2.5 MeV Van de Graaf accelerator was used for *in situ* channelling analysis using 1.5 MeV or

2 MeV He ions. Random and aligned backscattering spectra were measured as a function of the tilt angle in tilt planes through the (001) and (100) crystal directions. From the analysis of angular scans curves the dopant fractions located on substitutional, interstitial and random sites can be evaluated.

The relation between lattice site occupation, charge state and electrical conductivity in ion-implanted rutile cannot be evaluated without considering the large influence of defects. The increase of the disorder with ion dose is shown in Figure 1. The surface damage peak as well as the damage peak near the mean projected range of the implanted ions increase with ion dose and reach the random level at a dose of 1×10^{15} L^{a+}/cm^2, corresponding to a deposited energy density of 5 dpa (displacements per atom).

Figure 1. Random (a) and <001> aligned backscattering spectra as a function of ion fluence: virgin (b) 2×10^{14} (c), 3×10^{14} (d), 5×10^{14}(e) 1×10^{15}(f) and 2×10^{15} L^{a+}/cm^2 (g)

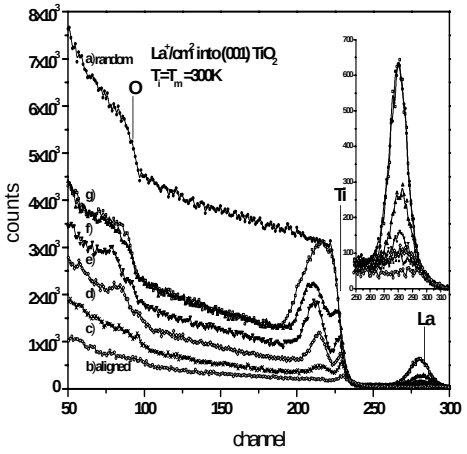

The reduction of the damage level of high dose implants occurs in two stages between 300 K and 500 K and between 700 K and 1200 K. The existence of two recovery stages in TiO_2 at higher temperatures has already been noted previously in isochronous annealing experiments [15]. It is noted that these recovery stages are lowered by about 200 K for high temperature implants.

The recovery at T_i = 500 K clearly starts from the surface, indicating that the surface acts as a sink for mobile defects. This is in contrast to isochronous annealing of amorphous TiO_2 where a partial recovery of 20% in the low temperature stage was noted to occur within the total layer while the main damage started to anneal from the crystalline/amorphous interface [15]. For partially disordered TiO_2 the recovery stage is also lowered by 200 K, in comparison with that of the amorphous phase, as can be seen in Figure 2.

High temperature implantation causes radiation enhanced annealing as well as radiation enhanced diffusion. In- and/or out-diffusion causes an increasing loss of La during implantation at increasing temperatures [16]. While in-diffusion is recognised by a tail in the La distribution the possibility of out-diffusion can not be excluded. Diffusion effects of the implanted species during isochronuos annealing have been observed previously for Hf in TiO_2 and Sn in TiO_2.

The damage in the disordered rutile phase can readily be annealed in agreement with previous observations where annealing stages even below 300 K were found [14]. This is to be contrasted to the amorphous phase annealing where a first stage of a partial recovery is observed near 500-600 K, while the main damage recovery occurs at 900 K and above (see Figure 2).

Figure 2. Normalised disorder peak vs. annealing temperature for samples (a) amorphised by 5×10^{14} H^{f+}/cm^2 at 77 K, (b) loaded with a He-beam charge of 8×10^{-4}C and (c), (d) two samples, partially damaged by implanting 2×10^{15} S^{n+}/cm^2 at 300 K

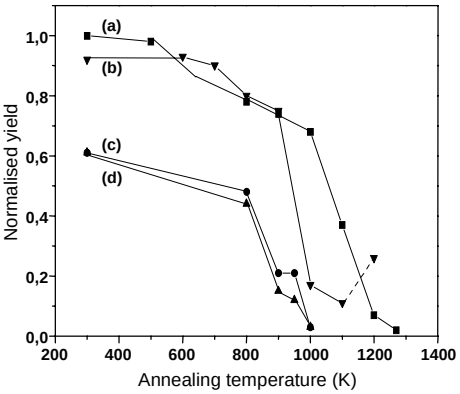

Up to now 18 different species have been implanted into TiO_2 and the lattice site occupation of 15 species was studied with RBS-C. At low concentrations (<0.1at%) all the ions (except La) were located substitutional on Ti lattice sites. With increasing implanted ion concentration many ions (In, Sb, Pb, Bi) are displaced from their substitutional lattice sites, mainly along the c-axis while others are randomly displaced (As, Hg). For ions with similar atomic radii but different charge states [e.g. Sn(+4), In(+3), Sb(+5)] those with charge state +4, as Ti, reveal the highest substitutional concentration ($f_s = 1.0$). This behaviour is attributed to the formation of impurity-defect complexes, where it is electrostatically favourable for different defects to associate for charge compensation. Supersaturation is reached for Pb, where charge compensation is not required [17,18]. As an example angular scan curves are shown for Sn, Pb and As in Figure 3, demonstrating the three possibilities mentioned above. It is speculated that displacements along the c-axis are due to a neighboured Ti vacancy or a Schottky trio, while for random displacement interactions with O vacancies prevail [18].

The temperature dependence of the electrical conductance, in the range between 300 K and 6 K, can be described by $lnG \sim^{-1}$ for low doses, $T^{1/2}$ for moderate doses with a partially amorphised/ disorderd rutile structure, and $T^{-1/4}$ for high doses with a highly disorderd rutile structure. The temperature dependence of the resistance, at different implantation doses, is shown in Figure 4a. It is seen that with increasing implantation dose from 4×10^{14} X^{e+}/cm^2 to 5×10^{16} X^{e+}/cm^2 the resistance at RT decrease from $10^5\Omega$ to $10^3\Omega$. With decreasing temperature the resistance increases strongly. The highest value of $10^{11}\Omega$ is limited by the measuring equipment.

In Figure 4b, the conductance lnG is plotted in an Arrhenius plot with the Xe-ion dose as a parameter. From the linear fit for the lowest dose the thermal activation energy can be derived and gives a value of $E_a = 43$ meV with a high correlation coefficient. Using the formula for the conductivity, the room temperature value is $\sigma_{300K} = 0.63\Omega^{-1}cm^{-1}$[8].

With increasing the dose, the conductance lnG obeys a $T^{1/2}$ behaviour, Figure 4c. This can be described in the theory that localised states near the Fermi energy, E_F, exists and hopping is responsible for the current transport. The Coulomb interaction between the electrons has to be taken in account. An activation energy of $E_a = 8.5$ meV was calculated and the conductivity at room temperature was $\sigma_{300K} = 3\Omega^{-1}cm^{-1}$.

Figure 3. Axial channelling scans of <100> and <001> oriented TiO_2 single crystals implanted with Sn, Pb and As atoms at 300 K and 260 keV, as indicated

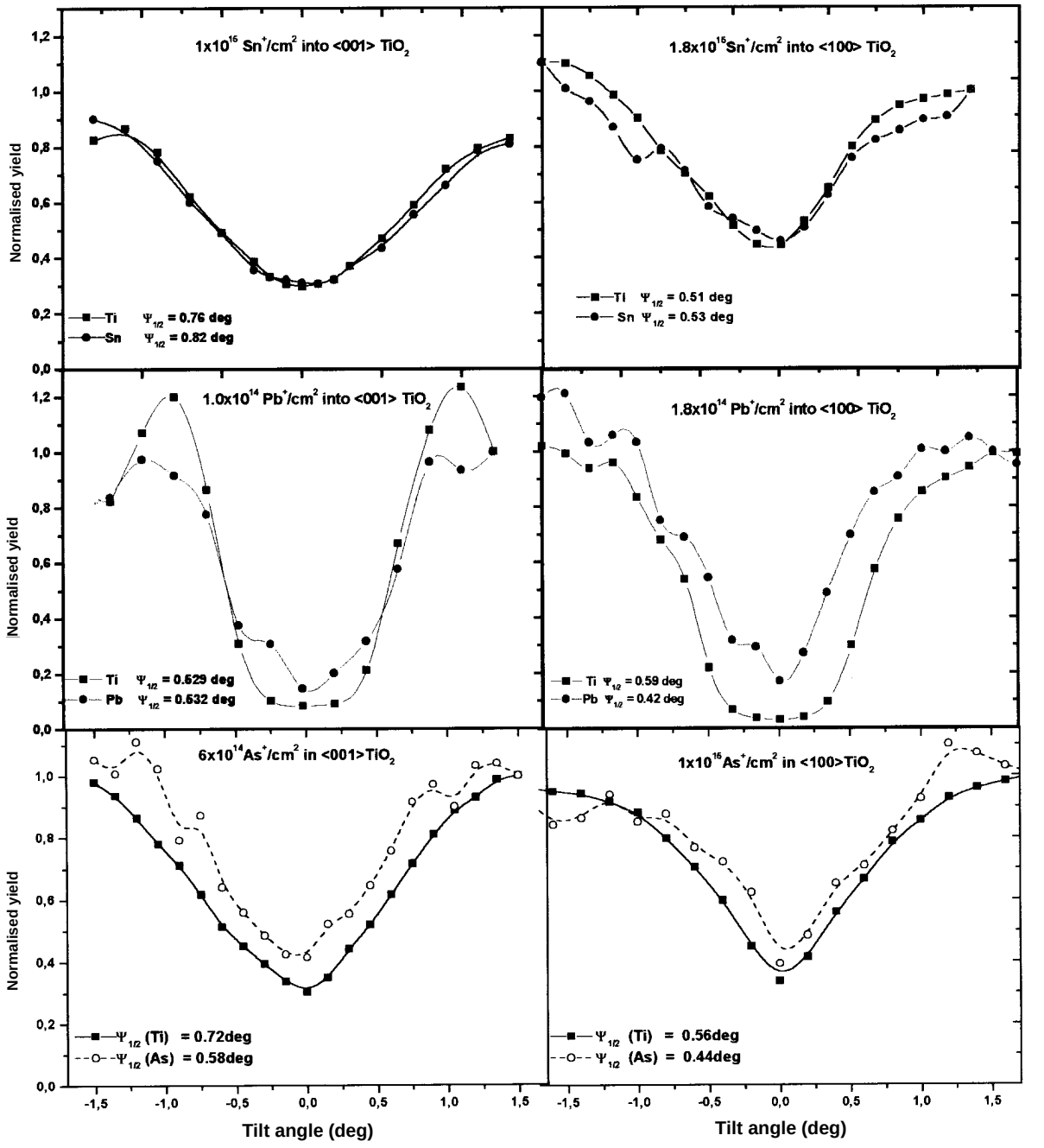

Figure 4. (a) Resistance vs. temperature of Xe irradiated TiO_2 crystals, (b,c,d) logarithm of the electrical conductance vs. T^{-1}, $T^{-1/2}$ and $T^{-1/4}$ demonstrating the thermal activation, range hopping with Coulomb repulsion, and variable range hopping near the metal insulator transition, with the fluence as a parameter

(a) 4×10^{14} Xe^+/cm^2, (b) 4×10^{15} Xe^+/cm^2, (c) 1.4×10^{16} Xe^+/cm^2 and (d) 5×10^{16} Xe^+/cm^2

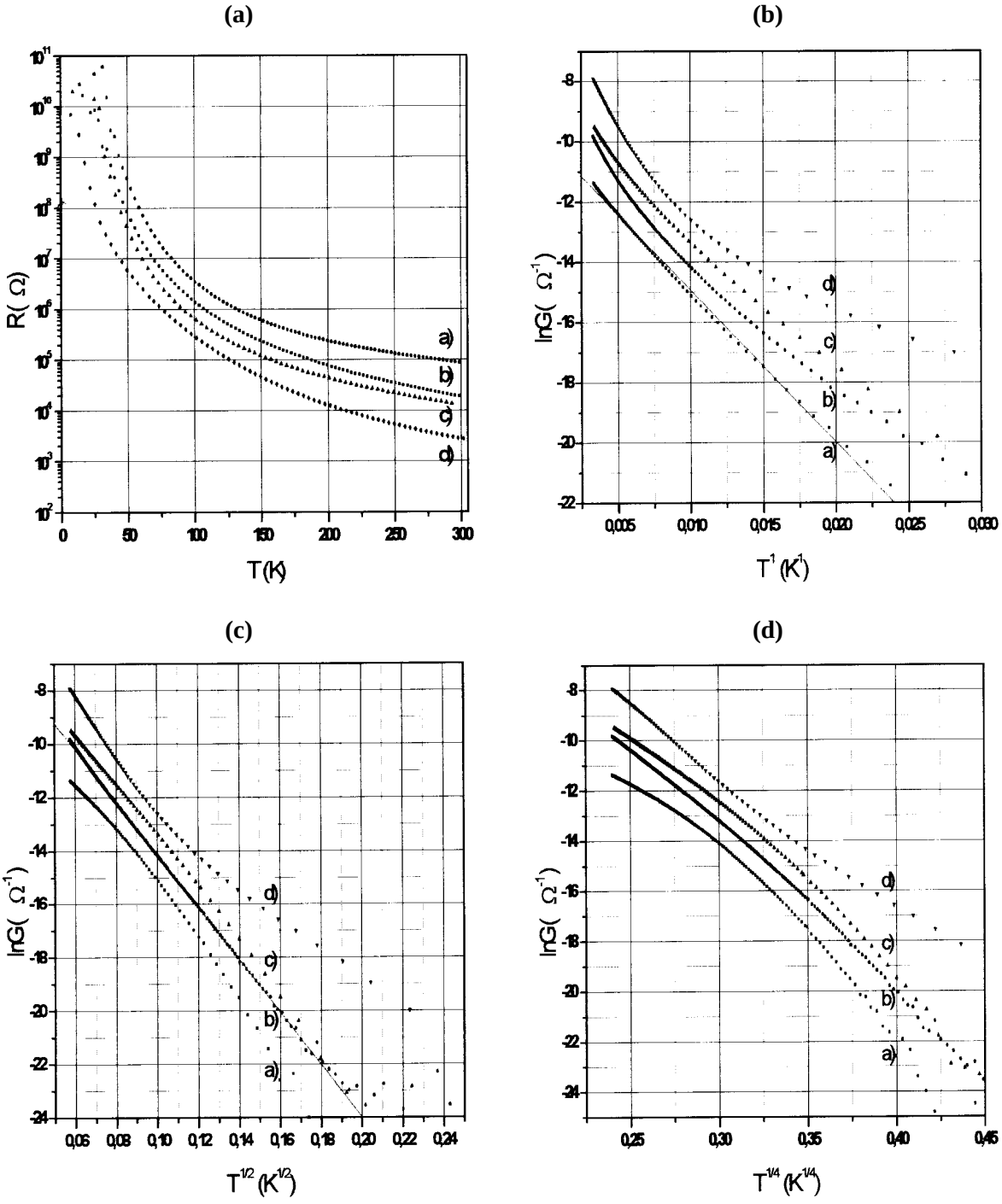

For the amorphous phase, Figure 4d, the density of the localised states increases, and variable range hopping is responsible for the current transport. The data can be fitted with a high accuracy in two temperature regimes by plotting lnG vs. $T^{1/4}$. In this case we calculated for the temperature range between 300 K and 215 K an activation energy of E_a = 4 meV and in the temperature range between 215 K and 33 K an activation energy of E_a = 5 meV which corresponds to $\sigma_{300K} = 20\Omega^{-1}cm^{-1}$ and $\sigma_{215K} = 5.8\Omega^{-1}cm^{-1}$. From this we conclude that for low doses single energy defect states exist which are thermally activated. With increasing disorder there are defect states with energies distributed over the band gap. Anderson localisation occurs and the current transport mechanism is due to hopping, especially variable range hopping between localised defect states. In the theoretical description of such a transport process it is assumed that when the density of electronic states is finite and the states are localised near the Fermi energy E_F, variable range hopping will occur and $ln\sigma$ is then proportional to $T^{1/4}$ [9]. If in addition Coulomb repulsion between carriers is taken into account, $ln\sigma$ is proportional to $T^{1/2}$. In the derivation of the latter dependence it is assumed that the one-electron density of states vanishes at the Fermi energy, E_F, resulting in a soft Coulomb gap. With increasing disorder/amorphisation the Coulomb gap is smeared out and $ln\sigma$ is proportional to $T^{1/4}$. The system is then nearer to the metal-semiconductor transition. The electron transport in this case is possibly due to different hopping processes which activated in different temperature regions. Previously, hopping between precipitates of the implanted species and as well as of Ti have been suggested as possible transport processes in high dose implanted samples [3].

As for W implants similar dependences as observed for Xe implants do occur we assume that the influence of the extra charge of elements with higher oxidation states is probably compensated by defects induced by ion implantation and with trapped electrons resulting in colour centres. A contribution to electrical conductivity can be expected when the implantation is performed under conditions which results in a low damage level.

In summary an attempt was made to study the relation between Ti-lattice site location, oxidation state of the implanted ion, and the electrical conductivity. It turned out that the oxidation state does not play a major role in the doping of TiO_2 at room temperature probably due to the fact that the doping centres are compensated by charged defects. Systematic defect annealing studies have to be performed to clarify the doping action of ions and defects in TiO_2. Studies in this respect are in progress.

Acknowledgement

The authors would like to thank S. Massing for performing the ion implantation and the Van de Graaff team for providing the He^+ analysing ion beam. This work was supported by the Volkswagenstiftung and the Al Balqa Applied University, Amman, Jordan.

REFERENCES

[1] P.O. Cox, Oxford University Press, New York (1992), and references therein.

[2] J.W. DeFord and O.W. Johnson, *J. Appl. Phys*. 54 (1983) 889, and references therein.

[3] S.M.M. Ramos, B. Canut, R. Brenier, L. Gea, L. Romana, M. Brunel and P. Thevenard, *Nucl. Instr. Meth*. 80/81 (1993) 1123.

[4] T.E. Parker and R. Kelly, in: Ion Implantation in Semiconductors and Other Materials, ed. by B.L. Crowder (Plenum, New York, 1973), p. 551.

[5] M. Guermazi, P. Thevenard, P. Faisant, M.G. Blanchin, and C.H.S. Dupuy, *Rad. Effects* 37 (1978) 99.

[6] W.D. Ohlsen and O.W. Johnson, *J. Appl. Phys*. 44 (1973) 1927.

[7] E. Iguchi, K. Yajima, T. Asahina and Y. Kanamori, *J. Phys. Chem Solids* 35 (1974) 597.

[8] R. Fromknecht, R. Auer, I. Khubeis, O. Meyer, *Nucl. Instr. Meth*. B120 (1996) 252.

[9] N.F. Mott, Metal-Insulator Transitions (Taylor and Francis, London, 1990).

[10] C.W. White, C.J. McHargue, P.S. Sklad, L.A. Boatner and G.C. Farlow, *Materials Science Reports* 4(2,3) (1989) 41.

[11] G.P. Pells, *Rad. Eff*. 64 (1982) 71.

[12] R.C. da Silva, E. Alves, L.M. Redondo, R. Fromknecht and O. Meyer, *Nucl. Instr. Meth.* B136/138 (1998) 442.

[13] I. Khubeis, O. Meyer, *Nucl. Instr. Meth*. B120 (1996) 257.

[14] I. Khubeis, R. Fromknecht, S. Massing, and O. Meyer, *Nucl. Instr. Meth*. B141 (1998) 332.

[15] I. Khubeis, O. Meyer, *Mater. Chem. Phys*. 38 (1994) 284.

[16] R. Fromknecht, O. Meyer, *Materials Chemistry and Physics* 45 (1996) 50.

[17] O.Meyer, I. Khubeis, R. Fromknecht, S. Massing, *Nucl. Instr. Meth*. B127/128 (1997) 624.

[18] O. Meyer, I. Khubeis, R. Fromknecht, S. Massing, *Nucl. Instr. Meth*. B136/138 (1998) 436.

A 3 MV TANDEM ACCELERATOR AT SEVILLE: THE FIRST IBA FACILITY IN SPAIN

Miguel A. Respaldiza [1,2], Francisco José Ager [1,2], Manuel Barbadillo-Rank [1], Javier Garcia-Lopez [1], Francisco José Madrigal [1] and María Dolores Ynsa [1,2]

[1] Centro Nacional de Aceleradores
Av. Thomas A. Edison, Parque Tecnológico Cartuja'93, E-41092 Sevilla, Spain
[2] Departamento de Física Atómica, Molecular y Nuclear, Universidad de Sevilla
P.O. Box 1065, E-41080 Sevilla, Spain

Abstract

The first Spanish tandem accelerator, of the Pelletron type, has recently been installed at the University of Seville. The laboratory has been created with the aim to fulfil the increasing demand for ion beam analysis existing in Spain. The facility mainly consists of a 3 MV accelerator with two ion sources and a capacity of seven beam lines, which will be used for interdisciplinary studies such as material research and modification, arts, archaeology, biology, medicine, environmental sciences and so on. The laboratory and the first tests of the accelerator performance are described.

Introduction

The Centro Nacional de Aceleradores (CNA) is born as a joint enterprise between the University of Seville, the Junta de Andalucía (Andalusian's regional government) and the Consejo Superior de Investigaciones Científicas (Spanish Council for Scientific Research) for the creation of the first Spanish ion beam facility. Our centre is intended as a multi-disciplinary research centre, its primary aim being material modification and analysis by making use of ion beam based techniques.

The national nature of our centre gives all Spanish researchers, from either private or public institutions, the possibility of incorporating research proposals in a wide variety of fields: material science, medicine, biology, geology, environmental sciences, art and archaeometry.

The initial investment of about 900 million pesetas (6 million US$) was financed with money from the European FEDER funds (70% from the European Union and 30% from the Junta de Andalucía), and it includes the expenses of the accelerator, its related equipment, and the building.

At present, the accelerator building and the control room is finished, together with two auxiliary laboratories. The construction of the main building (with libraries, offices, auditorium, etc.), has just started and it will be finished by the end of the next year. The accelerator hall has 1 m thick reinforced concrete walls, providing the biological shielding required by the production of neutrons by some ion beams. Furthermore, the expansion of the system has been contemplated, such as the installation of equipment for AMS.

The main characteristics of our facility include a 3 MV Pelletron accelerator from NEC, two ion sources and seven possible beam lines. Two beam lines are already set up; one is located at +30º and includes a Charles-Evans scattering chamber equipped with a four-axis goniometer, for RBS Channelling, PIXE and NRA analyses, and the other, at 0º, incorporates an experimental chamber for general testing and calibration. Additionally, an ion microprobe purchased from Oxford Microbeam Ltd. will soon be operational on the -15º beam line. An external beam line and a general-purpose chamber are also being designed.

The following detection systems and their related electronics have also come into service: Si(Li) detectors, including windowless detectors; an HpGe detector; Si barrier particle detectors; and a NaI(Tl) detector.

The first performance tests were successfully made during the spring of 1998, and the remaining tests are being performed at this moment (September 1998). The accelerator is due to be fully operational next autumn.

Facility description

The ions to be accelerated can be produced in two different ion sources, one based on radio frequency techniques, which generates negative ions from gases (H, He, N...), and a caesium sputtering source (SNICS) that gets negative ions from solid samples. The extraction is done using a 60 kV potential (see Figure 1).

The sources are connected to the +30º and -30º input ports of an injection magnet that selects the desired ion mass. The magnet has a capability of 15 amu-MeV maximum. The line also includes several instruments for focusing, steering and monitoring the beam and a vacuum station (see Figure 2).

Figure 1. Sources beam line assembly

1) turbo pump stations, 2) gaps, 3) injection magnet

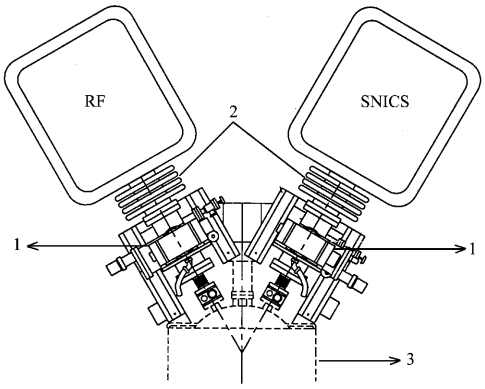

Figure 2. Injection beam line

1) injection magnet, 2) BPM (beam profile monitor), 3) slits, 4) Faraday cup, 5) turbo pump station, 6) Einzel lens

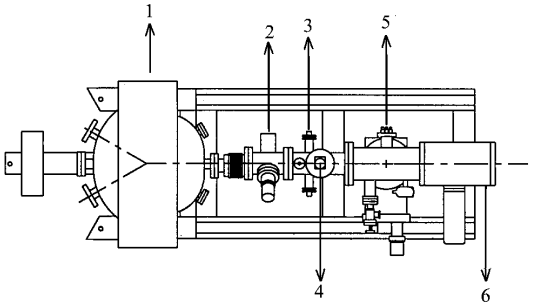

The selected ions are accelerated in a two-pellet chain 9SDH-2 Tandem accelerator (see Figure 3). The maximum terminal voltage is 3 MV. The ion charge state is changed to positive in the gas stripper located inside the terminal. The terminal voltage is stabilised with a double loop electronic feedback system with signals both from the pair of stabilising slits located after the analysing magnet and from two capacitive pick-off plates facing the terminal.

Figure 3. Accelerator tank

The beam line after the accelerator consists of the vacuum station and several devices for focusing, steering and monitoring the beam. The 90º analysing magnet for selecting the accelerated ion beam is located the end of this line (see Figure 4).

Figure 4. Post-accelerator beam line

1) turbo pump, 2) quadrupoles, 3) magnetic steerer, 4) BPM,
5) slits, 6) Faraday cup, 7) analysing magnet, 8) magnet power supply

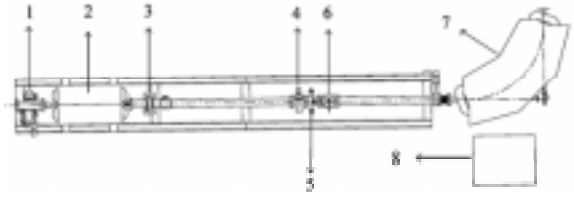

After this magnet there are an ion pump station, the energy slits and the devices for steering and focusing the beam. At the end of the line there is a magnet to switch the accelerated beam towards one of the seven possible experimental beam lines (see Figure 5).

Figure 5. Analysed beam line

1) ion pump, 2) BPM, 3) slits, 4) Faraday cup, 5) quadrupoles, 6) switching magnet

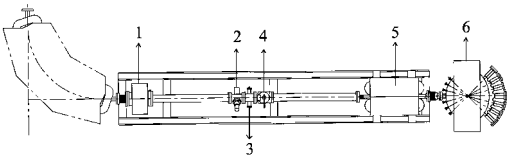

The accelerator is equipped with a special energy scanning system that allows one to vary in very fine steps the beam energy without changing the field in the analysing magnet.

The entire facility is remote controlled from an operator console located in the data acquisition room that is outside the accelerator concrete hall (see Figure 6).

Figure 6. Control and data acquisition room

Accelerator performance

Acceptance tests beam currents

Table 1 lists the series of tests negotiated with NEC as part of the performance specifications for our accelerator. For the choice of the different tests we have mainly taken into consideration the kind of beam and energy required for future experiments in our laboratory, as for instance RBS at medium and high energies, NRA including resonances, PIXE, ion implantation and irradiation of materials.

Table 1. Acceptance beam tests currents for different ion species

Particle	^{1}H [a, d]	^{1}H [a, d]	^{28}Si [a]	^{28}Si [a, d]	^{14}N [a]	^{4}He [b]	^{4}He [b]	^{4}He [b]	^{14}N [b]
Current (μA) [c]	5	0.8	30	5	4	1	0.8	0.8	1
Voltage (MV)	1.25	0.3	3	0.3	3	3	4/3	0.9	7/4

[a] Tests made using the RF charge exchange ion source.

[b] Tests made using the SNICS ion source

[c] Electrical current of the most probable charge state.

[d] Tests that have been already passed satisfactorily.

Moreover, the operation of the machine in extreme conditions of low and maximum voltage potential are checked. The measurements are performed after the switching magnet, at a deflection angle of 30°, two meters away from the output port of the magnet, through a 3 mm diameter aperture in front of a suppressed Faraday cup, which is representative of actual experimental conditions.

As the laboratory system has been installed recently, only some of the acceptance tests have been already completed, in particular those run at low and medium terminal voltage using the SNICS source. We are presently (September 1998) undergoing the remaining tests with the co-operation of an NEC engineer.

Beam energy calibration

A first series of measurements have been carried out for the absolute energy calibration of our Tandem accelerator using 991.86 keV $^{27}Al(p,\gamma)^{28}Si$ and 2409 keV $^{24}Mg(p,p'\gamma)^{24}Mg$ narrow resonances, respectively. From the above experiments the energy spread of the proton may also be determined. The γ-rays were detected with an 3"×3" NaI scintillator, located at 0º, with its front face at 1 cm from the experimental chamber. The ripple of the terminal voltage was measured simultaneously during the acquisition of the γ-rays spectra using an ADC in the Sample Voltage Analysis mode to monitor the capacitive pick-off (CPO) signal from the accelerator.

For the $^{27}Al(p,\gamma)^{28}Si$ reaction, energy steps of the proton beam of about $\Delta E \approx 140$ eV were achieved by setting the accelerator in slit mode and changing the magnetic field value at the analysing magnet by steps of 0.1 gauss. Figure 7 shows the excitation curve obtained with a 200 nm Al_2O_3/Ta film.

The disagreement between the value of the Generating Volt Meter (GVM) at the control console and the actual terminal voltage corresponding to the resonance energy is as follows: $\Delta V = V_{actual} - V_{GVM} = 2.5 \pm 0.5$ kV.

The experimental beam energy spread calculated from the edge in Figure 7 corresponds to less than 1 keV (FWHM) and the simultaneously measured voltage ripple was 180 volts (FWHM)*, corresponding to an energy spread of 360 eV for the proton beam. The excess width of about 600 eV could arise essentially from the stripping process, which up to now has not been optimised with respect to minimum energy broadening by varying the nitrogen gas pressure, as well as from the energy spread at the injection and from target surface contamination.

* This corresponds to the voltage ripple average value. We have found an important spread in the measured values of the terminal ripple, which indicates that the slit feedback system for the potential stabilization was not working properly. We are presently taking care of this problem.

Figure 7. Excitation curve for the 992 keV $^{27}Al(p,\gamma)^{28}Si$ resonance using an 200 nm thick Al_20_3/Ta film

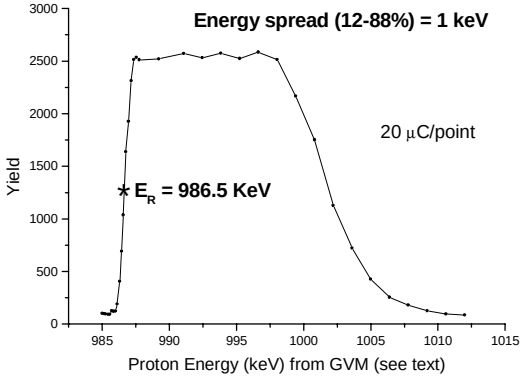

In Figure 8 is plotted the excitation curve for the $^{24}Mg(p,p'\gamma)^{24}Mg$ resonance at 2409 keV measured using a 200 nm thick MgO/Ta film. The observed discrepancy $\Delta V = V_{actual} - V_{GVM}$ is only 8 kV. These results are very satisfactory, as the relative error between the read beam energy (calculated from the GVM value) and the actual beam energy is lower than 1% for the two different energies explored. Further measurements at other energies will be performed in the near future to establish the general law for the observed deviation ΔV as a function of V_{GVM}.

Figure 8. Excitation curve for the 2409 keV $^{24}Mg(p,p'\gamma)^{24}Mg$ resonance using an 200 nm thick MgO/Ta film

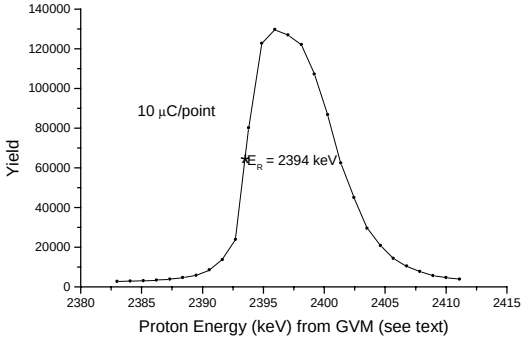

Acknowledgements

We warmly thank our colleagues from Paris University, G. Amsel and J. Moulin for their constant support all along this project and J.M. Guigner, E. Girard and I. Vickridge, for precious advice. The conversations with J. Salomon and T. Calligaro from the Louvre accelerator facility have been of great help. We thank G. Battistig from the Hungarian Research Institute for Materials Science in Budapest for providing us with the thin film targets.

ELECTRON EMISSION FROM HOLLOW ATOMS FORMED BELOW A SURFACE

N. Stolterfoht, M. Grether, D. Niemann, J.-H. Bremer, M. Rösler
Hahn-Meitner Institut, Bereich Festkörperphysik, Glienickerstr. 100, D-10109 Berlin, Germany

Abstract

Experimental and theoretical methods were used to study the formation of hollow atoms during the interaction of highly charged ions near the surface of a solid. To exhibit the static aspect of hollow atoms above and below a surface, results obtained from the density functional method were applied for electron charge densities plots. The dynamic properties of hollow atoms are revealed by means of a cascade model that includes the filling of inner shell orbitals via Auger transitions and collisional charge transfer. The theoretical results are compared with experiments using Auger spectroscopy. Besides Auger electrons the production of low-energy electrons are studied. These electrons are primarily produced by auto-ionising transitions in high Rydberg states of hollow atoms formed above the surface. The low-energy region exhibits structures that can be attributed to the production of surface and bulk plasmons.

Introduction

In the past, considerable interest has been devoted to studies of slow highly charged ions interacting with surfaces [1-12]. When a slow and highly charged ion approaches a surface, several electrons are resonally transferred from the conduction band of the solid to the ion. Thus, in front of the surface, a “hollow” atom is produced with many electrons in higher orbitals and empty intermediate shells [5,11]. The hollow atoms are affected by dielectronic processes such as auto-ionisation where the electron-electron interaction leads to the ejection of electrons and a relaxation of the electrons in the Rydberg orbitals.

The interaction of highly charged ions in front of the surface has been treated in detail by Burgdörfer *et al.* [6]. When the ion approaches the surface, it is known from the classical over-the-barrier model that resonant charge transfer takes place into orbitals whose outer boundary just touches the surface. Within the framework of the over-the-barrier model it is assumed that the transfer of the electrons is rapid and that the ion is essentially neutralised. Furthermore, the picture implies that lower lying orbitals are continuously filled, while higher lying orbitals are depopulated as the ion approaches the surface [12,6]. Electrons in higher lying orbitals are removed by ejection into the vacuum and, more probable, by re-entering into the solid. The flow of the Rydberg electrons back into the solid and the additional capture of electrons into lower orbitals are reasons for a shrinking of the electronic charge cloud. Hence, the diameter of the hollow atom decreases as it approaches the surface.

When the projectile hits the surface, the remaining Rydberg electrons are removed (peeled off) so that a highly charged ion is again produced [5,6,12]. Simultaneously, during the passage into the surface, the highly charged ion strongly attracts several electrons from the conduction band and, hence, it induces a negative charge cloud dynamically screening the nucleus [13,14]. The appearance of an intense screening cloud, denoted C, is the outstanding property of a slow highly charged ion moving below the surface. The C cloud gives rise to hollow atoms whose dimensions are much smaller than those produced outside the solid. Subsequently, as the hollow atom travels in the solid, the inner shell orbitals are successively filled by Auger transitions and collisional charge transfer [15].

To study the structure of hollow atoms, we evaluated the density of the induced charge cloud in a self-consistent manner within the framework of an atomic Hartree-Fock method and a density functional approach. This was done to visualise the electron clouds formed around the highly charged ions above and below the surface [16]. In both cases the induced electron densities are relatively intense so that non-linear theories are required to describe their formation. Hence, the use of self-consistent field methods is adequate. The calculations yield wave functions for the associated orbitals and Auger transition energies, which can be compared with experiment.

In this work, we report on experimental work performed with Ne^{9+} incident on Al and C. The experiments were carried out using very slow ions at energies as low as a few ten eV. Particular attention was devoted to the analysis of Auger electrons ejected below the surface. The measured Auger spectra reveal pronounced structures, which can be attributed to the filling state of the hollow atom. The analysis of the measured spectra shows that Auger spectroscopy is well suited to gain information about dynamic properties of a hollow atom moving just below the surface.

Experimental methods and results

The experiments were performed using the 14.5-GHz ECR source at the Ionenstrahl-Labor (ISL) of the Hahn-Meitner Institut in Berlin [17]. The ion source provides projectiles with energies up to 20q keV where q is the charge state of the extracted ions. The end of the beam line is equipped with a deceleration lens system to extract ions at energies as low as 5q eV. The beam line can be set on a high voltage so that the experimental apparatus can be operated on ground potential.

The experiments were conducted in an ultra-high-vacuum chamber including an electron spectrometer and facilities for surface preparation and examination. The apparatus has been described in detail previously by Köhrbrück *et al.* [9] so only a few details shall be given. The base pressure during the measurements was a few 10^{-10} mbar. Auger electron spectroscopy was used to verify the cleanness of the surface. After careful cleaning no contaminations of the surface by C, N, and O could be observed. Highly charged hydrogen like Ne^{9+} was used to bombard the targets Al and C. After the ions were accelerated, they were magnetically analysed and collimated to a diameter of about 1 mm at the position of the target. Electrons ejected by the interaction of the ions with the surface were measured with an electrostatic parallel-plate spectrometer whose observation angle could be varied in a wide range. The electron spectra were normalised to an absolute scale taking acceptance angle, resolution and transmission of the spectrometer and the efficiency of the channeltron into account.

A typical K-Auger spectrum for 0.4-keV Ne^{9+} incident on Al is given in Figure 1. The spectrum shows essentially three peaks that can be associated with the decay modes KL_1L_1, KL_1L_{23} and $KL_{23}L_{23}$ of Ne with a K vacancy. The structure at higher energies labelled *KLC* is produced by Auger transitions where an electron from the induced electron cloud C is ejected. Each peak of the *KLL* group involves contributions from Ne projectiles with different numbers n_L of electrons occupying the L shell. It is important to note that the relative intensities of the Auger peaks depend on the filling state of the hollow atom.

Figure 1. Spectrum of K-Auger electrons ejected by interaction of Ne^{9+} ions with an Al surface. The bar diagram is calculated using a cascade.

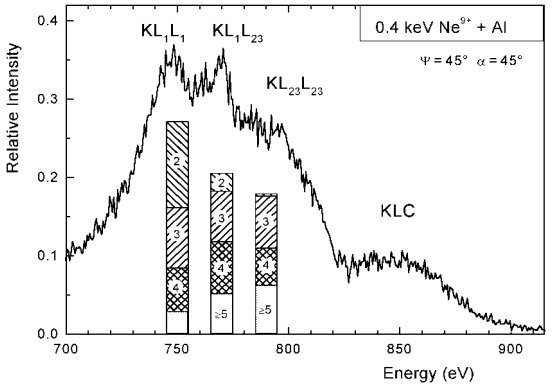

Figure 2 depicts further examples for K-Auger electron spectra. To demonstrate the influence of the solid, the spectra obtained with the solids C and Al are compared with previous results using an He gas target [18]. In the latter case, the projectile Ne^{6+} with an initial configuration $1s^22s^2$ is ionised in the 1*s* shell so that the $1s2s^{22}S$ state is produced. It decays via KL_1L_1 Auger transitions into the final state $1s^{21}S$ giving rise to monoenergetic electrons with energy of 652 eV. Another Auger maximum, observed at higher energies, is due to the configuration 1*s*2*s*2*p* produced by 1*s* ionisation of the projectiles in the initial metastable state $1s^22s2p^3P_0$ [18].

Figure 2. Comparison of electron spectra measured for Ne^{9+} impact on He gas targets and solid target C and Al. The spectrum from the He target [18] exhibits a prominent Auger line at 652 eV which originates from the Auger transition $1s2s^{22}S \rightarrow 1s^{22}S$. The corresponding line is shifted by 95 eV for the C and Al target due to solid state effects.

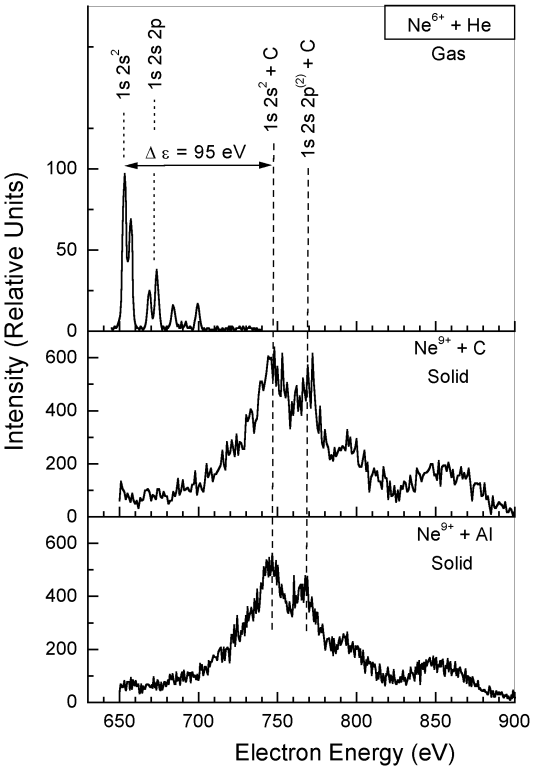

The two spectra obtained with Ne^{9+} incident on the solid targets C and Al contain lines for the same KL_1L_1 Auger transition $1s2s^{22}S \rightarrow 1s^{22}S$, but shifted to the energy of 748 eV. This shift is due to the influence of the solid producing a screening cloud around the ion. It is important to note that this energy shift produced by the solid is significant, i.e. 95 eV. On the other hand, it is surprising to see that the energy shift is the same for the solids C and Al so that the corresponding $1s2s^{22}S$ lines are found at a single energy of about 748 eV.

There are several indications that most of the emission of the K-Auger electrons takes place below the surface if the ion is directed under normal incidence to the surface plane. The most convincing evidence for the location of the K-Auger decay may be achieved from the angular distributions of the Auger electrons. In case of an above-surface emission the angular distribution is expected to be isotropic. Deviations from isotropy may occur outside the solid, however, the statistical average over a large number of states is likely to cancel such anisotropies. Inside the solid, definite anisotropy effects are expected due to the attenuation of the electrons during their transport to the surface. Electrons ejected at small angles with respect to the surface plane are subject to a significant attenuation due to longer travel distances of the electron in the solid. On the contrary, attenuation effects are relatively small for observation angles perpendicular to the surface plane.

The results by Köhrbrück *et al*. [19] using of the attenuation method are given in Figure 3. It is seen that the K-Auger emission from 0.135 keV Ne^{9+} incident on Al is strongly anisotropic. This shows for the present case that the K-Auger electrons are essentially ejected below the surface.

Figure 3. Angular distributions of K-Auger electron spectra for 0.135 keV Ne^{9+} incident on Al. The projectile angle of incidence is $\Psi = 45°$ and the observation angle relative to the surface plane is α whose values are indicated at the spectra. From Köhrbrück *et al*. [19].

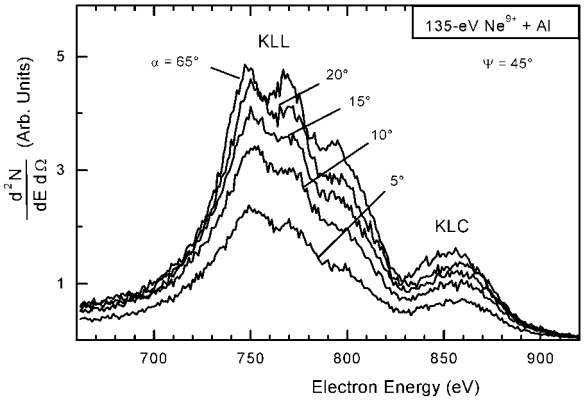

The same result was found by Grether *et al*. [20] for the spectral component observed at 748 eV. It should be added that the present scenario changes when projectiles are used under grazing incidence so that they are reflected from the surface [21]. In this case, the Auger electrons may be ejected between the topmost atomic layer and the jellium edge where anisotropies are produced by electron diffraction effects [22]. In the present work, however, experimental conditions are chosen where the ions enter into the solid. For this case, diffraction effects on Ne-K Auger electrons have been found to be small [15].

Static aspect of hollow atoms

In contrast to extensive studies of hollow atoms moving in front of the surface, less information is available about their behaviour below the surface. As noted before, highly charged ions have the outstanding property that they attract a significant amount of electrons in the solid to screen their nuclear charge. Hence, they induce the relatively large screening cloud denoted C. In this case it is evident that non-linear theories are required to adequately model the C cloud in the solid. Such a study of hollow atoms in a solid has recently been performed by Arnau *et al.* [13] who evaluated the screening function for Ne^{9+} in Al using a self-consistent field method. In the analysis, the density functional theory (DFT) was applied to the problem of a static charge impurity in jellium [23]. Thus screening functions were determined modelling the features of hollow projectile atoms. The solid-state effects were found to significantly influence the total energies of ions surrounded by jellium. More details are given in the previous work by Arnau *et al*. [13]. From total energy differences, the orbital energies for the multi-charged Ne ion (with one K-shell vacancy) in Al were calculated.

The KL_1L_1 transition in an atom with an occupied $n = 3$ orbital is found to be nearly equal to the energy of the corresponding Auger transitions in the solid. This finding is plausible, since the charge clouds for the two cases are found to be quite similar. However, it is not quite clear as to why the electrons in the isolated atom have to be placed in $n = 3$ and not e.g. in $n = 4$. It appears that the charge cloud induced in the solid is best modelled by atomic electrons located in the lowest lying orbital that is not bound in the solid. Although it is not fully understood, this rule is commonly used when energies for Auger transitions were determined for hollow atoms moving at the surface and inside the solid [19,24,25].

To visualise the hollow atom inside the solid, Figure 4 shows density plots of the electronic charge cloud. The bottom of the graph depicts the corresponding density. In this case it is seen that the 1*s* electron density is clearly separated from the induced charge cloud that maximises near 1.5 a.u. At about 0.8 a.u. the charge density exhibits a deep valley giving rise to a remarkable empty space which is a characteristic feature of the hollow atom. It appears that this feature is more pronounced in the solid as compared to that of the hollow atom located at large distances outside the surface.

Figure 4. Density plots of hollow, semi-hollow, and nearly filled Ne atoms in Al. The data are calculated by means of the density functional theory [23]. Note that the density is multiplied by the square of the distance *r*.

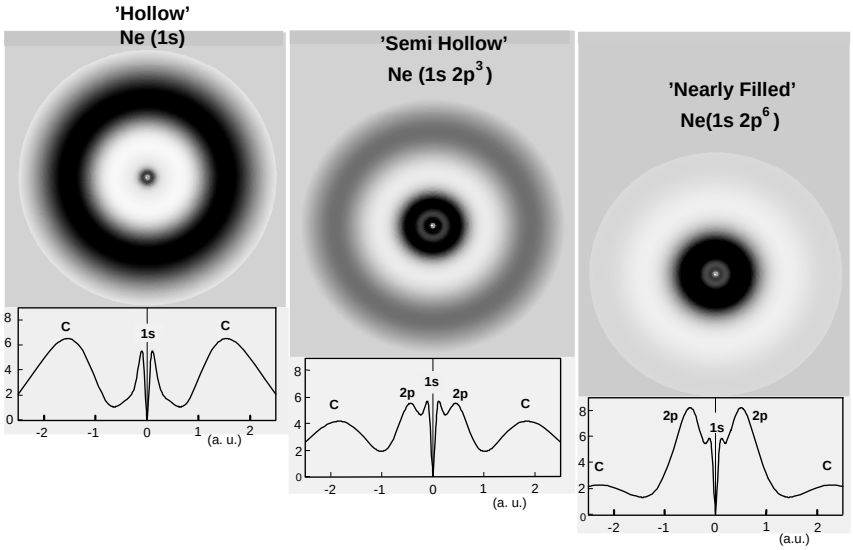

Figure 2 indicates that the Auger peaks for the Al and C solids have the same energy shift with respect to the He target. Hence, it follows under stationary conditions that the induced charge cloud is primarily a signature of the projectile whereas the influence of the solid is much less important. This phenomenon becomes plausible when one recalls that a highly charged projectile affects the solid in a non-perturbative manner. It should be realised that the induced charge density in its maximum is about a factor of five more intense than the background density of the conduction band electrons (jellium). This clearly shows the outstanding signature of the hollow atoms formed by a highly charged nucleus, i.e. the large charge cloud induced within the solid.

When the hollow atom moves inside the solid it suffers binary collisions with individual target atoms. In these collisions the L shell ($n = 2$) becomes more and more filled due to charge transfer between inner shells [15]. As expected the induced charge cloud around the projectile decreases in intensity as the filling state n_L of the L shell increases. Accordingly, as seen from Figure 4 the empty space diminishes as the hollow atom gets more and more filled in the L shell. When six electrons are located in the L shell, the induced electron density is barely visible. The mechanisms responsible for the filling of the hollow Ne atom will be treated next.

Dynamic aspects of hollow atoms

The dynamic properties of a hollow atom are its decay modes and life time associated with the successive filling of its empty inner space. Inside the solid the filling of the Ne L shell is governed by electron capture processes between inner orbitals of the projectile and a target atom that occur in

competition with the corresponding Auger transitions. Let $\sigma^c_{n_L}$ be the cross-section for the electron capture into the L shell characterised by the filling state n_L. The filling sequence of the hollow atom is determined by the collision rate $\Gamma^c_{n_L} = n_s v \sigma^c_{n_L}$ where n_s is the atomic density in the solid and v is the projectile velocity [19]. Hence, it is expected that the collision rate increases with the projectile velocity. Thus, the dynamic properties of the hollow atom are likely to be influenced by the variation of the projectile velocity.

To study the filling of the hollow Ne atom, Auger spectra were recorded as a function of the projectile energy. Figure 5 shows examples for Ne^{9+} impact on Al at relatively low projectile energies of 0.15, 0.4, and 0.8 keV. It is recalled that the spectral structures attributed to the transitions KL_1L_1, KL_1L_{23} and $KL_{23}L_{23}$ provide information about the filling state of the hollow atom. The Auger peaks observed at higher energies are associated with a relatively large filling state n_L of the hollow atom. It is seen that this Auger peak increases in intensity as the projectile energy increases.

Figure 5. Experimental K-Auger spectra for Ne^{9+} incident on Al at the energies of 0.15, 0.4 and 0.8 keV. The projectile angle of incidence is $\Psi = 45°$ and the observation angle relative to the surface plane is $\alpha = 45°$. The bar diagram is evaluated using the cascade model discussed in the text. The parameter n_L stands for the occupation number of the L shell.

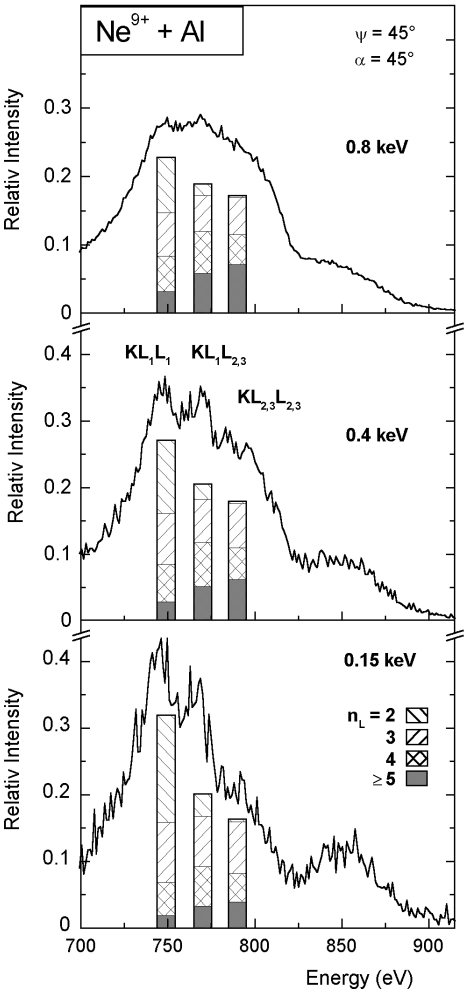

The same dependence can be verified from the bar diagrams which were calculated by means of the cascade model discussed above. It is noted that the theoretical data are not shown here with the aim to reproduce exactly the experimental spectrum. Rather, they are given to assist in its qualitative understanding. The first prominent peak at 748 eV corresponds primarily to the L-shell occupation numbers n_L = 2 and 3. The next peak at higher energies includes significant components from n_L = 4 and the third peak contains Auger intensities due to occupation numbers as large as n_L = 8.

The spectrum obtained for the projectile energy of 0.15 keV is dominated by small L-shell occupation numbers, i.e. the bar at 748 eV is relatively intense. Hence, the K-Auger transitions take place at the beginning of the L-shell filling sequence which indicates a relatively slow filling of the Ne L shell. Therefore, it is expected that the collisional capture processes are unimportant at the low projectile energy of 0.15 keV. With higher projectile energies the increasing intensity of the Auger peaks attributed to larger n_L values indicate that charge transfer becomes important.

To gain information about the onset of the collisional electron transfer, we performed calculations by means of the Landau-Zener model using model potential curves described in more details previously [26]. The transfer processes occur at curve crossings of the potential curves correlating with the L-shell orbitals of the collision partner Ne and Al [15]. In Figure 6, the results for the filling state of n_L = 0, 1 and 2 are shown as a function of the projectile energy. Indeed, the calculated cross-sections exhibits a threshold in a relative small projectile energy range. This finding is consistent with the increase of the spectral intensity associated with n_L = 6 - 8 in the experimental spectra. Therefore, both the theoretical and experimental results in Figure 5 show that the filling of the hollow atoms varies significantly in a relative small energy range.

Figure 6. Cross-sections for charge exchange from Al atoms into hollow neon atoms with the number n_L of L-shell electrons as a function of the projectile energy. The data are calculated using the Landau-Zener model with potential curves from a previous model [26].

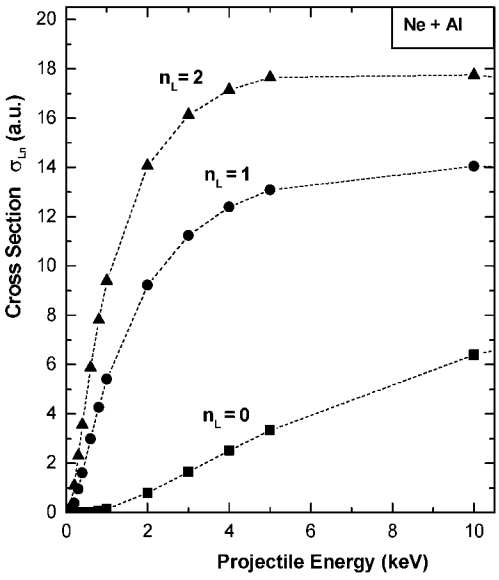

It should be added that previous studies of Auger spectra by Limburg *et al*. [27] and X-ray spectra by Briand *et al*. [5] are similar to the present one (Figure 5). In some cases these authors draw different conclusions for the effects changing the spectral structures. This is primarily due to the fact that they used other experimental parameters such as angle of incidence and impact energy.

For the present cases, it is recalled from our previous discussion that the emission of Ne-K Auger electrons occurs predominantly inside the solid. It is concluded that the filling of the hollow atoms is governed by the charge transfer between inner shells of the projectile and target atoms. From the present model the filling time of the hollow atom can be estimated. For instance, at the lowest projectile energies, the typical filling time, corresponding to the life time of the hollow atoms, is of the order of 10^{-14} sec. This time is much longer than a few 10^{-17} sec which is the time unit for atomic processes.

Acknowledgement

The early stage of this work was supported by the Human Capital and Mobility programme under the contract number CHRT-CT93-0103.

REFERENCES

[1] H.D. Hagstrum, *Phys. Rev*. 91, 543 (1953), ibid, 96 (1954) 325.

[2] U.A. Arifov, E.S. Mukhamadiev, E.S. Parilis and A.S. Pasyuk, *Zh. Tekh. Fiz*. 43 (1973) 375 [Sov. Phys. – Tech. Phys. 18 (1973) 240].

[3] M. Delaunay, M. Fehringer, R. Geller, P. Varga, and HP. Winter, *Europhys. Lett*. 4 (1987) 377.

[4] H.J. Andrä, *Nucl. Instrum. Methods* B 43 (1989) 306.

[5] J.P. Briand, L. de Billy, P. Charles, S. Essabaa, P. Briand, R. Geller, J.P. Desclaux, S. Bliman and C. Ristori, *Phys. Rev. Lett*. 65 (1990) 159.

[6] J. Burgdörfer, P. Lerner and F.W. Meyer, *Phys. Rev*. A 44 (1991) 5674.

[7] L. Folkerts, R. Morgenstern, *Europhys. Lett*. 13, 377 (1990) and L. Folkerts, R. Morgenstern, *Z. Phys*. D 21 (1991) S351.

[8] F.W. Meyer, S.H. Overbury, C.C. Havener, P.A. Zeijlmans van Emmichoven, D.M. Zehner, *Phys. Rev. Lett*. 67 (1991) 723.

[9] R. Köhrbrück, K. Sommer, J.P. Biersack, J. Bleck-Neuhaus, S. Schippers, P. Roncin, D. Lecler, F. Fremont and N. Stolterfoht, *Phys. Rev*. A 45 (1992) 4653.

[10] S. Schippers, S. Hustedt, W. Heiland, R. Köhrbrück, J. Kemmler, D. Lecler, J. Bleck-Neuhaus and N. Stolterfoht, *Phys. Rev*. A 46 (1992) 4003.

[11] J. Burgdörfer, Review of Fundamental Processes and Applications of Atoms and Ions, ed. C.D. Lin (World Scientific, Singapore, 1993) p. 517.

[12] F. Aumayr and HP. Winter, *Comments At. Mol. Phys*. 29 (1994) 275.

[13] J. Burgdörfer, C. Reinhold and F. Meyer, *Nucl. Instrum. Methods in Phys. Res*. B 98 (1995) 415.

[14] A. Arnau, R. Köhrbrück, M. Grether, A. Spieler, and N. Stolterfoht, *Phys. Rev*. A 51 (1995) R3399.

[15] N. Stolterfoht, A. Arnau, M. Grether, R. Köhrbrück, A. Spieler, R. Page, J. Thomaschewsk, A. Saal and J. Bleck-Neuhaus, *Phys. Rev*. A 52 (1995) 445.

[16] N. Stolterfoht, D. Niemann, M. Grether, A. Spieler, C. Lemell, F. Aumayr and H.P. Winter, *Nucl. Instrum. Methods in Phys. Res*. 124, 303 (1997).

[17] B. Martin, M. Grether, R. Köhrbrück, U. Stettner, H. Waldmann, Proceedings of the 11th International Workshop on Electron Cyclotron Resonance Ion Sources (ECRIS 11), (Groningen, 1993), p. 188.

[18] A. Itoh, D. Schneider, T. Schneider, T.J. Zouros, G. Nolte, G. Schiwietz, W. Zeitz and N. Stolterfoht, *Phys. Rev*. A 31 (1985) 684.

[19] R. Köhrbrück, M. Grether, A. Spieler, and N. Stolterfoht, R. Page, A. Saal and J. Bleck-Neuhaus, *Phys. Rev*. A 50 (1994) 1429.

[20] M. Grether, A. Spieler, R. Köhrbrück and N. Stolterfoht, *Phys. Rev*. A 52 (1995) 426.

[21] L. Folkerts, S. Schippers, D.M. Zener and F.W. Meyer, *Phys. Rev. Lett*. 74 (1995) 2204.

[22] J. Thomaschewski, J. Bleck-Neuhaus, M. Grether, A. Spieler, N. Stolterfoht, *Phys. Rev*. A 57, 3665 (1998).

[23] E. Zaremba, L.M. Sander, H.B. Shore and J.H. Rose, *J. Phys*. F 7 (1977) 1763.

[24] H.J. Andrä, A. Simionovici, T. Lamy, A. Brenac, A. Pesnelle, *Europhys. Lett*. 23 (1993) 361.

[25] S. Schippers, J. Limburg, J. Das, R. Hoekstra and R. Morgenstern, *Phys. Rev*. A 50 (1994) 540.

[26] N. Stolterfoht, in Progress in Atomic Spectroscopy, Part D, ed. H. Kleinoppen, (Plenum Press, New York, 1987) p. 415.

[27] H. Limburg, S. Schippers, I. Hughes, R. Hoekstra, R. Morgenstern, S. Hustedt, N. Hatke and W. Heiland, *Phys. Rev*. A 51 (1995) 3873.

SESSION VI

Application of PET

Chairman: S.M. Qaim

Chairman's summary

As an introduction to the session, the Chairman remarked that in recent years Positron Emission Tomography (PET) has gained considerable significance in diagnostic nuclear medicine and a large number of PET centres have been established world-wide. Several factors contributed to this progress, the most important ones being the construction of high intensity accelerators dedicated to radionuclide production, the development of high quality β^+ emitting tracers and the improvement in medicinal instrumentation. The ensuing talks were then devoted to those topics.

F. Tárkányi (ATOMKI Debrecen, Hungary) discussed the various types of accelerators available in the market for production of β^+ emitters. Cyclotrons accelerating both positively and negatively charged ions are used. In the latter case, the beam quality is better. Furthermore, the beam can be split into two or more units so that several simultaneous irradiations are possible. In general, cyclotrons accelerating either single particles ($E_p \leq 12$ MeV) or two particles ($E_p \leq 18$ MeV, $E_d \leq 10$ MeV) are used. All the major short-lived β^+ emitting radionuclides can be produced at those machines. Some efforts are underway to produce very small accelerators ($E_p \leq 4$ MeV) which could be placed in a hospital environment without any shielding. Evidently, such machines have to deliver ~1 mA currents to be able to produce radioisotopes in quantities sufficient for medical applications. The targetry problems are rather severe. Further feasibility studies are essential prior to introducing this technology.

S.M. Qaim (FZ Jülich, Germany) reviewed the production of positron emitting tracers. This interdisciplinary field involves a whole chain of expertise, starting with targetry and precursor production, followed in sequence by chemical synthesis and purification, and ending with the quality control of the medicinal product. Due to the high level of radioactivity involved, remote controlled methods have to be developed. Production should be considered under two aspects: (a) routine medicinal investigations, (b) research oriented studies. Regarding the first, low energy nuclear reactions at small-sized cyclotrons are used and the biomolecule of interest is labelled with one of the four major organic β^+ emitters: ^{11}C ($T_{½}$ = 20 min), ^{13}N ($T_{½}$ = 10 min), ^{15}O ($T_{½}$ = 2 min) and ^{18}F ($T_{½}$ = 110 min). The methods of production have been generally well worked out and today, for most of the commonly used radiopharmaceuticals, automated production units are commercially available. The production for research oriented studies, on the other hand, entails considerable research work, involving development of both new radiopharmaceuticals (labelled with one of the above mentioned β^+ emitters) and new β^+ emitters. The latter area of work is of more relevance to the activities of the NEA.

H. Herzog (FZ Jülich, Germany) outlined the PET instrumentation, modelling and clinical applications. The positron emitted by the administered radiopharmaceutical is annihilated within the tissue and the resulting photon pair is detected externally by a ring of scintillation detectors coupled to coincidence electronics. By using appropriate algorithms the measured radiation is reconstructed into tomographic images. The development of PET instrumentation over the last 20 years has led to systems with an image resolution of 4-5 mm. An analysis of primary PET images via biokinetic modelling furnishes parametric images of metabolic functions. Thus modelling is a very important feature of PET studies. A number of radiopharmaceuticals labelled with β^+ emitters are applied, the recent increase in PET installations, however, is due to the high sensitivity of the ^{18}FDG-PET to localise primary tumours and their metastases.

A concluding discussion suggested that the PET technology (incorporating all the three aspects mentioned above) is progressing rapidly. It is a fast and quantitative diagnostic tool. Furthermore, it is developing in a research tool for investigating drug effects and disease development on a molecular level. The field of study is financially well supported. As far as the NEA is concerned, only some limited action may be necessary (see the Executive Summary).

ACCELERATORS USED FOR ROUTINE PRODUCTION OF PET RADIOISOTOPES

Ferenc Tárkányi and Ferenc Szelecsényi
Institute of Nuclear Research of the Hungarian Academy of Sciences
P.O. Box 51, H-4001, Debrecen, Hungary

Abstract

Accelerator produced radioisotopes find wide application in the field of nuclear medicine. The positron emitters required for high resolution positron emission tomography (PET) are of particular interest. In the last decade efforts on development of accelerators and target technology have greatly increased. In this paper we give a survey on the recent trends and developments in the area of accelerators used for production of radioisotopes for PET.

Introduction

Over the past decade there has been an increase in the application of positron emitters for diagnostic purposes world-wide in the field of nuclear medicine. Application and development of PET technology including the accelerators used is driven by its usefulness and its financial availability. In the last decade a meaningful progress has been made in the field of PET accelerators.

During a PET investigation biomolecules labelled with radioisotopes are administered into the human body and are detected in coincidence by an array of detectors (PET). A limited number of radioisotopes and an almost unlimited number of compounds help increase the applicability of the PET technique. The production of labelled compounds, however, is only the first stage of any PET study.

The accelerator is just a technical tool for the manufacturing process of the necessary labelled molecule, which consist of the following main production steps:

- *Production of radioisotope:*
  - production of isotopically enriched row materials;
  - fabrication of bombardment targets;
  - accelerator operation for target bombardment;
  - radiochemical extraction of the radioisotope.
- *Production of the labelled compound:*
  - pharmaceutical manufacturing of the final product;
  - quality control during production stages and of the final product;
  - packing operations (if necessary);
  - distribution and delivery (in case of not local use).

The production steps strongly depend on the radioisotopes and the labelled compounds. The different steps are closely connected and they are built on each other. These main steps are usually followed by waste disposal of the highly radioactive waste and highly toxic chemicals.

The requirements to produce different radioisotopes for different applications lead to different installations and different accelerators. The accelerators used for the routine production of PET, SPECT (single photon emission computed tomography) and therapeutic radioisotopes can be classified on different basis (see Table 1).

Wide varieties of accelerators are available today. Both old and new generation accelerators have recently been used for production of PET isotopes. This synopsis is based on several overviews and progress reports discussing the future trends of medical isotope production, status and new developments of different accelerators and isotope production targetry. They can be found in the proceedings of various conferences, i.e. *Cyclotrons and their Applications, Targetry and Target Chemistry, European Particle Accelerator Conferences, Medical Aspects of Cyclotrons, Symposium*

Table 1. Classification of the accelerators used for isotope production

Aspects	Classification
Field of the application	Dedicated or multipurpose
Energy range	I (<5 MeV), II (<12 MeV), III (<20 MeV), IV (<40 MeV),V (<100 MeV), VI (<1 GeV)
Accelerated particle	Single, double or multiparticle
Principle of acceleration	Electrostatic, RFQ, linear accelerator , cyclotron, synchrocyclotron etc.
Beam intensity	Low (<10 μA), middle(<50 μA) and high (up to~1 mA)
Place of operation	Hospital, production company, research institute, etc.
Users of the products	Local, regional or world-wide

on Radiopharmaceutical Chemistry, and in corresponding journals, i.e. *Applied Radiation and Isotopes*, *Radiochimica Acta*, *Labelled Compounds and Radiopharmaceutical*. Brochures of different companies involved in commercial radioisotope production also provide useful information. In this overview we also use our experiences collected at installations at different technical levels and energy ranges. The requirement for PET radioisotope production – concerning the physical capability – can be easily fulfilled by the requirement of isotope production for SPET in all energy ranges, but routine PET production requires other aspects of optimisation. It is not an easy task to determine what is the optimal accelerator and what are the optimum energy ranges for production of PET isotopes. In the decision of the optimisation of the installation, the time period of the project and the running expenses are becoming more and more important.

In the following we summarise the requirements for the main physical parameters of the accelerator. We also describe the new trends and technological changes in the field of the dedicated machines.

Requirements for the physical parameters of the dedicated accelerator

According to the simple equation describing the yield of a nuclear reaction the accelerator has to provide:

- the required particle(s);
- with optimal energies;
- at high intensities.

A wide variety of radioisotopes has been proposed for PET applications. Recently three of them ^{11}C, ^{13}N, ^{15}O (so called bio-isotopes) and ^{18}F (used for replacing H and OH groups) are used nearly exclusively in the every day routine and nearly 50 other alternative positron emitting radioisotopes are still candidates for a broader application.

Reviewing the main production routes (see Tables 2 and 3), and the required amount of these radioisotopes, the following main conclusions can be deduced:

- The most important four isotope and the significant part of alternative PET isotopes can be produced via low energy (p,n), (p,α) and in a few case low energy deuteron induced reactions.
- In the remaining cases moderate energy reactions (p,2n), (p,3n), (d,2n), (d,3n) or very high energy spallation reactions are the most favourable or practically the only production routes.

- The proton induced reactions have the higher production yields and almost all radioisotope can be produced with protons (in a few exceptional cases the deuteron induced reactions are more productive).

- From the point of view of production of the bigger part of alternative radioisotopes, highly enriched targets are required with consequences of high price and the connected recovery problems.

- The requirement of PET investigations can be fulfilled with a moderate amount of radioisotopes from the point of view of available capacity from the accelerator side.

- Reviewing the possible targets the main important four isotopes and several other PET isotopes can be produced using easy handled gas or liquid target technology. The alternative positron emitters can be produced using solid targets.

Table 2 contains the optimum energies for the production of the four most frequently used PET isotopes. They are optimal from the point of view of the yield but not concerning economical factors. When the energy is higher, the used power or the impurity levels could be too high. When the energy is low the yield drops sharply and the target technology is becoming very difficult. The yield is proportional to the intensities, therefore it is good to have high intensities, but with uniform current distribution. Unfortunately, too high beam intensity can cause significant drop of the yields due to the loss of target atoms or of the produced activity.

As a final conclusion – from the point of view of the used radioisotopes and their productions routes – these physical requirements can be fulfilled with single (or double) particle machines having low or middle energies. The intensity is reversibly proportional with the energy but higher intensity gives higher flexibility and higher reliability.

Table 2. Production routes of the main PET isotopes

Radio isotope	Half-life	Main prod. route	Energy range (MeV)	Yield (mCi/μAh)	Target (%)	Energy category of the accelerator					
						I	II	III	IV	V	VI
^{11}C	20.4 min	**^{14}N(p,α)^{11}C**	10-3	103	99.6 (nat)		●	●			
		^{11}B(p,n)^{11}C	10-0	31.6	80.1 (nat)	●					
		^{10}B(d,n)^{11}C	10-0	16.8	19.9 (nat)	●					
		^{12}C(^{3}He,α)^{11}C	8-0	4.7	98.9 (nat)	●					
^{13}N	10.0 min	**^{16}O(p,α)^{13}N**	16-7	45	99.8 (nat)		●	●			
		^{12}C(d,n)^{13}N	8-0	15	98.9 (nat)	●					
		^{12}C(^{3}He,pn)^{13}N	8-0	1.8	98.9 (nat)	●					
^{15}O	2.0 min	**^{14}N(d,n)^{15}O**	8-0	64	99.6 (nat)	●	●	●			
		^{15}N(p,n)^{15}O	10-0	60	0.37 (enr)		●	●			
		^{16}O(^{3}He,α)^{15}O	10-0	4.4	99.8 (nat)	●					
^{18}F	1.83 h	**^{18}O(p,n)^{18}F**	16-3	80	0.2 (enr)		●	●			
		^{20}Ne(d,α)^{18}F	14-0	30	90.5 (nat)		●	●			
		^{16}O(^{3}He,p)^{18}F	10-0	4.6	99.8 (nat)	●					

The energy ranges and yields in the above table are estimations based on the most reliable literature sources. The reactions marked with bold letters are the most frequently employed ones.

Table 3. Alternative positron emitters and generator PET isotopes

Radio isotope	Half-life	Main production route	Energy range (MeV)	Yield (mCi/μAh) 100% enr. targ.	Target (%) natural isotopic abundance	Energy category of the accelerator					
						I	II	III	IV	V	VI
^{34m}Cl	32.2 min	^{34}S(p,n)	22-10	50	4.21 (nat)			●			
^{38}K	7.64 min	^{35}Cl(α,n)	20-7	5	75.77 (nat)			●			
		^{38}Ar(p,n)	16-12	21	0.063 (enr)			●			
		^{40}Ar(p,3n)	50-30		99.6 (nat)				●		
^{51}Mn	46.2 min	^{54}Fe(p,α)	16-10		5.8 (enr)			●			
^{52}Mn	5.59 days	^{52}Cr(p,n)	18-10	0.5	83.789 (enr)			●			
^{52}Fe	8.28 h	^{55}Mn(p,4n)	70-45		100 (nat)					●	
^{55}Co	17.5 h	^{54}Fe(d,n)	15-5	1.5	5.8 (enr)			●			
^{61}Cu	3.41 h	^{61}Ni(p,n)	12-9	17.5	1.1 (enr)		●	●			
		^{60}Ni(d,2n)	11-4	2.7	26.2 (enr)				●		
^{64}Cu	12.7 h	^{64}Ni(d,2n)	19-15	10.5	0.926 (enr)				●		
		^{64}Ni(p,n)	12-9	6.7	0.926 (enr)		●	●			
^{72}As	1.08 days	^{72}Ge(p,n)	14-6	9.4	27.66 (enr)			●			
^{75}Br	1.08 h	^{76}Se(p,2n)	30-22	100	9.36 (enr)				●		
		^{74}Se(d,n)	10-7	6.2	9.36 (enr)			●			
		^{78}Kr(p,α)	17-11	1.9	0.35 (enr)			●			
^{76}Br	1.62 h	^{76}Se(p,n)	16-10	8	9.36 (enr)			●			
		^{77}Se(p,2n)	25-16	7	7.63 (enr)				●		
^{82}Rb	6.47 h	^{82}Kr(p,n)	14.5-10	10	11.6 (enr)			●			
		^{83}Kr(p,2n)	30-23	22	11.5 (enr)				●		
^{83}Sr	1.35 days	^{82}Kr(α,3n)	30-15		11.6 (enr)				●		
		^{82}Kr(^{3}He,2n)	30-15		11.6 (enr)			●			
^{86}Y	14.7 h	^{86}Sr(p,n)	14-10	10.8	9.76 (enr)			●			
^{89}Zr	3.27 days	^{89}Y(p,n)	14-8	1.3	100 (nat)			●			
		^{89}Y(d,2n)	22-10		100 (nat)				●		
^{94m}Tc	52.0 min	^{94}Mo(p,n)	13-7	54	9.25 (enr)		●	●			
^{120}I	1.35 h	^{120}Te(p,n)	16-9	62	0.096 (enr)			●			
		^{122}Te(p,3n)	37-32	98	2.603 (enr)				●	●	
^{124}I	4.18 days	^{124}Te(p,n)	13-9	0.54	4.816 (enr)		●	●			
		^{124}Te(d,2n)	16-6	0.65	4.816 (enr)				●		
		^{125}Te(p,2n)	20-10	1.17	7.139 (enr)			●	●		
Generators parent (daughter)											
^{52}Fe(^{52m}Mn)	8.28 h (21.1 min)	^{nat}Ni(p,x)spall.	200-50		nat						●
		^{55}Mn(p,4n)	70-45		100 (nat)					●	
^{62}Zn(^{62}Cu)	9.26 h (9.74 min)	^{63}Cu(p,2n)	30-20	7.8	69.17 (nat)				●		
^{68}Ge(^{68}Ga)	271 days (1.14 h)	^{nat}Br(p,x)spall.	800	0.004	nat						●
		^{66}Zn(α,2n)	45-26	0.005	27.9 (enr)					●	
		^{nat}Ga(p,xn)	55-10	0.04						●	
^{82}Sr (^{82}Rb)	25.6 days (1.27 min)	^{nat}Mo(p,x)spall.	800	0.1	nat						●
		^{85}Rb(p,4n)	60-40	0.4	72.17 (nat)					●	
^{110}Sn(^{110}In)	4.11 h (1.15 h)	^{110}Cd(p,n)	11-8		12.51 (enr)			●			
^{118}Te(^{118}Sb)	6.0 days (3.6 min)	^{nat}Sb(p,x)	55-35		nat					●	
^{122}Xe(^{122}I)	20.1 h (3.62 min)	^{nat}I(p,6n)	85-55		nat					●	
		^{124}Xe(p,x)	43-35	13.5	0.1 (enr)						

There are numerous production routes of the isotopes listed in this table. In accordance with the aim of this paper we selected only a few but the most widely used ones. The yields and energy ranges listed in the above table are estimations based on the most reliable literature sources. In some cases the required radioisotope can be produced with an accelerator of a lower category but the available yield is also lower.

Technological requirements and solutions

The required physical parameters can be accomplished with different technological solutions and at different levels. As a result, the requirements of the accelerators, from the point of view of modern accelerator technology, are very modest. The final goal according to the final aim of the PET programme is to get a cheap, very reliable and easy to handle accelerator and targetry recognising the fact that the irradiation is only a step (first and important one) in the row of steps of production of the labelled compounds and of the final application. The isotope production can be considered as production of raw material for further processing, therefore the aim of which is similar to other serial production has to be the production of the necessary raw material as simple as possible. The amount and the quality of the row material both depend upon the used accelerator and the target technology. These two technological parts are so closely related that the requirements can be formulated together for both of them:

- external irradiations;
- high intensity extracted beam;
- low personal dose exposure during the maintenance;
- provision of target holding system;
- provision of high yield targets for production of most important isotopes;
- high reliability operation;
- simple engineering design;
- automated controls;
- low cost accelerator;
- easy and low cost shielding;
- small, light weight, easily sighted;
- low cost operation;
- reliability.

These requirements can be further completed with the usual service requirements to any industrial equipments, namely:

- efficient installation and commission;
- after-sales backup;
- availability of spare parts;
- confidentiality;
- reliability.

Technological progression in development of cyclotrons and the related targetry

Cyclotron

Surveying the recent developments in low and middle energy accelerator technology, and with reference to the demands for radioisotope production including positron emitters, and to the new trends in the PET investigations, we can conclude that very significant progress have been made in this field. The technology commercialised and the production of very specialised so-called “dedicated accelerators” have been started mainly in the areas of cyclotrons but also at linear accelerators. Radioisotope production with high performance targets and target handling systems were offered by accelerator producers as an option to the accelerator. The most important technological changes in the area of the dedicated cyclotrons can be summarised as follows:

- Since in a compact positive ion machine the extraction process limits the availability of high external currents, the negative ion cyclotrons, limited to proton and deuteron beams but having nearly 100% extraction efficiency (by means of stripping foils), have been introduced and commercially produced. The advantage of the negative ion machines besides the high intensity external beam is the possibility of extraction of two beams simultaneously, the simple change of the energy of the extracted beam, and the low activation of the cyclotron components.

- To ensure a high productivity in isotope production beam currents above mA are available by using high intensity external ion sources (if it is required).

- The method of the change of the energy of the extracted beam offers the possibility to construct fix energy, fix frequency, fix magnetic field machines allowing a very significant simplification of the construction and the services.

- Protons having energy higher than 40 MeV are not required in practice for production of all medically used radioisotopes. For production of the most important four PET isotopes it is sufficient to have 12 MeV, while for production of a broader range of isotopes protons up to 20 MeV are acceptable.

- The power requirements of the cyclotrons were significantly reduced by new deep valley, small hill magnetic field and more simple magnet and coil design. This **“**new magnetic structure” combines the advantages of both separated sector and compact pole structure. The power conversion from the electricity to the extracted beam with the new design was changed from 1% to 15%.

- To avoid the partial stripping of negative ions during acceleration the operating pressure has to be kept low in the negative ion cyclotrons. Small and simple vacuum chamber, large vacuum pumps, separately pumped external source in case of high intensities allow not only the necessary low vacuum pressure, but also the quick establishment of the required vacuum.

- The unnecessary activation of the machine parts was drastically reduced by using the highly efficient stripping extraction, the low activation materials and other new improvements. These improve the service of the machine and decrease the radiation dose collected by the operating personal. As a result the main part of the activity is produced not in the cyclotron but in the target.

- The reduced complexity and the new compact construction of the cyclotron change the installation space requirements. The new generation machines use circular box-shaped construction, where the yoke practically surrounds the vacuum chamber. The rf-amplifier is installed very close to the cyclotron and the power is directly connected to the cavity which is contained in the deep valleys. Vertical beam plane construction has been introduced in smaller machines resulting in minimal space and easy side access and no excess height allowance required.

- The reduction of space requirements makes it easier to build modular shelf shielding. The shelf shield significantly reduces the radiation in the cyclotron room which further reduces the requirements concerning size of the wall and the level of radioprotection.

- The new development in control electronics and the performed high simplifications in the construction of cyclotrons used for routine tasks make possible the complete computer control and monitoring all the systems, also including the targetry. Using industrial programmable logic controllers (PLC) full automation of all sub-units is carried out making the operation very reliable with minimal operator service.

- Most of the cyclotrons are built with resistive coils. Recently small (12 MeV) negative ion cyclotrons based on superconduction magnet technology have also appeared. Most of the above mentioned trends were taken into account in its construction, but in same case it contains different solutions, due to the magnet technology. The results are very encouraging, but it seems that the cyclotrons are still more complicated than other superconducting devices introduced in serial production.

PET targetry at cyclotron

During production of the necessary labelled compound not only the irradiation process but other steps (practically the whole process) have to be optimised. To optimise targets which supply high yields, high specific activities, can withstand to high power and can avoid the loss of expensive target materials is a complicated technological task. On the other hand there is a limited flexibility for installations and control of different targets at any cyclotrons. Therefore the importance of the development of the whole targetry and chemistry was recognised and introduced at all commercial cyclotron manufacturers, which built on the level of the latest technology and also built on each other avoiding unnecessary steps and incompatibility. The new feature of the isotope production is that the targetry became the part of the cyclotron.

A wide variety of technical solutions of target handling can be observed at the existing accelerators. The complexity of the target handling depends on many factors: the maximal energy and intensity used, the number of the required targets, the physical characteristics (solid, liquid, gas) of the targets, half life of the produced isotope, etc.

In principle a combination of multiplied beam ports (or beam lines) and multiplied targets on each beam port can be installed.

- In case of higher energy accelerators or smaller machines both of the earlier generations or at low energy dedicated superconductive cyclotrons, the targets are situated far from the accelerator either in the same room, or more frequently in a separate room if external beam

lines are used. In the case of external beams, target changers up to ten position are used which are based on linear translation or circular-revolver motion allowing a remote change of the different devices.

- In the case of smaller energy machines the targets are installed close to the cyclotron practically on the wall of the vacuum chamber of the accelerator allowing an easier shelf shielding both for the cyclotron and the target unit. The change of the targets is possible by changing the position of the extraction or using a small dimension target changers (carousel, translator, etc.).

- We have to mention that the negative ion technology allows a possibility for dual extraction allowing simultaneous irradiation at two beam ports.

- For production of the most important four PET isotopes high performance, standard target units were developed almost at all cyclotron. These modular targets, however, are designed to a special target port and target changer, therefore their installation at another cyclotron is not always easy.

Technological progression in development of other accelerators used for production of positron emitters

With the development and much broader use of PET technology new types of accelerators have also appeared. The final aim is to construct an alternative accelerator having a lower cost to build, install and operate. Also lower radiation, less shielding, better reliability and easier operation are required. One possibility is the further development and simplification of cyclotrons, while the other is the application of accelerators based on other acceleration principle. These new types of accelerators were developed mostly for low energy and still are undergoing tests or are only used for limited isotope production.

The construction of these other accelerators is not so intensive as the third generation of cyclotrons. Its development is moving towards two directions:

- development of economic high intensity low energy (<5 MeV) accelerator, where the low energy is compensated with the very high intensity;

- development of a competitive middle energy (<15 MeV) machine which is more economic compared to the cyclotrons.

Though these new accelerators have different acceleration principles, it is common in all that during the acceleration the particle travel a linear path. These type of accelerators (which are close to the practical applications) are the following:

- Radiofrequency linacs using radiofrequency quadrupoles (RFQ) for 2 MeV protons and deuterons and 8 MeV for ^{3}He particles. Its main characteristics are: (a) acceleration fix Z/A to fix energy and (b) limitation in energy: up to 0.08 c.

- Drift tube linacs (DTL) using high frequency resonators with about 3 m/MeV space requirement (in combination with RFQ first stage).

- New generation of direct high voltage accelerators with different creations of acceleration voltage:
  - Coaxial Cascade Accelerator (CCA);
  - Tandem Cascade Accelerator (TCA);
  - Nested High Voltage Generator (NHVG);
  - Electrostatic accelerators (Pelletron, etc.).

The radiofrequency quadrupoles and the direct voltage accelerators have low energies, therefore to meet the need of the radioisotope production they have to use high beam currents with consequences of the increased requirements to the targetry. Due to the high stopping power at low energies very thin windows have to be used, very high heat has to be transferred from the very low volume, and there are also increased hot chemistry problems in the target. Solving these problems resulted in a new direction in target technology: to develop targets capable of handling high currents at low energies. In principle all main isotopes can be produced with these accelerators, but in practice similar to the very low energy cyclotrons they are used only for production of ^{15}O via the $^{14}N(d,n)^{15}O$ reaction. It should be mentioned that none of these developments seems to be ideal for dedicated machines used in clinical practice.

The higher energy (12 MeV) DTL linacs in principle could compete with cyclotrons. Until now only lower energy (7 MeV) machines were built and increases of the energy up to higher energies have been proposed by adding additional accelerating segments. Only a limited number of prototype machines were built and, as we already mentioned, the technological development has been much slower than in the field of dedicated cyclotrons. Hopefully in the future rapid developments and more installations will allow broader use of PET, and for other medical and industrial applications.

Conclusions

A wide variety of accelerators dedicated to PET isotope production are available world-wide. It is not an easy task, however, to discuss what might be the ideal accelerator in the above field. Many factors have to be considered, taking into account physical parameters, economical factors and operational circumstances. Recently the third generation of traditional cyclotrons have developed a complete dominance in the area of PET technology. Similar to other commercialised technologies the trends in building PET cyclotrons move towards very similar machines with important emphases on cost, reliability and available targetry. The wide variety of commercially available manufactured cyclotrons were constructed with slightly different construction philosophies that resulted in machines with different strengths. In spite of the relative modest requirements, the small superconducting cyclotrons are still in a developing phase; their service and reliability are still far from that of the traditional machines. Novel designs of linear accelerators which promise good performance at lower cost, lower radiation, and easier operation are still in the early developing stage.

Usually the first and main question is the selection of the category of the required machines (which is based on the future isotope programme of the user): (1) to try to do everything in the field of production of broader range of PET and also of some SPECT isotopes; (2) in the field of the most important PET isotopes; (3) to buy a special low energy machines with proven target technology only for a more limited field. Recently 30-40 MeV energy machines are accepted as ideal ones for large

scale production of longer lived isotopes for SPECT and PET applications. For the production of most widely used PET isotopes the ~20 MeV and the ~10-12 MeV PET accelerators are the most popular ones. They can produce more than enough of the most important four isotopes and they are able to fulfil the distribution needs. There exist dedicated low energy cyclotrons and linear accelerators for economic production of specific radioisotopes. The available targetry, financial constructions, geography aspects, service, etc., are very important factors in the decision between the different models. The main problem in PET technology is no longer the reliable production of the radioisotope in the necessary amount, but to fulfil the new requirements required by regulatory in production of pharmaceutical.

The implementation of new accelerator technologies for production of PET radioisotopes is already in a good phase and will be further accelerated and simplified parallel with the progression of the PET as a financially supported clinical diagnostic tool.

PRODUCTION OF RADIOTRACERS FOR PET

Syed M. Qaim
Institut für Nuklearchemie
Forschungszentrum Jülich GmbH, D-52425 Julich, Germany

Abstract

The production of β^+ emitting tracers routinely used in PET studies is outlined. Some of the efforts involved in the development of new β^+ emitters are briefly discussed.

Introduction

Positron Emission Tomography (PET) has been gaining considerable significance in recent years in diagnostic nuclear medicine, both in routine patient care and as a research tool. Its success, however, depends strongly on the availability of suitable β^+ emitting tracers. We consider below their production for both purposes.

Routine production

Most of the PET studies to date are carried out with four short-lived organic positron emitters, viz. ^{11}C ($T_{1/2}$ = 20 min), ^{13}N ($T_{1/2}$ = 10 min), ^{15}O ($T_{1/2}$ = 2 min), and ^{18}F ($T_{1/2}$ = 110 min). The former three radionuclides are generally used on site. ^{18}F, on the other hand, is suitable for transport to PET centres without a cyclotron. There is also considerable interest in ^{68}Ga ($T_{1/2}$ = 68 min) and ^{82}Rb ($T_{1/2}$ = 1.3 min) which are obtained via long-lived generator systems. The routine production methods of the commonly used β^+ emitters are summarised in Table 1 [1,2].

Table 1. Routine methods of production of some commonly used positron emitters

Radioisotope	$T_{1/2}$	Mode of decay	Production data		
			Nuclear reaction	Energy range (MeV)	Thick target yield MBq(mCi)/μAh
^{11}C	20 min	β^+ (99.8) EC (0.2)	$^{14}N(p,\alpha)$	13→3	3820 (103)
^{13}N	10 min	β^+ (100)	$^{16}O(p,\alpha)$	16→7	1665 (45)
^{15}O	2 min	β^+ (99.9) EC (0.1)	$^{14}N(d,n)$ $^{15}N(p,n)$	8→0 10→0	2368 (64) 2220 (60)
^{18}F	110 min	β^+ (97) EC (3)	$^{18}O(p,n)$ $^{20}Ne(d,\alpha)$	16→3 14→0	2960 (80) 1110 (30)
^{68}Ge ↓ (generator)	271 d	EC (100)	RbBr(p,spall)	800, 500	0.15 (0.004)
^{68}Ga	68 min	β^+ (90) EC (10)			
^{82}Sr ↓ (generator)	25 d	EC (100)	Mo(p,spall) $^{85}Rb(p,4n)$	800 60→40	3.7 (0.1) 14.8 (0.4)
^{82}Rb	1.3 min	β^+ (96) EC (4)			

Organic β^+ emitters

The organic β^+ emitters are generally produced using low energy nuclear reactions like (p,n), (p,α), (d,n), (d,α), etc. The thick target yields of the most common production routes, calculated from the measured excitation functions, are shown in Figure 1 as a function of incident particle energy [1,2].

Figure 1. Integrated yields of some commonly used β^+ emitters expected from the most common production routes, plotted as a function of incident particle energy [1]

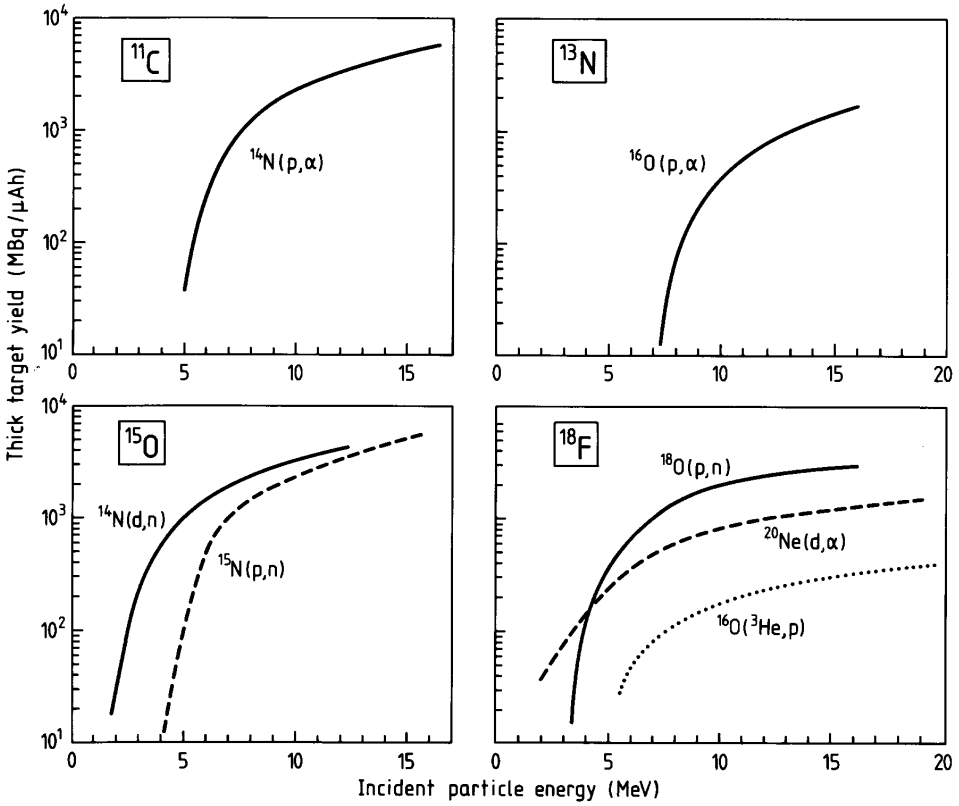

It should, however, be emphasised that the curves are only approximations since the calculation of the thick target yield from an excitation function showing large structures, such as for the light mass nuclei involved here, is rather uncertain. Nonetheless, from Figure 1 it is evident that, in principle, all four β^+ emitters can be produced at a small cyclotron.

For large scale production of short-lived β^+ emitters generally gaseous and liquid targets are used. Nuclear reaction cross-section data are needed to optimise the incident particle energy as well as the target thickness. In recent years, high intensity small cyclotrons, dedicated exclusively to medical radioisotope production, have been developed and considerable progress has also been achieved in targetry. The organic β^+ emitters can thus be easily obtained in Gbq amounts for preparation of a desired radiopharmaceutical.

The chemical form of the radioactive product obtained from a target depends upon the target filling and radiation chemical effects. The primary product known as “precursor” is the starting material for labelling of biomolecules with the β^+ emitter. A flow sheet of production of short-lived radiopharmaceuticals is given in Table 2. Since the final product is intended for medical use, stringent quality control methods have to be applied. Due to the short half-life of the radioisotope, a high starting activity is needed. This demands development of a special type of fast chemistry. Over the last ten years a new technology has emerged and today automated units [3] are commercially available which guarantee the delivery of the most commonly used β^+ emitting radiopharmaceuticals on a very reliable basis.

Table 2. Flow sheet of production of short-lived radiopharmaceuticals

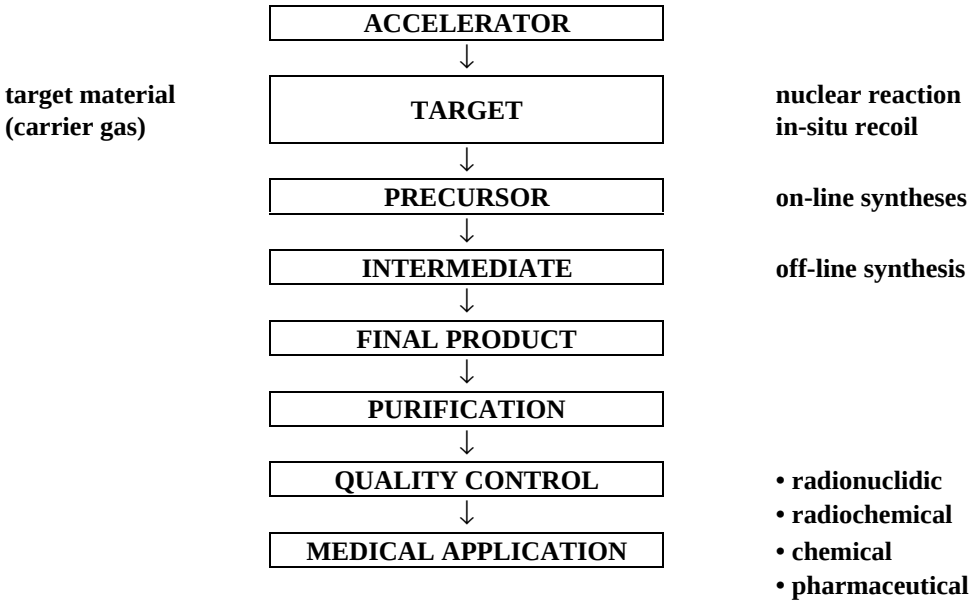

Several β^+ emitting radiopharmaceuticals are now routinely used in diagnostic nuclear medicine [2], especially in neurology, cardiology and oncology. Of major interest are the products [^{15}O]H_2O, n-[^{15}O]butanol, 2-[^{18}F]FDG, L-6[^{18}F]FDOPA, [^{13}N]H_3, [^{11}C]methionine, [^{11}C]acetate, and [^{11}C] or [^{18}F] fatty acids.

Generator produced β^+ emitters

The generator produced β^+ emitters find application mostly in PET studies at centres without a cyclotron. The parent isotopes of the two most commonly used systems (see Table 1), viz. ^{68}Ge and ^{82}Sr, are rather difficult to produce [4,5]. In both cases the method of choice is the spallation process. To date they are produced at large accelerators where long irradiations in parasitic positions are possible. The purification of the product involves several multi-step wet chemical processes. Preparation of generator columns demands considerable radiochemical skills [6,7] since sterility and apyrogenicity have to be guaranteed over a long period. Both the generator systems are commercially available.

Research related production

The research related production of β^+ emitting tracers can be considered under two headings:

a) development of new radiopharmaceuticals labelled with one of the above mentioned four organic β^+ emitters;

b) development of new β^+ emitters.

The development of new organ specific radiopharmaceutical belongs to the realm of organic radiochemistry, radiopharmacy and radiopharmacology. This line of work certainly constitutes the hard core of future development of PET as a research tool for studying molecular medicine in vivo, i.e. to learn how a disease develops on a biochemical level.

The development of a new β^+ emitter for PET application involves a study of several aspects such as nuclear data, high current targetry, chemical processing, etc. Furthermore, the radioisotope has to be tagged to a suitable compound. Thus preparation of a new positron emitting tracer entails considerable nuclear chemistry work.

The longer-lived β^+ emitting isotopes, in comparison to short-lived β^+ emitters, are useful for investigating slow physiological functions and can be easily transported to long distances. In general, the so-called "analogue approach" is practised whereby a H atom or a CH_3 group in a biomolecule is replaced by a β^+ emitting halogen isotope, e.g. ^{75}Br ($T_{1/2}$ = 1.6 h), ^{124}I ($T_{1/2}$ = 4.2 d), etc. [8,9] or an element having no β^+ emitter is represented by a homologue, e.g. S by ^{73}Se ($T_{1/2}$ = 7.1 h). Two other areas where the analogue approach has started gaining more attention entail quantitation of SPECT-pharmaceuticals via PET and study of uptake kinetics and dosimetry of β^- emitting therapeutic agents. This is possible due to the quantitative nature of PET studies. The β^+ emitters found useful for those investigations are listed in Table 3. Their methods of production have been worked out. Work on other β^+ emitters is under way in several laboratories.

Table 3. Positron emitting analogues of some radioisotopes used in SPECT and endoradiotherapy

SPECT isotope ($T_{1/2}$)	**β^+ emitting analogue ($T_{1/2}$, % β^+)**
^{67}Ga (78 h)	**^{68}Ga (68 min, 90)**
^{77}Br (56 h)	**^{75}Br (1.6 h, 75)** **^{76}Br (16 h, 57)**
^{99m}Tc (6 h)	**^{94m}Tc (52 min, 70)**
^{111}In (2.8 d)	**^{110m}In (69 min, 62)**
^{123}I (13.2 h)	**^{120g}I (1.3 h, 46)**
^{201}Tl (3 d)	**^{38}K (7.5 min, 100)**

Endoradiotherapy β^- emitter ($T_{1/2}$)	**β^+ emitting analogue ($T_{1/2}$, % β^+)**
^{89}Sr (50.5 d)	**^{83}Sr (32.4 h, 24)**
^{90}Y (2.7 d)	**^{86}Y (14.7 h, 34)**
^{125}I (60.2 d) **^{131}I (8 d)**	**^{124}I (4.1 d, 25)**

Concluding remarks

The radiotracers commonly used in PET studies are available on a routine basis. Future developments belong mostly to the domain of organic radiochemistry and radiopharmacology. The development of new β^+ emitters for PET investigations, on the other hand, involves, besides radiopharmaceutical work, a considerable amount of nuclear and technological effort, which is of relevance to the Nuclear Energy Agency (NEA). Extensive nuclear data measurements are needed to define the optimum production conditions of a radioisotope [10]. As an example, the data for the formation of ^{94m}Tc ($T_{1/2}$ = 52 min) via interactions of protons with highly enriched ^{94}Mo are shown in Figure 2 [11]. The optimum energy range for production is $E_p = 13 \rightarrow 7$ MeV: the calculated thick target yield of ^{94m}Tc amounts to 2 GBq (54 mCi)/μAh and the level of the isomeric impurity ^{94g}Tc ($T_{1/2}$ = 4.9 h) to 7%. Without a knowledge of the cross-section data, neither the product yield nor the level of impurity could be predicted with any certainty. In general, data up to 30 MeV are needed. However, in some special cases measurements in the medium energy range (up to 100 MeV) are necessary.

Figure 2. Excitation functions of ^{94}Mo(p,n)^{94m,g}Tc and ^{94}Mo(p,2n)^{93m,g}Tc processes. The optimum energy range for the production of ^{94m}Tc is shown by the shaded area.

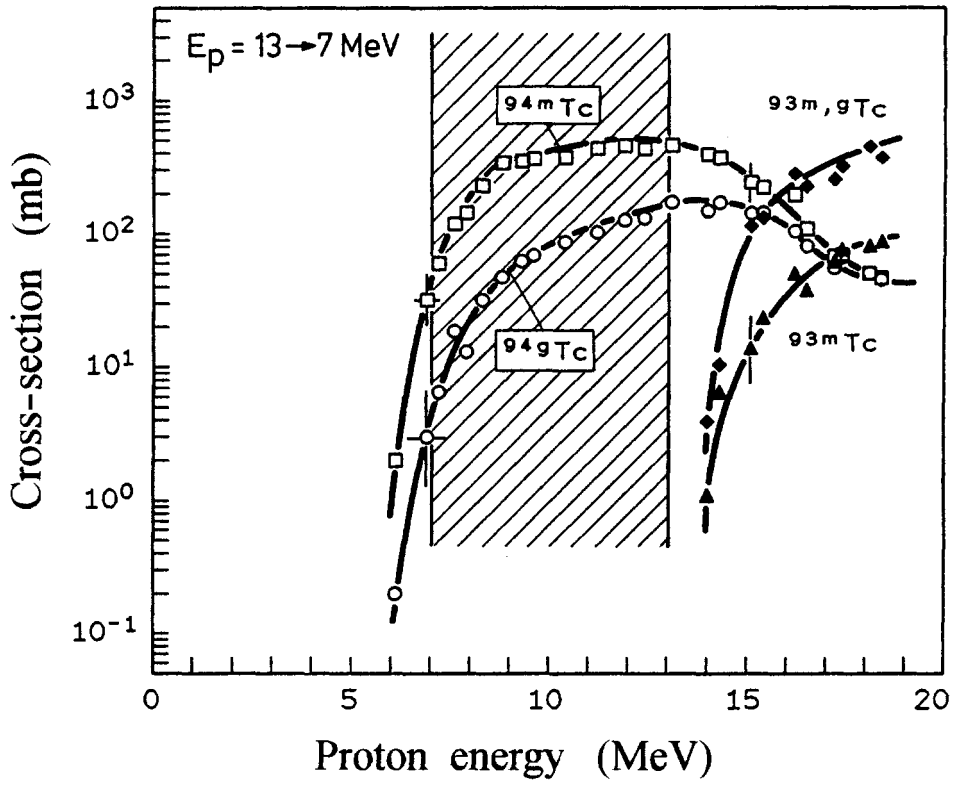

REFERENCES

[1] S.M. Qaim, J.C. Clark, C. Crouzel, M. Guillaume, H.J. Helmeke, B. Nebeling, V.W. Pike and G. Stöcklin, in *Radiopharmaceuticals for Positron Emission Tomography*, eds., G. Stöcklin and V.W. Pike, Kluwer Academic Publishers, Dordrecht, The Netherlands (1993), pp. 1-42.

[2] G. Stöcklin, S.M. Qaim and F. Rösch, *Radiochim. Acta* 70/71 (1995) 249.

[3] C. Crouzel, J.C. Clark, C. Brihaye, B. Lángström, C. Lemaire, G.J. Meyer, B. Nebeling and S. Stone-Elander, in Ref. 1, pp. 45-89.

[4] *The $^{82}Sr/^{82}Rb$ Generator*, eds. S.L. Waters and B.M. Coursey, *Appl. Radiat. Isot.* 38 (1987), 171 (special issue).

[5] S.M. Qaim, *Radiochim. Acta* 41 (1987), 111.

[6] R.M. Lambrecht, K. Tomiyoshi and T. Sekine, *Radiochim. Acta* 77 (1997), 103.

[7] F.F. Knapp, Jr. and S. Mirzadeh, *Eur. J. Nucl. Med.* 21 (1994), 1151.

[8] H.H. Coenen, S.M. Moerlein and G. Stöcklin, *Radiochim. Acta* 34 (1983), 47.

[9] G. Stöcklin, *Eur. J. Nucl. Med.* 19 (1992), 527.

[10] S.M. Qaim, *Radiochim. Acta* 30 (1982), 147.

[11] R. Rösch and S.M. Qaim, *Radiochim. Acta* 62 (1993), 115; *Erratum* 75 (1996), 227.

PET INSTRUMENTATION, MODELLING AND CLINICAL APPLICATION

H. Herzog
Institute of Medicine, Forschungszentrum Jülich, D-52425 Jülich, Germany
E-mail: h.herzog@fz-juelich.de

Abstract

Positron emission tomography (PET) is a diagnostic imaging method to investigate physiological and metabolic functions and their disorders in vivo. Dedicated ring systems of scintillation detectors measure the 511 keV γ-radiation produced in the course of the positron emission from radiolabelled metabolically active molecules. The development of PET instruments over the last 20 years has led to systems with an image resolution of 4-5 mm. Although a great number of radiopharmaceuticals labelled with positron emitters have been applied both for research and clinical purposes, the momentary success of PET is mainly based on the use of ^{18}F-fluorodeoxyglucose (FDG). FDG have been applied for many years to study diseases in the brain and heart. In the last years the increase of PET installations is based on the high sensitivity of the FDG-PET to localise primary tumours and their metastases.

Introduction

Most diseases are caused by disturbed metabolic functions. Nuclear medicine procedures are especially appropriate to investigate such disorders because the radiolabelled molecules, which are intravenously injected into the patient, take part in the human metabolism. If it is necessary to investigat these functions in a quantitative way one has to use positron emission tomography (PET), which is able to measure radioactivity within a human body in vivo in absolute terms. The specific physical properties of positron emitters are a first reason for this advantage. A second advantage of PET is the use of such positron emitters as ^{11}C, ^{13}N, ^{15}O or ^{15}F. The cold sister isotopes of these positron emitters are natural elements of the organic molecules which are necessary for the human metabolism. The purpose of this paper is to describe the physical and biochemical basics of PET, the newest developments of PET instrumentation, the method of functional modelling and finally some important clinical applications.

Physical basics of PET

PET is based on the emission of positron emitters which are emitted from nuclei having an excess of positive charge. After their emission positrons have a wave length of less than 1 mm or of several mm, until they are nearly stopped and meet an electron. In the following both particles annihilate and are transformed to photon energy, i.e. two photons each with an energy of 511 keV are produced and emitted into nearly opposite directions. This emission of the photon pairs is the same for all positron emitters so that a detector system can be optimised accordingly to this constant physical property. The photon pairs are measured by a system of detector rings in which the patient is situated (Figure 1). The detectors consist of areas of small scintillation crystals coupled to one or more photomultipliers. A photon pair is registered if one of its photons hits a detector element and the other hits one of the fan-like opposing detectors within the coincidence time window of, e.g. 12 nanoseconds. In this case the origin of the positron emission, which is also the position of the radiolabelled molecule, is assumed to be located on the line between the two detectors.

Figure 1. Majors components of a PET system

Photon pairs resulting from positron emission are detected by a ring of scintillation detectors coupled to coincidence electronics. By using appropriate algorithms the measured radiation is reconstructed into tomographic images.

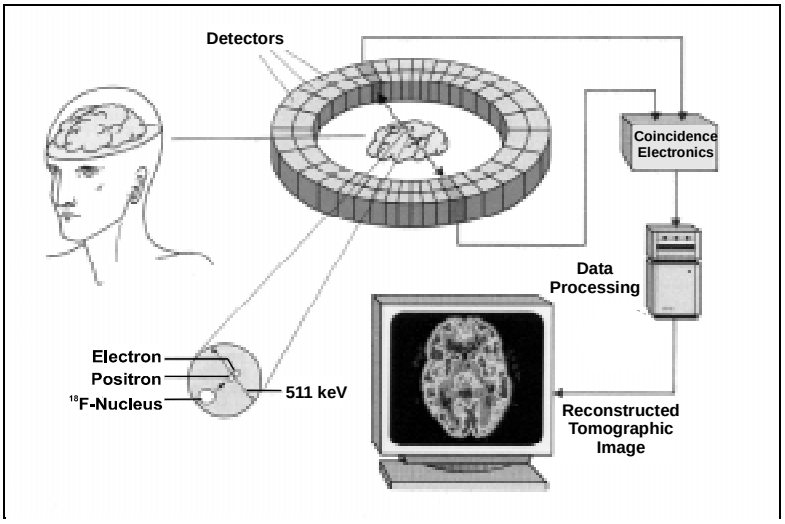

In the course of the PET measurement, which may range from some seconds to many minutes, a part of the photon pairs leaving the body in all directions is measured by the detectorring system. The registered photon pairs which represent a projection information of the activity distribution (Figure 2) are reconstructed into tomographic images. The reconstruction algorithms are similar to those of conventional radiological computed tomography (CT). The special advantage of PET is that not only does it give a distribution of count rate signals like in normal scintigraphy or in single photon emission computed tomography (SPECT), but it also yields the distribution of activity concentration in absolute terms of kBq/cm^3, for example. The main reason for this advantage is that the attenuation which affects the radiation within the human body can be accurately corrected. This is achieved by an additional transmission measurement during which a line source filled with positron emitting ^{68}Ge/^{68}Ga is surrounding the patient (Figure 2). The 511 keV radiation of the line source, which is attenuated within the body, is measured by detectors on the other side of the body. With the help of these measurements the projection equation of positron emission tomography, which is also given in Figure 2, can be corrected for the absorbed 511 keV radiation. Further necessary corrections are those for random coincidences, scattered coincidences and possible dead time losses. The development of PET devices during the last two decades has yielded an improvement of resolution from originally 15 mm to 4-5 mm. This progress had to be paid by a loss of sensitivity because the amount of radioactivity which is allowed to inject into a human was kept constant or even reduced so that less counts are measured in the smaller resolution elements. In order to circumvent this problem the so-called three-dimensional measurement mode has been suggested. Former PET instruments were able to measure only in a two-dimensional mode, i.e. only those photon pairs hitting the detectors within one ring were accepted. The three-dimensional mode also includes those photon pairs which are measured by detector elements of non-neighbouring rings. The increase of the detection angle resulted in a five-fold sensitivity, which can be utilised to improve the statistics of the acquired data, to lower the injected radioactivity – and in this way the radiation dose of the patient – or the duration of measurement. All modern PET scanners are capable of the two- or three-dimensional acquisition mode, some of them are designed only for the three-dimensional mode. The increase of sensitivity by looking at a volume instead of just a single plane has to be paid by an increase of random and scattered coincidences. Random coincidences are measured if within the coincidence time window two opposing detectors are hit by photons which belong to different positron emissions. This erroneous signal can be corrected relatively easily. Scatter coincidences occur if at least one photon of a photon pair is compton scattered and in this manner changes its direction. The pair of detectors hit by the two photons indicate a line of response which does not coincide with the site of the positron emission. In some situations scattered coincidences are measured to the same extent as true coincidences so that they produce a considerable error. Recently, some methods for correcting this error have been developed. There are, however, still problems with photons coming from outside the field of view. Such a situation may occur if a tumour in the abdomen has to be imaged and the bladder filled with radioactivity is not inside the field of view.

In order to reduce the scatter problem new detector materials are being developed. Whereas in planar scintigraphy and SPECT NaJ is the commonly used detector material, PET detectors apply BGO which has a higher detection efficiency and a faster decay time than NaJ. On the other hand the light output is only 15 % of that of NaJ so that the energy window of these detectors is relatively wide and is not well suited to discriminate scattered photons. Therefore, one has suggested LSO as a new scintillator material. It has a similar density as BGO and a decay time of 40 ns compared to 300 ns for BGO. Its main advantage is its five-fold light output, so that the smaller energy window accepts much less scattered incidences.

Figure 2. The PET emission scan measures the projection data P_E which include both the unknown activity distribution A(x,y) and the unknown attenuation distribution μ(x,y). The attenuation term is directly measured by the additional transmission measurement.

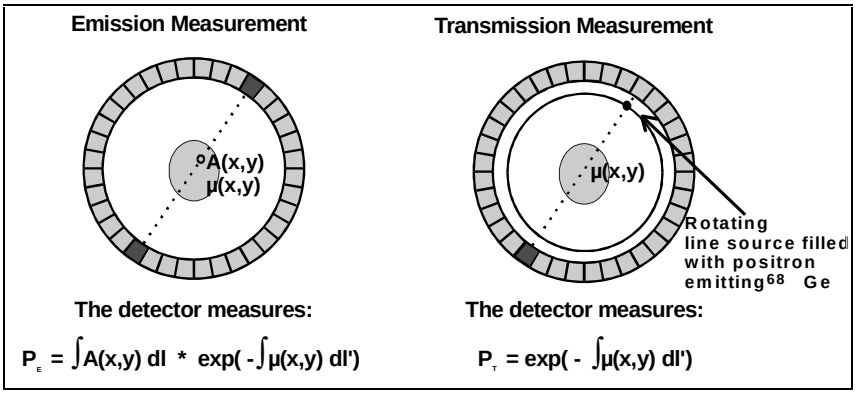

After all corrections have been applied to the originally measured radiation signals and after they have been reconstructed into tomographic images they are available as image matrixes calibrated in activity per volume. These images can be used for direct diagnosis or for further evaluations, e.g. for the conversion into images displaying a functional parameter.

From radioactivity to metabolic function

The exact way in which a PET study is performed, i.e. the length of a single PET acquisition and if a single static image or a dynamic sequence of PET images has to be measured, depends on the radiopharmaceutical used and on the specific metabolic functions to be investigated. Often, the diagnosis of a metabolic hypo- or hyper-function can be based on a single, so-called autoradiographic PET image which averages the distribution of a radiopharmaceutical over a certain time interval after injection, e.g. from 30 to 50 min. Especially in research, it is often not sufficient to evaluate just the primary image of activity distribution so that the PET image has to be transferred pixel by pixel into the parametric image of the metabolic functions being investigated.

For this purpose the PET measurement is combined with the measurement of the radioactivity in the blood, which can be regarded as an internal standard. This is done by using a biochemical or physiological model of the considered process. Mostly, these models are derived from a priori animal research.

Sometimes the autoradiographic activity image can already be used for this purpose. In other applications the temporal behaviour of the radiopharmaceutical within the investigated organ must be known and analysed. The relationship between the dynamics in blood and tissue can mathematically be described by one or more differential equations. The parameters of such an equation may represent the metabolic function, e.g. the blood flow of heart or brain or the density of cerebral neuroreceptors.

Clinical applications

The radiopharmaceutical mostly used is ^{18}F-fluorodeoxyglucose (FDG). Since its introduction in 1979 it has been developed into the working horse of PET because it can be applied in studies of brain, heart, and tumours [13]. Its importance for investigating the brain is based on the fact that the

brain gets 90% of its energy by oxidation of glucose and that many changes of brain function are related to changes of glucose consumption. The FDG uptake measured with PET is directly related to glucose consumption. A diminished FDG uptake indicates cerebral hypofunction, e.g. in epilepsy [4,7] (Figure 3), infarction [10], or dementia [5,12]. An increased uptake of glucose is found when the brain is more active due to external or mental stimulation. There is, for instance, an increased glucose consumption within the motor cortex during finger movements [15].

Figure 3 While the MR image of a patient suffering from focal epilepsy is normal the PET image shows a decreased uptake (arrow) of FDG in one temporal lobe in this way indicating the epileptic focus

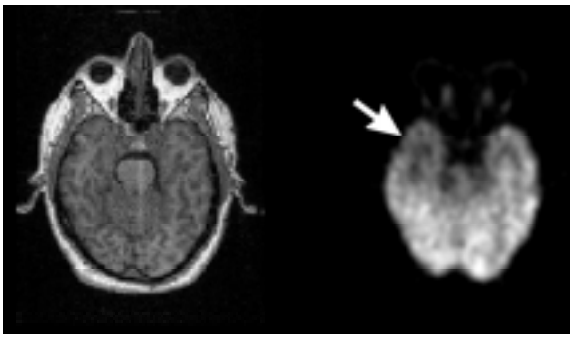

In cardiology FDG has become important for the diagnosis of tissue viability in the context of a myocardial infarction [14]. Those myocardial areas in the neighbourhood of an infarction which show nearly no uptake of ^{201}Thallium or ^{99m}Tc-Mibi in a SPECT study of perfusion are still vital, if they are able to take up FDG. Such an examination is important for the prognosis of a bypass surgery or a coronary angioplastic (PTCA) which aim to restore blood flow in badly perfused myocardial tissue.

In the early years of PET it had already been reported that FDG shows a high uptake in malignant tissue, especially in high-grade brain tumours [6]. It took, however, nearly a decade before the use of FDG to diagnose malignant tumours and their metastases throughout the entire body became the most frequent application of PET. Often, it is difficult to delineate metastases, when some time after the surgical removal of a primary tumour blood markers indicate the persistence of malignancy. It could be shown that in many tumours the FDG-PET is more sensitive than CT and magneto resonance tomography (MRT). Figures 4 and 5 display examples for this important PET application. The use of FDG-PET for the diagnosis of malignant tissue has caused an enormous increase of PET instrumentation especially in Europe and here again especially in Germany. Dependent on the reimbursement of such clinical investigations a further expansion of PET can be expected, as it is already the case in the United States after the reimbursement of FDG-PET has been approved by some insurance companies.

There are, however, many other important applications for PET, even if they are not as frequently used as the FDG-PET. In Parkinson's disease ^{18}F-DOPA helps to differentiate in the situation of unclear diagnosis [2]. ^{11}C-methionine is able to delineate the extent of a brain tumour better than other nuclear medical or non-nuclear medical imaging procedures [1].

In spite of many clinical applications PET is often regarded as a research tool when compared to other imaging methods like CT or MRT. A major area of PET research is that of cerebral neurotransmitter-receptor systems. These represent the biochemical interphase of cerebral information

Figure 4. This patient had underwent surgical removal of the primary ovarian cancer. CT gave no hint of metastases. The FDG-PET, however, revealed many metastases in the abdomen, indicated here as white spots.

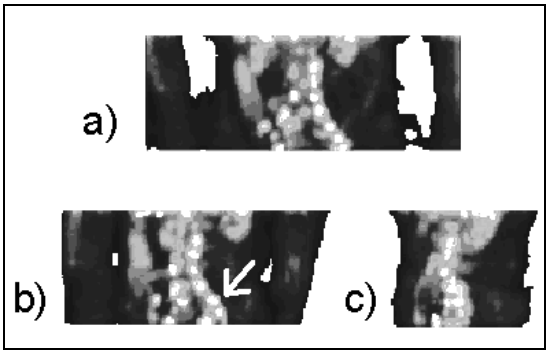

Figure 5. In this patient who had underwent surgery of a primary prostate cancer increasing blood tumour markers indicated the persistence of malignancy. Several unknown metastases (circle) were found by the FDG whole body PET.

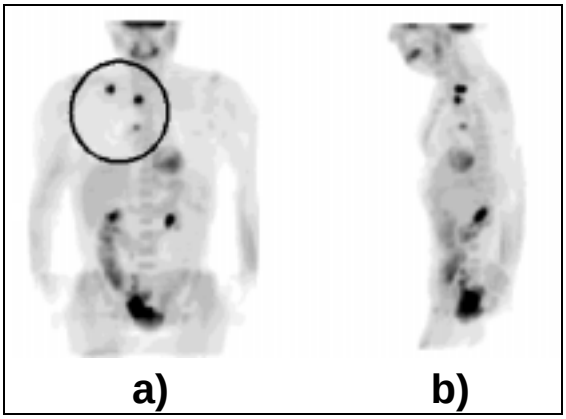

exchange, where most brain-sensitive drugs interfere. Examples of such drugs are caffeine, psychopharmaceuticals, cocaine opium, etc. Changes of the transmitter-receptor systems are known or are supposed in many psychiatric diseases. Therefore, PET research of the neuroreceptor system deals with diseases such as depression or schizophrenia. One objective is to learn more about the biochemistry of such diseases, another is to study interactions between drugs and endogenous transmitter and receptor molecules.

A second research field is the investigation of neuronal activation caused by external or mental stimulation. It has already been described above that cortical areas show higher glucose consumption when, e.g. an arm or a hand is moved. It has been shown in many studies that such cortical areas also exhibit an increased blood flow which can be measured with the help of ^{15}O-labelled water or ^{15}O-labelled butanol. In the last few years numerous PET studies have helped to investigate motor, sensory and cognitive functions of the human brain. An example for such an investigation is shown in Figure 6. Although, such studies are mostly dedicated to basic research they are sometimes used clinically. It may be interesting for a surgeon who is going to remove a brain tumour located near the motor hand area, how far this region is apart from the tumour so that he is able to spare it.

Figure 6. The dark shaded areas exhibit maxima of blood flow increase indicating cerebral activation during the process of learning word pairs. These areas were measured with PET and superimposed on the MRT image for better orientation. Significant activations were detected in the visual cortex (1), the anterior cingulum (2), and the left frontal cortex (3) [Ref. 9].

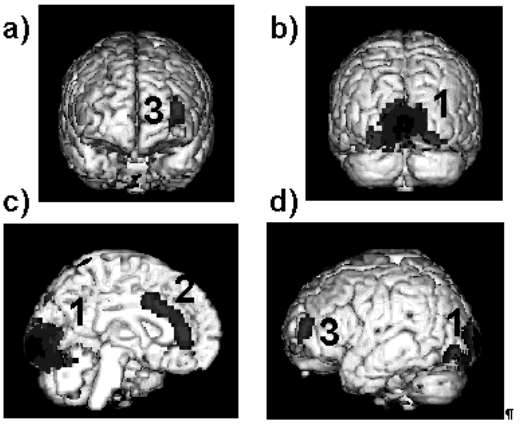

A third research area is the development and application of positron emitters other than the commonly used ^{15}O, ^{13}N, ^{11}C, and ^{18}F. In our own centre we investigated the use of the positron emitting ^{86}Y to examine the biokinetics and the radiation dose of radiotherapeuticals which are labelled with the beta emitter ^{90}Y [8]. While ^{90}Y cannot be quantitatively measured from outside the body it is the advantage of PET to permit such measurements when ^{90}Y is substituted by ^{86}Y. Since the biochemistry of molecules labelled with either of the two isotopes is identical, one can directly conclude from the quantitative results obtained with PET and ^{86}Y to those valid for the ^{90}Y-labelled radiotherapeutical. By this approach the individual radiation dose which is caused by the radiotherapy can be estimated individually for the single patient.

Again, this last application is an excellent example for the increasing variety of PET research and possible applications. Being a tool to study biochemistry in vivo PET is not restricted to only a couple of radiopharmaceuticals or to a single organ, but can be utilised to study hundreds of biomedical pathways all over the human body.

REFERENCES

[1] M. Bergstrom, V.P. Collins, E. Ehrin *et al*., Discrepancies in Brain Tumor Extent as Shown by Computed Tomography and Positron Emission Tomography Using [68Ga]EDTA, [11C]Glucose, and [11C]Methionine., *J Comput Assist Tomogr* 1983 Dec.; 7(6):1062-1066 (1983)

[2] D.J. Brooks, V. Ibanez, G.V. Sawle, Differing Patterns of Striatal 18F-Dopa Uptake in Parkinson's Disease, Multiple System Atrophy, and Progressive Supranuclear Palsy, *Ann Neurol* 28:547-555 (1990).

[3] P.S. Conti, D.L. Lilien, K. Hawley *et al*., PET and [18F]-FDG in Oncology: A Clinical Update, *Nucl Med Biol* 23: 717-735 (1996).

[4] T.J. Cummings, D.C. Chugani, H.A.T. Chugani, Positron Emission Tomography in Pediatric Epilepsy, *Neurosurg Clin N Am* 6: 465-472 (1995).

[5] M.J. de Leon, A.E. George, S.H. Ferris *et al*., Regional Correlation of PET and CT in Senile Dementia of the Alzheimer Type, *AJNR Am J Neuroradiol* 4:553-556 (1983).

[6] G. DiChiro, R.R. DeLaPaz, R.A. Brooks *et al*., Glucose Utilization of Cerebral Gliomas Mesured by [^{18}F]Fuorodeoxyglucose and Positron Emission Tomography, *Neurology* 32:3323-1329 (1982).

[7] J. Engel Jr, D.E. Kuhl, M.E. Phelps, P.H. Crandall, Comparative Localization of Epileptic Foci in Partial Epilepsy by PCT and EEG, *Ann Neurol* 12:529-537 (1982).

[8] H. Herzog, F. Rösch, G. Stöcklin, C. Lueders, S.M. Qaim, L.E. Feinendegen, Measurement of Pharmacokinetics of Yttrium-86 Radiopharmaceuticals with PET and Radiation Dose Calculation of Analogous Yttrium-90 Radiotherapeutics, *J Nucl Med* 34: 2222-2226 (1993).

[9] B.J. Krause, U. Halsband, D. Schmidt *et al*., Neurofunctional Correlates of Encoding and Retrieval in Declarative Associative Learning, *Neuro Image* 5: S620 (1997).

[10] T. Kuwert, M. Hennerici, K.-J. Langen, A. Aulich, H. Herzog, L.E. Feinendegen, Regional Cerebral Glucose Consumption Measured by Positron Emission Tomography in Patients with Unilateral Thalamic Infarction, *Cerebrovasc Dis* 1: 327-336 (1991).

[11] T. Kuwert, H.W. Lange, K.-J. Langen, H. Herzog, A. Aulich, L.E. Feinendegen, Cortical and Subcortical Glucose Consumption Measured by PET in Patients with Huntington's Disease, *Brain* 113: 1405-1423 (1990).

[12] A. Nordberg, Application of PET in Dementia Disorders, *Acta Neurol Scand Suppl* 168:71-76 (1996).

[13] M.E. Phelps, J.C. Mazziotta, H.R. Schelbert, Positron Emission Tomography and Autoradiography, Raven Press, New York (1986).

[14] O. Ratib, M.E. Phelps, S.C. Huang, E. Henze, C.E. Selin, H.R. Schelbert, Positron Emission Tomography with Deoxyglucose for Estimating Local Myocardial Glucose Metabolism. *J Nucl Med* 23:577-586 (1982).

[15] G. Wunderlich, U. Knorr, H. Herzog, J.W.C. Kiwit, H.-J. Freund, R.J. Seitz, Precentral Glioma Location Determines the Displacement Cortical Hand Representation, *Neurosurgery* 42: 18-27 (1997).

LIST OF PARTICIPANTS

BRAZIL

Prof. Fernando ZAWISLAK
Instituto de Fisica
Universidade federal do Rio Grande do Sul
C. Postal 15051, Campus do Vale, 91501-970
PORTO ALEGRE, RS

Tel: +55-51-316-6427
Fax: +55-51-319-1762
E-mail: zawislak@if.ufrgs.br

GERMANY

Dr. H. HERZOG
Institut für Medizin
Forschungszentrum Jülich GmbH
D-52425 JULICH

Tel: +49-2461-61-5913
Fax: +49-2461-61-2770
E-mail: h.herzog@fz-juelich.de

Prof. Karl MAIER
Institut für Strahlen- und Kernphysik
der Universitaet Bonn
Nussallee 14-16, D-53115 BONN

Tel: +49-228-73-2381
Fax: +49-228-73-2505
E-mail: maier@iskp.uni-bonn.de

Dr. Otto MEYER
Forschungszentrum Karlsruhe
Institut für Nuklear Festkorperphysik
KARLSRUHE D-76021

Tel: +49-724782-3940
Fax: +49-724782-4624
E-mail: Meyer@INFP.FZK.de

Prof. Syed M. QAIM
Institut fuer Nuclearchemie
Forschungszentrum Juelich
Postfach 1913, D-52425 JUELICH 1

Tel: +49-2461-61-3282
Fax: +49-2461-61-2535
E-mail: s.m.qaim@fz-juelich.de

Dr. Nikolaus STOLTERFOHT
Hahn-Meitner-Institut
Glienicker Strasse 100, D-14109 BERLIN

Tel: +49-30-8062-2340
Fax: +49-30-8062-2293
E-mail: Stolterfoht@hmi.de

Dr. Elke WENDLER
Friedrich-Schiller-Universitaet Jena
Institut fuer Festkoerperphysik
Max-Wien-Platz 1, D-07743 JENA

Tel: +49-3641-947333
Fax: +49-3641-947302
E-mail: wendler@pinet.uni-jena.de

HUNGARY

Dr. Gabor BATTISTIG
Research Institute for Technical Physics
and Materials Science
P.O.Box 49, H-1525 BUDAPEST

Tel: +36-1-395.92.20 ext. 2661; 2962
Fax: +36-1-395.92.84
E-mail: battisti@mfa.kfki.hu

Dr. István FOLDVARI
Department of Crystal Technology
Research Institute for Solid State
Physics and Optics
Hungarian Academy of Sciences
Konkoly-Thege.u.29-33 P.O.Box 49
H-1121 BUDAPEST
Tel: +361-395-9220/Ext. 13-76
Fax: +361-2754105
E-mail: foldvari@power.szfki.kfki.hu

Dr. Ferenc PASZTI
KFKI-Research Institute for Particle
and Nuclear Physics KFKI-RMKI
P.O.Box 49, H-1525 BUDAPEST
Tel: +36-1395 9220 (ext. 1959)
Fax: +36- 1395 9151
E-mail: paszti@rmki.kfki.hu

Dr. F. TARKANYI
Institute of Nuclear Research
Hungarian Academy of Sciences
Bem ter 18/c Pf. 51, H-4001 DEBRECEN
Tel: +36-52-417266
Fax: +36-52-416181
E-mail: tarkanyi@atomki.hu

ITALY

* Dr. Enzo MENAPACE
Applied Physics Division
Agency for New Technologies, Energy
and Environment (ENEA)
Via Don Fammelli 2
I-40127 BOLOGNA
Tel: +39-51-6098239
Fax: +39-51-6098359
E-mail: menapace@risc990.bologna.enea.it

JAPAN

Dr. Masafumi HIROSE
Research & Development Center
Sumitomo Heavy Industries, Ltd.
2-1-1 Yato-cho, Tanashi-city
TOKYO 188-8585
Tel: +81-424-68-4476
Fax: +81-424-68-4477
E-mail: msf_hirose@shi.co.jp

Dr. Yoshiko ITOH
The Institute of Physical and Chemical
Research (RIKEN)
Hirosawa, Wako-Shi
SAITAMA 351-01
Tel: +81-48-467-9464
Fax: +81-48-461-5301
E-mail: yitoh@postman.riken.go.jp

Mr. Terunobu NAKAJYO
Research & Development Center
Sumitomo Heavy Industries, Ltd.
2-1-1 Yato-cho, Tanashi-city
TOKYO 188-8585
Tel: +81-424-68-4476
Fax: +81-424-68-4477
E-mail: trn_nakajyo@shi.co.jp

Dr. Sohei OKADA
Takasaki Establishment
Japan Atomic Energy Research Institute
1233 Watanuki, Takasaki
GUNMA 370-1292
Tel: +81-27-346-9650
Fax: +81-27-346-9690
E-mail: bazooka@taka.jaeri.go.jp

Prof. Shoichirou TANIGAWA
Institute of Materials Science
Tsukuba University
Tsukuba-shi
IBARAKI 305
Tel: +81-298-53-5135
Fax: +81-298-55-7440
E-mail: tanigawa@esys.tsukuba.ac.jp

NETHERLANDS

Prof. A. Tom van VEEN
IRI Delft University of Technology
Mekelweg 15, 2629JB DELFT
Tel: +31-15-2782801
Fax: +31-15-2784622
E-mail: avveen@iri.tudelft.nl

PORTUGAL

Dr. Eduardo ALVES
Instituto Tecnologico e Nuclear
Estrada Nacional 10
2685 SACAVEM
Tel: +351-1-9550021/ Ext. 1124
Fax: +351-9941525
E-mail: ealves@itn1.itn.pt

Dr. Luis C. ALVES
Instituto Tecnológico e Nuclear
Estrada Nacional 10
2685 SACAVEM
Tel: +351-1-9550021
Fax: +351-1-9941525
E-mail: lcalves@itn1.itn.pt

Dr. Carlos A. Lopes GIL
Physics Department, University of Coimbra
P-3000 COIMBRA
Tel: +351-39-410628
Fax: +351-39-829158
E-mail: cargil@gemini.ci.uc.pt

Mr. Paulo Mendes GORDO
Physics Department, University of Coimbra
P-3000 COIMBRA
Tel: +351-39-410629
Fax: +351-39-829158
E-mail: pgordo@gemini.ci.uc.pt

Dr. Adriano J.R. Pedroso de LIMA
Physics Department, University of Coimbra
P-3000 COIMBRA
Tel: +351-39-410627
Fax: +351-39-829158
E-mail: lima@lipc.fis.uc.pt

Dr. Jose G. MARQUES
Instituto Tecnologico e Nuclear
Estrada Nacional 10
2685 SACAVEM
Tel: +351-1-9550021
Fax: +351-9941039
E-mail: jmarques@itn1.itn.pt

Dr. Marco Duarte NAIA
Physics Department of UTAD
Departamneto de Fisica
Universidade de Tras-os-Montes e Alto Douro
quinta de Prados, 5000 VILA REAL
Tel: +351-59-320338
Fax: +351-59-320480
E-mail: duarte@marao.utad.pt

Mr. Luis PRUDENCIO
Instituto Tecnológico e Nuclear
Estrada Nacional 10
2685 SACAVEM
Tel: +351-1-9550021/ Ext. 1151
Fax: +351-1-9941525
E-mail: luisp@itn1.itn.pt

Dr. Maria Fernanda da SILVA
Instituto Tecnologico e Nuclear
Estrada Nacional 10
2685 SACAVEM
Tel: +351-1-9550021
Fax: +351-9941525
E-mail: mfs@alf1.cii.fc.ul.pt

Dr. Rui Coelho da SILVA
Instituto Tecnologico e Nuclear
Estrada Nacional 10
2685 SACAVEM

Tel: +351-1-9550021/ Ext. 1121
Fax: +351-9941525
E-mail: rmcs@itn1.itn.pt

Prof. Jose Carvalho SOARES
Centro de Fisica Nuclear
da Universidade de Lisboa
Avenida Prof. Gama Pinto 2
P-1699 LISBOA Codex

Tel: +351-1-7904985
Fax: +351-1-7954288
E-mail: soaresjc@alf1.cii.fc.ul.pt

SPAIN

Dr. Miguel Angel RESPALDIZA
Centro Nacional de Aceleradores
Parque Tecnologico Cartuja'93
Avda. Thomas A. Edison s/n, Isla de la Cartuja
41092 SEVILLA

Tel: +34-95-4460553
Fax: +34-95-4460145
E-mail: respaldiza@cica.es

UNITED KINGDOM

Dr. Mark BREESE
Surrey University

Tel:
Fax:
E-mail: m.breese@cern.ch

UNITED STATES OF AMERICA

Dr. Michael NASTASI
Los Alamos National Laboratory
MS-K765
LOS ALAMOS, NM 87545

Tel: +1 505-667-7007
Fax: +1 505-665-2992
E-mail: nasty@lanl.gov

INTERNATIONAL ORGANISATIONS

Dr. Joao Guilherme CORREIA
Div. EP/SC, CERN
CH-1211 GENEVA 23, Switzerland

Tel: 0041 22 767 64 91
Fax: 0041 22 767 89 90
E-mail: guilherme.correia@cern.ch

Dr. Claes NORDBORG
OECD Nuclear Energy Agency
Le Seine St-Germain
12, Boulevard des Iles
92130 ISSY-LES-MOULINEAUX, France

Tel: +33-0-14524-1090
Fax: +33-0-14524-1110
E-mail: nordborg@oecd.org
nordborg@nea.fr

** Regrets to have been unable to attend.*

OECD PUBLICATIONS, 2, rue André-Pascal, 75775 PARIS CEDEX 16
PRINTED IN FRANCE
(66 1999 04 1 P) ISBN 92-64-17025-1 – No. 50583 1999